

**UNIVERSIDADE DE SÃO PAULO  
INSTITUTO DE FÍSICA DE SÃO CARLOS**

**Krissia Zawadzki**

**Density-functional theory for single-electron transistors**

**São Carlos**

**2018**



**Krissia Zawadzki**

## **Density-functional theory for single-electron transistors**

Thesis presented to the Graduate Program  
in Physics at the Instituto de Física de São  
Carlos, Universidade de São Paulo, to obtain  
the degree of Doctor in Science.

Concentration area: Basic Physics

Advisor: Prof. Dr. Luiz Nunes de Oliveira  
Co-advisor: Profa. Dra. Irene D'Amico

**Corrected version**

**(Original version available on the Program Unit)**

**São Carlos**  
**2018**

I AUTHORIZE THE REPRODUCTION AND DISSEMINATION OF TOTAL OR PARTIAL COPIES OF THIS DOCUMENT, BY CONVENCIONAL OR ELECTRONIC MEDIA FOR STUDY OR RESEARCH PURPOSE, SINCE IT IS REFERENCED.

Zawadzki, Krissia

Density-functional theory for single-electron  
transistors / Krissia Zawadzki; advisor Luiz Nunes de  
Oliveira; co-advisor Irene D'Amico - revised version --  
São Carlos 2018.

168 p.

Thesis (Doctorate - Graduate Program in Física Básica) -  
- Instituto de Física de São Carlos, Universidade de São  
Paulo - Brasil , 2018.

1. Density functional theory. 2. Numerical  
renormalization-group. 3. Kondo effect . 4. Single  
electron transistor. I. Oliveira, Luiz Nunes de, advisor.  
II. D'Amico, Irene, co-advisor. III. Title.

*In memory of Andrzej Zawadzki, Regina Zawadzka and Eduardo Zawadzki*



## **ACKNOWLEDGEMENTS**

I would like to express my gratitude to all people who directly or indirectly supported the work developed in the present thesis. I would like to especially thank those with whom I could share some of the steps in my path towards the PhD degree. I sincerely do not believe I could conclude this journey without their support and the kindest words will not be enough to properly acknowledge you all.

I would like to open my huge list of acknowledgements by thanking my advisor, Prof. Luiz Nunes Oliveira. Luiz, with his knowledge, patience and kindness is one of the most special human beings I have ever met in my life. Along the past ten years, Luiz has not only taught me physics, he also showed me the value of learning. With his wizard tricks to make complicated things easy, Luiz inspired me the desire to learn to share knowledge with other people. I consider him more than a mentor: an academic father without whom I would not have achieved most of the victories I had. I feel fortunate to had the opportunity to start my academic journey under his supervision and I wish one day I could make him proud to have mentored me.

Alongside with Luiz, my co-advisor, Prof. Irene D'Amico has a special place in my acknowledgements list. Irene is an example of researcher, advisor and person. With her ability of multitasking, Irene was able not only to advise me in research, but also to showed me the importance of having a balanced life. She is my academic mother, always careful with my well being and my progress as a PhD student. We probably will never forget that sleepless nights of March, the relief in the end, and our dream to celebrate together with maracuja caipirinhas. Irene was the major responsible for the little success I achieved this year. For me, Irene represents the figure of strong woman in Physics and I would like to thank her very much for receiving me as a supervisee and for being a supportive friend during the past four years.

Besides the support of my academic parents, I am fortunate to have my family. Andressa, my beloved twin sister, is an inspiration for me: I consider her the copy “which worked”. I have to confess that, sometimes, I could rely only on her success to be happy by myself. As all siblings, we had our fights and controversies, but we were always there for each other. Only we know the difficulties we had in our childhood and teenage and the meaning of reaching a PhD level. Our ties extend frontiers. I am really proud to see her now as a post-doc in Copenhagen after all the mess that happened last year. I am grateful for the few times she let me share my fears and made me calm. Equally important was the support of my mother, Jane and my aunt, Lelzinda. Zinda was one of the most important characters of my journey in science, always encouraging me and Andressa to study and to follow our dreams.

A very special family member I have to devote all my gratitude is Vinicius. Even though I tried to resist in assuming that he has become my family, I can now admit that we are a family indeed. During the last 7 years, Vinicius has been my love and my best friend, a person with whom I could share everything and who has always been there for me. We took care of each other, respecting our differences. It might sound exaggerating, but I doubt I could reach the last sentence of this thesis without Vinicius in my life these last months. Neither the most colorful picture nor the most beautiful speech are enough to thank him for everything he has been doing for me. I also would like to thank his family, who received me with open arms as a new daughter.

I would like to thank my closest friends Joseana McGyver, Marta, Thereza and Paulo Matias. Joseana has been a special friend for me, always listening, always there for everything. I wish she could believe how great she is in all aspects. Marta has become my mother in São Carlos and Thereza my younger sister. We all have many things in common and worked together in difficult times as family does. Paulo was one of the most brilliant friends I have met and I would like to thank him infinitely for all the support as a friend and as our “stackoverflow” guy.

My special acknowledgements to my group colleagues in Brazil, Celso and Luiz Henrique; and, in York, Marta, Marcela and Amy. I feel fortunate to have met these friends in my research journey and I would like to thank all of them for the support in academia and life. I have a special gratitude for Celso’s family, including him, Linda, Maria Cecilia and Davi. Even though my friendship with Luiz is recent, our time together has made us close friends and I am sure, in future, we will remember our “PhD times” with laughs and good thoughts. Marta is one of the characters in my list of strong women and I have no words to describe how happy I am for her recent achievements. She has been living in a special part of my heart as my Spanish sister and I am sure she will be there forever. Marcela is my Colombian sister, with whom I shared also funny adventures, including a duck attack and those days in which we wrote a whole paper from scratch in a week. I have to thank Amy for the good chat times in York and, importantly, for her politeness and her “fudge care service”. I also have to thank Simone and Milan, my “postdoctoral brothers”. Milan, I would never forget your ability to find random songs suiting random moments and your kindness. I would like to thank the efforts of all these four special mates in making me believe I could be a good researcher, even though I am still doubting it.

I cannot let out of this list those friends who were able to help me with motivation words, hugs, good vibrations and kindness even though the time and spatial scales had separated us physically. They are: Leandro, Luísa, Cayke Barbie, Hudson, Gustavo “Bixão”, Aline Ink, Camila Beli, Tiago “Tafarel”, Tatiana, Schlosser and Foca. People which have just been recently in my life but offered their support in very important moments which happened during these past months: Guilherme Baiano, Renata, Carlos “Charlinho”, Iara,

Rosana, Kharen, Natália and Camila Cardoso. Your company in nice chat sections, boosted with coffee, tea, beer, cookie and ice cream has made my life sweeter. Of course, I could not forget this special group of ladies and gentlemen from the Python community of São Carlos (grupy Sanca and Pyladies) and the friends who were in the SIFSC's organising committee in the IV and V editions of the event.

I think this is a special opportunity to also thank the professors who were responsible for my learning process during my journey in Physics: Liderio, Valter, Gonzalo, Luciano, Paulo Miranda, Reginaldo, Tereza, Agostinho, Egues, Leonardo Maia, Rodrigo and Miled. Also, I have to thank the professors with whom I had the opportunity to work with (as a TA or as a monitor) in various activities at IFSC: Tito, Fernando, Diogo Soares, Sérgio, Fred, João Renato. Also, I would like to thank all the students with whom I have been in contact while being a monitor or a TA at IFSC. Additionally, I would like to express my gratitude to the non-local professors who gently offered their help in my research career as collaborators: Adrian, Vivian and Roberto. The contributions of all of them were very important to keep my passion for science warmed up and in constant heating.

I would like to thank Dr. Ana Luísa, Dr. Celso, Dra. Ada Letícia and Gisele for being my guardian angels and for helping with my physical and mental health over the past years.

I would like to acknowledge Cristina, Silvio, Ricardo, Beth, Mariana, Edvane and Lhaís. They integrate the team of most efficient and kind secretaries at IFSC. Also, I would like to thank the librarians Neusa and Cristina for the support with references and revision of this document.

Finally, I acknowledge CNPq for the financial support in my PhD scholarship in Brazil as well as CAPES and Santander for funding part of my studies abroad through mobility programs.



*“Nothing in life is to be feared, it is only to be understood. Now is the time to understand more, so that we may fear less.”*

*Marie Curie*



## ABSTRACT

ZAWADZKI, K. **Density-functional theory for single-electron transistors.** 2018. 168p. Thesis (Doctor in Science) - Instituto de Física de São Carlos, Universidade de São Paulo, São Carlos, 2018.

The study of transport in nano-structured devices and molecular junctions has become a topic of great interest with the recent call for quantum technologies. Most of our knowledge has been guided by experimental and theoretical studies of the single-electron transistor (SET), an elementary device constituted by a quantum dot coupled to two otherwise independent free electron gases. The SET is particularly interesting because its transport properties at low temperatures are governed by the Kondo effect. A methodological difficulty has nonetheless barred theoretical progress in describing accurately realistic devices. On the one hand, Density-Functional Theory (DFT), the most convenient tool to obtain the electronic structure of complex materials, yields only qualitatively descriptions of the low-temperature physical properties of quantum dot devices. On the other hand, a quantitative description of low-temperature transport properties of the SET, such that obtained through the solution of the Anderson model via exact methods, is nonetheless unable to account for realistic features of experimental devices, such as geometry, band structure and electron-electron interactions in the electron gases. DFT describes the electron gases very well, but proves inadequate to treat the electronic correlations introduced by the quantum dot. This thesis proposes a way out of this frustrating dilemma. Our contribution is founded on renormalization-group (RG) concepts. Specifically, we show that, under conditions of experimental interest, the high and low temperatures regimes of a SET corresponds to the weakly-coupling and strongly-coupling fixed points of the Anderson Hamiltonian. Based on an RG analysis, we argue that, at this low-temperature fixed point, the entanglement between impurity and gas-electron spins introduces non-local correlations that lie beyond the reach of local- or quasi-local-density approximations, hence rendering inadequate approximations for the exchange-correlation energy functional. By contrast, the weak-coupling fixed point is within the reach of local-density approximations. With a view to describing realistic properties of quantum dot devices, we therefore propose a hybrid self-consistent procedure that starts with the weak-coupling fixed point and takes advantage of a reliable numerical method to drive the Hamiltonian to the strong-coupling fixed point. Our approach employs traditional DFT to treat the weak-coupling system and the Numerical Renormalization-Group (NRG) method to obtain properties in the strong-coupling regime. As an illustration, we apply the procedure to a single-electron transistor modeled by a generalized one-dimensional Hubbard Hamiltonian. We analyze the thermal dependence of the conductance in the SET and discuss its behavior at low-temperatures, comparing our results with other self-consistent approaches and with experimental data.

**Keywords:** Density-functional theory. Numerical renormalization-group. Kondo effect. Single-electron transistor.

## RESUMO

ZAWADZKI, K. **Teoria do funcional da densidade para transístores de um elétron.** 2018. 168p. Tese (Doutorado em Ciências) - Instituto de Física de São Carlos, Universidade de São Paulo, São Carlos, 2018.

O estudo de propriedades de transporte em dispositivos nano estruturados e junções moleculares tornou-se um tópico de grande interesse com a recente demanda por novas tecnologias quânticas. Grande parte do nosso conhecimento tem sido guiado por trabalhos experimentais e teóricos de um dispositivo conhecido como transístor de um elétron (SET), o qual é constituído por um ponto quântico acoplado a dois gases de elétrons independentes. O SET é particularmente interessante devido as suas propriedades de transporte a baixas temperaturas, as quais são governadas pelo efeito Kondo. Uma dificuldade metodológica, no entanto, tem barrado novos avanços teóricos para se obter uma descrição precisa de dispositivos realistas. Por um lado, a teoria do funcional da densidade (DFT), uma das ferramentas mais convenientes para calcular a estrutura eletrônica de materiais complexos, provê uma descrição apenas qualitativa das propriedades de transporte de transístores quânticos a baixas temperaturas. Por outro lado, uma descrição quantitativa satisfatória do SET a baixas temperaturas, tal como a modelagem e solução do modelo de Anderson via métodos exatos, é incapaz de levar em conta características realistas de dispositivos complexos, tal como geometria, estrutura de bandas e interações inter eletrônicas nos gases de elétrons. Embora a DFT os descreva bem, ela é inadequada para tratar correlações introduzidas pelo ponto quântico. Na presente tese propomos uma alternativa para este dilema. Nossa contribuição é fundamentada em conceitos de grupo de renormalização (RG). Especificamente, mostramos que, em condições de interesse experimental, os regimes de altas e baixas temperaturas em um SET correspondem aos pontos fixos de acoplamento fraco e forte do Hamiltoniano de Anderson. Baseando-nos em na análise do RG, mostramos que, no ponto fixo de baixas temperaturas, o emaranhamento entre a impureza e os spins dos gases eletrônicos introduz correlações não-locais que não podem ser descritas com abordagens DFT baseadas em aproximações locais ou quase locais para o potencial de troca e correlação. Em contraste, o ponto fixo de acoplamento fraco pode ser descrito por aproximações locais. Com o objetivo de obter uma descrição realista das propriedades de transístores quânticos, propomos um procedimento auto-consistente que começa do ponto fixo de acoplamento fraco e se aproveita de um método numérico eficiente para levar o Hamiltoniano para o ponto fixo de acoplamento forte. Nossa abordagem emprega DFT para tratar o sistema no limite de acoplamento fraco e o método de Grupo de Renormalização Numérico (NRG) para obter propriedades no regime de acoplamento forte. Como ilustração, aplicamos o procedimento para um transístor de um elétron modelado através do Hamiltoniano de Hubbard generalizado. Analisamos a dependência térmica da

condutância no SET discutindo seu comportamento a baixas temperaturas e comparamos nossos resultados com outras abordagens auto-consistentes e resultados experimentais.

**Palavras-chave:** Teoria do funcional da densidade. Grupo de renormalização numérico. Efeito Kondo. Transistor de um elétron.

## LIST OF FIGURES

Figure 1 – Jacob ladder with the most used approximations for density functionals.	29
Figure 2 – single-electron transistor (SET).	34
Figure 3 – Equivalent electric circuit used to represent the SET.	35
Figure 4 – Energy diagram for the modes (on and off) of a single-electron transistor and Coulomb blockade.	36
Figure 5 – Current (conductance) peak oscillations observed in a single-electron transistor in Coulomb blockade regime.	37
Figure 6 – Resistivity in materials and the Kondo effect.	38
Figure 7 – The Kondo screening cloud.	42
Figure 8 – Kondo effect in a single-electron transistor.	43
Figure 9 – Experimental realization of a single-electron transistor (SET) and measurement of the conductance as a function of gate voltage in the presence of the Kondo effect.	44
Figure 10 – Model for a single-electron transistor (SET).	45
Figure 11 – Conductance $\mathcal{G}(T)$ in a SET as a function of the scaled temperature $T/T_K$ .	51
Figure 12 – Occupation number $n_d$ and assymetry index $\alpha_s$ obtained from experimental points by Grobis et al. <sup>1</sup> .	52
Figure 13 – The main contribution of DFT to Quantum Mechanics was simplifying the solution of the many-body problem by coding all the information in the density $n(\mathbf{r})$ - an object of three coordinates - simpler than the many-body wave function $ \Psi(\mathbf{r}_1, \mathbf{r}_2, \dots, \mathbf{r}_N)\rangle$ , - an object of $3N$ variables.	54
Figure 14 – Self-consistent cycle proposed by Kohn and Sham.	60
Figure 15 – Functionals for the exchange-correlation energy and the exchange-correlation potential within the BALDA.	64
Figure 16 – Results for density functional calculations using BALDA for one dimensional optical lattices submitted to an asymmetric trapping potential.	66
Figure 17 – Results of self-consistent calculations using FVC BALSDA for obtaining the ground-state density and magnetization profiles of an open Hubbard chain with $L = 100$ sites, $N_\uparrow = 30$ , $N_\downarrow = 20$ fermions.	67
Figure 18 – Exchange-correlation functional as a function of the occupation number obtained through the parametrization due to Bergfield.	69
Figure 19 – Ground state conductance $\mathcal{G}_d$ in a SET as a function of the gate voltage $V_G$ obtained from self-consistent calculations using Bergfield's parametrization.	70

Figure 20 – Ground-state conductance $\mathcal{G}_d$ in a SET as a function of the gate voltage $V_G$ in the presence of a scattering potential $W$ to the leads for $\Gamma = 0.004D$ and $U/\Gamma = 1$ and $U/\Gamma = 10$ .	71
Figure 21 – Ground-state conductance $\mathcal{G}_d$ in a SET as a function of the gate voltage $V_G$ in the presence of a scattering potential $W$ to the leads for $\Gamma = 0.01D$ and $U/\Gamma = 1$ and $U/\Gamma = 10$ .	72
Figure 22 – Example of the linear approximation over the dispersion relation of the non-interacting homogenous Hubbard Hamiltonian.	80
Figure 23 – Logarithmic discretization of the conduction band.	82
Figure 24 – Gap from $\epsilon = 0$ of eq. (4.38) as a function of the lattice size $L$ from $L = 2$ to $L = 10^6$ .	85
Figure 25 – Example of distribution of momenta $k$ for $L = 500$ sites for $\Lambda = 3.0$ , $M = 3$ and $\kappa = 32$ .	87
Figure 26 – Example of logarithmic discretization of a sinusoidal band $\epsilon_k = -2t \sin k$ for $L = 500$ sites for $\Lambda = 3.0$ , $M = 3$ and $\kappa = 32$ .	88
Figure 27 – Iterative growing of the Lanczos chain for the single impurity Anderson model.	92
Figure 28 – Iterative cycle of the NRG algorithm to impurity problems.	94
Figure 29 – Single-particle levels $\tilde{\varepsilon}_j$ ( $j = 0, \dots, 4$ ) of the renormalized Anderson Hamiltonian $\mathcal{H}_N$ along odd iterations $N$ for $\Gamma = 10^{-5}D$ .	97
Figure 30 – Evolution of eigenvalues of the Hamiltonian $\mathcal{H}_N$ along iterations $N$ for the symmetric case: $\Gamma = 0.01$ , $U = 0.5$ and $\epsilon_d = -0.25$ .	98
Figure 31 – Conductance $\mathcal{G}$ as a function of the gate voltage $V_G$ for temperatures ranging from $T \gg T_K$ and $T \ll T_K$ .	101
Figure 32 – Universal zero bias conductance $\mathcal{G}_s$ scaled by the Kondo temperature and the fixed points of the symmetric Anderson Hamiltonian for a single-electron transistor.	102
Figure 33 – Hybrid self-consistent calculation combining DFT and NRG calculations to solve the Kohn-Sham Anderson system.	111
Figure 34 – Schematic representation of the mapping the Anderson Hamiltonian into a Hubbard-like model with inhomogeneous parameters: hoppings $t_j$ , on-site Coulomb repulsion $U_j$ and on-site external potentials $V_j$ .	113
Figure 35 – Dispersion relation obtained in the DFT module implementing the self-consistent Kohn-Sham calculation to solve the band Hamiltonian in eq. (5.4) for $L = 1000$ and $U_b/t = 0, 0.01, 0.1, 0.5$ and $1.0$ and no scattering potential $W^* = 0$ .	114
Figure 36 – Lanczos coefficients $t_n$ (cyan empty squares) and $\eta_n$ (magenta crosses) calculated for the band Hamiltonian in eq. (5.4) with $L = 1000$ , $U_b/t = 0.1$ and $W^*/t = -0.1$ .	115

Figure 37 – Comparison of the conductances $\mathcal{G}_d$ and $\mathcal{G}_0$ as a function of the temperature $T$ for $L = 1000$ and $L \rightarrow \infty$ and few model parameters:	116
Figure 38 – Fitting of NRG data points to the universal map in eq. (2.43) adjusting the Kondo temperature $T_K$ and the phase shift $\delta$ .	117
Figure 39 – Kondo screening cloud in a single-electron transistor from the weakly to the strongly coupled regimes.	120
Figure 40 – Conductance $\mathcal{G}_d$ in a SET as a function of the gate voltage $V_G$ and its thermal dependence in different coupling regimes.	123
Figure 41 – Conductance $\mathcal{G}_d$ in a SET with a conduction band with finite momenta as a function of the gate voltage $V_G$ and its thermal dependence in different coupling regimes.	125
Figure 42 – Results for the ground-state conductance $\mathcal{G}_d(T \rightarrow 0)$ as a function of the gate voltage $V_G$ obtained with different approaches from the weakly to the strong correlated regime.	128
Figure 43 – Ground-state conductance $\mathcal{G}_d(T \rightarrow 0)$ as a function of the gate voltage $V_G$ obtained with the KSA procedure for a homogeneous conduction band with coupling $U_b = 0.1t$ and model parameters $\Gamma = 2.0D$ , $U = 10.0D$ (open blue diamonds), compared with results for $U_b = 0.0$ (red solid line).	129
Figure 44 – Results for the ground-state conductance $\mathcal{G}_d(T \rightarrow 0)$ as a function of the gate voltage $V_G$ obtained with the KSA procedure for a homogeneous conduction band with applied potential $W = -0.3D$ , coupling $U_b = 0.1t$ (blue diamonds) and model parameters $\Gamma = 2.0D$ , $U = 10.0D$ and comparison with results for $U_b = 0.0$ (solid red lines).	130
Figure 45 – Results for the ground-state conductance $\mathcal{G}_d(T \rightarrow 0)$ as a function of the gate voltage $V_G$ obtained with the KSA procedure for a homogeneous conduction band with coupling $U_b = t$ (blue diamonds) and model parameters $\Gamma = 2.0D$ , $U = 10.0D$ and comparison with results for $U_b = 0.0$ (solid red lines).	132
Figure 46 – Results for the ground-state conductance $\mathcal{G}_d(T \rightarrow 0)$ as a function of the gate voltage $V_G$ obtained with the KSA procedure for a homogeneous conduction band with applied potential $W = -0.3D$ , coupling $U_b = t$ (blue diamonds) and model parameters $\Gamma = 2.0D$ , $U = 10.0D$ and comparison with results for $U_b = 0.0$ (solid red lines).	132
Figure 47 – Sectors of charge and spin active in the iteration $N = -1$ (cyan squares) and their corresponding number of states (white numbers). This iteration comprises a chain with a single site representing the impurity level $c_d$ , whose possible states are depicted on the right.	153



## LIST OF TABLES

Table 1 – Off-diagonal matrix elements of $H_N$ . The factors appearing in front of the invariants correspond to the Clebsch-Gordan coefficients $\alpha_{g,g'}$ . Unlisted combinations of genders $g$ and $g'$ vanish. . . . .	157
--	-----



## **LIST OF ABBREVIATIONS AND ACRONYMS**

BA	Bethe Ansatz
BALDA	Bethe Ansatz Local Density Approximation
DMRG	Density Matrix Renormalization Group
DFT	Density Functional Theory
FL	Frozen Level fixed point
FP	Fixed Point
HK	Hohenberg-Kohn
HF	Hartree-Fock
KS	Kohn-Sham
KSA	Kohn-Sham Anderson
LDA	Local Density Approximation
LSDA	Local Spin Density Approximation
LM	Local Moment fixed point
NRG	Numerical Renormalization Group
RG	Renormalization Group
SET	Single electron transistor



## CONTENTS

<b>1</b>	<b>INTRODUCTION</b>	<b>27</b>
1.1	Transport in quantum dots and novel technologies	27
1.2	Density Functional Theory, Strongly Correlated Systems and the Kondo effect	28
1.3	Density Functional Theory and the Renormalization-Group: a fruitful collaboration	30
<b>2</b>	<b>KONDO EFFECT IN NANO STRUCTURES</b>	<b>33</b>
2.1	Single-electron transistor and quantum dot technologies	33
2.2	The Kondo effect and its manifestation in quantum dots	37
2.3	Anderson Hamiltonian for a single-electron transistor	43
2.3.1	Zero-bias conductance and universal mapping	47
<b>3</b>	<b>DENSITY FUNCTIONAL THEORY</b>	<b>53</b>
3.1	Basic elements in Density Functional Theory	53
3.1.1	Hohenberg-Kohn Theorems	55
3.1.2	Kohn-Sham system and self-consistent calculation	57
3.1.3	The exchange-correlation functional	60
3.1.3.1	Local Density Approximation (LDA)	62
3.2	Density Functional Theory and strongly correlated systems	62
3.2.1	Bethe Ansatz Local Density Approximation	63
3.3	DFT and the Kondo problem	66
3.3.1	Parametrization of the exchange-correlation functional based on the Bethe Ansatz solution of the Anderson Hamiltonian	66
<b>4</b>	<b>RENORMALIZATION-GROUP</b>	<b>73</b>
4.1	Model Hamiltonians and the Renormalization-Group	73
4.1.1	Renormalization-Group	76
4.2	Numerical Renormalization-Group	77
4.2.1	Logarithmic discretization	79
4.2.1.1	Logarithmic Discretization of bands with finite degrees of freedom	83
4.2.2	Lanczos transformation	88
4.2.3	Iterative Diagonalization	90
4.3	Numerical Renormalization-Group analysis of the Kondo problem	93
4.3.1	Local Moment	102
4.3.2	Kondo regime	103

4.3.3	Frozen level . . . . .	103
4.3.4	Fixed points and Density Functional Theory . . . . .	104
<b>5</b>	<b>THE KOHN-SHAM ANDERSON SYSTEM AND THE HYBRID SELF-CONSISTENT CALCULATION . . . . .</b>	<b>107</b>
<b>5.1</b>	<b>The non-interacting Kohn-Sham Anderson system . . . . .</b>	<b>107</b>
5.1.1	Applying the Kohn-Sham Anderson formulation for a single-electron transistor	112
<b>6</b>	<b>RESULTS . . . . .</b>	<b>119</b>
<b>6.1</b>	<b>Coupling regimes and the Kondo screening cloud in a single-electron transistor . . . . .</b>	<b>119</b>
6.1.1	Conductance in the continuum limit of conduction states vs bands with finite number of degrees of freedom . . . . .	122
<b>6.2</b>	<b>Ground-state conductance from the Kohn-Sham Anderson hybrid procedure . . . . .</b>	<b>124</b>
<b>7</b>	<b>CONCLUSIONS AND FUTURE PERSPECTIVES . . . . .</b>	<b>133</b>
	<b>REFERENCES . . . . .</b>	<b>137</b>
	<b>APPENDIX . . . . .</b>	<b>145</b>
	<b>APPENDIX A – DENSITY FUNCTIONAL APPROXIMATIONS BEYOND THE LOCAL DENSITY APPROXIMATION . . . . .</b>	<b>147</b>
<b>A.1</b>	<b>Generalized Gradient Approximation (GGA) . . . . .</b>	<b>147</b>
<b>A.2</b>	<b>Meta GGA . . . . .</b>	<b>148</b>
<b>A.3</b>	<b>Hybrid functionals and the Adiabatic Connection . . . . .</b>	<b>148</b>
<b>A.4</b>	<b>Random Phase Approximation (RPA) . . . . .</b>	<b>149</b>
	<b>APPENDIX B – THE NUMERICAL RENORMALIZATION-GROUP IMPLEMENTATION . . . . .</b>	<b>151</b>
<b>B.1</b>	<b>Sectors (<math>Q, S</math>), primitive and truncated basis . . . . .</b>	<b>151</b>
<b>B.2</b>	<b>Calculating the matrix elements of the Hamiltonian <math>H_N</math> . . . . .</b>	<b>155</b>
<b>B.3</b>	<b>Calculation of invariants . . . . .</b>	<b>157</b>
<b>B.4</b>	<b>Calculation of properties . . . . .</b>	<b>158</b>
	<b>APPENDIX C – ANALYTICAL STEPS WITHIN THE NUMERICAL RENORMALIZATION GROUP . . . . .</b>	<b>161</b>
<b>C.1</b>	<b>Lanczos coefficients in Wilson's formulation . . . . .</b>	<b>161</b>

<b>C.2</b>	<b>Numerical Renormalization-Group approach for impurity models . . . . .</b>	<b>161</b>
C.2.1	Continuous base . . . . .	162
C.2.2	Logarithmic discretization . . . . .	163
C.2.3	Lanczos transformation . . . . .	166



## 1 INTRODUCTION

In the last four decades, analytical reasoning combined with numerical methods have fuelled explosive expansion of condensed matter theory. At the same time, novel techniques have ignited parallel expansion in laboratories. We have witnessed progress in manipulation and probing, which have allowed control of matter at the atomic scale and observation of quantum phenomena with remarkable accuracy. Examples are found in nuclear magnetic resonance, scanning tunneling microscopy and lithography.<sup>2</sup> On the theoretical front, while model Hamiltonians and exact techniques have guided our understanding of quantum phenomena, numerical methods have yielded qualitative and quantitative understanding of many condensed matter systems.<sup>3</sup> To cite but a few examples of the most reliable tools allowing diagonalization and computation of physical properties for model Hamiltonians, we mention the Bethe Ansatz (BA)<sup>4</sup> exact diagonalizations; and numerical implementations of Renormalization-Group (RG) algorithms.<sup>3,5,6</sup> Beyond model Hamiltonians, the study of materials has gained a new perspective thanks to computations based on Density Functional Theory (DFT).<sup>7,8</sup>

In this context, the collaboration between theoretical, experimental and computational physicists were crucial to bring Quantum Mechanics to its current state of the art: the age of quantum technologies.<sup>9</sup> A new generation of solid state materials and the advances in lithography allowed to reduce the size of transistors, below the semiclassical scale. Semiconductor devices can be built on the scale of few nanometers and allow to control a single-electron in the so-called quantum dots.<sup>10</sup> Before coming to the laboratory and, then, to our daily lives, these novel technologies have been largely investigated theoretically and probed via computational simulations. Importantly, by means of theoretical and numerical studies, it is possible to study quantum devices suiting novel technologies and also devise materials with special properties.

### 1.1 Transport in quantum dots and novel technologies

The single-electron transistor (SET) has been one of the most studied quantum dot device.<sup>11</sup> Proposed in the 80's, the SET is one of the most recurrent systems for studying quantum tunneling. This elementary nano-structured device has gained special attention because it displays the Kondo effect, an anomalous behavior of the conductance at low temperatures.<sup>12</sup> The Kondo effect in the SET is the most enhanced signature of the strongly correlated regime, a challenging limit to tackle in the study of quantum phenomena technologies. In the presence of strong correlations, quantum interactions become complex and give rise to interesting phenomena, such as phase transitions and

critical properties. In developing novel quantum technologies, it is therefore crucial to understand how the strongly correlated regime arise.

In the context of transport through the SET, most of our understanding was guided by the Anderson Hamiltonian,<sup>13</sup> which models the device and yields excellent agreement with universal aspects of experimental results.<sup>14,15</sup> Importantly, this theoretical study is possible analytically via BA or numerically via the Numerical Renormalization-Group (NRG).<sup>16</sup> The increasing complexity of nano-structured devices that have followed the SET has made challenging the task of modeling them and, in particular, describing accurately their transport properties in the strongly correlated regime.<sup>17</sup> In the latter, the interactions are highly affected by the electronic structure of materials, introducing a non-trivial ingredient defeating the traditional formulation in terms of analytical solutions obtained for model Hamiltonians.<sup>18</sup> What is worse, even at the level of approximation based on model Hamiltonians, finding exact analytical solutions is limited to few situations. In that sense, a general approach to the description of quantum devices in complex regimes must include a numerical framework allowing for a realistic description of materials, so Density Functional Theory seems to be a promising route to be explored.

## 1.2 Density Functional Theory, Strongly Correlated Systems and the Kondo effect

Density Functional Theory was one of the most important scientific advances of the XX-th century. At the core of DFT there are two ingredients. The first is the existence of a bijective relation between the ground-state electronic density and the ground-state wave function, established by the so-called Hohenberg-Kohn Theorem.<sup>19</sup> The second is the Kohn-Sham formulation,<sup>20</sup> according to which an interacting problem can be mapped onto a fictitious non-interacting system subject to an external potential that reproduces the density of the original problem.

From the birth of DFT in the 60's to the contemporary massive use of packages for ab-initio computations, the density functional approach has evolved tremendously, becoming the favorite tool for material science and electronic structure calculations.<sup>21</sup> Despite the progress, there are challenges in successfully applying density functional approaches to general quantum problems.<sup>22,23</sup> For instance, DFT fails to predict gaps in semiconductors accurately, or to describe chemical reactions. Its extension to excited states remains difficult. Beyond these examples, one the most known Achilles' heel of DFT is the treatment of strongly correlated systems, a serious limitation that bars application to quantum devices.<sup>22–24</sup>

Many density functionals have been proposed in an attempt to describe or handle certain classes of materials, nowadays, there are thousands of available functionals. The level of precision of the approximations is followed by their complexity: the more complex

the more accurate. This relation is usually illustrated as the Jacob ladder for DFT, as in Fig. 1.

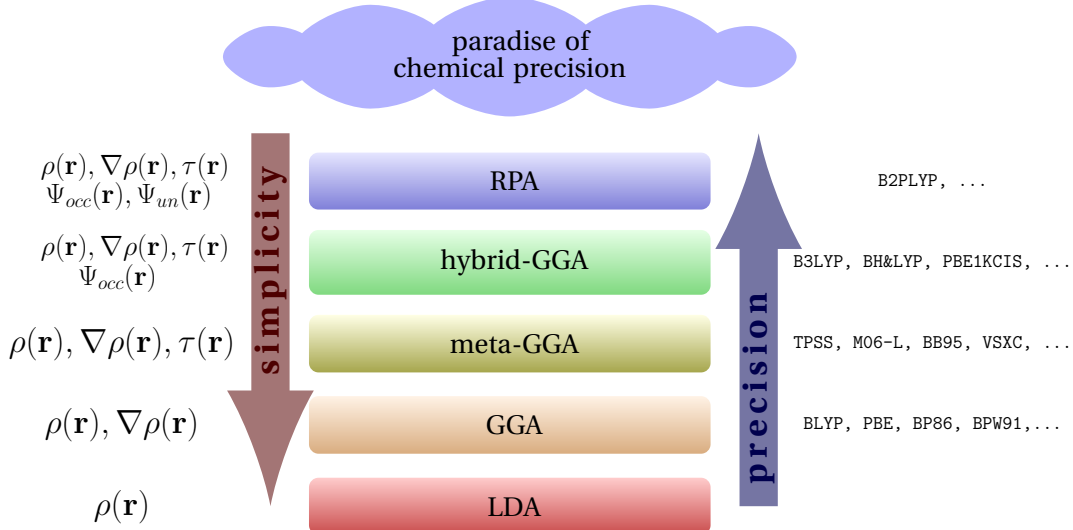


Figure 1 – Jacob ladder with the most used approximations for density functionals. Advances in DFT were mainly motivated by the need to model realistic systems and have allowed the construction of new functionals suiting them. The more precise the approximations, the more complex they are, meaning that the approximation to the exchange-correlation functional will depend on a number of ingredients. In the first stair, we have the so-called Local Density Approximation (LDA), in which the exchange-correlation functional depends only on the local density of an uniform electron gas. The level immediately above, known as Generalized Gradient Approximation (GGA), the gradient of the density is included. Following GGA, we have the meta-GGA, in which the kinetic energy enters as a correction to the exchange-correlation functional. In hybrid GGA, beyond the dependence on the density  $\rho(r)$ , its gradient  $\nabla\rho(r)$ , and the kinetic energy  $\tau(r)$ , the exchange-correlation functional also accounts for occupied orbitals  $\Psi_{occ}$  of the Kohn-Sham system. Finally, the most complex approximation is known as Random Phase Approximation, in which the unoccupied orbitals  $\Psi_{un}$  are also included. A calculation at the level of RPA can be as complex as solving the many-body Schrodinger equation.

Source: By the author.

The same trend of material science is followed in the density functional treatment of strongly correlated systems. Up to date, the few existing approaches were devised for specific problems, serving in most cases only for pedagogical purposes given their restrict applicability to more sophisticated systems. In this context, the Bethe Ansatz (BA)<sup>25</sup> has been used to extract approximations for density functionals upon which parametrized expressions are constructed. Among the most well known parametrizations, there is the Bethe Ansatz Local Density Approximation (BALDA),<sup>26</sup> an approximation for the exchange-correlation functional derived from the the Bethe Ansatz solution of the one-dimensional Hubbard model. The BALDA approach has been successfully applied to study quantum systems modeled by Hubbard-like Hamiltonians, such as ultracold fermions and atoms in optical lattices.<sup>26–30</sup> With the same spirit of BALDA, a density functional

approach to describe the ground-state conductance in the single-electron transistor was proposed by Bergfield.<sup>31</sup> In their work, a parametrization for the exchange-correlation functional potential was obtained from the BA solution of the Anderson Hamiltonian, through which they were able to reproduce the conductance plateau characteristic of the Kondo effect. As mentioned, in the study of general semiconductor nano-structures, even considering their impressive performance, an approach similar to the Bergfield is limited, as it requires the exact solution of the model upon which the approximation for the functional can be carried out.

### **1.3 Density Functional Theory and the Renormalization-Group: a fruitful collaboration**

In order to tackle the strongly correlated regime of quantum devices, the development of approximations for the exchange-correlation functional would require to go beyond the first step of the Jacob ladder - the so-called Local Density Approximation (LDA), as the strong correlated regime gives rise to long range interactions. Ideally, the evolution of DFT would result in a general methodology, from which one would be able to compute properties of realistic systems with accuracy comparable to the best available experimental techniques.

Very recently, approaches alternative to parametrizations have been appearing in the spotlights of the DFT community. Density Functional approaches integrated with well-established many-body methods, such as the Density Matrix Renormalization-Group (DMRG),<sup>32,33</sup> the Quantum Monte Carlo (QMC)<sup>34</sup> and Machine Learning (ML) have appeared in the literature with promising results for strongly correlated systems.<sup>24,33,35–37</sup>

The accurate numerical frameworks offered by DFT calculations combined with methods based on Renormalization-Group (RG) therefore have a huge potential in the future of many-body simulations and, in particular, in applications to quantum technologies. On one side, Density Functional Theory offers a tool allowing for a highly precise electronic structure calculation, an important ingredient in the study of transport properties of quantum dots in the strongly correlated regime. On the other side, numerical implementations of the Renormalization Group method allow to simulate many-body quantum systems and their properties, from the weakly to the strongly correlated regime.

In fact, the current state-of-the-art in Density Functional and Renormalization-Group techniques invites the development of a hybrid procedure through which we can explore transport properties in nano-structured devices. The present thesis offers a concrete example. Here, we propose a generalized procedure combining Density Functional Theory and Numerical Renormalization Group calculations to obtain the transport properties of strongly correlated nano-structured devices. The basis of our method is the fixed point structure of the NRG transformation and its correspondence with the Kohn-Sham system

---

in Density Functional Theory. Specifically, we propose an iterative procedure integrating DFT and NRG computations in such a way that the transport properties of quantum devices can be computed self-consistently. In the DFT stage, parameters of quantum dot devices, such as the band structure and the hybridization function, are calculated; in the RG stage, which uses these parameters to diagonalize the Anderson Hamiltonian, the iterative flow enables to access very low temperatures. The combination yields the thermal dependence of the conductance, a function of special important because it is experimentally accessible.

To illustrate our proposal, we will apply the hybrid method to study the conductance in a single-electron transistor in the low temperature regime. The SET offers a rich testbed for our approach because there are many experimental and analytical results. In particular, the SET was subject of study in the context of DFT: as mentioned, a parametrization for the exchange-correlation functional describing a SET has been proposed and proven accurate.

We will show that the new procedure is able to accurately reproduce the zero bias conductance for the SET in all correlation regimes. Our results are compared with the ground-state conductance obtained from self-consistent DFT calculations using Bergfield's parametrization and the BALDA and exact calculations of the conductance at very low temperatures obtained through the NRG diagonalization. We show the new procedure to be able to reproduce the characteristic profile of the conductance in the presence of the Kondo effect as accurately as the parametrization specific to the SET. The excellent agreement of our results with exact NRG calculations for the SET and, crucially, the potential to be extended to general nano-structured devices, indicates the new procedure as a promising approach to the study of transport in quantum dots.



## 2 KONDO EFFECT IN NANO STRUCTURES

The Kondo effect is one the most studied problems in condensed matter physics. As a perfect example of how quantum correlations give rise to phenomena manifesting in the macroscopic world, it remained an interesting topic especially after the discovery of the Kondo effect in quantum dots in the 90's and, more recently, in new materials such as graphene.

Most of our knowledge about anomalous transport at nano scales was guided by the study of a simple device known as single-electron transistor (SET), with a wide survey of experimental and theoretical results.<sup>11, 12, 38–41</sup> In particular, the modeling of the SET in terms of the single impurity Anderson Hamiltonian provided a deep understanding of the low-temperature phenomenology of quantum devices and, in particular, how strong correlations affect their physical properties.

In this chapter, we will briefly present the single-electron transistor and explore the emergence of the Kondo effect in the low-temperature regimes. Then, we will discuss the mapping of the SET into an impurity problem modeled by the Anderson Hamiltonian and show how it allows to recover properties measured in the lab, such as the zero-bias conductance.

### 2.1 Single-electron transistor and quantum dot technologies

The single-electron transistor (SET)<sup>11</sup> was one of the first devices in which charge quantization and anomalous transport was probed at quantum scales. It was first fabricated by Fulton and Dolan<sup>42</sup> in 1987 at Bell Labs and has been further improved since then with new fabrication techniques and the introduction of new semiconductor materials.

The most elementary single-electron transistor consists of a small island of a conductive material connected to two metallic leads (source and drain) through thin oxides (tunneling junctions) and also coupled to a gate electrode through a capacitive material. Later, the metallic materials were replaced by semiconductors with depletion of two dimensional gas (2DEG). Due to its small size, the energy levels  $\epsilon_n$  of the island are discrete and spaced by  $\Delta_n$ . The island is also referred to quantum dot, given the possibility to control the number  $n_d$  of electrons that can be confined on it. The process of charging-uncharging the device is understood in terms of a simple sketch of an electrical circuit representing a SET, as shown in Fig. 3. The two tunnel junctions are represented by capacitors coupled to resistors with capacitances  $C_s$  and  $C_d$  and resistance  $R_s$  and  $R_d$ , and the three terminals allow to apply potentials  $V_s$ ,  $V_d$  and  $V_G$  to source, drain and the quantum dot, respectively. In terms of this circuit, one can define the charging energy

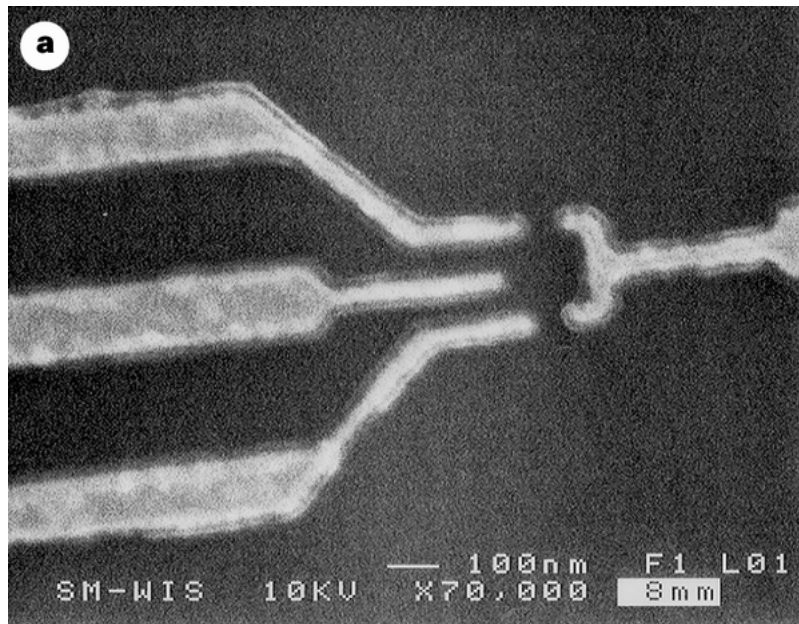


Figure 2 – single-electron transistor (SET). The most elementary SET comprises two metallic leads  $S$  (source) and  $D$  (drain) bridged by a small region known as island or quantum dot. A resistive material bridges the dot and the leads forming tunneling junctions. A gate electrode with potential  $V_G$  is coupled to the quantum dot through a capacitive material. Adjusting  $V_G$  allows to control the number of electrons  $n_d$  confined in the quantum dot. The electrons in the metallic leads form an electron gas. When an infinitesimal potential difference is applied between the  $S$  and  $D$  gases and the gate voltage is suitable adjusted, electrons can tunnel between the gases through the dot. The characteristic of the materials (resistances and capacitances), its size and the temperature of the operability ensure the tunneling of a single electron at each time. Source: GOLDHABER-GORDON et al. <sup>12</sup>

$E_c$  of the device, i.e., the energy that an electron must have to tunnel from one plate of the source capacitor  $C_S$  to the island  $C_G$  and from there to the other plate of the drain capacitor  $C_D$ . As electrons in that island interact via Coulomb electrostatic forces,  $E_c$  is defined as

$$E_c = \frac{e^2}{2C_\Sigma}, \quad (2.1)$$

where  $e$  is the elementary charge and  $C_\Sigma = C_S + C_D + C_G$  is the self capacitance of the system comprising source, drain, and gate.

A current in the device is expected when a bias  $dV = V_s - V_d$  is created between the source and drain leads. The manipulation of the potential  $V_G$  enters in the device as the key ingredients allowing the control of charging processes. By changing the gate voltage  $V_G$  (negative or positive value), it is possible to shift the energy levels  $\epsilon_n$  of the quantum dot and adjust its Fermi level  $\mu_{QD}$  to be at the Fermi level of the junctions  $\mu_s$  and  $\mu_d$ , as illustrated in Fig. 4. An electron can tunnel through the quantum dot if it receives enough energy to overcome the electrostatic barrier  $E_c$  in the island and then

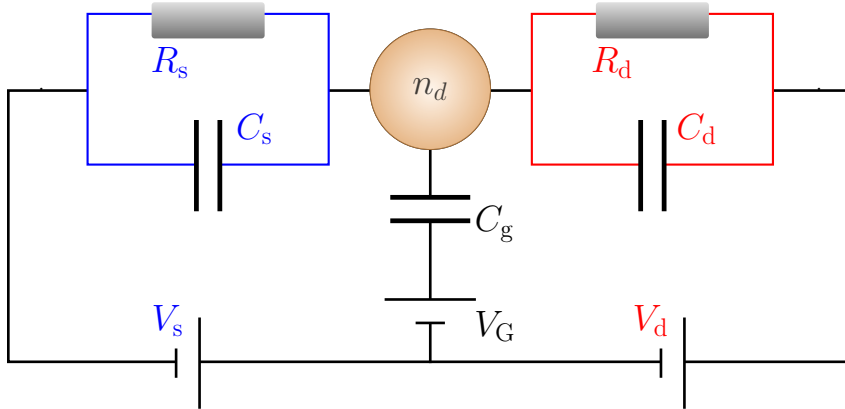


Figure 3 – Equivalent electric circuit used to represent the SET: capacitors associated to the source, drain and gate electrodes, and the tunneling barriers are represented by resistors. The circuits of the leads are represented by a parallel association of the resistors with capacitors  $R_s$  and  $C_s$  and  $R_d$  with  $C_d$ . The quantum dot is coupled to a capacitor  $C_g$  and a font for controlling the gate voltage  $V_G$ . The difference of potential between the source and drain leads are controlled by two fonts with voltages  $V_s$  and  $V_d$ , respectively.

Source: By the author.

populate one available level  $\epsilon_n$ , the level just above the Fermi level of the quantum dot. In the absence of available levels, electrons cannot flow from the source and to the drain, so that the quantum dot is occupied with a fixed number of electrons. The dot will allow transfer of one electron if an available level in the dot is aligned with the Fermi levels of the junctions. The barrier blocking transferring of charge is referred to *Coulomb blockade*. The operability of the device in the *Coulomb blockade* is constrained by three conditions: (i) the bias voltage must be lower than  $dV < e/C_\Sigma$ , (ii) the resistance of the tunneling junctions must be much higher than the quantum of resistance  $R_t = h/e^2$ , where  $h$  is the Planck constant, so that the transfer of exactly one electron at time to the quantum dot is ensured; and (iii) the temperatures must be  $k_B T \ll E_c$ , as thermal excitations can activate tunneling. In practice, these conditions translates in having very low temperatures and small capacitances.

In the zero bias regime ( $dV = 0$  or  $dV$  is infinitesimal), transport of electrons is enabled whenever  $V_G$  aligns  $\mu_{\text{QD}}$  with  $\mu_s = \mu_d$  and current is detected in multiples of  $V_G$ , so that the quantum dot is occupied with a fixed number of electrons, as in the Coulomb blockade. At low temperatures, of the order of 1K, the curve of the current versus the applied gate voltage depicts a sequence of equally spaced sharp peaks<sup>43–45</sup>, as shown in Fig. 5. The position of peaks occur at special values of  $V_G$  for which the dot is occupied by a half-integer number of electrons. The tunneling condition for the special  $V_G$  is

$$C_\Sigma V_G = e \left( n_d + \frac{1}{2} \right), \quad (2.2)$$

so that the spacing between peaks is found to occur in multiples of  $V_G = e/C_\Sigma$ .

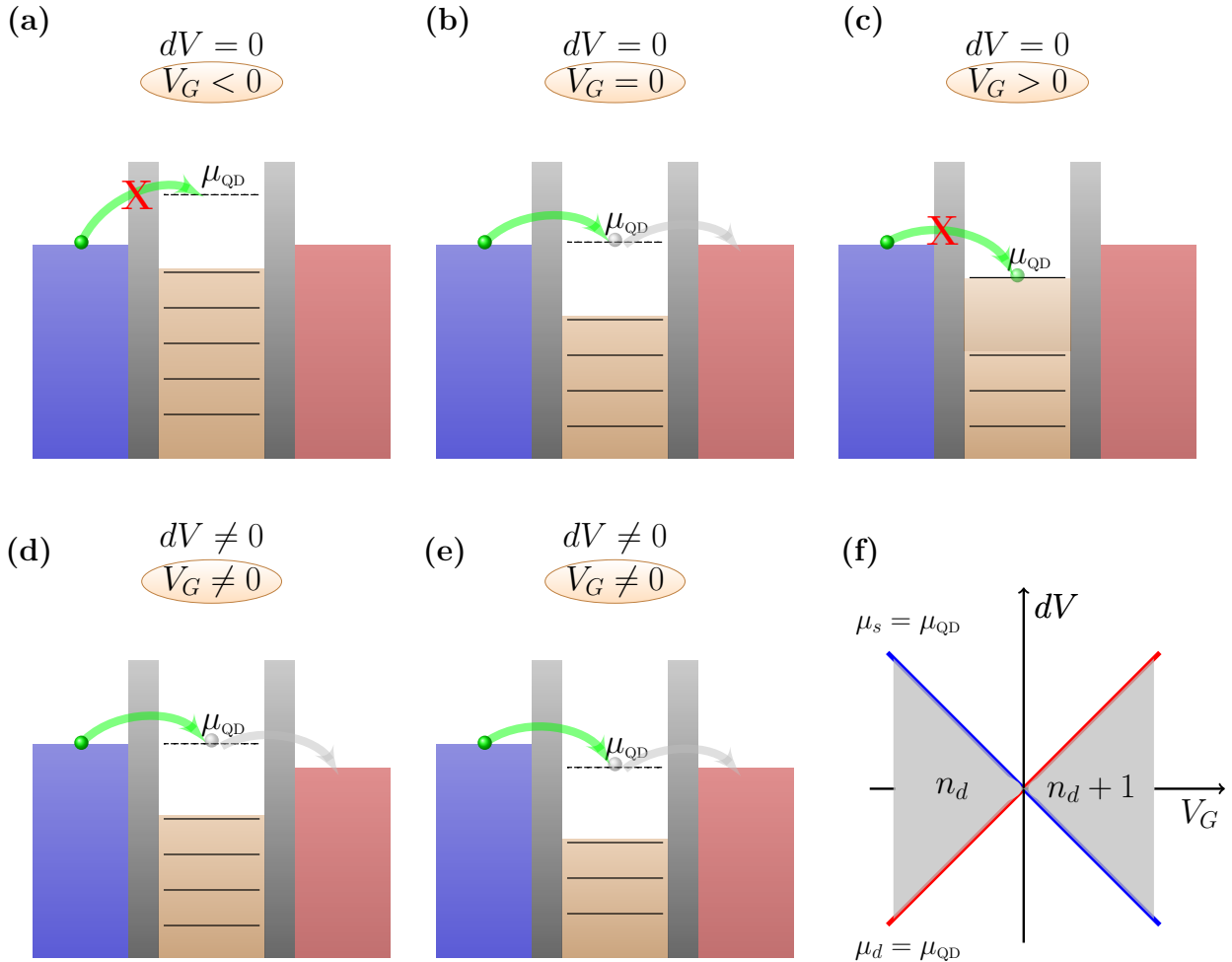


Figure 4 – Energy diagram for the modes (on and off) of a single-electron transistor and Coulomb blockade. By adjusting the gate voltage  $V_G$ , the Fermi level of quantum dot  $\mu_{QD}$  (orange) resonates with the Fermi levels  $\mu_s$  (blue) and  $\mu_d$  (red) of the leads, allowing electrons to tunnel between source and drain. The Coulomb repulsion introduces an energy cost of  $E_c$  to charge the device when one of its energy levels can be populated. If no levels are available, no electron can flow and the system is in “off” mode, as illustrated in panels (a) and (c). The relation between the bias  $dV = \mu_s - \mu_d$  and the  $V_G$  voltages can turn “on” the device if  $V_G$  is chosen to make  $\mu_{QD}$  lie between  $\mu_s$  and  $\mu_d$ , as shown in panels (b), (d) and (e). Diagram (f) represents the compensations between  $dV$  and  $V_G$  that must be carried out so that device operates in “on”, “off” or in the Coulomb blockade modes. Filled gray areas corresponds to the situation in which the dot has a fixed number of electrons and operates in Coulomb blockade. Blue and red lines corresponds to the voltage setup  $dV$  and  $V_G$  for having  $\mu_s = \mu_{QD}$  or  $\mu_d = \mu_{QD}$ , respectively, and also separate the modes “on” or “off” of the device. The increasing of successive  $n_d \rightarrow n_d + 1$  for all modes can be obtained by extrapolating the diagram in a sequence of multiples of  $V_G$ ’s.

Source: By the author.

Adjusting  $V_G$  so that  $\mu_{QD} = \mu_s$  or  $\mu_{QD} = \mu_d$  corresponds to the operability of the device in “on” mode or Coulomb blockade mode, as illustrated in panel (f) of figure 4. Notice that for  $dV \neq 0$  (out of low bias regime), electrons can flow even if  $V_G \neq 0$ . The

effect of  $dV \neq 0$  in the curve  $I$  vs  $V_G$  illustrated in Fig. 5 is to increase the line width of the oscillations.

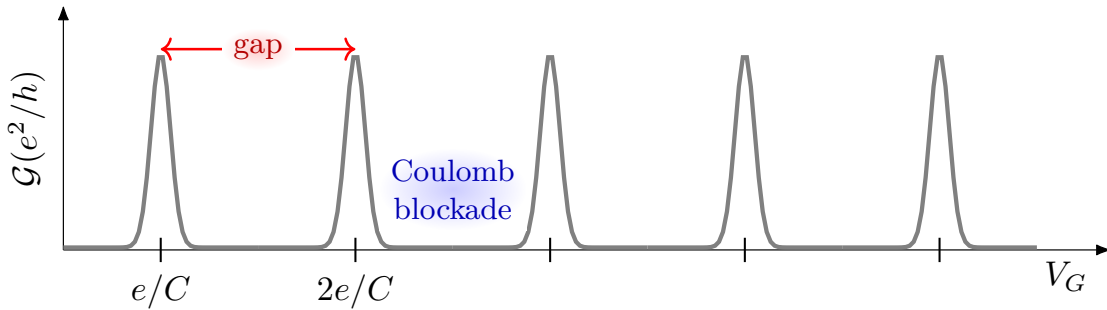


Figure 5 – Current (conductance) peak oscillations observed in a single-electron transistor in Coulomb blockade regime. When the quantum dot has already an electron the repulsive Coulomb interaction blocks the flow of current. Adjusting the gate voltage by  $V_G = e/2C_\Sigma$  allows to shift unoccupied levels, so that electrons can tunnel through the quantum dot. Notice that the peaks, associated with the addition of one electron, occur when the applied gate voltage  $V_G$  is a multiple of  $e/C_\Sigma$ .

Source: By the author.

After the first SET's, a new generation of nano-structured devices appeared to cover a wide range of applicability in quantum technologies. In particular, from the similarity between the interactions taking place in a SET with that of an impurity interacting with delocalized electrons in a metal emerged the seminal inspirations to explore the Kondo effect in quantum dot devices.<sup>12,39,40,46,47</sup> This idea was successfully explored by a group of researchers from MIT in 1998,<sup>12</sup> who proposed a new fabrication protocol to use the SET as platform allowing for a high control of the Kondo effect. In the following section, we will briefly review the Kondo problem with focus on its manifestation in a single electron transistor.

## 2.2 The Kondo effect and its manifestation in quantum dots

The Kondo effect was one of the most intriguing phenomena in condensed matter physics.<sup>38</sup> Its origins date back to 1934 with the observation by Haas, Boer and van den Berg of an anomalous behavior in the resistance of gold at low temperatures.<sup>48</sup> At the time, this fact was in contradiction with the Sommerfeld model of conduction in metals, which predicts that an increase in temperature is accompanied by an increase in the resistivity, whereas as the material is cooled the resistivity is expected to monotonically decrease until saturates in a residual value associated with the extrinsic resistivity. On the contrary, Haas's first measurements revealed a minimum of resistance around 1K-10K followed by an increase during further cooling. Three years later, they investigated the position of the minimum with the concentration of impurities in alloys and noticed the strange behavior to manifest only for magnetic impurities.<sup>49</sup>

A 30 years journey separates Haas' observations and the successful solution to the puzzle. During these years, it became clearer that the presence of impurities, vacancies and defects gave an important contribution to the scattering processes that remain at very low temperatures. A theoretical picture capable to explain the increase in the resistivity after a minimum temperature was reached came only in the 60's, thanks to developments by Phillip W. Anderson and Jun Kondo, who immortalized their names in two of the the most recurrent model Hamiltonians in condensed matter physics.<sup>13,50</sup>

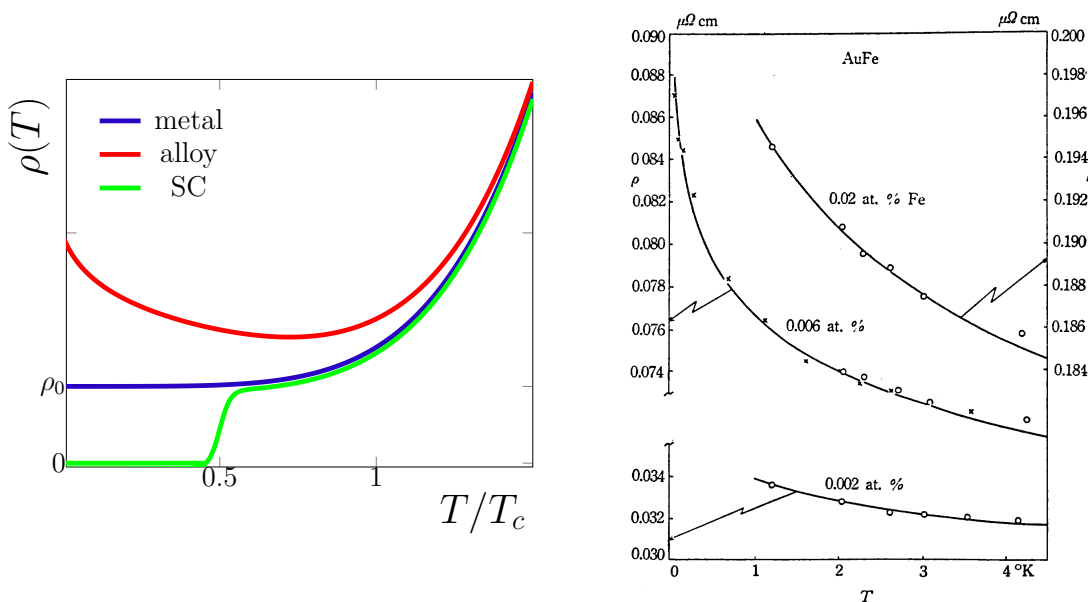


Figure 6 – Resistivity in materials and the Kondo effect. (a) Behavior of resistivity as a function of temperature for metals (blue), alloys (red), and superconductors (green). According to the Drude model for conduction in metals, while cooling the sample to the limit  $T \rightarrow 0$ , the resistivity is expected to saturate in the residual (extrinsic) value  $\rho_0$ . In the 30's an experimental observation revealed that instead of going to  $\rho_0$  as  $T \rightarrow 0$ , the resistivity reached a minimum and then started to increased as the material was cooled. The explanation for this puzzle came only in 1964 thanks to Jun Kondo, who made his name to the most known phenomenon related to anomalous transport behavior: the Kondo effect. Kondo explained that the presence of magnetic impurities in the host metal promotes scattering processes that are enhanced as  $T \rightarrow 0$ . (b) Results for the resistivity as a function of the temperature in dilluted alloys of AuFe extracted from Kondo's paper. Excellent agreement was found between experimental data (circle marks) and his results (black lines).

Source: (a) Adapted from KOUWENHOUVEN,<sup>38</sup> (b) KONDO.<sup>50</sup>

In 1961, Anderson analyzed the formation of localized magnetic moments in transition metal ions and introduced a simple model describing the interaction between free electrons of a host metal with a localized electron on the d-orbital of an impurity.<sup>13</sup> In its simplest version, the Hamiltonian known as *Single Impurity Anderson Model* (SIAM), comprises three terms: the conduction band  $H_{CB}$ , the impurity  $H_d$  Hamiltonians and the

coupling between them  $H_{\text{int}}$ . Explicitly,

$$H_{\text{SIAM}} = H_{\text{CB}} + H_d + H_{\text{int}}. \quad (2.3)$$

The first term is defined as

$$H_{\text{CB}} = \sum_{\mathbf{k}, \sigma} \epsilon_{\mathbf{k}} c_{\mathbf{k}\sigma}^{\dagger} c_{\mathbf{k}\sigma}, \quad (2.4)$$

where  $\epsilon_{\mathbf{k}}$  is the dispersion describing the conduction band electrons of the metallic host with momentum  $\mathbf{k}$ ,  $c_{\mathbf{k}\sigma}$  and  $c_{\mathbf{k}\sigma}^{\dagger}$  are annihilation and creation operators, and  $\sigma = \uparrow, \downarrow$  stems for the spin. Associated with  $\epsilon_{\mathbf{k}}$  there is the density of states (DoS)  $\rho(\epsilon)$ , normally assumed constant near the Fermi level and extends from  $-D$  to  $D$ .

The second term describes the energy  $\epsilon_d$  of the impurity in the d localized level whose double occupation is penalized by the Coulomb repulsion  $U$ . This contribution is local and reads

$$H_d = \epsilon_d (n_{d\uparrow} + n_{d\downarrow}) + U n_{d\uparrow} n_{d\downarrow}, \quad (2.5)$$

where  $n_{d\sigma} = c_{d\sigma}^{\dagger} c_{d\sigma}$  is the number operator measuring the occupation of the d level.

Finally, the last term of eq. (2.3) corresponds to the hybridization between the conduction band and the localized level of the impurity. It is defined as

$$H_{\text{int}} = \sum_{\mathbf{k}\sigma} V_{d\mathbf{k}} (c_{\mathbf{k}\sigma}^{\dagger} c_{d\sigma} + c_{d\sigma}^{\dagger} c_{\mathbf{k}\sigma}), \quad (2.6)$$

where  $V_{d\mathbf{k}}$  is related to the hybridization function

$$\Gamma(\epsilon) = \pi \sum_{\mathbf{k}} |V_{d\mathbf{k}}|^2 \delta(\epsilon - \epsilon_{\mathbf{k}}). \quad (2.7)$$

In the case in which the density of states and the coupling parameter are independent of momenta, i.e.,  $\rho(\epsilon) = \frac{1}{2D}$  and  $V_{d\mathbf{k}} = V$ , the hybridization is constant  $\Gamma(\epsilon) = \Gamma$ . In his discussion, Anderson argued that, in the limit of low temperatures and for  $\Gamma \ll -\epsilon_d, U + \epsilon_d$  (the zero of energy is at  $\epsilon = 0$ ), the states of the impurity that are singly occupied were energetically favorable, and, as the impurity acquires a moment, the coupling of the electrons surrounding the impurity should be antiferromagnetic.

Inspired by this insight and the puzzle in explaining the anomalous resistivity, Kondo was able to derive an expression for the resistivity accounting for contributions due to the presence of impurities.<sup>50</sup> The paper “Resistance Minimum in Dilute Magnetic Alloys”, from 1964, marks the seminal contribution to the understand of the Kondo effect. His starting point was a model describing the antiferromagnetic spin interaction between the metal and the impurity. The latter, later named Kondo Hamiltonian, reads

$$H_K = H_{\text{CB}} + J \mathbf{S}_0 \cdot \mathbf{S}_d, \quad (2.8)$$

where  $J > 0$  is the exchange-coupling,  $\mathbf{S}_d$  denotes the spin of the impurity and

$$\mathbf{S}_0 = \frac{1}{2N} \sum_{\mathbf{k}, \mathbf{q}} \sum_{\mu, \nu} c_{\mathbf{k}\mu}^\dagger \vec{\sigma}_{\mu\nu} c_{\mathbf{q}\nu} \quad (2.9)$$

represents the spin of the conduction band with  $N$  electrons and  $\vec{\sigma} = \sigma_x \hat{i} + \sigma_y \hat{j} + \sigma_z \hat{k}$  are the Pauli matrices.

From the Hamiltonian in eq. (2.8), Kondo calculated the scattering probability of a free electron in the conduction band in the presence of an impurity, arriving in the following expression for the resistivity

$$\mathcal{R}(T) = \mathcal{R}_0 + aT^2 + bT^5 + c_m [1 - J\rho(\epsilon_F)\ln(T)], \quad (2.10)$$

where  $\mathcal{R}_0$  is the intrinsic resistivity,  $a$  and  $b$  are constants and stem from the contributions due to electron-electron and electron-phonon scattering processes,  $\rho(\epsilon_F)$  is the density of states of the conduction band at the Fermi energy  $\epsilon_F$ , and

$$c_m = \frac{3\pi m J^2 S(S+1)}{2e^2 \hbar \epsilon_F}, \quad (2.11)$$

represents the resistivity arising from the impurity, where  $S$  denotes spin,  $m$  is the mass of the electron, and  $\hbar$  is the Planck constant.

The logarithmic term, surviving and increasing as  $T \rightarrow 0$ , entered as the key ingredient to explain the experimental results obtained in alloys, as shown in figure 6.

The connection between the Anderson and the Kondo Hamiltonians in the limit of weak hybridization  $\Gamma \ll U, \epsilon_d$  and low-energies was derived later by Schrieffer and Wolf, who introduced an effective coupling  $J$  relating both models in terms of their parameters.  
<sup>51</sup> In their formulation, the effective coupling  $J_{\mathbf{k}, \mathbf{q}}$  between electrons with momenta  $k$  and  $q$  electrons is calculated as follows

$$J_{\mathbf{k}, \mathbf{q}} = -V_{\mathbf{k}} V_{\mathbf{q}} \left( \frac{1}{\epsilon_{\mathbf{k}} - (\epsilon_d + U)} + \frac{1}{\epsilon_{\mathbf{q}} - (\epsilon_d + U)} - \frac{1}{\epsilon_{\mathbf{k}} - \epsilon_d} - \frac{1}{\epsilon_{\mathbf{q}} - \epsilon_d} \right) \quad (2.12)$$

We note that in the limit of low-lying energy scales  $\epsilon_{\mathbf{k}}, \epsilon_{\mathbf{q}} \rightarrow 0$  and for constant hybridization  $V_{d\mathbf{k}} = V_{d\mathbf{q}} = V$ , the last expression becomes

$$\rho J = \frac{2}{\pi} \left( \frac{\Gamma}{|\epsilon_d|} + \frac{\Gamma}{\epsilon_d + U} \right), \quad (2.13)$$

where  $\rho$  is the density of states of the conduction band.

At this point, we focus our attention on the energy scales dominating the Kondo effect. In terms of the Anderson Hamiltonian, they are defined by the interplay between the hybridization  $\Gamma$  and the energies of the impurity level  $\epsilon_d$  and  $U$ , as well as their translation to the effective coupling  $J$  of the Kondo model at low temperatures. Recalling

Kondo's result for the resistivity, an essential scale is the temperature  $T_K \propto e^{-1/\rho J}$  below which scattering is enhanced due to the fact that the impurity acquires moment and forms a singlet state with the metallic electrons. Spin-flip processes promoted by virtual transitions between spins of the conduction band and the impurity take place and the impurity becomes an efficient scattering center, with conduction electrons trying to screen its moment. Additionally, for  $T < T_K$  a pronounced characteristic of the Kondo effect emerges in the spectral density of the impurity level  $\rho_d(\epsilon)$ : the coupling between the metallic electrons and the impurity results in the appearance of a narrow peak in  $\rho_d$  with width proportional to  $T_K$  at the Fermi level of the metals.

The Kondo temperature  $T_K$  is ultimately related to the so-called radius  $\xi_K$  of the Kondo screening cloud, a polarized region forms and entangles the free electrons with the localized impurity moment. See Fig. 7. The “radius” of the Kondo cloud is usually estimated as  $\xi_K = \hbar v_F / k_B T_K$ , where  $v_F$  is the Fermi velocity and  $k_B$  is the Boltzmann constant. The radius  $\xi_K$  was never experimentally determined so far and has been the subject of controversy for many years.<sup>52–57</sup> As we will discuss later, the issue about the real extension of the Kondo screening cloud has became a new puzzle with the discovery of Kondo effect in quantum dots.<sup>58–61</sup>

As mentioned, the Kondo effect depends vitally on virtual exchange processes arising only when the occupation of the impurity is odd. With this picture in mind, we are now ready to discuss the correspondence between the problem of a magnetic impurity in a metallic host and the interactions occurring in quantum dots. When the occupation number of the quantum is odd, it acquires a magnetic moment and behaves as a magnetic impurity. The leads can hybridize with the quantum dot if the resistances of the tunnel junctions allows for a strong coupling entangling the dot and the metallic electrons. Below a critical temperature, two peaks are expected to appear in the density of states (DoS) of the quantum dot, each one in resonance with the Fermi levels  $\mu_s$  and  $\mu_d$ . Figure 8 illustrates the analogy between the Kondo effect in a SET with the Kondo regime of an impurity system, such as the Anderson model.

From Kondo's paper to the fabrication of the first single-electron transistor, it did not take too long for that theoretical predictions of the Kondo effect in nano-structured devices to appear in the physics community. This common wish was finally satisfied in the late 90's with a new SET proposed by Golhaber-Gordon and colleagues.<sup>12</sup> Having at hand a lithography protocol allowing for a finer pattern of metallic gates, and a high-precision setup for growing a small GaAs/AlGaAs heterostructure containing a two-dimensional electron gas, they were able to realize a device whose typical scales  $\Gamma$ ,  $U$  and  $\epsilon_d$  could match those needed to tune the Kondo effect within the range of experimentally accessible temperatures.

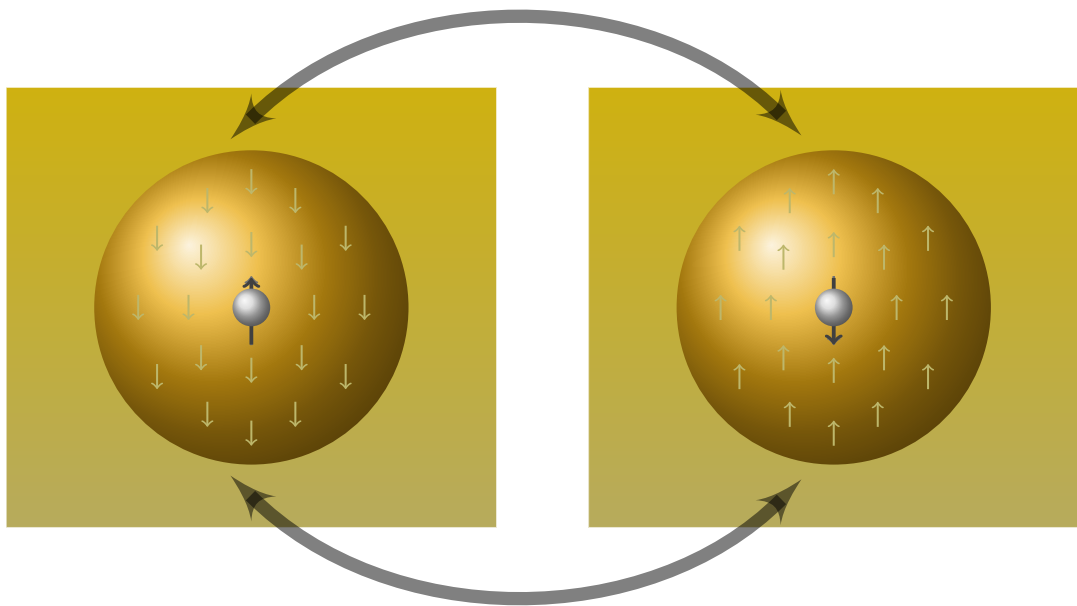


Figure 7 – The Kondo screening cloud. Below a characteristic temperature  $T_K$ , known as the Kondo temperature, a polarized region surrounding the impurity forms in order to screen the localized magnetic moment. This region is referred to the Kondo screening cloud. Spin-flip process occur for the electrons whithin the cloud as well as the impurity moment. The ground state therefore is composed by a singlet state entangling these conduction electrons with the impurity. In the early years of the Kondo problem, theorists argued that the spatial extension of the Kondo cloud behaves as  $\xi_K \propto T_K^{-1}$ , a scale that for typical materials is of the order of  $\mu\text{m}$ . After the discovery of the Kondo effect in nanoscopic quantum dots, this issue has become a new puzzle warming up the Kondo problem, and making the controversy subject of a large collection of investigations.

Source: By the author.

In analogy with the increase in resistivity in metallic alloys, the Kondo effect in quantum dots is characterized by an anomalous behavior in transport properties. As the temperature is lowered, when the number of electrons in the quantum dot is odd, the unpaired electron at the Fermi level entangles with the electrons at the Fermi level of the leads and form a singlet. In this situation, the Coulomb blockade is lifted because electrons can flow even when  $\mu_{\text{QD}}$  is not aligned with the Fermi level of the leads. As a consequence, the conductance  $\mathcal{G}_d$  as a function of the gate voltage  $V_G$ , previously illustrated in 5, acquires a plateau between two consecutive peaks. <sup>12, 14, 43, 44</sup> Compare Figs. 5 and 9. The plateau, called the *Kondo plateau*, becomes more pronounced as the system is cooled. Experimentally, the measurements of  $\mathcal{G}_d$  as a function of  $V_G$  in a SET behave as in figure 9. Such a detailed probe of the Kondo plateau was only possible with advances in experimental techniques allowing for highly accurate measurements. At the same time, advances in lithography made possible the fabrication of more sophisticated devices. <sup>1, 40, 62–65</sup>

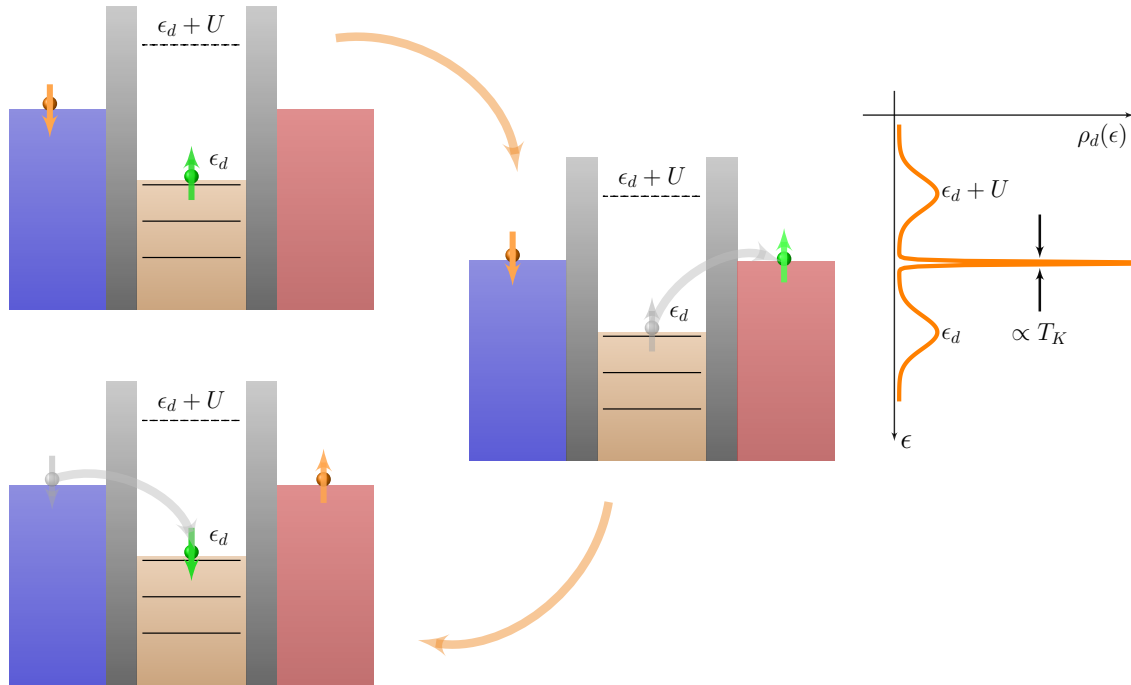


Figure 8 – Kondo effect in a single-electron transistor. In 1998 a paper published in Nature by Goldhaber-Gordon and colleagues opened an entire new avenue in the study of the Kondo effect in quantum dots. They were able to fabricate the first SET whose features matched the parameters of the Anderson Hamiltonian. The physics of the Kondo effect has a strong analogy with the processes occurring in a SET: when the occupation number of the quantum dot is odd it behaves as a magnetic impurity. At low temperatures, spin-flips are energetically favorable and occur by means of virtual transitions. Consider an initial state in which the dot is occupied with a spin  $\uparrow$  and  $\mu_s > \mu_d$  with  $dV \approx 0$ . The energetic cost for an electron at the source to occupy the level immediately above the Fermi level of the dot is larger than for the electron at the dot to transit virtually to the source lead. From these virtual transitions arise the spin-flip processes characteristic of the Kondo effect at very low temperatures and are a consequence of the sharp peak appearing in the spectral density of the quantum dot in resonance with the Fermi level of the leads.

Source: By the author.

With the previous historical background, we can now turn to a more theoretical analysis of quantum dot devices in terms of model Hamiltonians. In the following, we will present the adapted version of the Anderson Hamiltonian for a single-electron transistor and discuss how it can be used to predict its properties, such as the Kondo plateau in the curve of the conductance.

## 2.3 Anderson Hamiltonian for a single-electron transistor

As explained in the previous section, the analogy between a quantum dot and an impurity system allows to model a single-electron transistor by means of the single

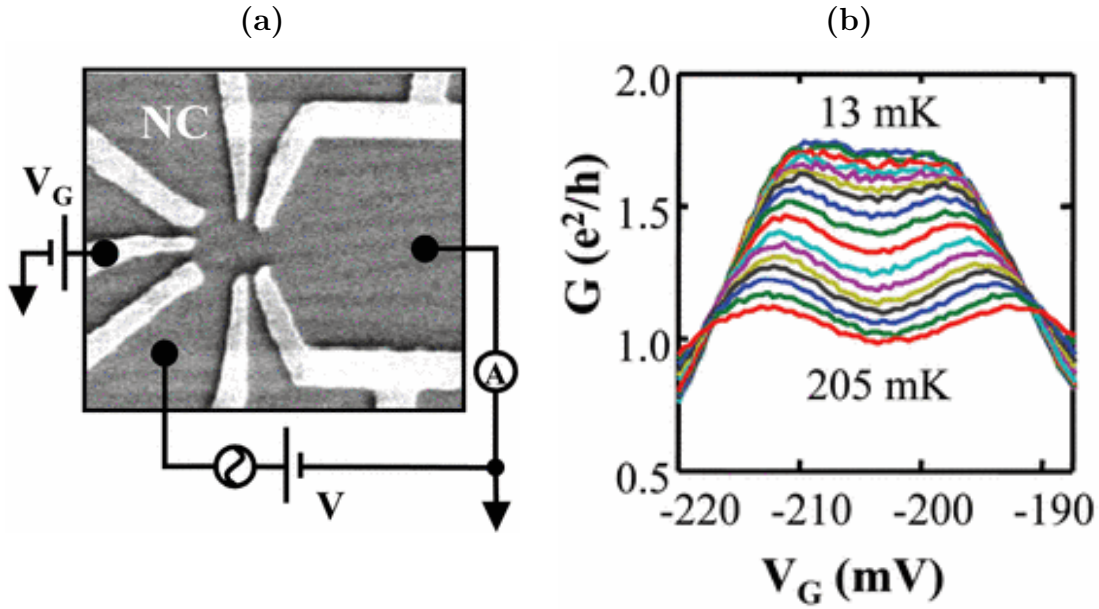


Figure 9 – Experimental realization of a single-electron transistor (SET) and measurement of the conductance as a function of gate voltage in the presence of the Kondo effect. (a) Scanning electron microscope image of a typical semiconductor SET grown on a GaAs/AlGaAs heterostructure. The area of the dot is of order of  $0.04\mu\text{m}^2$ , allowing for a level spacing  $\Delta\epsilon \approx 100\mu\text{eV}$  and a charging energy  $E_c \approx 1\text{meV}$ . (b) Experimental conductance of the SET as a function of the gate voltage  $V_G$  when the temperature is decreased. The range of temperatures considered are below  $205\text{mK}$ . In the limit  $T \rightarrow 0$ , the conductance approaches its minimum in the intervals  $V_G$  for that the occupation in the quantum dot is even, increasing until a plateau when the number of electrons is odd. The conductance plateau, below the unity of conductance quantum  $G = 2e^2/\hbar$  indicates that the coupling of the dot with the gases is asymmetric.

Source: GROBIS et al.<sup>1</sup>

impurity Anderson model.<sup>41,66,67</sup> In a general form, the adapted version of the Anderson Hamiltonian for a quantum dot device is defined as follows

$$H_{\text{SET}} = H_{\text{leads}} + H_{\text{QD}} + H_{\text{int}}. \quad (2.14)$$

First, the two-dimensional electron gases in the source and drain leads are represented by two conduction bands *L* (*left*) and *R* (*right*), respectively. The corresponding term of the Hamiltonian reads

$$H_{\text{leads}} = \sum_{kL,\sigma} \epsilon_{kL} c_{kL,\sigma}^\dagger c_{kL,\sigma} + \sum_{kR,\sigma} \epsilon_{kR} c_{kR,\sigma}^\dagger c_{kR,\sigma}, \quad (2.15)$$

where,  $c_{k\alpha,\sigma}^\dagger$  ( $\alpha = L, R$ ) are the creation operators that add an electron with momentum  $k\alpha$  and spin  $\sigma = \uparrow, \downarrow$  in the level  $\epsilon_{k\alpha}$ . We consider equal bands ( $\epsilon_{k\alpha} = \epsilon_k$ ) with  $N$  levels and density of states  $\rho(\epsilon)$ ,  $\epsilon \in [-D, D]$ , so the bandwidth is  $2D$ . In the thermodynamical limit ( $N \rightarrow \infty$ ) the band forms a continuum of states. Note that in contrast to eq. (2.4), the band is mapped onto a one-dimensional problem, i.e.,  $\epsilon_{\mathbf{k}} = \epsilon_k$ .

The Hamiltonian describing the quantum dot is written as

$$H_{\text{QD}} = V_G(n_{d\uparrow} + n_{d\downarrow}) + U n_{n\uparrow} n_{d\downarrow}, \quad (2.16)$$

where  $V_G$  is the gate voltage,  $U$  is the Coulomb repulsion and is related to the charging energy  $E_c$  of the quantum dot,  $n_{d\sigma} = c_{d\sigma}^\dagger c_{d\sigma}$  is the occupation number and  $c_{d\sigma}$  ( $c_{d\sigma}^\dagger$ ) are the annihilation (creation) operators.

Finally, the hybridization term in eq. (2.6) is re-written as

$$H_{\text{int}} = \sum_{\sigma} \left[ V_L (f_{0L,\sigma}^\dagger c_{d\sigma} + c_{d\sigma}^\dagger f_{0L,\sigma}) + V_R (f_{0R,\sigma}^\dagger c_{d\sigma} + c_{d\sigma}^\dagger f_{0R,\sigma}) \right], \quad (2.17)$$

where  $V_{\alpha} = \sqrt{\Gamma_{\alpha}/\rho\pi}$  ( $\alpha = L, R$ ) is the couplings between the quantum dot with the left(source) and right(drain) leads, the latter being characterized by a density of states  $\rho$ . The coupling is defined by means of the Wannier states

$$f_{0\alpha,\sigma} = \frac{1}{\sqrt{N}} \sum_{k\alpha,\sigma} c_{k\alpha,\sigma}. \quad (2.18)$$

Note that  $\Gamma_{\alpha}$  ( $\alpha = L, R$ ) are associated with the tunneling junctions in the source and drain leads and are determined by their resistance.

A sketch of a single-electron transistor modeled by the Anderson Hamiltonian in eq. (2.14) is shown in figure 10.

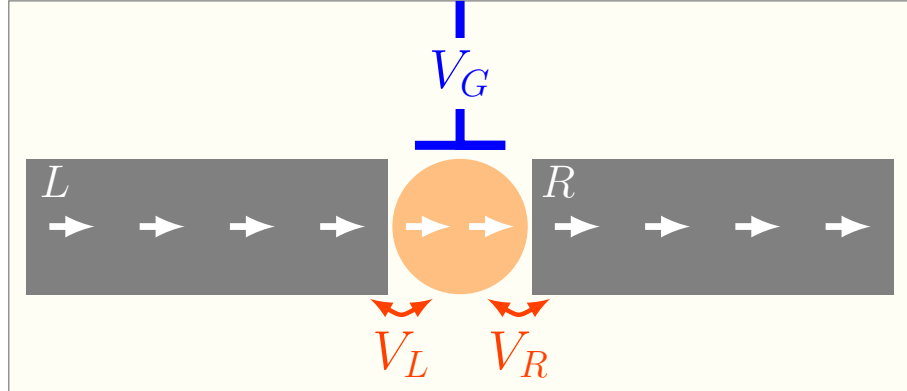


Figure 10 – Model for a single-electron transistor (SET). The source and drain leads are mapped into two conduction bands on the left  $L$  and right  $R$  sides of the quantum dot. The coupling between them are made by the hopping amplitudes  $V_{\alpha}$  ( $\alpha = L, R$ ). The occupation number of the quantum dot is controlled by the gate voltage  $V_G$ . If an infinitesimal bias is created between the  $L$  and  $R$  conduction bands, electrons can flow through the quantum dot.

Source: ZAWADZKI et al. <sup>15</sup>

An external potential  $W$  can be applied to the leads and must be identical ( $W_L = W_R$ ) to ensure the system is in equilibrium. The related term in the Hamiltonian is

$$H_{\text{leads},W} = H_{\text{leads}} + \frac{W}{N} \sum_{k,q,\alpha} c_{k\alpha}^\dagger c_{q\alpha}. \quad (2.19)$$

The Hamiltonian defined in eq. (2.14) can be re-written in a more convenient basis which allows to decouple it in a contribution independent of the quantum dot and another that recovers the traditional form of the single-impurity Anderson Hamiltonian of eq. (2.3). To this aim, we define odd and even combinations of the metallic states  $c_{k,L}$  and  $c_{k,R}$ :

$$a_k = \frac{V_L c_{k,L} + V_R c_{k,R}}{V} \quad (2.20)$$

$$b_k = \frac{V_R c_{k,L} - V_L c_{k,R}}{V}, \quad (2.21)$$

where

$$V \equiv \sqrt{V_L^2 + V_R^2}. \quad (2.22)$$

Note that for symmetric couplings  $V_L = V_R$ ,

$$a_k = \frac{c_{k,L} + c_{k,R}}{\sqrt{2}} \quad (2.23)$$

$$b_k = \frac{c_{k,L} - c_{k,R}}{\sqrt{2}}. \quad (2.24)$$

Plugging eqs. (2.20) and (2.21) into (2.14), corrected with (2.19), we obtain a new decoupled Hamiltonian

$$H = H_A + H_B, \quad (2.25)$$

where

$$H_B = \sum_k \epsilon_k b_k^\dagger b_k + \frac{W}{N} \sum_{k,q} b_k^\dagger b_q, \quad (2.26)$$

and

$$H_A = \sum_k \epsilon_k a_k^\dagger a_k + W f_0^\dagger f_0 + V(f_0^\dagger c_d + H.c.) + H_{QD}, \quad (2.27)$$

where the new Wannier state  $f_0$  reads

$$f_0 = \frac{1}{\sqrt{N}} \sum_k a_k. \quad (2.28)$$

We can recognize  $H_A$  as essentially the single impurity, single-band Anderson Hamiltonian. On the other hand,  $H_B$  corresponds to a free band subject to a scattering potential  $W$  and decoupled from the quantum dot.

Many properties of a single-electron transistor can be studied from the Anderson model, including spectral and transport properties. The latter will be the subject of the following section.

### 2.3.1 Zero-bias conductance and universal mapping

As explained in section (2.1), a current can flow through the quantum dot when an infinitesimal bias  $dV$  is created between the source and the drain leads, and if the Fermi level of the quantum dot is accessible.<sup>41</sup> To study transport in the zero-bias regime  $dV \approx 0$ , we can carry out a perturbative analysis whose starting point is the Hamiltonian

$$H_{\text{bias}}(t) = -e \frac{\Delta\mu}{2} \sum_k (c_{kR}^\dagger c_{kR} - c_{kL}^\dagger c_{kL}) \exp^{\eta t/\hbar}, \quad (2.29)$$

where  $\Delta\mu = \mu_s - \mu_d$ ,  $e$  is the electrical charge,  $\hbar$  is the Planck constant, and  $t$  is the instantaneous time and  $\eta$  is an infinitesimal.

We then account for the current flowing into the  $R$  lead by means of the current operator

$$I = \frac{dq_R}{dt} = -\frac{ie}{\hbar} [H_A, \sum_k c_{kR}^\dagger c_{kR}], \quad (2.30)$$

where  $i$  is the imaginary unit.

In the linear-response regime the zero-bias conductance  $\mathcal{G}(T)$  as a function of the temperature  $T$  can be calculated from all possible transitions between states  $|\Psi_m\rangle$  of the unperturbed  $H_A$  that arise from the perturbation  $H_{\text{bias}}$ . Explicitly,

$$\mathcal{G}(T) = -\frac{i}{Z\hbar} \int_{-\infty}^0 dt \sum_m \exp^{-\beta E_m} \langle \Psi_m | [I, H_{\text{bias}}(t)] | \Psi_m \rangle, \quad (2.31)$$

where

$$Z = \sum_m \exp^{-\beta E_m}, \quad (2.32)$$

is the partition function,  $E_m$  is the energy of the eigenstate  $|\Psi_m\rangle$  and  $\beta = 1/k_B T$ .

Working out the calculation of eq. (2.31) on the basis of  $a_k$ 's and  $b_k$ 's, we obtain the following expression for the conductance

$$\mathcal{G}(T) = \mathcal{G}_2 \pi \Gamma_W \alpha_s \int d\epsilon \rho_d(\epsilon, T) \left( -\frac{\partial f(\epsilon)}{\partial \epsilon} \right), \quad (2.33)$$

where

$$\mathcal{G}_2 \equiv \frac{2e^2}{h} \quad (2.34)$$

is the conductance quantum,

$$\Gamma_W = \frac{\Gamma}{1 + \pi^2 \rho^2 W^2} \quad (2.35)$$

is the tunelling width,

$$\alpha_s \equiv \frac{4V_L^2 V_R^2}{V^2} \quad (2.36)$$

is the asymmetry index, unitary for the case in which the leads are symmetrically coupled to the quantum dot;  $\rho$  is the spectral density of the conduction band  $a_k$ ,  $f(\epsilon)$  is the Fermi function and  $\rho_d$  is the spectral density of the quantum dot.

The spectral density  $\rho_d$  in (2.31) is calculated as follows

$$\rho_d(\epsilon, T) = \frac{1}{f(\epsilon)} \sum_{m,n} \frac{e^{-\beta E_m}}{Z} |\langle \Psi_n | c_d^\dagger | \Psi_m \rangle|^2 \delta(E_m - E_n - \epsilon), \quad (2.37)$$

where  $|\Psi_n\rangle$  and  $|\Psi_m\rangle$  are eigenstates of the  $H_A$  in eq. (2.27), whose energies are  $E_n$  and  $E_m$ , respectively. Note that, according to eq. (2.31) the matrix element  $\langle \Psi_n | c_d^\dagger | \Psi_m \rangle$  measures the transition probability to transfer an electron between the eigenstates  $|\Psi_n\rangle$  and  $|\Psi_m\rangle$  of  $H_A$  and is ultimately related to the occupation  $n_d$  in state  $|\Psi_m\rangle$  via a completeness relation. The set of mathematical steps from eq. (2.31) to (2.33) can be obtained following Appendix C of YOSHIDA et al.<sup>41</sup> Note that, there,  $\alpha$  is absent and the combinations of operators in eqs. (2.23) and (2.24) must be considered in accordance with  $H_A$  in (2.27).

From the solution of the Anderson Hamiltonian for a fixed set of model parameters ( $\Gamma$ ,  $V_G$  and  $U$ ), we can obtain the ingredients entering in eq. (2.33) and then calculate the zero-bias conductance for a range of temperatures from  $T \gg T_K$  to  $T \rightarrow 0$ . As mentioned in the introduction, the solution of the Anderson Hamiltonian can be carried out analytically via Bethe Ansatz (BA) or numerically by means of the Numerical Renormalization-Group (NRG).<sup>16,68–70</sup> The latter offers an efficient platform for calculating properties of quantum devices similar to a SET, with excellent agreement with experimental results.<sup>15,41</sup> A detailed explanation of the Numerical Renormalization Group procedure as well as its treatment for solving the Anderson Hamiltonian will be given in Chapter 4.

Important to the present discussion of transport in the zero-bias regime of a SET is how the profile of  $\mathcal{G}_d$  will be determined by the relation between the model parameters  $\Gamma$ ,  $U$ ,  $V_G$  and the temperature. As previously explained, the dynamics of the device would be controlled by the gate voltage, as it defines the charging energy  $E_c = \min(|V_G|, U + V_G)$  and shifts the levels of the dot, which are  $\epsilon_{d,0} = 0$  (empty),  $\epsilon_{d,1} = V_G$  ( $\uparrow$  or  $\downarrow$ ) and  $\epsilon_{d,2} = 2V_G + U$  (doubly occupied). For  $-U < V_G < 0$ , the lowest level is singly occupied, so that the dot acquires a magnetic moment. The extremes of this interval are two charge-degeneracy points, while the point  $V_G + 2U = 0$  is the symmetric point, at which the Anderson Hamiltonian preserves particle-hole symmetry.

At high temperatures, the device cannot be charged for gate voltages other than the charge-degeneracy points. The curve of the conductance  $\mathcal{G}_d$  as a function of  $V_G$  behaves as that of fig. 5, in which no transport is measured for  $-U < V_G < 0$ . As the temperature is lowered, the coupling between the dot and the leads favors spin-flip processes and the Kondo effect arises: the coupling favors transport and non-zero conductance is observed between the peaks at  $V_G = -U$  and  $V_G = 0$ . These processes are enhanced as the temperature is further cooled down to the Kondo temperature, so that for  $T \ll T_K$  the Kondo cloud

forms and entangles the metallic electrons to the dot. The entanglement allows ballistic transport and the Kondo plateau arises.

It is interesting to analyze the dot occupation and its consequence to transport in terms of the Friedel sum rule.<sup>71,72</sup> To motivate this discussion, we remind our interpretation of the Kondo screening cloud. In an impurity system, we have provided the picture of the Kondo screening cloud as being a polarized region surrounding the impurity and involving the displaced electrons of the conduction band. One can ask how the charge is distributed in the vicinity of the impurity and of the Wannier orbital  $f_0$  due to the displacement of electrons scattered by the quantum dot.<sup>41,71–73</sup> To answer this question, we can recall to the Friedel sum rule, which relates the phase shifts of the metallic electrons scattered within the Kondo cloud with the occupation in the dot, so we can write

$$n_d = \frac{2}{\pi}(\delta - \delta_W), \quad (2.38)$$

where  $\delta_W$  is the phase shift due to the presence of the potential  $W$ , calculated as

$$\tan \delta_W = -\pi \rho W. \quad (2.39)$$

Note that for  $W = 0$ , electrons whose energy is below  $V_G$  are not phase shifted, i.e.,  $\delta = 0$ , whereas for those with energy  $\epsilon \gg V_G$  are shifted by  $\pi$ . Electrons with energies  $\epsilon \ll V_G$  close to the Fermi level are shifted by  $\pi/2$ .

In the two extremes of temperature,  $T \ll T_K$  and  $T \gg T_K$ , it is straightforward to calculate the dot spectral density  $\rho_d$ <sup>14</sup> and show that it is given in terms of the phase shifts as follows

$$\rho_d^* = \frac{1}{\Gamma_W} \sin^2(\delta^* - \delta_W), \quad (2.40)$$

where the symbol  $*$  denotes one of the two thermal limits and  $\Gamma_W$  is defined in eq. (2.35).

Examining the phase shift at the symmetry point  $V_G = -U/2$  is particularly illustrative, as the symmetry point is associated with the gate voltage for which the Kondo plateau manifest in opposition to the Coulomb blockade regime.<sup>41,73,74</sup> While in the absence of Kondo effect the conductance vanishes at  $V_G = -U/2$ , it starts to increase as the temperature is lowered, reaching the quantum of conductance  $\mathcal{G}_2$  for  $T \ll T_K$ . In terms of the phase shifts, for  $T \gg T_K$ , the coupling can be disregarded, few electrons are scattered and the phase-shift of those at the Fermi level is  $\delta = 0$ . By contrast, at very low temperatures compared with the Kondo thermal scale  $T_K$ , the broadening of the coupling allows ballistic transport of the electrons at the Fermi levels of the leads, so that their phase shift is  $\delta = \pi/2$ . At the symmetry point  $V_G = -U/2$  the zero bias conductance is a universal function  $G_s$  of the temperature scaled by the Kondo temperature.<sup>15,41</sup> The universal relation for  $V_G = -U/2$  is written as

$$\bar{\mathcal{G}}_d \left( \frac{T}{T_K} \right) = \mathcal{G}_2 G_s \left( \frac{T}{T_K} \right). \quad (2.41)$$

For other model parameters, the phase shifts can assume any value within the interval  $-\pi/2 \leq \delta \leq \pi/2$ . Especially at low temperatures, the conductance for  $V_G \neq -U/2$  will be below the quantum of conductance and will be closer to unity as  $V_G$  favors the occupation in the quantum dot. For a set of model parameters resulting in an effective coupling  $J$  allowing for the Kondo effect, gate voltages limited by the charge-degeneracy points, i.e.,  $-U < V_G < 0$ , are associated with the Kondo plateau in the limit  $T \rightarrow 0$ . For general model parameters, neither the amplitude of the conductance nor its dependence on the temperature will match the universal relation in eq. (2.41).<sup>15,41</sup> However, adapting the latter in the form of a linear mapping yields the general relation

$$\bar{\mathcal{G}}_d \left( \frac{T}{T_K} \right) = \alpha G_s \left( \frac{T}{T_K} \right) + \beta, \quad (2.42)$$

where  $\mathcal{G}_d$  is given in the unities of the conductance quantum  $\mathcal{G}_2$ , the coefficients  $\alpha$  and  $\beta$  are determined from the limits of  $\mathcal{G}_d$  for  $T \ll T_K$  and  $T \gg T_K$ .

Plugging eq. (2.40) into eq. (2.33), we are able to determine  $\alpha$  and  $\beta$  and obtain the following linear mapping

$$\bar{\mathcal{G}}_d \left( \frac{T}{T_K} \right) - \frac{\mathcal{G}_2}{2} = \left( \frac{\mathcal{G}_2}{2} - G_s \left( \frac{T}{T_K} \right) \right) \cos 2(\delta - \delta_W). \quad (2.43)$$

The universal mapping 2.43 for the zero bias conductance generalizes eq. (2.41) for any model parameters. It provides a formula to determine the conductance in the limit  $T \rightarrow 0$ , the Kondo temperature  $T_K$  and the phase shifts  $\delta^*$ . Note that, without particle-hole symmetry, i.e. gate voltages  $V_G \neq -U/2$ , the effective phase shift  $\delta - \delta_W$  will result in a conductance always smaller than  $\mathcal{G}_2$  at very low temperature regimes, even with  $V_G = -U/2$  and  $W \neq 0$ . The Kondo temperature  $T_K$  is also a function of the model parameters, as they define the coupling  $J$ . The universal relation (2.43) is proven to accurately match experimental data obtained in transport measurements in a single-electron transistor, as reported by Ref. <sup>15</sup>. In the latter paper, we have carried out an extensive Renormalization-Group analysis of the Anderson Hamiltonian and its accuracy in reproducing transport properties of realistic devices. Figure 11 compares the universal mapping in eq. (2.43) with experimental data points for the zero-bias conductance provided by Grobis et al, previously reported in a publication.<sup>1</sup> A set of 34 gate voltages was considered. The inset shows the estimates for the Kondo temperature  $T_K$  for each  $V_G$ . The agreement between the experimental data with the analytical curve  $\mathcal{G}_J$  in Fig. 11 reveals an important result which will be a crucial ingredient for the approach proposed in the present thesis: the universal properties of realistic SETs can be accurately modeled by the Anderson Hamiltonian.

An issue to be further investigated concerns the non-universal properties of realistic quantum dots. In Ref. <sup>15</sup>, we also discussed the fidelity of the Anderson Hamiltonian in reproducing non-universal features of a single-electron transistor. Using, again, the results

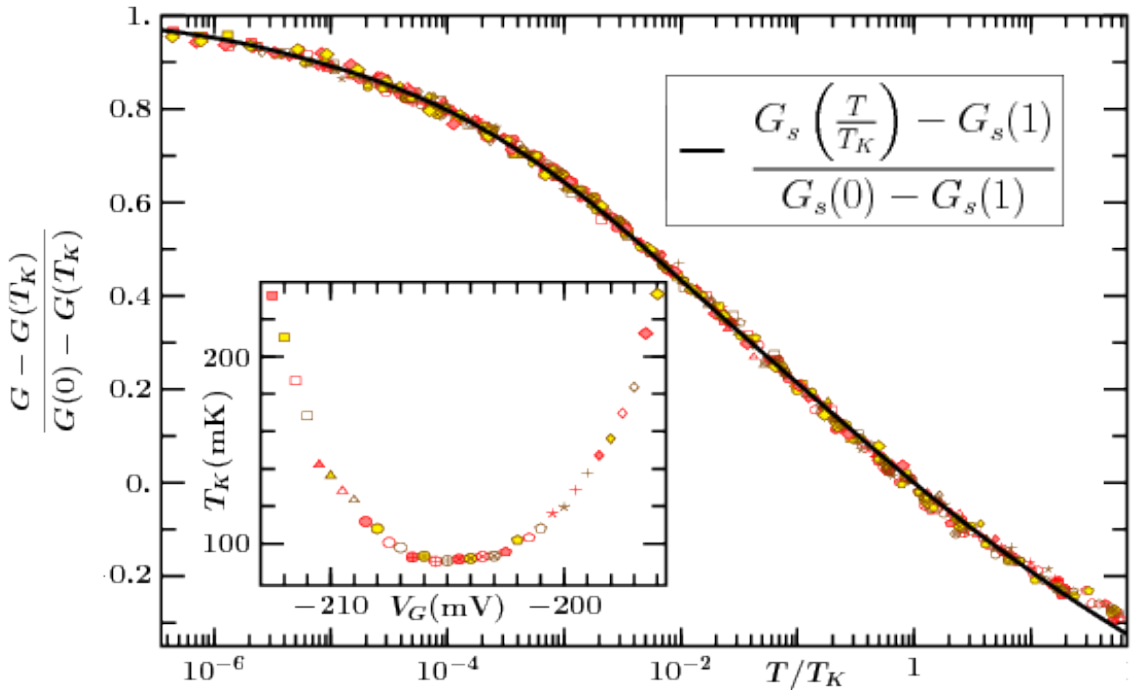


Figure 11 – Conductance  $\mathcal{G}(T)$  in a SET as a function of the scaled temperature  $T/T_K$ , where  $T_K$  is the characteristic temperature in which the Kondo effect arises. Colored markers represent experimental data for 34 samples of gate voltage  $V_G$ . Black solid line correspond to NRG calculations of  $\mathcal{G}(T/T_K)$  for the Anderson impurity model.

Source: ZAWADZKI et al. 15

by Grobis et al. 1, we have shown that the values of properties such as the assymetry index  $\alpha_s$  and the occupation number  $n_d$  at very low temperatures counterintuitively deviate from the expected results for the Anderson model in the limit  $T \rightarrow 0$ . The deviation is illustrated in Fig. 12, where the occupation  $n_d$  is shown as blue circles and the assymetry index is represented by orange squares. When considering the expected values for both properties in the limit  $T \rightarrow 0$  of the Anderson Hamiltonian, the experimental results are in poor agreement:  $\alpha_s$  and  $n_d$  should be constant for the entire set of gate voltages  $-212 < V_G < 195$ , which defines the Kondo plateau. On contrary, the measurements reveal deviations related to the non-universal aspect of such properties. In that sense, while dealing with equilibrium transport, the connection between realistic SETs and molecular junctions with an analytical formulation based on the Anderson Hamiltonian can be tackled ultimately through the universal zero-bias conductance.

The analysis of the zero-bias conductance and its relation with the phase shifts will appear again along this thesis. For instance, the connection between the occupation  $n_d$  in the limit  $T \rightarrow 0$  and ground-state conductance will be discussed in chapter 3, specifically in the subsection devoted to the density functional approach for transport in a SET. In chapter 4, we will further explore the structure of the Anderson Hamiltonian in the limits

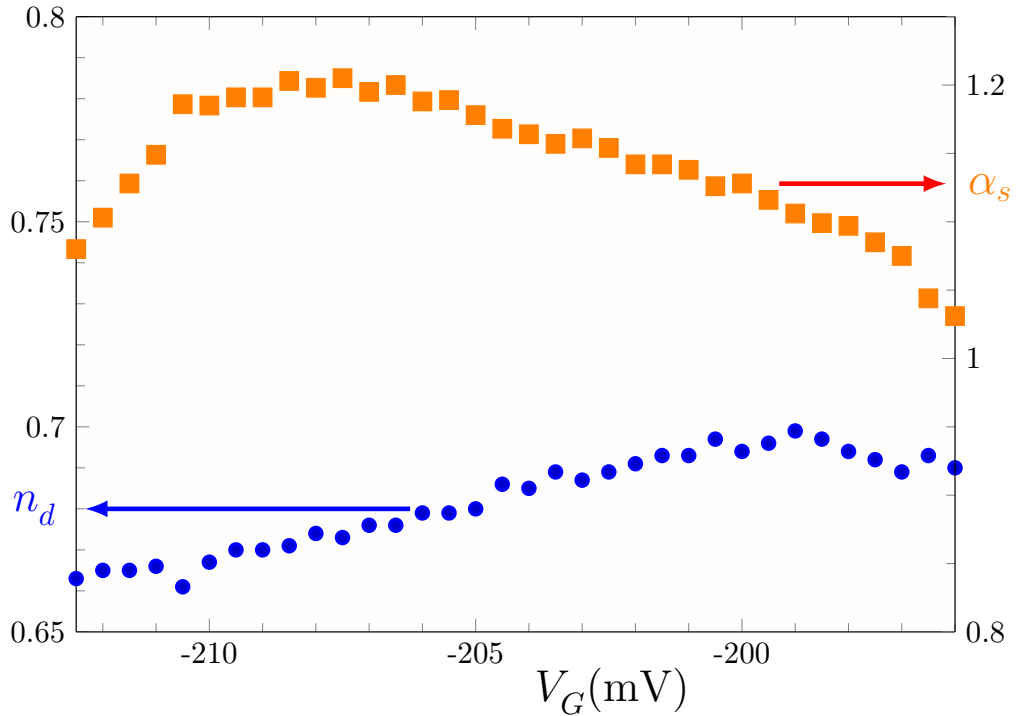


Figure 12 – Occupation number  $n_d$  and asymmetry index  $\alpha_s$  obtained from experimental points by Grobis et al.<sup>1</sup>. When considering the limit of very low temperatures of the Anderson Hamiltonian, both properties are predicted to be constant and equal to the unity. Instead, experimental data points reveal that the asymmetry index and the occupation number retain non-universal features that the Anderson Hamiltonian in its traditional form is unable to capture.

Source: ZAWADZKI et al.<sup>15</sup>

$T \ll T_K$  and  $T \gg T_K$  from the point of view of the Numerical Renormalization-Group. We will show that the RG analysis of these thermal limits provide a simpler way to obtain eq. (2.40) and then derive the coefficients entering the linear mapping of eq. (2.42).

Now, having acquired the basis of transport in quantum dots and understood the correlation effects responsible for many-body phenomena, such as the Kondo effect, we can move to the one of the issues at the focus of the present thesis: is it possible to obtain a realistic description of experimental quantum devices in which the Kondo effect manifest?

The next chapter aims to answer this question. We have argued that DFT provides a precise framework for electronic structure calculations of complex materials and have commented on the non-interacting picture adopted in Kohn-Sham calculations. We will introduce the formalism of DFT with emphasis on the limitations of density functional approaches for strongly correlated system. We will also discuss works dealing with the Kondo problem in quantum dots in a DFT framework.

### 3 DENSITY FUNCTIONAL THEORY

Density Functional Theory (DFT) revolutionized the quantum mechanical treatment of the many body problem and allowed to study atoms, solids and molecules with unprecedented details. Based on the Hohenberg–Kohn theorem, which states that the ground state  $|\Psi\rangle$  is an unique functional  $F[n(\mathbf{r})]$  in one-to-one correspondence with the ground-state density  $n(\mathbf{r})$ , DFT simplified the task of calculating physical properties by seeking  $\mathbf{n}(\mathbf{r})$  instead of determining  $|\Psi\rangle$  from the Schrödinger equation.<sup>19,20</sup>

Since its foundation in the 60's, DFT has continuously contributed with many analytical and numerical tools to condensed matter theory: the techniques used to perform ab-initio calculations have evolved over time and nowadays we have an entire zoo of functionals and packages available to perform simulations in solid state systems.<sup>7,21,23,75</sup> In spite of its success in electronic structure calculations and popularity in material science, there are challenges in density functional theory, the most daunting being its extension for strongly correlated systems.<sup>22–24,37</sup>

In the present chapter, we will introduce the sequence of ideas underlying the basis of Density Functional Theory and contextualize the problem tackled by the present thesis among the current DFT challenges.

#### 3.1 Basic elements in Density Functional Theory

The density functional formulation for any many-body problem is usually grounded in two key works: the basic DFT theorems due to Hohenberg and Kohn (HK)<sup>19</sup> and the self-consistent solution proposed by Kohn and Sham (KS-DFT).<sup>20</sup>

Consider, for instance, an electronic system with  $N$  particles described by the Hamiltonian

$$\hat{H} = \hat{T} + \hat{U} + \hat{V}, \quad (3.1)$$

where  $\hat{T}$  represents the operator associated with the observable  $T$  for the kinetic energy,  $\hat{U}$  describes the sum over all interaction between particles with corresponding observable  $U$ , and  $\hat{V}$  accounts for the contribution of each individual particle due to the presence of a external potential  $V(\mathbf{r})$ . Notice that  $\hat{U}$  describes the contributions of all two-body interactions, while  $\hat{V}$  accounts solely for one-body contributions.

Usually, one is interested in the solution of the system in eq. (3.1) when  $\hat{U}$  represents the standard Coulomb repulsion and the potential is local. It follows that the Hamiltonian

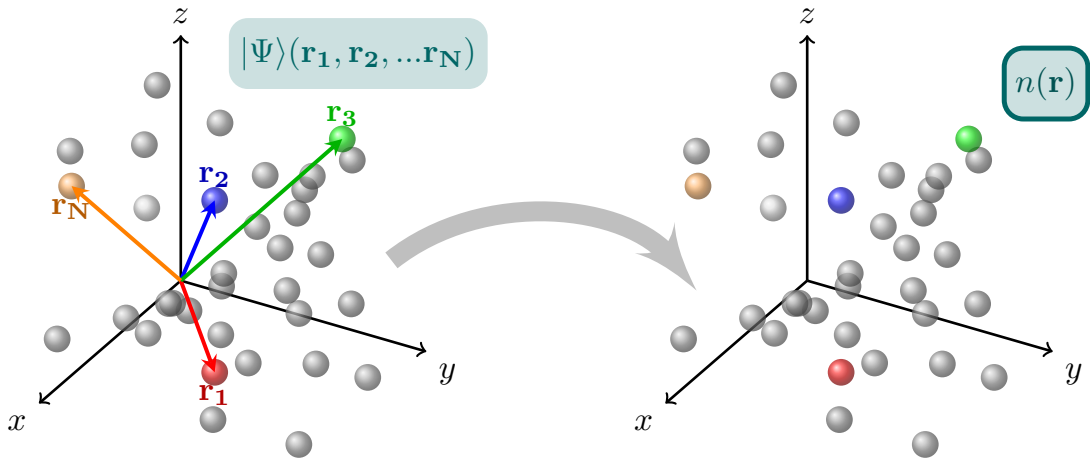


Figure 13 – The main contribution of DFT to Quantum Mechanics was simplifying the solution of the many-body problem by coding all the information in the density  $n(\mathbf{r})$  - an object of three coordinates - simpler than the many-body wave function  $|\Psi(\mathbf{r}_1, \mathbf{r}_2, \dots, \mathbf{r}_N)\rangle$ , - an object of  $3N$  variables.

Source: By the author.

in eq. (3.1) is expressed as

$$\hat{H} = \sum_{i=1}^N \frac{\hat{\mathbf{p}}_i^2}{2m_i} + \frac{1}{2} \sum_{i=1}^N \sum_{j \neq i=1}^N \frac{e^2}{|\hat{\mathbf{r}}_i - \hat{\mathbf{r}}_j|} + \sum_{i=1}^N V(\hat{\mathbf{r}}_i), \quad (3.2)$$

where  $\hat{\mathbf{p}}_i$  and  $\hat{\mathbf{r}}$  are the operators associated with the momentum and the position, respectively, and  $m_i$  is the mass of particle  $i$ . For uniform systems,  $m_i = m$  for all  $i$ .

The solution of the system in eq. (3.2) by means of the Schrödinger equation yields a spectrum of  $K$  energies  $\{E_k\}$  ( $k = 0, 1, \dots, K - 1$ ) and the corresponding eigenstates  $\{|\Psi_k(\mathbf{r})\rangle\}$ , where  $k$  labels a quantum number in a Hilbert space of dimension  $K$  and  $\mathbf{r} = (\mathbf{r}_1, \mathbf{r}_2, \dots, \mathbf{r}_N)$ . Usually the electronic system comprises a very large number of particles, so  $K \rightarrow \infty$ , so the spectrum and the Hilbert space comprise infinite  $k$ 's. Especially, the ground-state wave-function  $|\Psi_0\rangle$  is the eigenstate for which  $E$  is minimum. The ground-state energy  $E_0$  therefore satisfies the variational principle allowing us to write <sup>76</sup>

$$E_0 = \min_{\Psi} [\langle \Psi | \hat{H} | \Psi \rangle] = \langle \Psi_0 | \hat{H} | \Psi_0 \rangle. \quad (3.3)$$

From the ground-state wave-function  $|\Psi_0(\mathbf{r})\rangle$  one is able to calculate the ground-state density  $n_0(\mathbf{r})$  as

$$\begin{aligned} n_0(\mathbf{r}) &= \langle \Psi_0 | \hat{n}(\mathbf{r}) | \Psi_0 \rangle \\ &= \sum_{i=1}^N \left[ \int d\mathbf{r}_1 \int d\mathbf{r}_2 \dots \int d\mathbf{r}_N \Psi_0^*(\mathbf{r}_1, \mathbf{r}_2, \dots, \mathbf{r}_N) \delta(\mathbf{r} - \mathbf{r}_i) \Psi_0(\mathbf{r}_1, \mathbf{r}_2, \dots, \mathbf{r}_N) \right], \end{aligned} \quad (3.4)$$

where  $n_0(\mathbf{r})$  satisfies

$$\begin{aligned} n_0(\mathbf{r}) &\geq 0 \\ N &= \int d\mathbf{r} n_0(\mathbf{r}). \end{aligned} \quad (3.5)$$

The relation between the ground-state wave function  $|\Psi_0(\mathbf{r})\rangle$  and the ground-state density  $n_0(\mathbf{r})$  is the key ingredient in the density functional approach.

### 3.1.1 Hohenberg-Kohn Theorems

The Hohenberg-Kohn theorems state that there is an univocal map between the ground-state wave function  $|\Psi_0(\mathbf{r})\rangle$ , the ground-state density  $n_0(\mathbf{r})$ , in such a way that if one is able to obtain  $n_0(\mathbf{r})$  all the ground-state properties are immediately available as long as their density functional is known. In a density functional formulation instead of seeking for the wave function, an object which requires solving the Schrödinger equation for  $3N$  variables in  $3D$ , we are able to calculate any ground-state observable by simply finding the ground-state density, an object of 3 coordinates.

The first HK Theorem demonstrates that the ground-state density  $n_0(\mathbf{r})$  univocally determines the external potential  $V(\mathbf{r})$ . The proof considers the existence of two external potentials  $V(\mathbf{r})$  and  $V'(\mathbf{r})$ , with  $V(\mathbf{r}) - V'(\mathbf{r}) \neq \text{const}$ , yielding two distinct non-degenerate wave-functions  $\Psi_0 \neq \Psi'_0$ , which produce the same ground-state density  $n_0(\mathbf{r})$ . If both potentials  $V'(\mathbf{r})$  and  $V(\mathbf{r})$  yield the ground state density, we should have

$$\begin{aligned} \langle \Psi'_0 | \hat{H}' | \Psi'_0 \rangle &< \langle \Psi_0 | \hat{H}' | \Psi_0 \rangle \\ E'_0 &< \langle \Psi_0 | \hat{H} | \Psi_0 \rangle + \langle \Psi'_0 | \hat{H}' - \hat{H} | \Psi'_0 \rangle \\ E'_0 &< E_0 + \langle \Psi'_0 | \hat{V}' - \hat{V} | \Psi'_0 \rangle \\ E'_0 &< E_0 + \int d\mathbf{r} n(\mathbf{r})(V'(\mathbf{r}) - V(\mathbf{r})). \end{aligned} \quad (3.6)$$

On the other way around,

$$\begin{aligned} \langle \Psi_0 | \hat{H} | \Psi_0 \rangle &< \langle \Psi'_0 | \hat{H} | \Psi'_0 \rangle \\ E_0 &< \langle \Psi'_0 | \hat{H}' | \Psi'_0 \rangle + \langle \Psi'_0 | \hat{H} - \hat{H}' | \Psi'_0 \rangle \\ E_0 &< E'_0 + \langle \Psi'_0 | \hat{V} - \hat{V}' | \Psi'_0 \rangle \\ E_0 &< E'_0 + \int d\mathbf{r} n(\mathbf{r})(V(\mathbf{r}) - V'(\mathbf{r})). \end{aligned} \quad (3.7)$$

Addition of conditions (3.6) and (3.7) leads to an inconsistency, as

$$E'_0 + E_0 < E_0 + E'_0. \quad (3.8)$$

This proves that there is a unique external potential  $V(\mathbf{r})$  yielding the ground-state density  $n_0(\mathbf{r})$ :  $n_0(\mathbf{r}) \leftrightarrow V(\mathbf{r})$ .

The second Hohenberg-Kohn theorem establishes a functional relation between the ground-state energy  $E_0$  and the ground-state density  $n(\mathbf{r})$ , allowing us to write a universal functional  $F[n]$  comprising the kinetic energy  $T$  and the two-body interaction  $U$ , which is valid for any external potential  $V(\mathbf{r})$ . The universal functional for the ground-state energy is defined as

$$F[n] = T[n] + U[n]. \quad (3.9)$$

According to the second HK theorem, the ground-state energy is a functional of the ground-state energy

$$E[n] = F[n] + V[n], \quad (3.10)$$

where,  $V[n] = \int d\mathbf{r} n(\mathbf{r}) V(\mathbf{r})$  is also a functional of  $n$ .

From eq. (3.10), one can carry out the minimization over all anti-symmetric wave-functions  $\Psi$  yielding the density  $n_0$  to find the ground-state energy.<sup>77</sup> Mathematically, one solves

$$E[n] = \min_{\Psi \rightarrow n_0} (F[n] + V[n]). \quad (3.11)$$

In order to appreciate this result, we recall eq. (3.4), according to which  $\Psi_0 \leftrightarrow n_0$  and the functional for the ground-state energy in eq. (3.10). Provided that the ground-state energy  $E$  satisfies the variational principle, the second Hohenberg-Kohn theorem yields the ground-state energy  $E_0$  by minimizing  $E[n]$  in eq. (3.10) with respect to  $n$ , i.e.,

$$E_0 = \min_{n \rightarrow n_0} \left[ F[n] + \int d\mathbf{r} n(\mathbf{r}) V(\mathbf{r}) \right]. \quad (3.12)$$

Although the existence of  $F[n]$  and  $E[n]$  is guaranteed, there is no straightforward nor general recipe to obtain an explicit functional form for  $E[n]$  in any problem. The main challenge is to express the terms related to the kinetic energy  $T$  and the two-body interaction  $U$  as functionals of the many-body density  $n(\mathbf{r})$ . In practice, obtaining an analytical expression for  $E[n]$  and other ground-state observables is a very difficult task even for few particle interacting systems.

In the absence of particle-particle interactions represented by the operator  $\hat{U}$ , the universal functional reduces to the functional associated with the kinetic energy, which is defined as

$$T_s[n] = \min_{\Psi \rightarrow n} \langle \Psi[n] | \hat{T} | \Psi[n] \rangle, \quad (3.13)$$

where the wave-functions  $\Psi$  are calculated as Slater determinants of single-particle orbitals  $\varphi_i(\mathbf{r})$ .

The non-interacting picture allows for an analytical treatment similar to that of the Hartree-Fock self-consistent solution, in which the many-body problem is regarded as

if each particle moves freely in the presence of an effective potential, as prescribed by the Thomas-Fermi theory. This fact and the density functional ideas inspired the proposal of Kohn and Sham for carrying out the minimization process in an auxiliary free-electron system, the so-called KS-DFT self-consistent solution.

### 3.1.2 Kohn-Sham system and self-consistent calculation

The main idea in the approach devised by Kohn and Sham is to imagine that an interacting system, such as that of eq. (3.2), can be represented by a fictitious system of non-interacting particles subject to an effective external potential.<sup>20</sup> The so-called Kohn-Sham potential accounts for the sum over all the effect contributions due to each particle and is defined as

$$\hat{V}_{\text{KS}}(\mathbf{r}) = \sum_{i=1}^N V_{\text{KS}}(\hat{\mathbf{r}}_i). \quad (3.14)$$

Given the map between ground-state wave-functions, densities and potentials,  $\hat{V}_{\text{KS}}$  is chosen so that the ground-state density  $n_{\text{KS}}(\mathbf{r})$  of the non-interacting system matches the ground-state density  $n_0(\mathbf{r})$  of the many-body problem, i.e.,

$$n_{\text{KS}}(\mathbf{r})|_{\hat{V}_{\text{KS}}} \equiv n_0(\mathbf{r}). \quad (3.15)$$

The fictitious electron gas is defined by a single-particle Hamiltonian

$$\hat{H}_{\text{KS}} = \hat{T}_s + \hat{V}_{\text{KS}}, \quad (3.16)$$

where,  $\hat{T}_s$  is the kinetic-energy operator, and  $\hat{V}_{\text{KS}}$  is defined from the minimization of the universal functional re-written as

$$F[n] = T_s[n] + U_H[n] + E_{\text{xc}}[n], \quad (3.17)$$

where

$$U_H = \frac{e^2}{2} \int d\mathbf{r} \int d\mathbf{r}' \frac{n(\mathbf{r})n(\mathbf{r}')}{|\mathbf{r} - \mathbf{r}'|} \quad (3.18)$$

represents the functional for the classical electrostatic interaction and is known as the Hartree energy, and

$$E_{\text{xc}}[n] \equiv (T[n] - T_s[n]) + (U[n] - U_H[n]) \quad (3.19)$$

defines the so-called exchange-correlation energy functional.

In order to obtain explicitly  $V_{\text{KS}}(\mathbf{r})$ , we carry out the minimization procedure. We start by assuming that  $E[n_0]$  does not change under an infinitesimal change  $\delta n$  in the ground-state density. Mathematically, this statement is expressed as follows

$$\delta E[n] = E[n_0] - E[n_0 - \delta n] = 0. \quad (3.20)$$

The ground-state of the fictitious electron gas is defined by

$$E_{0,\text{KS}} = \min_{\Psi_{0,\text{KS}} \rightarrow n} \langle \Psi_{0,\text{KS}} | T_s[n] + U_H[n] + E_{\text{xc}}[n] + V[n] | \Psi_{0,\text{KS}} \rangle. \quad (3.21)$$

Plugging eq. (3.17) and (3.21) into (3.20), we find that

$$\begin{aligned} V_{\text{KS}}(\mathbf{r}) &\equiv V_H(\mathbf{r}) + V_{\text{xc}}(\mathbf{r}) + V(\mathbf{r}) \\ &= -\frac{\delta T_s[n]}{\delta n}, \end{aligned} \quad (3.22)$$

where  $V_H \equiv \frac{\delta U_H[n]}{\delta n}$  and  $V_{\text{xc}}(\mathbf{r}) \equiv \frac{\delta E_{\text{xc}}[n]}{\delta n}$  are functional derivatives.

The definition in eq. (3.17) connects the interacting Hamiltonian  $\hat{H}$  to the single-particle system  $\hat{H}_{\text{KS}}$  by means of an one-body potential, namely,  $V_{\text{KS}}$  incorporating all the many-body effects due to the interaction between particles and many-body contributions to the kinetic energy. Specifically, since  $U_H$  is known and  $T_s$  can be treated exactly, the energetic corrections due the couplings between particles are ultimately ascribed to the exchange-correlation term.

The second equality in eq. (3.22) has a correspondence with the solution of the single-particle Schrödinger equation

$$\left( \frac{-\hbar^2 \nabla_{\mathbf{r}}}{2m} + V_{\text{KS}}(\mathbf{r}) \right) \varphi_q(\mathbf{r}) = \epsilon_q \varphi_q(\mathbf{r}), \quad (3.23)$$

where  $q = 1, \dots, Q$ ,  $Q$  is the number of occupied Kohn-Sham orbitals  $\varphi_q$  and  $\epsilon_q$  are the Kohn-Sham energies.

Having at hand the Kohn-Sham outputs  $\varphi_q(\mathbf{r})$  and  $E_q$  it is straightforward to calculate the ground-state density

$$n_{\text{KS}}(\mathbf{r}) = \sum_{q=1}^N |\varphi_q(\mathbf{r})|^2, \quad (3.24)$$

and the ground-state energy

$$E_0 \stackrel{\text{KS}}{=} \sum_{q=1}^N \epsilon_q - \int d\mathbf{r} n(\mathbf{r}) (V_H + V_{\text{xc}}) + U_H + E_{\text{xc}}. \quad (3.25)$$

The Kohn-Sham formulation to carry out the minimization and therefore obtain ground-state density  $n_0$  and the corresponding ground-state energy  $E_0$  employs a self-consistent approach similar to that of the Hartree-Fock method. We will describe the general approach as follows. Starting in iteration  $k = 0$ , the Kohn-Sham Hamiltonian  $\hat{H}_{\text{KS}}^k$  is calculated for an initial guess for the ground-state density  $n^{k=0}$ . The Kohn-Sham Hamiltonian is then diagonalized and the Kohn-Sham orbitals  $\varphi_q$  are used in the calculation of a new density  $n^{k+1}$ . The latter is compared with  $n^k$  and the difference

$$|n^{k+1}(\mathbf{r}) - n^k(\mathbf{r})| < \delta \quad (3.26)$$

is monitored.

The limit  $\delta \rightarrow 0$  defines the convergence criteria. For practical KS-DFT computations,  $\delta$  is a very small number. In the case in which the difference between densities are lower than the threshold  $\delta$ , we found  $n^k$  is the ground-state density and the algorithm converged. In the opposite case,  $|n^{k+1}(\mathbf{r}) - n^k(\mathbf{r})| > \delta$ , the procedure is iterated and the new Kohn-Sham Hamiltonian  $\hat{H}_{\text{KS}}^{k+1}$  is calculated from the density  $n^{k+1}$ . To ensure instabilities spoiling convergence, usually  $n_{k+1}$  is replaced by a mixture with  $n^k$ . For instance, the simplest mixture considers

$$n^{k+1} = (1 - \beta)n^k + \beta n^{k+1}, \quad (3.27)$$

where  $\beta \ll 1$  is a small number. The iterative procedure is then iterated until the convergence is reached, using the steps described above.

At the level of the ideas discussed above, the density functional approach for the many-body problem is exact. In introducing the Hohenberg-Kohn theorems, we have already pointed at the challenge to express properties as functionals of the density, such as the functionals  $F[n]$  and  $E[n]$  for ground-state energy. Now, we may note that in the Kohn-Sham proposal for DFT, this difficult is transferred to the functional for the exchange correlation energy  $E_{\text{xc}}[n]$ . Although eq. (3.17) is exact, and the expressions for  $U_H[n]$  and  $T_s[n]$  are available, the same is not true for the so-called exchange-correlation potential  $V_{\text{xc}}[n]$ . Given that the entire KS calculation assumes the knowledge of  $V_{\text{KS}}[n]$ , the difficult in implementing a self-consistent DFT calculation is now transferred to  $V_{\text{xc}}[n]$ . For practical calculations,  $V_{\text{xc}}[n]$  must therefore be approximated.

We stress that the previous explanation of a KS-DFT self-consistent computation is illustrative. In practice, robust implementations of density functional calculations are more complex and include a series of and technical details, such as the definition of the basis set to project the Kohn-Sham orbitals, the convergence criteria for the energy, the mixture of orbitals besides mixture of the densities, and other tricks. Many packages and codes for state-of the art DFT computations abound. Examples are the Viena Ab initio Simulation package (VASP), QUANTUM EXPRESSO, ABINIT, Exciting, Octopus, CASTEP, and many others.<sup>78–83</sup> For the purposes of the present thesis, the description provided suffices, as we will explain in Section 3.2, where we will discuss implementation of the KS-DFT self-consistent procedure for typical model Hamiltonians describing strongly correlated systems.

In the following, we will discuss the exchange-correlation functional and the simplest level of approximation considered in density functional calculations.

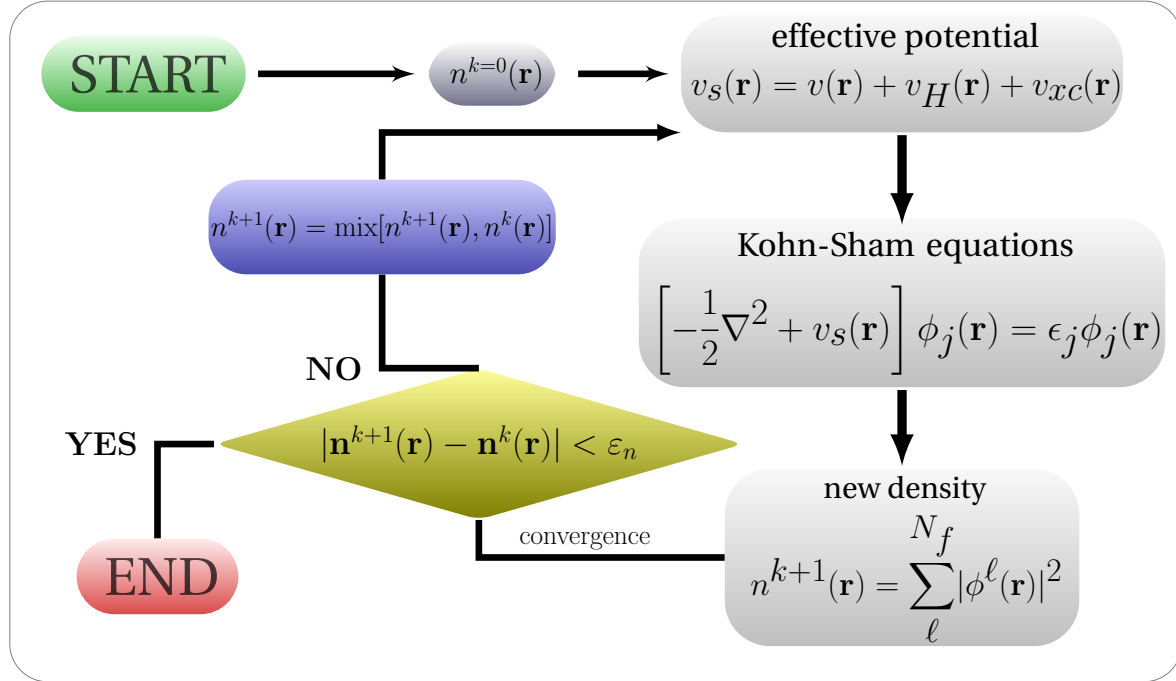


Figure 14 – Self-consistent cycle proposed by Kohn and Sham. Starting from an initial guess for the many-body density  $n^{k=0}(\mathbf{r})$  in the very first iteration  $k = 0$ , one can calculate the effective potential  $v_{KS}$  of the auxiliary system and solve the corresponding Hamiltonian  $H_{KS}$  in eq. (3.16). From the ground-state  $\Psi_{KS}(\mathbf{r}_1, \mathbf{r}_2, \dots, \mathbf{r}_N)$ , one can therefore obtain the density  $n_{KS}^k$ . The latter is compared with  $n_{KS}^{k-1}$  and if the difference is less than a cut-off  $\epsilon_n$ , the cycle is stopped. Otherwise, the cycle is repeated until the convergence criteria is reached and, at the end of each iteration  $k$ , the densities  $n_{KS}^k$  and  $n_{KS}^{k+1}$  are mixed.

Source: By the author.

### 3.1.3 The exchange-correlation functional

The exchange-correlation functional  $E_{xc}[n]$  can be decomposed in order to split the contributions that can be handled exactly and the others that must be approximated.<sup>23,84</sup> Indeed, this was proposed in the definition of  $E_{xc}[n]$  in eq. (3.17), where the functional for the energy  $E[n]$  was written in terms of the contributions that can be calculated exactly ( $T_s[n]$ ,  $U_H[n]$ , and, in general,  $V[n]$ ), and the term to be approximated, namely, the exchange-correlation functional  $E_{xc}$ . The latter is therefore decomposed into two terms

$$E_{xc}[n] \equiv E_x[n] + E_c[n], \quad (3.28)$$

where  $E_x[n]$  and  $E_c[n]$  are the exchange and correlation functionals, respectively.

The exchange functional  $E_x[n]$  accounts for the largest contribution to the exchange-correlation energy and is an implicit functional of the density. Resorting to the definition of the exchange energy in the Hartree-Fock approach,  $E_x[n]$  can be calculated from the

Kohn-Sham orbitals as

$$E_x[n] \equiv -\frac{e^2}{2} \sum_{q,p=\text{occ}} \int d\mathbf{r} \int d\mathbf{r}' \frac{\varphi_q^*(\mathbf{r}) \varphi_p^*(\mathbf{r}') \varphi_p(\mathbf{r}) \varphi_q(\mathbf{r}')}{|\mathbf{r} - \mathbf{r}'|}, \quad (3.29)$$

where  $\text{occ}$  denotes the occupied Kohn-Sham orbitals to enter in the sum.

For strongly correlated systems, on the other hand, the functional accounting for the correlation  $E_c$  corresponds to a large contribution, orders of magnitude larger than  $E_x$ . Although one could be tempted to calculate  $E_x$  and regard the corrections to  $E_{xc}$  to the correlation term in DFT calculations, usually, the approximation for full  $E_{xc}$  is implemented. The practical reason for this choice is that carrying out the calculation of  $E_x$  yields poor accuracy in many properties of interest. A deep understanding of this consequence from the theoretical point of view came with the concept of exchange and holes, according to which the exact definition for the exchange-correlation functional reads

$$E_{xc}[n] \equiv \frac{e^2}{2} \int d\mathbf{r} n(\mathbf{r}) \int d\mathbf{r}' \frac{\rho_{xc}(\mathbf{r}, \mathbf{r}' - \mathbf{r})}{|\mathbf{r} - \mathbf{r}'|}, \quad (3.30)$$

where  $\rho_{xc}$  is the exchange-correlation hole density per electron.

The physical interpretation of the previous definition is a Coulomb-like interaction between an electron at position  $\mathbf{r}$  with an exchange-correlation hole charge distributed in a shell  $\mathbf{r}'$  surrounding  $\mathbf{r}$ . While  $\rho_{xc}$  is typically localized around  $\mathbf{r}$ , the same is not true for the exchange term only. This explain why the use of the exact exchange in eq. (3.29) is avoided, as the approximation for the correlation contribution would require a non-local approach in order to compensate the delocalization of  $\rho_x(\mathbf{r}, \mathbf{r}')$ .

Considering that DFT is, in practice, a computational approach to study many-body problems, the numerical resources involved in implementing it in real applications are enormous. With the previous considerations on definition and calculation of the exchange-correlation functional, the lesson to be learned is that approximations constitute an essential component of the DFT program. There are known ways to carry out the approximation in different levels, in such a way that the sophistication of approximations defines the so-called Jacob's ladder. The simplest level is known as *Local Density Approximation* (LDA), in which  $v_{xc}[n]$  depends only on the local density  $n(\mathbf{r})$ . In a second level, known as *Generalized Gradient Approximation* (GGA),  $v_{xc}[n]$  is defined in terms of the local densities and also in terms of fluctuations of the densities given by  $\nabla n(\mathbf{r})$ . Beyond LDA and GGA, in increasing order of complexity are approaches known as meta-GGA, hybrid functionals and fully nonlocal functionals (also known as RPA, from random-phase approximation). We briefly review the levels of approximation in Appendix A. Below, we will briefly introduce the general form of LDA and comment on its range of applicability.

### 3.1.3.1 Local Density Approximation (LDA)

The simplest approach to construct an approximation for the exchange-correlation functional  $E_{\text{xc}}[n]$  considers many-body corrections as local and resorts to a uniform electron gas. In other words,  $E_{\text{xc}}$  depends only on the electronic density in each point of space  $n(\mathbf{r})$  and the expression for  $E_{\text{xc}}$  is calculated as that of an uniform system. Mathematically, this translated in the following expression

$$E_{\text{xc}}^{\text{LDA}} = \int d\mathbf{r} \epsilon_{\text{xc}}^{\text{uni}}[n(\mathbf{r})], \quad (3.31)$$

where  $\epsilon_{\text{xc}}^{\text{uni}}$  is the exchange-correlation energy density of a uniform electron gas.

LDA was designed to suit systems depicting slowly varying densities. After the first ideas to approximate the exchange-correlation functional via LDA a very large number of works in material science had successfully employed LDA in ab-initio calculations, an impressive result given the simplicity of the approach. Examples include calculations of atomic structure, elastic and vibrational constants in metals. Nonetheless, it did not take too long to see the failures of LDA, in particular, in calculations for quantum chemistry. LDA is known to underestimate lattice parameters for metals and insulators, overestimate the binding energy of molecules and solids, get the incorrect order for phase stability of molecular conformations or crystal bulk, spoil energetics in magnetic materials and is far to achieve good results in a description of Van der Walls interactions. Moreover, among the list of applications where non-locality plays an important role and therefore prevents the use of LDA, we have strongly correlated systems.

## 3.2 Density Functional Theory and strongly correlated systems

Most model Hamiltonians in condensed matter physics being given in terms of electrons on lattices; for them a somewhat modified version of DFT is defined – Lattice Density Functional Theory.<sup>85</sup> All the foundations of DFT, including the HK theorems and the Kohn-Sham self-consistent solutions can be adapted so that the integrals over space coordinates are replaced by sums over lattice sites.<sup>85,86</sup> A function  $E(n_1, n_2, \dots)$  of the lattice occupations is substituted for the function  $E[n]$ . \* For simplicity, we will denote the function by the traditional symbol  $E[n]$ . The need to describe strongly correlated phenomena by means of a feasible approximation for the exchange-correlation functional were the inspiration for novel approaches to construct  $v_{\text{xc}}$  based on the exact solution of model Hamiltonians. Below, we will present two parametrizations based on the exact solution obtained from the Bethe Ansatz.

---

\* It is a function instead of a functional due to the discrete treatment of on-site densities.

### 3.2.1 Bethe Ansatz Local Density Approximation

One of the few examples in which the LDA is able to describe strongly correlated systems is an approach known as Bethe Ansatz Local Density Approximation or BALDA.<sup>86</sup> Based on the exact Bethe Ansatz solution for the infinite homogeneous Hubbard Hamiltonian, the BALDA provides a simple expression for the in-site correlation functional and, as the exchange contribution vanishes,  $v_c[n] = v_{xc}^j[n]$ . The latter reads

$$v_{xc}^{j,\text{BALDA}}[n] = v_{xc}^{\text{hom}}[n]|_{n \rightarrow n^j}, \quad (3.32)$$

where it is implicit the dependence on the parameters of the homogeneous model, such as the Coulomb repulsion  $U$  in the case of the Hubbard Hamiltonian in the absence of external potentials.

Within the BALDA,  $v_{xc}^{\text{hom}}(n_j)$  in eq. (3.32) can be calculated from the per-site ground-state energy  $e(n, U)$  of the one-dimensional homogeneous Hubbard model obtained via the Bethe Ansatz.<sup>86,87</sup> Following Lieb and Wu, to carry out such calculation, one has to solve the coupled integral equations

$$\rho(x) = \frac{1}{2\pi} + \frac{\cos x}{\pi} \int_{-\infty}^{\infty} dy \sigma(y) \frac{U/4t}{(U/4t)^2 + (y - \sin x)^2} \quad (3.33)$$

and

$$\sigma(y) = \frac{1}{\pi} \int_{-Q}^{+Q} dx \rho(x) \frac{U/4t}{(U/4t)^2 + (y - \sin x)^2} - \frac{1}{\pi} \int_{-\infty}^{+\infty} dy \rho(y') \frac{U/4t}{(U/4t)^2 + (y - y')^2}, \quad (3.34)$$

where  $Q$  is associated with the density of the system and is determined by

$$\int_{-Q}^{+Q} dx \rho(x) = n, \quad (3.35)$$

and  $\sigma(y)$  is normalized according to

$$\int_{-\infty}^{\infty} dy \sigma(y) = \frac{n}{2}. \quad (3.36)$$

From  $\rho(x)$ , the per-site ground-state energy is then calculated as

$$e^{BA}(n \leq 1, U) = -2t \int_{-Q}^{+Q} dx \rho(x) \cos x. \quad (3.37)$$

For  $n > 1$ , particle-hole symmetry allows to obtain

$$e^{BA}(n > 1, U) = e^{BA}(2 - n, U) + (n - 1)U. \quad (3.38)$$

Conveniently, an approximated parametrized form was proposed for the ground-state per-site energy of eq. (3.37).

$$e^{BALDA}(n, U) = -\frac{2\beta}{\pi} \sin\left(\frac{n\pi}{\beta}\right), \quad (3.39)$$

where  $\beta = \beta(u)$  ( $u = U/t$ ) can be determined from the solution of the equation

$$-\frac{2\beta}{\pi} \sin\left(\frac{\pi}{\beta}\right) = -4 \int_0^\infty dx \frac{J_0(x) J_1(x)}{x[1 + e^{ux/2}]}.$$
 (3.40)

Using the parametrization in eq. (3.39) and plugging it into eq. (3.32), we obtain the following expression for the exchange-correlation functional in the BALDA:

$$v_{xc}(n) = -2 \left[ \cos\left(\frac{n\pi}{\beta}\right) - \cos\left(\frac{n\pi}{2}\right) + \frac{U}{4}n \right].$$
 (3.41)

Figure 15 shows the profile of the functionals for the exchange correlation energy  $E_{xc}[n]$  and the exchange correlation potential  $v_{xc}[n]$  for various coupling ratios  $U/t$ , ranging from  $U = t$  to  $U = 100t$ .

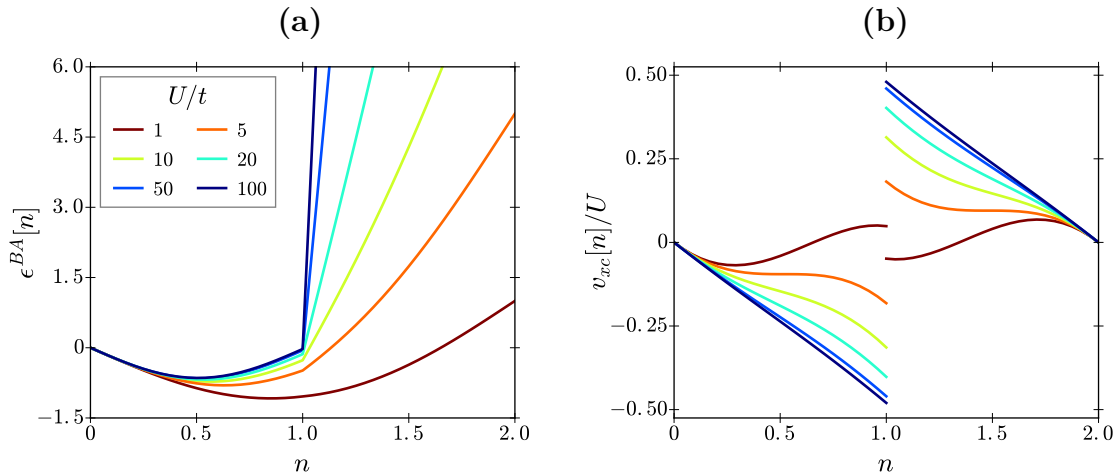


Figure 15 – Functionals for the exchange correlation energy  $E_{xc}[n]$  (a) and potential  $v_{xc}[n]$  (b) obtained with the Bethe Ansatz Local Density Approximation (BALDA) for  $U = t, 5t, 10t, 50$  and  $100t$ . Note that the discontinuity at half-filling  $n = 1$  is enhanced as  $U/t$  grows.

Source: Adapted from LIMA et al. <sup>27</sup>

Recently, Franca and collaborators have upgraded the BALDA with the *Local Spin Density Approximation* (LDSA) version of the former BALDA approach, a parametrization that is frequently referred as BALDSA or FVC.<sup>88</sup> The spin components of the density  $n_\uparrow$  and  $n_\downarrow$  were included in the functional of the ground-state energy and in  $\beta$ . In the FVC parametrization, eq. (3.39) is written as

$$\epsilon^{FVC}(n_\uparrow, n_\downarrow, U) = -\frac{2\beta}{\pi} \sin\left(\frac{n\pi}{\beta}\right) \cos\left(\frac{m\pi}{\gamma}\right),$$
 (3.42)

where  $n = n_\uparrow + n_\downarrow$  and  $m = n_\uparrow - n_\downarrow$  and

$$\beta(n_\uparrow, n_\downarrow, U) = \beta(U)^{\alpha(n_\uparrow, n_\downarrow, U)},$$
 (3.43)

$$\alpha(n_\uparrow, n_\downarrow, U) = \left( \frac{4n_\uparrow n_\downarrow}{(n_\uparrow + n_\downarrow)^{15/8}} \right)^{\sqrt[3]{U}}, \quad (3.44)$$

$$\gamma(n_\uparrow, n_\downarrow, U) = 2 \exp \left( \frac{\sqrt{U}}{1 - (\frac{n_\uparrow - n_\downarrow}{n_\uparrow + n_\downarrow})^{3/2}} \right). \quad (3.45)$$

A feature shared by BALDA and BALSDA parametrizations is the discontinuity of the exchange-correlation potential  $v_{xc}$  at half-filling ( $n = 1$ ), which marks the existence of a gap and a Mott-insulator transition in the ground-state of the Hubbard model.<sup>26, 27, 29, 88, 89</sup> For  $n = 1$  (half-filling), the system is a Mott-insulator for non-vanishing coupling ( $U \neq 0$ ), whereas for  $n = 2$  it is a band-insulator.

Other important aspect to be considered in the BALDA refers to its accuracy for small systems, a feature that was investigated in the first paper due to Lima and colleagues.<sup>26</sup> The same feature had been already studied in terms of DMRG solution of finite chains.<sup>90, 91</sup> In fact, as BALDA is constructed from a solution that holds for the infinite Hubbard model, accounting for finite-size and boundary effects requires re-scaling the original parametrization.<sup>92</sup> Nevertheless, BALDA has been frequently used in benchmarks tests for new functional approaches for small systems.<sup>93</sup>

Within BALSDA, one can compute the expression for the exchange-correlation functional as a function of  $n_\uparrow$  and  $n_\downarrow$  from the partial derivatives of the FVC parametrization in (3.42) and arrive in two expressions for  $v_{xc}^\sigma[n_\uparrow, n_\downarrow]$  ( $\sigma = \uparrow, \downarrow$ ) for a given parameter setup  $U/t$  as in eq. (3.41). Explicitly,

$$\begin{aligned} v_{xc}^\sigma[n_\uparrow, n_\downarrow](u = U/t) = & -\frac{2}{\pi} \left[ \beta'_\sigma \sin \left( \frac{(n_\uparrow + n_\downarrow)\pi}{\beta} \right) \cos \left( \frac{(n_\uparrow - n_\downarrow)\pi}{\gamma} \right) \right. \\ & + \pi \left[ 1 - (n_\uparrow + n_\downarrow) \frac{\beta'_\sigma}{\beta} \right] \cos \left( \frac{(n_\uparrow + n_\downarrow)\pi}{\beta} \right) \cos \left( \frac{(n_\uparrow - n_\downarrow)\pi}{\gamma} \right) \\ & \left. - s_\sigma \pi \frac{\beta}{\gamma} \left[ 1 - (n_\uparrow - n_\downarrow) \frac{\gamma'_\sigma}{\gamma} \right] \sin \left( \frac{(n_\uparrow + n_\downarrow)\pi}{\beta} \right) \sin \left( \frac{(n_\uparrow - n_\downarrow)\pi}{\gamma} \right) \right], \end{aligned} \quad (3.46)$$

where  $s_\sigma = +1$ , for  $\sigma = \uparrow$  and  $s_\sigma = -1$ , for  $\sigma = \downarrow$ ,

$$\beta'_\sigma(u) \equiv \frac{\partial \beta}{\partial n_\sigma} = \log(\beta(u)) \beta(n_\uparrow, n_\downarrow, u) \alpha'_\sigma, \quad (3.47)$$

$$\alpha'_\sigma \equiv \frac{\partial \alpha}{\partial n_\sigma} = \sqrt[3]{u} \left( n_{-\sigma} - \frac{15}{8} \frac{n_\uparrow n_\downarrow}{(n_\uparrow + n_\downarrow)} \right) \frac{\alpha(n_\uparrow, n_\downarrow, u)}{n_\uparrow n_\downarrow}, \quad (3.48)$$

and

$$\gamma'_\sigma \equiv \frac{\partial \gamma}{\partial n_\sigma} = (-1)^\sigma \frac{3\sqrt{u}(n_\uparrow + n_\downarrow)^{1/2}(n_\uparrow - n_\downarrow)^{1/2}}{\left[ (n_\uparrow + n_\downarrow)^{3/2} - (n_\uparrow - n_\downarrow)^{3/2} \right]^2} \gamma(n_\uparrow, n_\downarrow, u) n_{-\sigma}. \quad (3.49)$$

Since the seminal paper due to Lima et al many articles have reported good results in applying BALDA for lattice models.<sup>26–30</sup> For instance, it was proven accurate to describe cold atoms in trapping potentials, inhomogeneous lattices and also impurity problems. Two examples of calculations using BALDA and BALSDA are shown in Figs. 16 and 17. We reproduced these results by implementing a code to perform self-consistent calculations in spin chains.

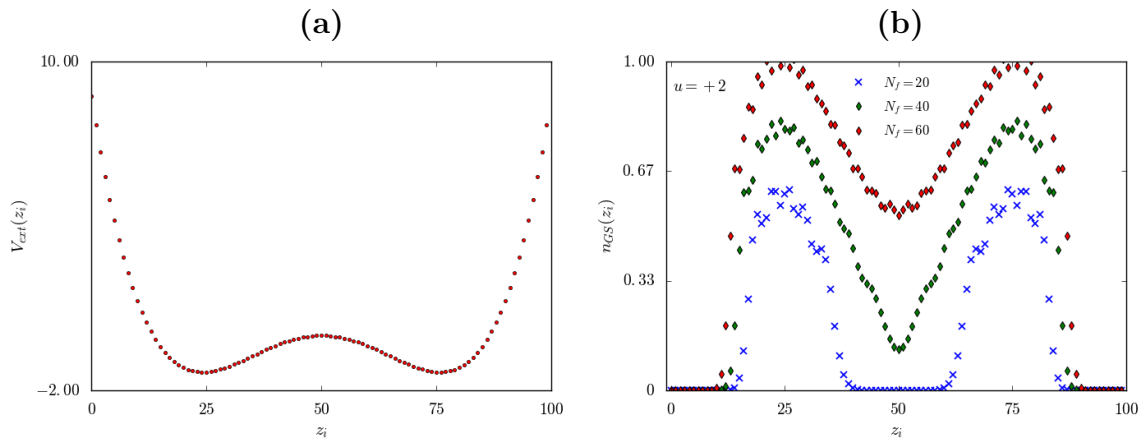


Figure 16 – Results for density functional calculations using BALDA for one-dimensional optical lattices submitted to an asymmetric trapping potential for  $u = U/t = 2$ . Such a coupling strength is typical for experiments with cold atoms and optical lattices. (a) A trapping potential with form of a power series  $V(z_i)/t = \sum_\ell V_\ell(z_i - L/2)^\ell$ , where  $L$  is the number of lattice sites and  $V_\ell$  are coefficients, controls the confinement of electrons in each site of the lattice  $z_i$ . Here,  $L = 100$ . The latter are given in terms of power series with strengths  $V_2/t = 1.6 \times 10^{-2}$ ,  $V_3/t = 1.6 \times 10^{-4}$  and  $V_4/t = 1.92 \times 10^{-5}$ . (b) Converged on-site densities at different fillings  $N_f = 20, 40, 60$ . Note that the sites for which the potential  $V(z_i)$  is minimum will end with a higher density.

Source: Adapted from XIANLONG et al.<sup>28</sup>

### 3.3 DFT and the Kondo problem

#### 3.3.1 Parametrization of the exchange-correlation functional based on the Bethe Ansatz solution of the Anderson Hamiltonian

The interest in molecular junctions and other nano-structured devices lead DFT experts seek for new approaches to describe transport using density functional tools.<sup>31, 94–97</sup> Bergfield and colleagues pioneered the first attempts of DFT approaches to study the Kondo effect in quantum dots.<sup>31</sup> Their proposal, inspired by the qualitative view of such systems in terms of models, as discussed in chapter 2, presents a parametrization for the exchange-correlation potential based on the Bethe Ansatz solution of the Anderson Hamiltonian.<sup>68, 69</sup>

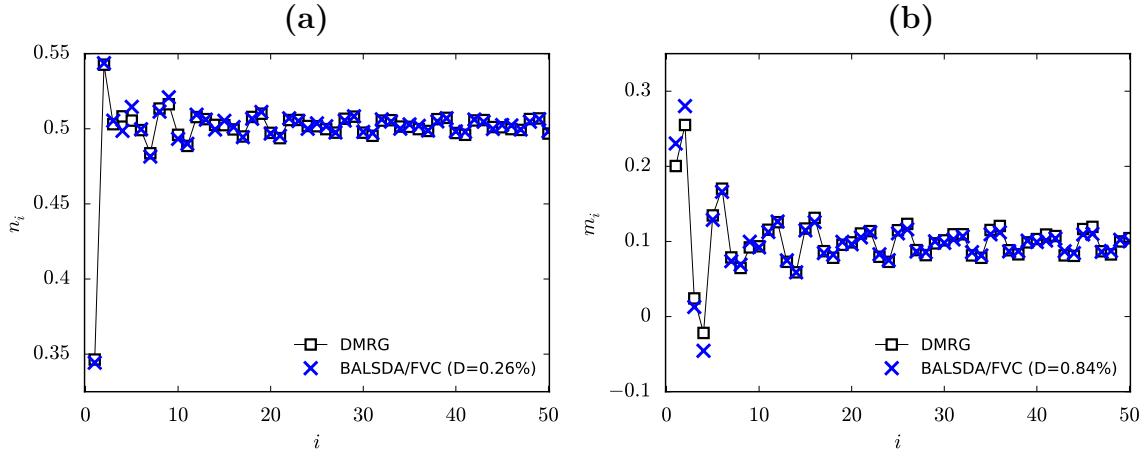


Figure 17 – Results of self-consistent calculations using FVC BALSDA for obtaining the ground-state density and magnetization profiles of an open Hubbard chain with  $L = 100$  sites,  $N_\uparrow = 30$ ,  $N_\downarrow = 20$  fermions. The coupling is  $U = 4t$ . Blue crosses depict results obtained self-consistently from FVC BALSDA and black empty squares represent results obtained from DMRG calculations. (a) Local Densities  $n_i$  and corresponding (b) magnetizations  $m_i$ . Percentage deviations, summed over all sites, of the LSDA densities from the DMRG ones are given in parentheses. DMRG results obtained with ITensor.

Source: Adapted from FRANÇA et al. <sup>88</sup>

For this, they used the non-interacting Green function

$$G^{\text{KS}}(\epsilon) = \frac{1}{\epsilon - v_{\text{KS}} + i\Gamma} \quad (3.50)$$

as an input for the expression of the Friedel sum rule relating the occupation number  $n_d$  with scattering phase shift  $\delta$  induced by  $V_G$ .

From the latter, one is able to obtain the occupation  $n_d^{\text{KS}}$  in the quantum dot by solving self-consistently the equation

$$n_d^{\text{KS}} = 1 + \frac{2}{\pi} \tan^{-1} \left( \frac{\epsilon_F - v_{\text{KS}}(n_d^{\text{KS}})}{\Gamma} \right), \quad (3.51)$$

where  $\epsilon_F$  are the Fermi level of the free electron gases and

$$v_{\text{KS}}(n_d) = V_G + \frac{U}{2} n_d + v_{\text{xc}}(n_d). \quad (3.52)$$

The Bethe Ansatz solution of the Anderson Hamiltonian yields the exact occupation  $n_d$  in the interacting system, through which the exact Kohn-Sham potential can be extracted from the relation

$$v_{\text{KS}} = \epsilon_F + \Gamma \cot \left( \frac{\pi n_d}{2} \right). \quad (3.53)$$

This idea was explored by Bergfield and colleagues. <sup>31</sup> In order to provide a more practical route to calculate the exchange-correlation functional and cover all parameter

space, a parametrized form for  $v_{\text{xc}}$  is proposed. Importantly, in the strongly correlated regime ( $U/\Gamma \rightarrow \infty$ ), the exchange-correlation potential acquires a step at integer particle numbers and its derivative is a Lorentzian. On the opposite limit ( $U/\Gamma \rightarrow 0$ ), up to  $U \approx \Gamma$ ,  $v_{\text{xc}}$  is a smooth function of the coupling  $U$ , and rough approximations for  $v_{\text{xc}}$  such as Hartree-Fock are expected to perform well. Guided by BA solution in the limits  $U \rightarrow \infty$  and  $U = 0$ , an adaptation of the expression for  $v_{\text{xc}}$  is approximated for  $\Gamma/U \rightarrow 0$  to  $\Gamma/U \leq 1$ . The first limit yields the following approximate functional

$$v_{\text{xc}}(U, \Gamma)_{U \rightarrow \infty} = \frac{U}{2} \left[ 1 - n_d - \left( \frac{2}{\pi} \right) \tan^{-1} \left( \frac{\pi^2 U (1 - n_d)}{8\Gamma} \right) \right]. \quad (3.54)$$

To extend eq. (3.54) for finite  $U$  the following parametrization is proposed

$$v_{\text{xc}}(U, \Gamma) = \alpha \frac{U}{2} \left[ 1 - n_d - \frac{2}{\pi} \tan^{-1} \left( \frac{1 - n_d}{\sigma} \right) \right], \quad (3.55)$$

where both adimensional parameters  $\alpha$  and  $\sigma$  are functions of the ratio  $\Gamma/U$  between the coupling of the quantum dot and the Coulomb repulsion.

We note that the last term on the right-hand side of eq. (3.55) grows by a factor  $\pi$  between the limits  $n_d \ll 1$  and  $n_d \gg 1$ , as  $\tan^{-1}$  jumps by  $\pi$  when  $n_d \rightarrow^+ 1$ . The parameter  $\sigma$  therefore determines the width in which  $v_{\text{xc}}$  changes. In its turn, the parameter  $\alpha$  weighs the amplitudes of the exchange-correlation potential  $v_{\text{xc}}(n_d)$  and its peak  $\partial v_{\text{xc}}(n_d)/\partial n_d$  as a function of the ratio  $\Gamma/U$  and it is related to charge quantization. In the limit  $U \rightarrow \infty$ , eqs. (3.55) and (3.54) match as  $\alpha \rightarrow 1$  and  $\sigma \rightarrow 8\Gamma/(\pi^2 U)$ .

By exactly solving eq. (3.52) via BA for a given ratio  $\Gamma/U$  and performing a least-squares fitting of eq. (3.55) to find  $\alpha$  and  $\gamma$  with the constraints previously discussed, the authors of Ref. <sup>31</sup> proposed the following expressions

$$\alpha \left( \frac{\Gamma}{U} \right) = \frac{U}{U + 5.68\Gamma} \quad (3.56)$$

and

$$\sigma \left( \frac{\Gamma}{U} \right) = 0.811 \frac{\Gamma}{U} - 0.390 \frac{\Gamma^2}{U^2} - 0.168 \frac{\Gamma^3}{U^3}. \quad (3.57)$$

The previous parametrization was proven accurate to describe the conductance through a Anderson junction at zero temperature in all coupling regimes, i.e., between the limits  $\Gamma/U \rightarrow 0$  and  $\Gamma/U \rightarrow \infty$ . Figure 18 show the proposed parametrized functional of eq. (3.55) (main plot) and its first derivative (inset) for ratios  $U/\Gamma = 1, 5, 10, 20, 50, 100$ , which allow to explore from the weakly  $U = \Gamma$  to the very strong coupled regime  $U = 100\Gamma$ .

The results for the ground-state conductance  $\mathcal{G}_d$  in a SET as a function of the applied gate voltage  $V_G$  obtained by solving eq. (3.51) self-consistently is shown in Fig.

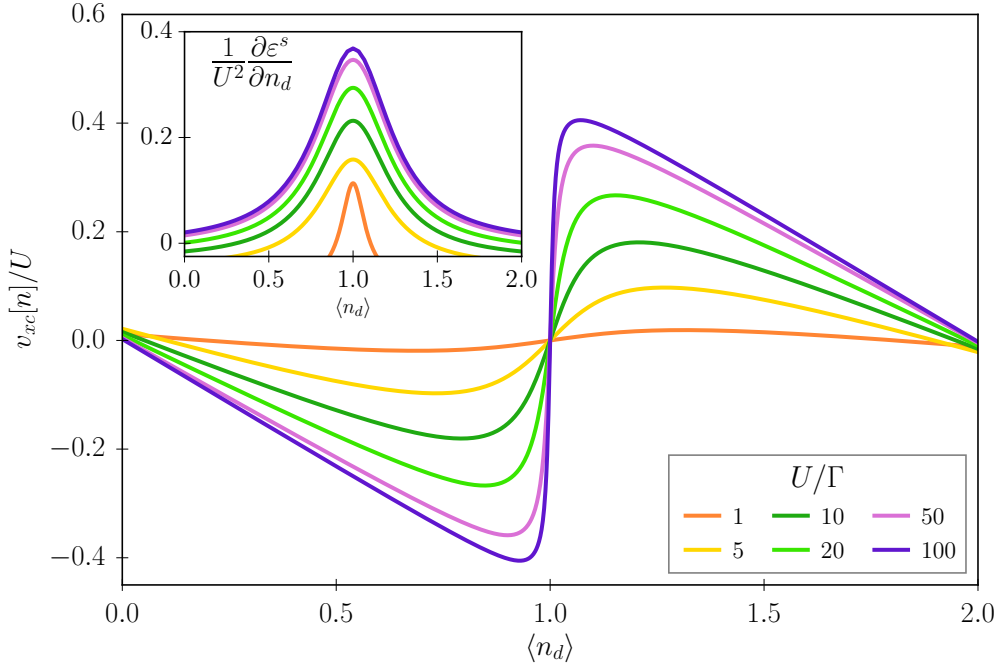


Figure 18 – Exchange-correlation functional  $v_{\text{xc}}(n_d)$  parametrized by eqs. (3.55), (3.56) and (3.57) as a function of the occupation  $n_d$  for couplings  $U/\Gamma = 1, 5, 10, 20, 50, 100$ . The inset depicts the first derivative  $\partial v_{\text{xc}} / \partial n_d$  weighted by  $1/U^2$  as a function of  $n_d U / \Gamma$ .

Source: Adapted from BERGFIELD et al. <sup>31</sup>

<sup>19</sup>, where three correlation regimes are considered:  $U = \Gamma$  weakly coupled,  $U = 10\Gamma$  intermediately coupled,  $U = 100\Gamma$  strongly coupled. Note that the Kondo plateau forms for  $U = 10\Gamma$  and becomes flat in the region  $-U < V_G < 0$  for  $U \gg \Gamma$ .

Later, the same group reported an improved version of the parametrized functional in which the fitting of the parameter  $\sigma$  is constrained by the charge susceptibility  $\bar{\chi}_d = U \frac{dn_d}{d\mu}$ , a quantity related to the slope of  $v_{\text{xc}}$  at the particle-hole symmetric point  $n_d = 1$ . <sup>95</sup>

Together with the work by Bergfield et al., the Kondo effect in quantum dots has become subject of many other inspiring density functional approaches. <sup>94–99</sup> Regardless of their instructive purpose, they can not be extended to the study of more complex devices, as mentioned in Chap. 2. Consider, for instance, the absence of any dependence of the parametrization in (3.54) on the leads structure of a more general Anderson junction. As  $v_{\text{xc}}[n]$  only deals with the quantum dot, and ignores details of the leads, one does not expect it to accurately reproduce the transport properties in more general situations. A simple example to illustrate this limitation is the application of an external potential  $W$  to the leads, as in eq. (2.19) or when their conduction band is no longer a free electron gas.

In Figs 20 and 21 we present results for the ground-state zero bias conductance  $\mathcal{G}_d$  as a function of the gate voltage  $V_G$  for two coupling regimes - weak ( $\Gamma = U$ , panels **(a)**) and intermediate ( $\Gamma = 10U$ , panels **(b)**) - and three values of scattering potentials

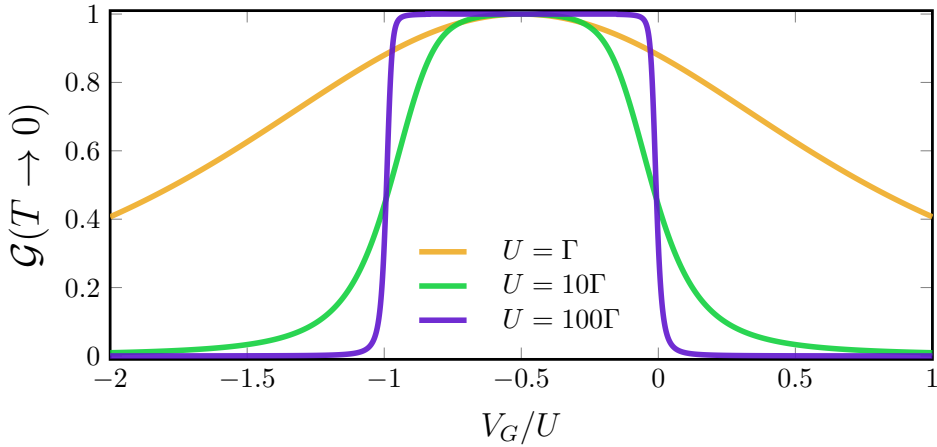


Figure 19 – Ground state conductance  $\mathcal{G}_d$  in a SET as a function of the gate voltage  $V_G$  obtained from self-consistent calculations using the parametrization for  $v_{xc}$  based on the Bethe Ansatz solution of the Anderson model due to Bergfield and colleagues. Three coupling regimes are considered: weak ( $U/\Gamma$ , orange line), intermediate ( $U = 10\Gamma$ , green line) and strong ( $U = 100\Gamma$ , purple line). In the original paper, the authors compared results of self-consistent calculations using their parametrization with self-consistent calculations using Hartree-Fock and the conductance in  $T = 0$  obtained with the BA. They show a perfect match with the exact BA conductance in all coupling regimes.

Source: Adapted from BERGFIELD et al. <sup>31</sup>

$W/D = -0.01$  and  $-0.1$  applied to the metallic leads. Note that the DFT results, plotted as crosses, deviate from NRG calculations as  $W$  is increased. These results indicate that even with the explicit inclusion of  $W$  in the calculation of phase shifts - eqs. (2.38) and (3.51) - the self consistent calculation based solely on the parametrization for the functional of the quantum dot misses non-local effects due to the coupling to the leads. The application of  $W$  in the Wannier orbitals  $f_0$  changes the number of electrons in the junctions with effects in the phase shifts of the conduction electrons scattered by the dot.

Besides the exact parametrization for the quantum dot, in a first analysis, we can be tempted to investigate this specific problem by carrying out self-consistent calculations on an inhomogeneous lattice. With this example in mind, we can return to our problem of a single-electron transistor then compare the available parametrizations suiting model Hamiltonians, such as BALDA. This idea will be further explored in chapter 6.

Now that we have understood how Density Functional Theory deals with many-body systems and discussed its application for the problem of transport in a single-electron transistor, we can move to the gold standard method to simulate properties of the SET very accurately: the Numerical Renormalization-Group. The latter will be introduced in the next chapter.

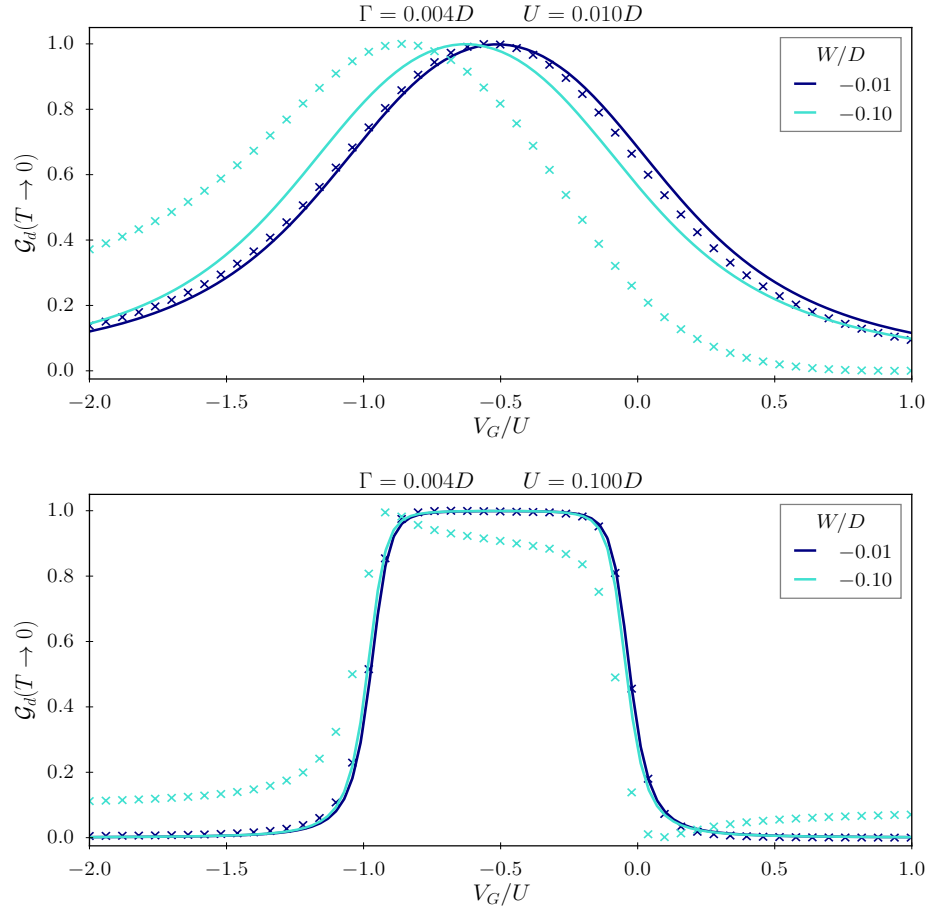


Figure 20 – Ground-state conductance  $G_d$  in a SET as a function of the gate voltage  $V_G$  in the presence of a scattering potential  $W$  to the leads. Model parameters are  $\Gamma = 0.004D$  and  $U/\Gamma = 1$  and  $U/\Gamma = 10$ . Full lines depict the results obtained with NRG calculations in the limit  $T \rightarrow 0$  and crosses represent results obtained from self-consistent calculations using the BA parametrization for the Anderson model.

Source: By the author.

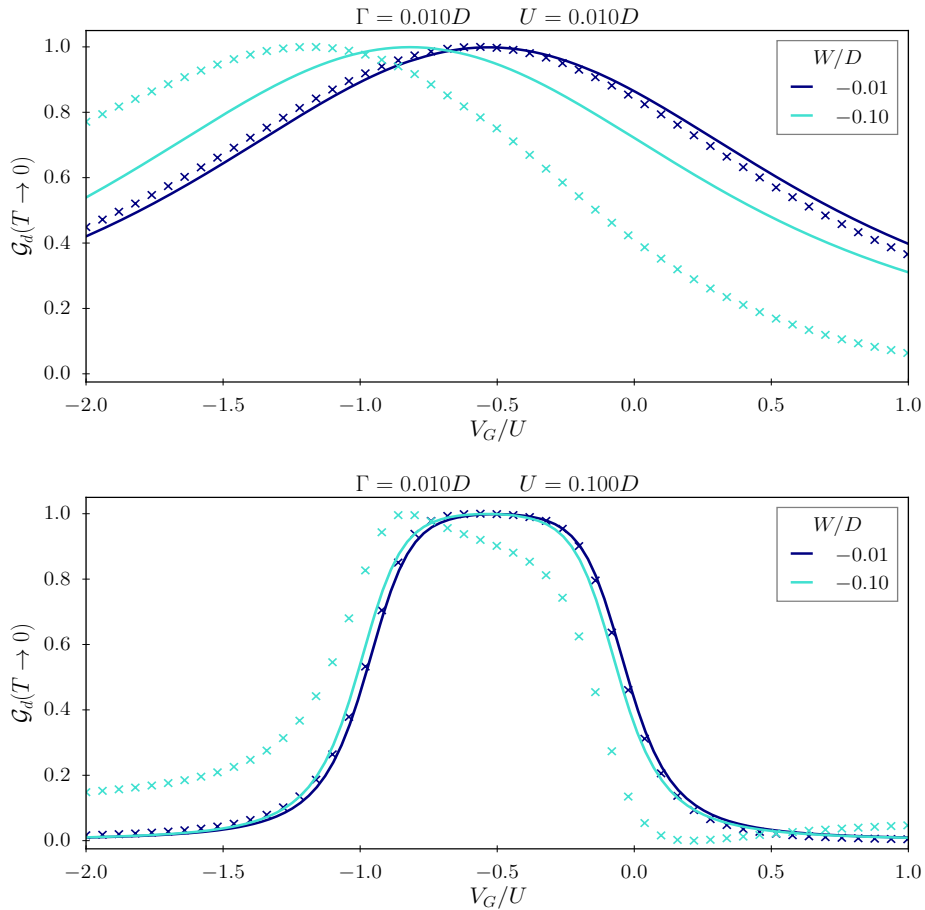


Figure 21 – Ground-state conductance  $G_d$  in a SET as a function of the gate voltage  $V_G$  in the presence of a scattering potential  $W$  to the leads. Model parameters are  $\Gamma = 0.01D$  and  $U/\Gamma = 1$  and  $U/\Gamma = 10$ . Full lines depict the results obtained with NRG calculations in the limit  $T \rightarrow 0$  and crosses represent results obtained from self-consistent calculations using the BA parametrization for the Anderson model.

Source: By the author.

## 4 RENORMALIZATION-GROUP

The concept of Renormalization Group (RG) arose in the middle of the 20th century with the urge to describe many-body problems for which the quantum field and perturbation theories presented pathological results due to the unexpected divergences.<sup>16, 70</sup> The outstanding proposal to implement a numerical RG scheme to the Kondo problem, which contributed to Kenneth Wilson winning the Nobel prize in 1982, established the renormalization idea in computational physics and inspired the development of powerful procedures allowing for solving models describing strongly correlated systems.

The Numerical Renormalization Group (NRG)<sup>16, 70</sup> and the Density Matrix Renormalization Group (DMRG)<sup>6, 100, 101</sup> methods are the best well known examples of essentially exact renormalization-group algorithms. Both are based on strictly controllable approximations, but while the NRG method is adequate to treat impurity systems, the DMRG method covers a wide range of model Hamiltonians, such as the Hubbard and the Heisenberg models and their variations.<sup>3, 70, 101</sup> Combinations of the two procedures have been reported.<sup>70</sup>

As mentioned in Chap. 2, the study of the single-electron transistor by means of NRG solution of the Anderson Hamiltonian provided remarkable insights into the Kondo regime of quantum dots. The present chapter is devoted to the Numerical Renormalization-Group method and its implementation in the diagonalization of the Anderson Hamiltonian. We will present the formalism of the RG procedure and explain how NRG was formulated by Wilson. We will also discuss the fixed points of the NRG transformation and contextualize their importance in the problem of the SET.

### 4.1 Model Hamiltonians and the Renormalization-Group

As discussed in our introduction to DFT in section 3.1, the solution of many-body problems becomes more and more difficult as the number of particles of the system is increased and their interactions become complex. In order to study quantum systems and explore their phenomenology we have to resort to simplifications, paying the price in the accuracy of our approximations. While in the weakly correlated regime, ab-initio and DFT approaches described condensed matter systems adequately, in the opposite limit, we have the so-called model Hamiltonians, simplified mathematical descriptions of particles on a lattice, from which it is possible to explore phase transitions, universalities and recover interesting phenomena emerging in strongly correlated regimes.

Even at the level of simplification promoted by a model, the solution is still complicated due to the growth of the Hilbert space as the number of lattice sites is

increased. Nonetheless, we are often interested in the low energy spectrum of condensed matter models, from which we can extract low lying excitations and then calculate thermodynamical properties. In this respect, an approach providing a good description of a given energy scale of interest is more than convenient because it allows to reduce the number of degrees of freedom. The idea of reducing dimensionality in order to better resolve the physics in energetic scales around ground-states is exactly the motivation for the Renormalization-Group procedure.<sup>3,5</sup>

To give a flavour of this need to reduce dimension, let us consider a generic model Hamiltonian describing  $N$  bodies, where the latter can describe particles or spins in sites of a lattice:

$$\hat{H} = \sum_{i=1}^N \sum_{j \neq i=1}^N \hat{T}_{i,j} + \sum_{i,j=1}^N \hat{U}_{i,j} + \sum_{i=1}^N \hat{V}_i, \quad (4.1)$$

where the first term  $\hat{T}_{i,j}$  describes two-body interactions (e.g. spin-spin correlations, hopping, and other mechanism of transfer/exchange of particles or spins), the second term  $\hat{U}_{i,j}$  defines a repulsive interaction between particles (e.g. Coulomb repulsion), and the third  $\hat{V}_i$  corresponds to a single-particle interaction (e.g., external potential or magnetic field).

The solution of the Hamiltonian in eq. (4.1) requires the diagonalization of the corresponding matrix Hamiltonian  $H$ , whose dimension is defined by the Fock space  $\mathcal{H}$  of interest. The Fock space  $\mathcal{H}$  of  $N$  sites includes all possible states all sites can assume. Provided that each site  $i$  has its own Fock space  $\mathcal{H}_i$  of dimension  $d_i$ , the full Hilbert space  $\mathcal{H}_N$  of  $N$  sites will have dimension  $D_N = d_i^N$ , comprising a basis of states  $\{|\alpha_p\rangle\}$  ( $p = 1, \dots, D_N$ ). As a consequence, the corresponding matrix Hamiltonian  $H$  in  $\mathcal{H}_N$  will have dimension  $D_N \times D_N = d_i^N \times d_i^N$ , with matrix elements defined by

$$H_{q,p} = \langle \alpha_q | \hat{H} | \alpha_k \rangle, \quad (4.2)$$

where  $p, q = 1, \dots, D_N$ .

The calculation of  $H_{q,p}$  requires us to understand the action of the one and two-body operators of the Hamiltonian in eq. (4.1) on a given state  $|\alpha\rangle$  of the basis of interest in  $\mathcal{H}_N$ . We note that two-body terms of  $\hat{H}$  have the general form

$$\hat{O}_{i,j} = \hat{O}_i \otimes \hat{O}_j, \quad (4.3)$$

where  $\hat{O}_i$  and  $\hat{O}_j$  are one-body operators acting on sites  $i$  and  $j$ , respectively, and are defined in  $\mathcal{H}_i$ .

A very convenient matrix algebra manipulation invites us to define modified operators  $\hat{\mathcal{O}}_i$  and  $\hat{\mathcal{O}}_{i,j}$  in the expanded Fock space, i.e.,

$$\hat{\mathcal{O}}_i = \hat{O}_i \bigotimes_{k \neq i=1}^N \mathbb{1}_k, \quad (4.4)$$

and

$$\hat{O}_{i,j} = \hat{O}_i \otimes \hat{O}_j \bigotimes_{k \neq i \neq j=1}^N \mathbb{1}_k, \quad (4.5)$$

where  $\mathbb{1}_k$  is the identity operator defined in  $\mathcal{H}_k$ . Note that the last term on the right-hand side of eq. (4.5),  $\bigotimes_{k \neq i \neq j=1}^N \mathbb{1}_k$  results in the identity matrix of dimension  $d^{N-2}$ .

For a typical condensed matter model, the first term in eq. (4.1) describes interactions occurring between first-neighbors sites ( $j = i \pm 1$ ), while the second term is usually defined as the Coulomb interaction between spins up and down on the same site, so that  $U_{i,j} = U_{i,i}$  as the sum in  $j$  accounts only for  $j = i$ . This allows us to employ eq. (4.5) to diagonalize the Hamiltonian iteratively by the adding each term at once, i.e.

$$\hat{H}_N = \mathbb{1}_N \otimes \hat{H}_{N-1} + \hat{T}_{N,N-1} \bigotimes_{i=1}^{N-2} \mathbb{1}_i + (\hat{U}_{N,N} + \hat{V}_N) \bigotimes_{i=1}^{N-1} \mathbb{1}_i. \quad (4.6)$$

Consider the case of electrons on a lattice:  $H$  will be a matrix of dimension  $4^N \times 4^N$ , as the local Hilbert space have dimension 4: a site can be empty, singly occupied with a spin up or down or doubly occupied with two spins. The symmetries of  $H$  allow to handle the full diagonalization in pieces, as  $H$  can be decomposed in blocks conserving quantum numbers. For instance, if  $H$  conserves charge  $Q$  and spin  $S$ , the full spectrum can be recovered by solving block Hamiltonians in sectors  $H(Q, S)$ , whose dimension is  $R_N < D_N$ . In practice, however, symmetries do not remediate the constraint in the size of the problem. Few humans can perform analytical diagonalization of matrices larger  $3 \times 3$ . Computationally, the limitation in the size of the problem relies on architecture and memory.\*

Unfortunately, the maximum number of iterations  $N$  that can be calculated is not large enough as required for the thermodynamical limit  $N \rightarrow \infty$  of a typical condensed matter model. As mentioned, the low-lying eigenstates are the main target in the study of condensed matter models, so that we can diagonalize them in an effective Hilbert space with reduced dimension. With the previous discussion, we had a flavor of the importance of symmetries, which are key ingredients to retain only the degrees of interest and this idea can be implemented in an iterative way. Now, we can briefly introduce the RG and contextualize Wilson's idea to carry out a numerical implementation of RG to solve the Kondo problem.

---

\* For instance, in a 64-bit architecture, each double floating point number occupies 64 bits and the largest integer index is  $2^{63} - 1$ . While storing a matrix of size  $4^{32} \times 4^{32}$  can be tempting, the maximum cache available will not allow to allocate such a large object. Finally, diagonalization algorithms have complexity  $\mathcal{O}(n^3)$ . A bit of computer numerology shows that the largest lattice size is up to about ten sites. Of course, this previous analysis considers modern architectures. If we go back to the decades in which Wilson devised his first numerical calculations, more limitations were found.

#### 4.1.1 Renormalization-Group

The essence of the Renormalization-Group is the scale invariance of physical systems.<sup>5,102</sup> For example, if the energy has scale invariant properties, the RG formulation provides a recipe to map each energetic scale in terms of an effective interaction described in terms of the important degrees of freedom to preserve the invariance.

Mathematically, this idea is better translated in terms of a transformation  $\tau$  which applied to a system  $\mathcal{H}(\mathbb{K})$  with corresponding degrees of freedom  $\mathbb{K} = (K_1, K_2, K_3, \dots)$  yields a new effective Hamiltonian  $\mathcal{H}'$  associated with a new set  $\mathbb{K}' = (K'_1, K'_2, K'_3, \dots)$ , i.e.,

$$\begin{aligned}\tau\mathcal{H}(\mathbb{K}) &= \mathcal{H}'(\mathbb{K}') \\ \tau(\mathbb{K}) &= \mathbb{K}'.\end{aligned}\tag{4.7}$$

The successive applications of  $\tau$  yield to access energy scales each time lower. In our example of energy invariance, the mapping  $\mathcal{H}(\mathbb{K}) \rightarrow \mathcal{H}'(\mathbb{K}')$  is equivalent to access a lower energy scale  $\epsilon'_k$  from a higher energy scale  $\epsilon_k$ , so that the connection between them requires the existence of a ratio  $\Lambda > 1$  for which  $\epsilon_k \rightarrow \epsilon_k/\Lambda$ . It follows that if we start from scale  $\epsilon_k$ ,  $N$  successive applications of  $\tau$  yields  $\epsilon_k/\Lambda^N$ .

An important property of the RG transformation is the existence of *fixed points*  $\mathbb{K}^*$  that remain invariant under  $\tau$ , i.e.,

$$\tau(\mathbb{K}^*) = \mathbb{K}^*. \tag{4.8}$$

In order to appreciate the importance of this formalism at the time Wilson proposed the NRG, we can return to our historical review of the Kondo effect in chapter 2. In the 70's, after the insightful works by Anderson and Kondo, an interesting question that was not completely understood was the zero temperature behavior of the impurity with weak antiferromagnetic coupling to the conduction band.<sup>13,50</sup> All attempts to carry out a perturbative analysis failed due to the divergence in the coupling constant  $g = J^2 \ln(D/k_b T)$  in the limit  $T \rightarrow 0$ . In particular, in his work "A poor man's derivation of scaling laws for the Kondo problem", Anderson reported an exciting but frustrated attempt to carry out a perturbative RG approach to the Kondo Hamiltonian in order to describe the crossover between the high (a limit in which the degrees of freedom form a continuum) and the low (a limit in which the system is characterized by the strong coupling between the impurity and the metal) temperature regimes.<sup>103</sup> Although good results were found for high temperatures, a theoretical approach connecting this regime to the limit  $T \rightarrow 0$  was still missing. Wilson realized that an accurate description of the crossover would require a better choice of the energetic intervals to perform the RG transformation and proposed a numerical approach to solve the Kondo problem. His paper titled "The renormalization group"<sup>16</sup> from 1975 marks the birth to the Numerical Renormalization-Group procedure. The latter will be explored next.

## 4.2 Numerical Renormalization-Group

The Numerical Renormalization-Group method designed by Wilson was the first throughously successful approach to the Kondo problem.<sup>5, 16, 16, 104, 105</sup> At the core of Wilson’s solution there was the definition of a new basis of states, which he called *Kondo basis*, describing the conduction band in such a way to account for its coupling to the impurity. In the Kondo basis, the conduction band is approximated by an infinite set of discrete states distributed around the impurity in “onion” layers scaled by a parameter  $\Lambda \geq 1$ . The discretization of the conduction band is made on a logarithmic mesh, the  $n$ -th interval is therefore represented by an energy scale of order  $\approx \Lambda^{-n/2}$ . This definition is crucial in the Kondo problem because it allows to distinguish states interacting strongly and weakly to the impurity, the first corresponding to metallic Wannier states localized around the impurity and the latter being spherical shells.

By means of the Kondo basis and a RG transformation, the solution of the Kondo Hamiltonian is performed iteratively: in the very first iteration we solve the subsystem comprising the impurity coupled to the first Wannier state; in the second iteration, the second conduction state of the Kondo basis is added and we solve the larger subsystem comprising this state plus the first Wannier state and the impurity; in the next iterations, the remaining states of the Kondo basis are added and the corresponding subsystem solved and so on. More importantly, each iteration provides the access to energy scales each time lower, so that it is possible to refine the description of excitations close to the Fermi level, which are important to describe the low temperature regime.

As previously discussed, during an iterative diagonalization the growth of the Hilbert space prevents the exact calculation of a very large number of iterations. To tackle this issue, the NRG procedure employs a systematic truncation in order to retain only the low energetic degrees of freedom, which are nonetheless the ones needed to describe physical properties, such as the specific heat, magnetic susceptibility and conductance. The truncation, referred as *ultraviolet truncation*, is implemented by keeping only the states with energy  $\epsilon < E_{UV}$  at each iteration, where  $E_{UV}$  is the ultraviolet cut-off<sup>16</sup>. With increasing iterations, the enlarged Hilbert space  $\mathcal{H}_N$  is built from the tensorial product between the local Hilbert space of the  $N$ -th site and the truncated Hilbert  $\tilde{\mathcal{H}}_{N-1}$  space of the previous iteration.

Finally, to keep the calculation running up to a given number of iterations an additional truncation is performed: it replaces the infinite element basis of states  $f_n$  ( $n = 0, 1, \dots \infty$ ) the NRG by a maximum number  $N$  of states associated with an energy scale of interest. Also known *infrared truncation*, it limits the number of iterations up to the energy scale of interest  $E_{min}$ , which is associated with the temperature. We can think that the diagonalization starts at high-temperature (high on the scale of the thermal scale

corresponding to the bandwidth  $D$  of the conduction band) and is further cooled along iterations until  $k_B T \ll D$  and  $T \rightarrow 0$ .

Note that this idea corresponds to implement the recursive solution of eq. (4.6) by means of the RG transformation in eq. (4.7) in order to solve the Kondo or Anderson Hamiltonian in an effective Hilbert space with an appropriate set of degrees of freedom.

In a nutshell, the NRG algorithm can be summarized in the following steps:

1. Discretization of the conduction band  $\epsilon_k$  in a logarithmic scale according to the parameter  $\Lambda$ ;
2. Lanczos transformation of the conduction band to an infinite, discrete basis of fermionic operators  $\{f_n\}$  ( $n = 0, 1, \dots, N$ ), whose seed  $f_0$  corresponds to the Wannier state coupled to the impurity;
3. Projection of the model Hamiltonian upon the basis  $\{g_d, f_n\}$  ( $n = 0, \dots, N$ ), where  $g_d$  are the states of the impurity -  $g_d = c_d$  for the Anderson model or  $g_d = \hat{S}_d$  for the Kondo model and scaling;
4. *Infrared truncation* of the infinite chain in order to reach the temperature of interest;
5. Iterative diagonalization of the scaled Hamiltonian and *ultraviolet truncation*. At each iteration, the outputs  $\epsilon, \Psi$  (eigenvalues and eigenstates) of the diagonalization of  $H_N$  are used to calculate physical observables.

The previous concepts provide the necessary tools to apply the NRG procedure to the Anderson Hamiltonian presented in Chap. 2. Through the NRG, we are going to define the Anderson Hamiltonian as

$$H = \sum_k \epsilon_k c_k^\dagger c_k + \epsilon_d n_d + U n_{d\uparrow} n_{d\downarrow} + \tilde{V}(f_0^\dagger c_d + H.c.), \quad (4.9)$$

where the seed  $f_0$  is the Wannier state coupled to the impurity.

And then, solve it by projecting it into the iterative form

$$H_N = \sum_{n=0}^N t_n (f_n^\dagger f_{n+1} + H.c.) + \epsilon_d n_d + U n_{d\uparrow} n_{d\downarrow} + \tilde{V}(f_0^\dagger c_d + H.c.), \quad (4.10)$$

where  $t_n$  are coefficients depending on  $\Lambda$  and  $N$  is limited by the *infrared truncation* condition, defined as

$$t_N < k_B T. \quad (4.11)$$

The changes of basis connecting eqs. (4.9) and (4.10) as well as the numerical details involved in the iterative diagonalization of  $H_N$  are explained below.

### 4.2.1 Logarithmic discretization

The first step of the NRG calculation comprises the logarithmic discretization of the conduction band. As we pointed out, the choice of the logarithmic mesh was the key ingredient in the RG approach proposed by Wilson: it allowed to reproduce the continuum limit of the conduction band close to the Fermi level and, at the same time, access energetic scales associated with the limits of high and very low temperatures. Another important aspect of the NRG solution is the projection of the interaction between the impurity and the conduction band in terms of a single state  $f_0$ , which remains preserved along the iterative solution.

To carry out the logarithmic discretization of the conduction band we start from the Hamiltonian  $H_{\text{CB}}$  describing the free electrons of the metal. Here, to simplify the notation, we are considering an isotropic, half-filled conduction band, so that the definition given in eq. (2.4) is written in terms of a single coordinate  $k$  instead of a vector, i.e.,

$$H_{\text{CB}} = \sum_k \epsilon_k c_k^\dagger c_k, \quad (4.12)$$

where  $\epsilon_k$  is the dispersion relation and  $0 \leq k \leq \infty$ .

The eigenenergies  $\epsilon_k$  are limited to the interval  $[-D_-, +D_+]$  and are described by a density of states

$$\rho(\epsilon) = \sum_k \delta(\epsilon - \epsilon_k) \quad (4.13)$$

normalized by

$$\int_{-D_-}^{D_+} d\epsilon \rho(\epsilon) = 1. \quad (4.14)$$

At this point, a brief comment is pertinent. In principle, the logarithmic division of the interval  $[-D_-, +D_+]$  can be carried out for any dispersion relation  $\epsilon_k$  describing a continuous set of modes  $k$ . In the traditional approach for the Anderson Hamiltonian, the dispersion relation is approximated by a linear function around the Fermi level  $\epsilon_F = 0$  and the limits in which this approximation holds corresponds to the points  $-D_-$  and  $+D_+$ . To understand this approximation, we can consider the solution of non-interacting homogeneous Hubbard Hamiltonian, which yields  $\epsilon_k = -2t \cos k$ ,  $|k| \leq \pi/2$  being a continuous variable in the thermodynamical limit (i.e. infinite number of lattice sites). Close to the Fermi level, the trigonometric function can be accurately approximated by  $\epsilon_k \approx v_F(k - k_F)$ , where  $v_F$  is the Fermi velocity and  $k_F$  is the Fermi momentum. See figure 22. Note that when the linear approximation is considered the density of states is constant and given by  $\rho = 1/2D$ .

We stress that in the vast majority of NRG approaches for impurity models the description of the logarithmic discretization of the conduction band is made using this

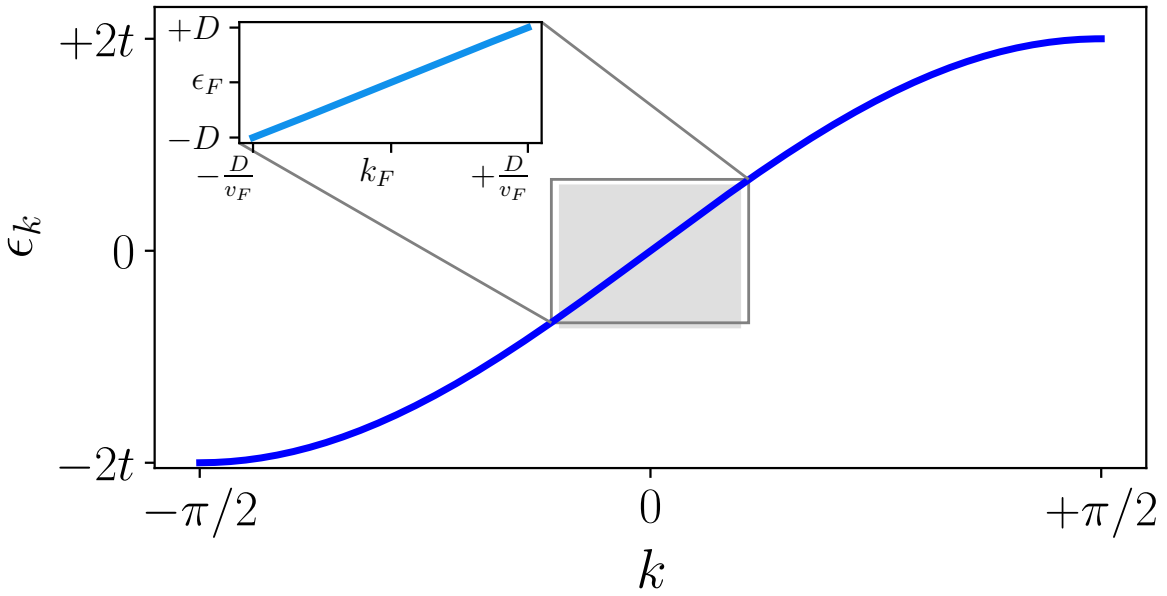


Figure 22 – Example of the linear approximation over the dispersion relation of the non-interacting homogenous Hubbard Hamiltonian. Major plot depicts the continuous set of eigenvalues of the sinusoidal dispersion relation  $\epsilon_k$  in the first Brillouin zone  $|k| \leq \pi/2$ . The shaded zone highlights the set of energies and momenta for which the dispersion can be considered linear, as shown in the inset.

Source: By the author.

the approximation of a linear dispersion. Here, we will follow the notation by Bulla et al. and carry the explicit dependence of the density of states  $\rho(\epsilon)$  on the energy in order to account for general bands.<sup>106</sup> This choice will help us in the extension of the logarithmic discretization to a conduction band described by a finite degrees of freedom presented in 4.2.1.1.

With the previous considerations and before entering in the first change of basis to re-define the operators  $c_k$  in logarithmic mesh, it is convenient to define a new basis connecting the momenta  $\mathbf{k}$  with a set of continuous energies  $\epsilon$ :

$$c_\epsilon = \mathcal{N}_\epsilon \sum_{\mathbf{k}} \delta(\epsilon - \epsilon_{\mathbf{k}}) c_{\mathbf{k}}, \quad (4.15)$$

where the normalization factor  $\mathcal{N}_\epsilon = \rho(\epsilon)^{-1/2}$  is calculated from the traditional commutation relation  $\{c_\epsilon^\dagger, c_{\epsilon'}\} = \delta(\epsilon - \epsilon')$ .

By inverting eq. (4.15), we find

$$c_{\mathbf{k}} = \int_{-D_-}^{+D_+} d\epsilon \sqrt{\rho(\epsilon)} c_\epsilon. \quad (4.16)$$

Now, we can re-write the Hamiltonian of eq. (4.12) by identifying

$$H_{CB} = \int_{-D_-}^{+D_+} d\epsilon \epsilon c_\epsilon^\dagger c_\epsilon. \quad (4.17)$$

The term of the Hamiltonian describing the interaction between the conduction band and the impurity

$$H_{\text{int}} = \sum_k V_k (c_k^\dagger c_d + H.c.) \quad (4.18)$$

is therefore written as

$$H_{\text{int}} = \int_{-D_-}^{+D_+} d\epsilon (h(\epsilon) c_\epsilon^\dagger c_d + H.c.), \quad (4.19)$$

where  $h(\epsilon) = \sqrt{\rho(\epsilon)} V(\epsilon)$ ,  $\epsilon$  is the continuous form of the dispersion relation  $\epsilon_k$  and  $V(\epsilon)$  is the hybridization potential expressed in terms of the continuous energy  $\epsilon$ <sup>106</sup>.

The functions  $\epsilon$  and  $h(\epsilon)$  are related to the hybridization function  $\Gamma(\epsilon)$  defined in Chap. 2 in eq. (2.7). The connection is made via

$$\Gamma(\omega) = \pi \frac{d\Delta_\epsilon(\omega)}{d\omega} h^2[\epsilon(\omega)], \quad (4.20)$$

where  $\Delta_\epsilon(\omega)$  is the inverse of  $\epsilon$ .

Relation (4.19) also defines the Wannier orbital  $f_0$  in the continuous basis

$$f_0 = \mathcal{N}_\epsilon \int_{-D_-}^{+D_+} d\epsilon c_\epsilon, \quad (4.21)$$

where  $\mathcal{N}_\epsilon = \int_{-D_-}^{+D_+} d\epsilon \rho(\epsilon)$ .

Having at hand the Hamiltonians  $H_{\text{CB}}$  and  $H_{\text{int}}$  projected into the new basis  $\{c_\epsilon\}$ , we can now define the logarithmic mesh. We divide the interval  $[-D_-, D_+]$  into subintervals  $I_m$  according to a parameter  $\Lambda \geq 1$  corresponding to the ratio between consecutive energetic scales. In the limit  $\Lambda \rightarrow 1$ , the closer we get to an uniform linear mesh. Here, we will also use an additional parameter  $0 < z \leq 1$  corresponding to a torsion phase in the logarithmic energies. The introduction of the parameter  $z$  by Oliveira et al (popular in the literature as “z-trick” or “z-averaging”) yields the access of intermediate scales of energy in the logarithmic discretized band, those being indispensable in the calculation of excitation properties and thermodynamical averages. In that sense, averaging over  $z$  provides an alternative route to retrieve the continuous limit of states, with more detail of intermediate values of energy compared to Wilson’s original formulation for the logarithmic discretization.<sup>107,108</sup> Computationally, the main advantage of the z-averaging is that it allows to perform NRG calculations for larger values of  $\Lambda$  (for instance  $\Lambda = 5$ ) and yields improved accuracy if properties are averaged by  $z$ .<sup>108</sup>

The dicretization is shown in figure 23.

The boundaries of the logarithmic intervals are defined as

$$\begin{aligned} \mathcal{I}_m^+ &= [\varepsilon_m^+, \varepsilon_{m-1}^+] \\ \mathcal{I}_m^- &= [\varepsilon_{m-1}^-, \varepsilon_m^-] \quad (m = 0, 1, 2, 3, \dots), \end{aligned} \quad (4.22)$$

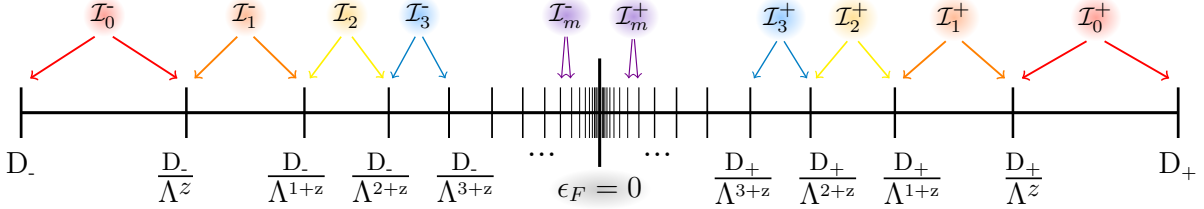


Figure 23 – Logarithmic discretization of the conduction band. The bandwidth  $[-D, +D]$  is divided in a sequence of intervals logarithmically spaced according to a dimensionless parameter  $\Lambda > 1$  and a torsion  $0 < z \leq 1$ . This choice allows to connect consecutive energetic scales via  $\epsilon'_k = \epsilon_k/\Lambda$ , the latter being a recurrent property of impurity problems.

Source: By the author.

where

$$\varepsilon_m^\pm = \begin{cases} \pm D_\pm, & m = 0 \\ \pm D_\pm \Lambda^{-m-z}, & \text{otherwise} \end{cases}. \quad (4.23)$$

Each interval has width

$$d_m^\pm = D_\pm \Lambda^{-m-z} (1 - \Lambda^{-1}). \quad (4.24)$$

Note that in the limit  $\Lambda \rightarrow 1$ , the discretization scheme is linear, so that each interval  $I_m$  has the same width. If the intervals are made as little as possible, we recover the continuum limit.

Within each interval  $I_m^\pm$  ( $m = 0, 1, 2, \dots \infty$ ) we define a complete set of fermionic operators  $a_m$  and  $b_m$  representing an effective mode retaining all the energies  $\epsilon$  contained inside  $I_m^\pm$ . We therefore define for  $m = 0$ :

$$\begin{aligned} a_0 &= \frac{1}{\sqrt{D_+(1 - \Lambda^{-1})}} \int_{D_+ \Lambda^{-z}}^{D_+} d\epsilon c_\epsilon \\ b_0 &= \frac{1}{\sqrt{D_-(1 - \Lambda^{-1})}} \int_{D_-}^{D_- \Lambda^{-z}} d\epsilon c_\epsilon, \end{aligned} \quad (4.25)$$

and for  $m \geq 1$ :

$$\begin{aligned} a_m &= \frac{1}{D_+^{1/2}} \frac{\Lambda^{(m+z-1)/2}}{(1 - \Lambda^{-1})^{1/2}} \int_{I_m^+} d\epsilon c_\epsilon \\ b_m &= \frac{1}{D_-^{1/2}} \frac{\Lambda^{(m+z-1)/2}}{(1 - \Lambda^{-1})^{1/2}} \int_{I_m^-} d\epsilon c_\epsilon, \end{aligned} \quad (4.26)$$

where the normalization constants can be calculated from the commutator  $\{a_m^\dagger, a_m'\}$ .

In the basis of operators  $\{a_m, b_m\}$ , the conduction band Hamiltonian is described by the effective modes inside  $I_m^\pm$  with mean energies  $\mathcal{E}_m^\pm$ , i.e.,

$$H_{CB} = (\mathcal{E}_0^+(z, \Lambda) a_0^\dagger a_0 + \mathcal{E}_0^-(z, \Lambda) b_0^\dagger b_0) + \sum_{m=1}^{\infty} (\mathcal{E}_m^+(z, \Lambda) a_m^\dagger a_m + \mathcal{E}_m^-(z, \Lambda) b_m^\dagger b_m). \quad (4.27)$$

To calculate the mean energies  $\mathcal{E}_{m\pm}$ , we follow Refs. [107, 108](#) in which the definition is

$$\mathcal{E}_m^\pm(z, \Lambda) = \frac{\int_{\mathcal{I}_{m\pm}} d\epsilon \rho(\epsilon)}{\int_{\mathcal{I}_m^\pm} \frac{d\epsilon}{\epsilon} \rho(\epsilon)}. \quad (4.28)$$

The previous definition prevents the need to add by hand a correction factor  $A_\Lambda$  in Numerical Renormalization-Group calculations following Wilson's original definition for the mean energies. The factor  $A_\Lambda$  is given by

$$A_\Lambda = \frac{\Lambda + 1}{\Lambda - 1} \frac{\log \Lambda}{2}. \quad (4.29)$$

The last step of the logarithmic discretization previous to the Lanczos transformation requires the definition of the operator  $f_0$  in the basis  $\{a_m, b_m\}$ . Plugging eqs. [\(4.25\)](#) and [\(4.26\)](#) into [\(4.21\)](#), we get

$$f_0 = \frac{1}{\sqrt{\bar{\gamma}}} \sum_m \gamma_m^+ a_m + \gamma_m^- b_m, \quad (4.30)$$

where

$$(\gamma_m^\pm)^2 = \int_{\mathcal{I}_m^\pm} d\epsilon \Gamma(\epsilon), \quad (4.31)$$

and

$$\bar{\gamma} = \sum_{I_{m+}} (\gamma_m^+)^2 + \sum_{I_{m-}} (\gamma_m^-)^2 = \int_{-D_-}^{D_+} d\epsilon \Gamma(\epsilon). \quad (4.32)$$

The previous formalism can be used to discretize conduction bands with density of states  $\rho(\epsilon)$  and hybridization functions  $\Gamma(\epsilon)$  more general than the flat half-filled band with constant hybridization, which is traditional approach for the Anderson and Kondo Hamiltonians. For instance, in Bulla et al the logarithmic discretization of a pseudo-gapped band was reported.[106](#) We emphasize that all the previous definitions hold when the conduction band is described by a continuous set of degrees of freedom or, in other words, in the thermodynamical limit. For the discussion we will present later when returning to the problem of describing transport in quantum nano devices it will be convenient to extend the logarithmic discretization procedure to the cases in which the conduction band is not represented by a continuous of states. This special case is the subject of the following subsection.

#### 4.2.1.1 Logarithmic Discretization of bands with finite degrees of freedom

The logarithmic discretization introduced previously needs to be adapted for a finite system. In the traditional formulation for the Anderson Hamiltonian, for which the

band forms a continuum of states, one considers only the low-lying energies  $|\epsilon| < D$ ,  $D$  being the bandwidth, and approximate the density of states as flat  $\rho(\epsilon) = 1$ . In the case of band represented by a finite number of degrees of freedom, these previous approximations must be analyzed because boundary effects become important as the number of degrees of freedom are reduced. Also, the spacing between finite modes  $k$  prevents the employment of the standard procedure due to the absence of an infinite number the energetic levels close to the Fermi level  $\epsilon_F = 0$ . In a pictorial explanation, the finite set of momenta  $k$  would be translated as empty energetic intervals as  $m \rightarrow \infty$ , which are the intervals closer to  $\epsilon_F = 0$  in fig. 23. In the broadband limit  $\rho = 1/2D$ , the continuum makes that all intervals for  $m \rightarrow 0$  are populated with an uniform number of states.

Consider, for instance, a tight-binding Hamiltonian describing  $L$  free fermions in a one dimensional lattice,

$$H = -t \sum_{i=1}^{L-1} c_i^\dagger c_{i+1} + c_{i+1}^\dagger c_i, \quad (4.33)$$

whose diagonal form is

$$H = \sum_{k=1}^L \epsilon_k d_k^\dagger d_k, \quad (4.34)$$

where

$$\epsilon_k = -2t \cos k, \quad (4.35)$$

and  $k$  and  $d_k(d_k^\dagger)$  are ultimately determined by the boundary conditions.

For open boundary conditions,

$$k = \frac{\pi\ell}{L+1} \quad \ell = 1, \dots, L, \quad (4.36)$$

and

$$d_k^\dagger = \sqrt{\frac{2}{L+1}} \sum_{i=1}^L \sin(ki) c_i. \quad (4.37)$$

The fact that  $L$  is finite gives rise to two energetic scales  $\Delta$  and  $\tilde{D}$  corresponding to minimum and maximum values of  $\epsilon_k$ , respectively.  $\Delta$  introduces a “gap” nearby  $\epsilon = 0$  with value

$$\Delta = 2t \cos \left( \frac{\pi L}{2(L+1)} \right), \quad (4.38)$$

which can be approximated as  $\Delta \approx 2t/L^{-1}$ , as shown in fig 24.

In order to proper account for these scales in the band structure, we introduce an alternative discretization procedure. Consider the linearly spaced set of momenta  $k_\ell$ , such

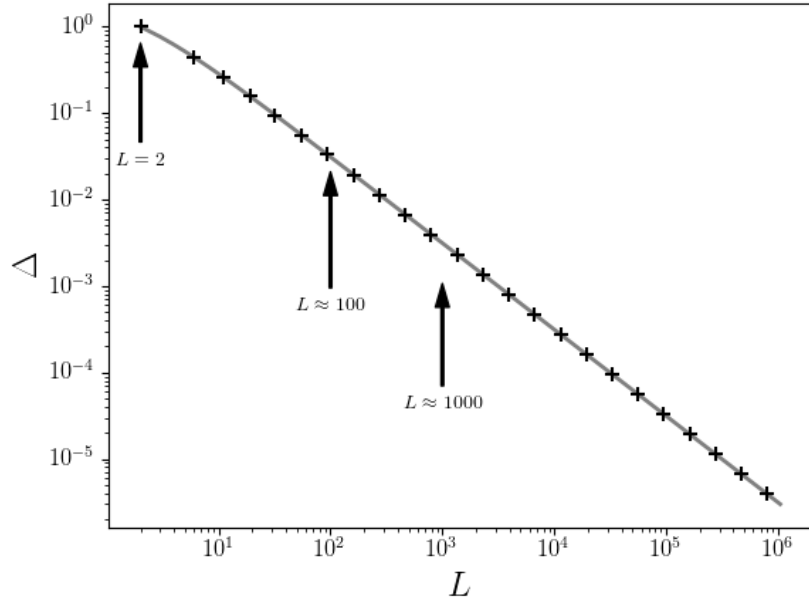


Figure 24 – Gap from  $\epsilon = 0$  of eq. (4.38) as a function of the lattice size  $L$  from  $L = 2$  to  $L = 10^6$ .

In the case of a free metallic band in 1D, the parity of the number of sizes is reflected on the existence of the level  $\epsilon_k = 0$ . For  $L$  even, the absence of the zero of energy introduces a gap between the low-lying energy modes.

Source: By the author.

as those in eq. (4.36). We divide the band into  $\mathcal{L} - 1$  intervals  $I_{\ell\pm}$  ( $\ell = 0, 1, \dots, \mathcal{L} - 1$ ), such that

$$|k_{\ell-1\pm}| < k < |k_{\ell\pm}|, \quad k \in I_{\ell\pm}, \quad (4.39)$$

where

$$k_{\ell\pm} = \pm(\ell + 1)\delta_k, \quad (4.40)$$

and

$$\delta_k = \frac{(k_D - k_\Delta)}{L}, \quad (4.41)$$

where  $k_D$  is the momentum associated with the most energetic energy  $\epsilon_k$  and  $k_\Delta$  is the momentum associated with the lowest energy  $\Delta$ .

Notice that the first momenta in the positive or negative intervals are defined as being the gap  $k_\Delta$  in eq. (4.41).

To generate the set of intervals in a logarithmic mesh, we chose an arbitrary dimensionless parameter  $\lambda > 1$  and substitute

$$\ell \rightarrow \frac{\lambda^\ell - 1}{\log \lambda} \quad (4.42)$$

so that the limits  $k_{\ell\pm}$  in eq. (4.40) are re-defined as follows

$$k_{\ell\pm} = \pm k_\Delta \pm \delta_k \left( \frac{\lambda^\ell - 1}{\log \lambda} \right) \quad (\ell = 0, 1, \dots, \mathcal{L} - 1), \quad (4.43)$$

where  $\mathcal{L}$  is defined by the equality

$$\begin{aligned} k_{\mathcal{L}-1+} &= k_D \\ \mathcal{L} &= \frac{\log((L-1)\log\lambda + 1)}{\log\lambda} + 1. \end{aligned} \quad (4.44)$$

As  $\lambda \rightarrow 1$ ,  $\mathcal{L}$  approaches  $L$  and we recover the linear sequence.

We want to further reduce the number of intervals from  $\mathcal{L}$  to  $M$ , so we divide  $\mathcal{L}$  by a real number  $\kappa$  so that

$$M \equiv \frac{\mathcal{L}}{\kappa} \quad (4.45)$$

is an integer.

Next, we define a new dimensionless parameter  $\Lambda > 1$  by

$$\Lambda = \lambda^\kappa, \quad (4.46)$$

so that for any integer  $\ell = \kappa m$  ( $m = 0, 1, \dots, M - 1$ ),  $\Lambda^m = \lambda^n$ .

By doing this, we obtain a set of  $M$  intervals  $\mathcal{I}_{m\pm}$  limited by the momenta

$$k_{m\pm} = \pm k_\Delta \pm \delta_k \left( \kappa \frac{\Lambda^m - 1}{\log \Lambda} \right) \quad (m = 0, 1, \dots, M). \quad (4.47)$$

By imposing that  $k_M$  coincides with  $k_D$ , we can determine  $\kappa$  as a function of  $\Lambda$  through the relation

$$\kappa = \left( \frac{k_D}{\Delta_k} - 1 \right) \frac{\log \Lambda}{\Lambda^M - 1} \quad (4.48)$$

Now, the interval boundaries  $k_{m\pm}$  become independent of  $\kappa$  and are solely determined by the discretization parameter  $\Lambda$

$$\begin{aligned} k_{m\pm} &= \pm \Delta_{k\pm} + (k_{D\pm} - \Delta_{k\pm}) \frac{\Lambda^m - 1}{\Lambda^M - 1} \\ (m &= 0, 1, \dots, M). \end{aligned} \quad (4.49)$$

The values of momenta  $k_{m\pm}$  define a support mesh in the logarithmic scale.

Notice that in the limits  $m = 0$   $k_0 = k_\Delta$ ,  $m = M$  and  $k_M = k_D$ , preserving the logarithmic relation. Also, in the limit when  $\Lambda \rightarrow 1$ , we recover the linear sequence of

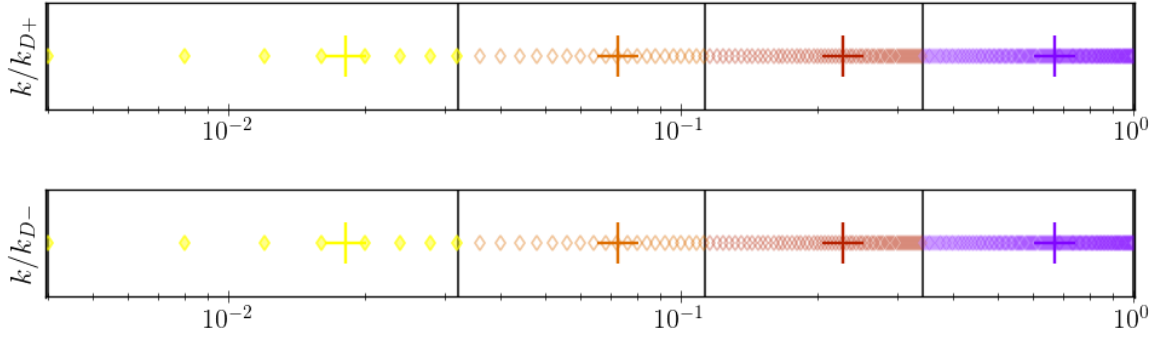


Figure 25 – Example of distribution of momenta  $k$  for  $L = 500$  sites for  $\Lambda = 3.0$   $M = 3$  and  $\kappa = 32$ . Each color corresponds to a logarithmic interval with  $m = 0$  being represented by purple and  $M$  represented by yellow. The boundaries of the logarithmic spaced intervals  $\mathcal{I}_{m\pm}$  are shown as black lines. The mean values  $\bar{k}_{m\pm}$  of the momenta in the support mesh are depicted as crosses. Note that for  $L = 2000$  the gap around  $\epsilon_k = 0$  is of order of  $L^{-1}$ .

Source: By the author.

momenta. The distribution of the original momenta  $\{k\}$  on the new logarithmic mesh is exemplified in Fig. 25.

For each interval  $\mathcal{I}_{m\pm}$ , ( $m = 0, \dots, M - 1$ ) we can now define the Fermi operator

$$a_{m\pm}^\dagger = \mathcal{N}_m \sum_{k \in \mathcal{I}_{m\pm}} c_{k\pm}^\dagger, \quad (4.50)$$

where the normalization factor  $\mathcal{N}_m$  can be determined by  $\{a_m^\dagger, a_m\} = 1$  resulting in

$$\mathcal{N}_m^{-2} = \sum_{k \in \mathcal{I}_{m\pm}} 1. \quad (4.51)$$

At this point, it is convenient to renormalize the momenta  $k_m$  dividing eq. (4.49) by  $k_D - \Delta_k$ , so that  $k_D = k_M \rightarrow 1$ . It follows that

$$\mathcal{N}_m^{-2} = \frac{1}{2} \frac{\Lambda - 1}{\Lambda^M - 1} \Lambda^m. \quad (4.52)$$

In the basis  $\{a_m\}$ , the conduction band Hamiltonian is re-written as

$$H = \sum_m \mathcal{E}_{m\pm} a_{m\pm}^\dagger a_{m\pm}, \quad (4.53)$$

with  $E_{m\pm}$  being the mean energies inside the  $m$ -th interval and defined by

$$\mathcal{E}_{m\pm} = \mathcal{N}_m^2 \sum_{k \in \mathcal{I}_{m\pm}} \bar{\epsilon}_k, \quad (4.54)$$

where  $\bar{\epsilon}_k$  are the normalized energies.

We illustrate the distribution of energies in the logarithmic sequence of intervals and the calculated mean energies  $\mathcal{E}_{m\pm}$  in Fig. 26.

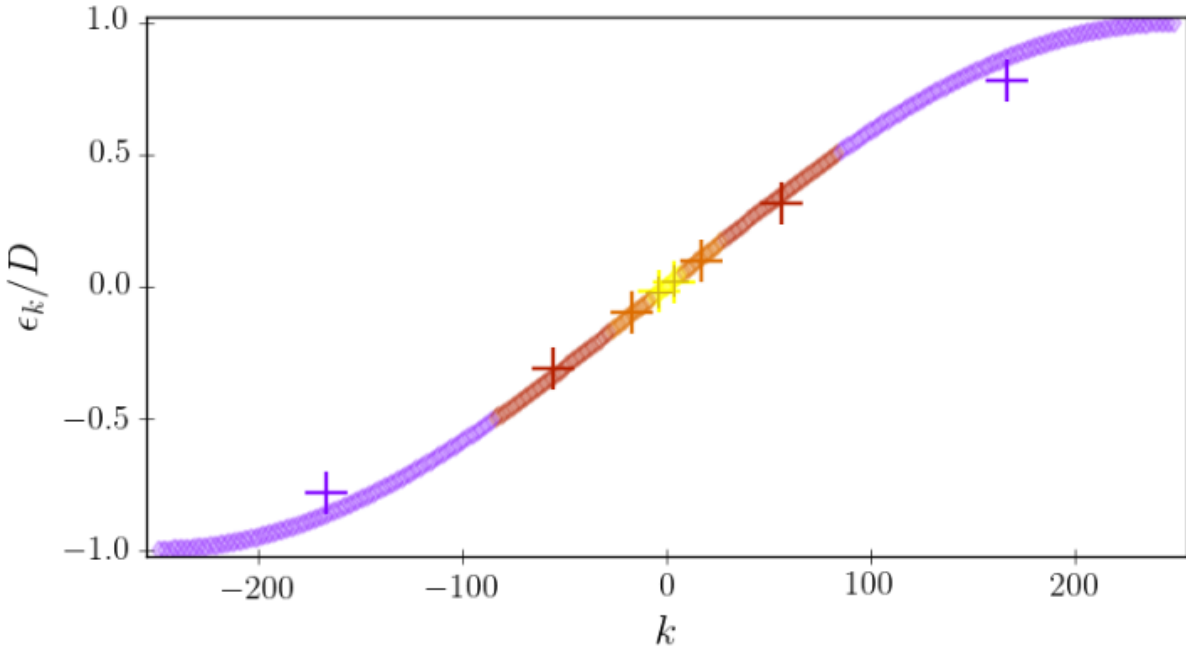


Figure 26 – Example of logarithmic discretization of a sinusoidal band  $\epsilon_k = -2t \sin k$  for  $L = 500$  sites for  $\Lambda = 3.0$   $M = 3$  and  $\kappa = 32$ . Each color corresponds to a logarithmic interval with  $m = 0$  being represented by purple and  $M$  represented by yellow. The mean values of energies  $\mathcal{E}_{m\pm}$  calculated from eq. (4.54) are shown as crosses.

Source: By the author.

We can then re-write the operator  $f_0$  as

$$f_0 = \sum_m (u_{0,m} a_{m+} + v_{0,m} a_{m-}), \quad (4.55)$$

where

$$\begin{aligned} u_{0,m} &= \frac{1}{\mathcal{N}} \sqrt{\sum_{k \in \mathcal{I}_{m+}} 1} \\ &= \sqrt{2} \Lambda^{-m/2} \sqrt{\frac{\Lambda^M - 1}{\Lambda - 1}} \end{aligned} \quad (4.56)$$

and, similarly,

$$\begin{aligned} v_{0,m} &= \frac{1}{\mathcal{N}} \sqrt{\sum_{k \in \mathcal{I}_{m-}} 1} \\ &= \sqrt{2} \Lambda^{-m/2} \sqrt{\frac{\Lambda^M - 1}{\Lambda - 1}} \end{aligned} \quad (4.57)$$

The set of mean energies  $\mathcal{E}_{m\pm}$  and coefficients of  $f_0$  defined, we are able to generate the sequence of operators  $f_n$  ( $n = 1, \dots, M - 1$ ) of the Lanczos basis.

#### 4.2.2 Lanczos transformation

Finally, we will construct the discrete basis  $\{f_n\}$  upon which the Hamiltonian will be numerically diagonalized. Our task is now to express the conduction band Hamiltonian

as

$$H_{\text{CB}} = \sum_{n=0}^{\infty} \left[ (t_n f_n^\dagger f_{n+1} + H.c.) + \eta_n f_n^\dagger f_n \right]. \quad (4.58)$$

To this end, we define the basis of orthonormal operators  $\{f_n\}$ :

$$f_n = \sum_m u_{nm} a_m + v_{nm} b_m, \quad (4.59)$$

obeying the commutation relations  $\{f_n^\dagger, f_{n'}\} = \delta_{n,n'}$ .

The inverse transformation is also provided

$$\begin{aligned} a_m &= \sum_n u_{nm} f_n \\ b_m &= \sum_n v_{nm} f_n. \end{aligned} \quad (4.60)$$

The traditional formulation explained in subsection 4.2.1 considers a conduction band with continuum momenta close to the Fermi level. Notice that here we already have the coefficients  $u_{0m} = \frac{\gamma_{m+}}{\sqrt{\gamma}}$  and  $v_{0m} = \frac{\gamma_{m-}}{\sqrt{\gamma}}$  in eqs. (4.31) and (4.32), respectively. In the case of finite momenta  $k$ , we have  $u_{0,m}$  and  $v_{0,m}$  explicitly in eq. 4.56.

In order to determine the coefficients  $t_n$  and  $\eta_n$  defined in eq. (4.58) we employ a recursive procedure matching each  $n$ -th term with the corresponding diagonal  $\eta_n$ , co-diagonal  $t_n$  energies, as well as the coefficients of the Lanczos basis  $u_{n,m}$  and  $v_{n,m}$ . The details of the mathematical steps needed to obtain the recursion relation are explained in Appendix C.

After few steps of algebra we can identify the diagonal and co-diagonal coefficients in zero-th order with

$$\eta_0 = \sum_m \left[ \mathcal{E}_{m+} u_{n,m}^2 + \mathcal{E}_{m-} v_{n,m}^2 \right], \quad (4.61)$$

and

$$t_0^2 = \sum_m (\mathcal{E}_m^+ - \eta_0)^2 u_{0,m}^2 + (\mathcal{E}_m^- - \eta_0)^2 v_{0,m}^2. \quad (4.62)$$

Note that the diagonal coefficients weight the difference between energetic contributions of states below and above the Fermi level. They vanish for a symmetric conduction band as  $\mathcal{E}_{m+} = \mathcal{E}_{m-}$

The coefficients defining the state  $f_1$  are identified as

$$\begin{aligned} u_{1,m} &= \frac{1}{t_0} (\mathcal{E}_m^+ - \eta_0) u_{0,m} \\ v_{1,m} &= \frac{1}{t_0} (\mathcal{E}_m^- - \eta_0) v_{0,m}. \end{aligned} \quad (4.63)$$

The remaining coefficients of the Lanczos basis  $\{f_n\}$  ( $n=2,3,\dots$ ) can be calculated recursively from the relations

$$\begin{aligned}\eta_n &= \sum_m (\mathcal{E}_m^+ u_{n,m}^2 + \mathcal{E}_m^- v_{n,m}^2) \\ t_n^2 &= \sum_m (\mathcal{E}_m^+ u_{n,m}^2 + \mathcal{E}_m^- v_{n,m}^2) - t_{n-1}^2 - \eta_n^2,\end{aligned}\quad (4.64)$$

and

$$\begin{aligned}u_{n+1,m} &= \frac{1}{t_n} [(\mathcal{E}_m^+ - \eta_n) u_{n,m} - t_{n-1} u_{n-1,m}] \\ v_{n+1,m} &= \frac{1}{t_n} [(\mathcal{E}_m^- - \eta_n) v_{n,m} - t_{n-1} v_{n-1,m}].\end{aligned}\quad (4.65)$$

In practice, to avoid numerical error propagation, we compute the set of  $u_{n,m}$  and  $v_{n,m}$  for a given  $n$  and use a Gram-Schmidt procedure to assure that the basis for the  $f_n$  operators is orthonormalized. The outputs from this calculation are the coefficients  $t_n$  and  $\eta_n$  which enter in the iterative diagonalization of the impurity Hamiltonian.

The Lanczos transformation is the last step of the NRG approach requiring an analytical treatment.<sup>†</sup> The next stage is the iterative diagonalization of the impurity Hamiltonian in the basis of  $\{c_d, f_n\}$ , which requires the knowledge of coefficients  $t_n$  and  $\eta_n$ . We briefly introduce details of implementation below.

#### 4.2.3 Iterative Diagonalization

The projection of the single impurity Anderson model into the Lanczos basis yields the following Hamiltonian

$$H_N = \sum_{n=0}^{N_{\max}-1} [t_n (f_n^\dagger f_{n+1} + H.c.) + \eta_n f_n^\dagger f_n] + V(f_0^\dagger c_d + H.c.) + H_d, \quad (4.66)$$

where the number  $N_{\max}$  of iterations is defined by the *infrared truncation* in eq. (4.11).

It is convenient to normalize the eigenvalues of the previous Hamiltonian in order to have the smallest ones of the order of the unit in the asymptotic limit. We therefore introduce a scaling factor  $\mathcal{D}_N$  defined as

$$\mathcal{D}_N = t_{n \gg 1} \approx \mathcal{D}_{n \gg 1} = D \frac{1 - \Lambda^{-1}}{\log \Lambda} \Lambda^{-n/2}, \quad (4.67)$$

with error estimated as  $\mathcal{O}(\Lambda^{-n})$ .

---

<sup>†</sup> Analytical treatment in the sense that we have to perform changes of basis involving definitions prior to the calculation of the ingredients of the Lanczos basis  $\{f_n\}$ . We already pointed out that the coefficients  $t_n$  and  $\eta_n$  are calculated numerically using a Gram-Schmidt procedure. In practice, carrying out all steps up to the iterative diagonalization can be performed numerically if  $\rho(\epsilon)$  is extracted from numerical calculations, such as density functional theory.

It follows that the Hamiltonian to be solved numerically is

$$\mathcal{H}_N = \frac{1}{\mathcal{D}_N} \left( \sum_{n=0}^{N_{\max}-1} [t_n(f_n^\dagger f_{n+1} + H.c.) + \eta_n f_n^\dagger f_n] + V(f_0^\dagger c_d + H.c.) + H_d \right), \quad (4.68)$$

where the normalization factors are calculated according to (4.67).

Inspection of (4.68) allows us to identify the RG transformation connecting the Hamiltonians in successive iterations. Explicitly,

$$\tau[\mathcal{H}_{N-1}] \equiv \mathcal{H}_N = \sqrt{\Lambda} H_{N-1} + \frac{t_{N-1}}{\mathcal{D}_N} (f_{N-1}^\dagger f_N + H.c.) + \frac{\eta_N}{\mathcal{D}_N} f_N^\dagger f_N. \quad (4.69)$$

Note that eq. (4.69) is equivalent to eq. (4.6) for the Anderson Hamiltonian. In order to carry out the diagonalization of the matrix Hamiltonian the basis set to project the operator in eq. (4.68) must be defined. We note that at each iteration  $N$ , the size of the chain is  $N + 2$ , as the  $c_d$  and  $f_0$  levels are included, as shown by figure 27. As mentioned, the growing of the many-body Hilbert space of the chain of size  $N + 2$  is prevented to not be  $4^{N+2}$  through the *ultraviolet cut-off*. The accuracy of NRG calculations is highly dependent on the ultraviolet truncation, with error being a decreasing function of the parameter  $E_{UV}$ . At the same time, the computational cost grows as  $\Lambda \rightarrow 1$  and  $E_{UV} \gg D$ .

The iterative diagonalization is carried out as follows. Starting from the impurity Hamiltonian  $N = -1$ , the Hamiltonian  $H_{N=-1} = H_d$  is diagonalized, all the eigenstates  $|\Psi_r\rangle$  ( $r = 0, \dots, R - 1$ ) and eigenvalues  $\epsilon_r$  are kept. Note that in  $N = -1$ ,  $R = 3$  or  $4$  as the eigenstates  $\Psi_r$  match the possibilities of fermionic states of the impurity and, in the absence of external magnetic fields, the eigenstates  $c_{d\uparrow}$  and  $c_{d\downarrow}$  are degenerate, so that we can keep just one of them. In the second iteration, the basis set grows by a factor of 4 and the states to project the Hamiltonian  $\mathcal{H}_N$  are

$$|\psi_p\rangle^{N=0} = |f_{0\mu}\rangle \otimes |\Psi_r\rangle^{N=-1}, \\ p = 0, \dots, 4 \times R - 1 \quad (4.70)$$

where  $\mu = 0, \uparrow, \downarrow, \uparrow\downarrow$ .

From the diagonalization of  $\mathcal{H}_0$ , the lowest energy  $\epsilon_{gs}^{N=0}$  is identified and subtracted from all eigenvalues, so that  $\epsilon_r^{N=0} \rightarrow \epsilon_r^{N=0} - \epsilon_{gs}^{N=0}$  and  $\epsilon_{gs}^{N=0} \rightarrow 0$ . We then apply the *ultraviolet truncation* in order to retain only  $R$  eigenvalues  $\epsilon_r$  and eigenvectors  $|\Psi_r\rangle$  ( $r = 0, 1, \dots, R - 1$ ), so that  $\epsilon_{R+1} > E_{UV}$ . In the next iteration, and the in following ones ( $n = 2, 3, \dots, N$ ), the basis set is built similarly to eq. (4.70). Explicitly

$$|\psi_p\rangle^n = |f_{n\mu}\rangle \otimes |\Psi_r\rangle^{n-1}, \\ r = 0, \dots, R^{n-1} - 1 \quad (4.71)$$

$c_d$ 

$$H_{-1} = H_d = \epsilon_d n_d + U n_{d\uparrow} n_{d\downarrow}$$

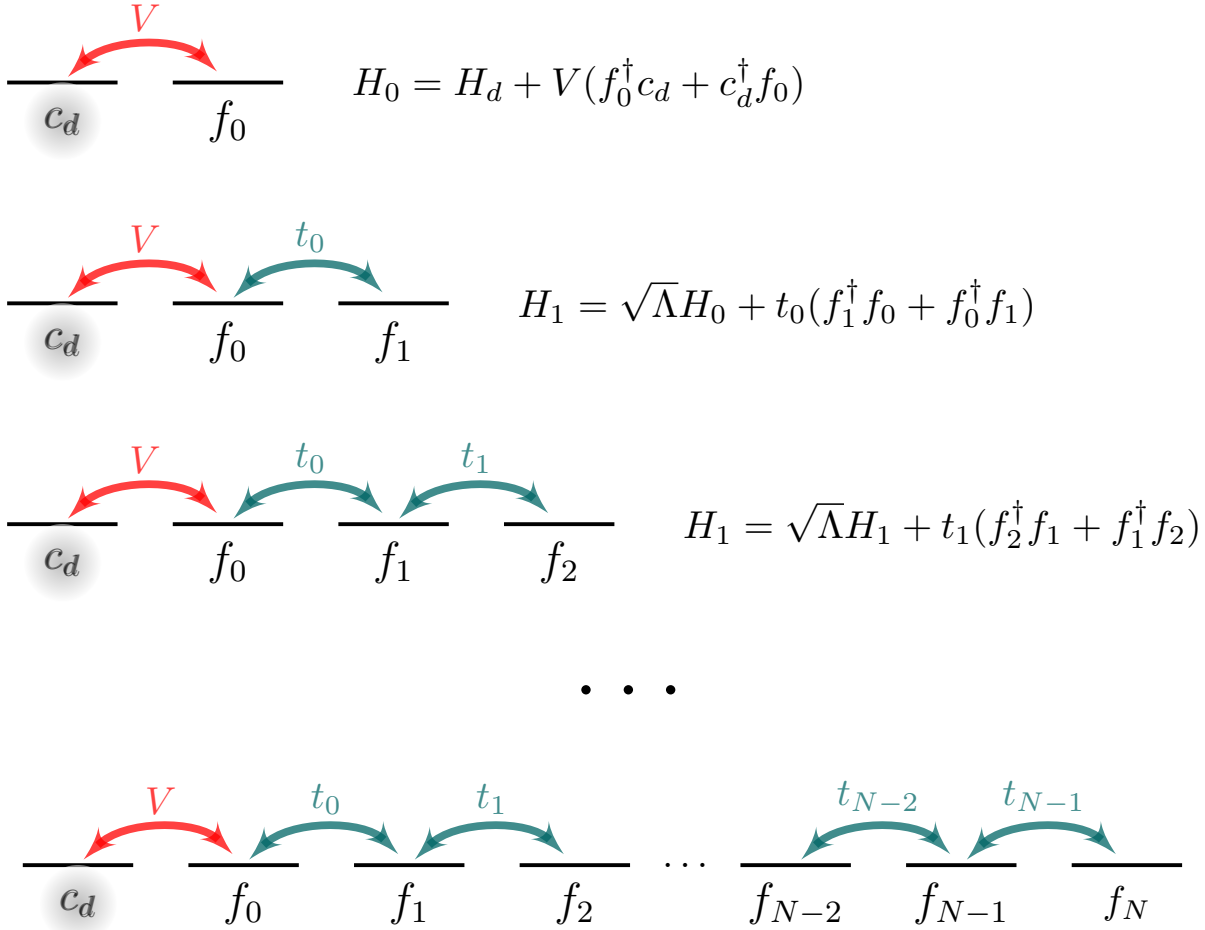


Figure 27 – Iterative growing of the Lanczos chain for the single impurity Anderson model. The very first iteration  $N = -1$  considers solely the impurity level, so that  $H_{N=-1} = H_d$ . In the second step,  $N = 0$ , the Wannier state  $f_0$  is introduced and the new Hamiltonian accounts for the coupling  $V$  between the conduction band and  $c_d$ . At each iteration  $N$  the size of the chain is  $N + 2$ . The *ultraviolet cut-off* prevents the growing of the Hilbert space, which would have dimension  $4^{N+2}$ , otherwise. Without the truncation, such scaling would restrict the maximum number of Lanczos states  $f_n$  to a dozen of sites. The maximum number of iterations  $N$  to be computed is determined by the thermal scale of interest and is calculated according to eq. (4.11)

Source: By the autor.

where  $\mu = 0, \uparrow, \downarrow, \nparallel$  and  $R^{n-1}$  are the number of truncated eigenstates in the iteration  $n - 1$ .

We name the bases of the  $N$ -th iteration  $\{|\psi_p\rangle^N\}$  *primitive basis* (before diagonalization) and  $\{|\Psi_r\rangle^N\}$  *truncated basis* (after diagonalization and truncation) of the  $N$ -th iteration, respectively.

At this point, it is important to note that the RG transformation in eq. (4.69) provides an easy recipe to calculate the diagonal  $\langle \psi_p | \mathcal{H}_N | \psi_p \rangle$  and off-diagonal  $\langle \psi_p | \mathcal{H}_N | \psi'_p \rangle$  matrix elements of the projected Hamiltonian. The former are simply the eigenvalues of the previous iteration  $\epsilon_r$  multiplied by  $\sqrt{\Lambda}$ . The latter, which are ultimately related to the hopping connecting neighbor sites  $f_n$  and  $f_{n-1}$ , requires the calculation of matrix elements generated in the iteration  $n - 1$ , which have the form  ${}^{n-1}\langle \Psi_r | f_{n-1}^\dagger | \Psi_{r'} \rangle^{n-1}$ , where the superscript refers to the iteration index ( $n - 1$  refers to the iteration before  $n$ ). The eigenvalues  $\epsilon_r^n$ , the eigenstates  $|\Psi_r\rangle^n$  and the matrix elements  ${}^{n-1}\langle \Psi_r | f_{n-1}^\dagger | \Psi_{r'} \rangle^{n-1}$  are therefore the minimal ingredients of the iterative diagonalization. They also are useful in the calculation of physical observables, as we will exemplify in Appendix B when we show how to compute the zero bias conductance through the single-electron transistor from NRG ingredients.

Usually, a single run of a NRG code takes few minutes to perform the complete iterative cycle, calculating properties and exporting results in output files. An important trick that can be implemented in order to make the computation more efficient uses our previous discussion about the importance of the symmetries in helping to break the Hilbert space in smaller subspaces upon which the Hamiltonian can be written in block-diagonal. The conservation of charge and spin in the Anderson Hamiltonian allows us to further reduce the dimension of the matrices to be diagonalized: each tuple of quantum numbers  $Q$  and  $S$  defines a smaller Hilbert space with primitive basis elements  $\{|\psi_p\rangle\}$  ( $p = 0, \dots, P - 1$ ), which are therefore labeled also by the two quantum numbers, i.e.  $|\psi_p\rangle \rightarrow |Q, S, S_z, p\rangle$  ( $p = 0, \dots, P(Q, S) - 1$ ), where, now,  $P(Q, S)$  counts the number of states with same charge and spin in the  $N$ -th iteration. The details of the implementation of a NRG code including the definition of the primitive and truncated basis in the subspaces  $(Q, S)$ , as well as the calculation of the matrix elements of the Hamiltonian  $\mathcal{H}_N$  are presented in appendix B.

In summary, the NRG solution of impurity models, such as the SIAM, can be illustrated by figure 28.

With the previous picture and the discussion of the Kondo effect in quantum dots in chapter 2 we are ready to examine the Anderson Hamiltonian for a single-electron transistor from the perspective of the Renormalization-Group. In the following section, we will devote our attention to the fixed points of the RG flow and their physical interpretation in terms of the universal conductance through a single-electron transistor.

### 4.3 Numerical Renormalization-Group analysis of the Kondo problem

In chapter 2, we presented a historical review of the Kondo problem and reasoned on the success of the NRG solution with respect to all previous approaches: NRG was the first approach capable to describe the crossover from the high-temperature to the

### Logarithmic discretization of the BC

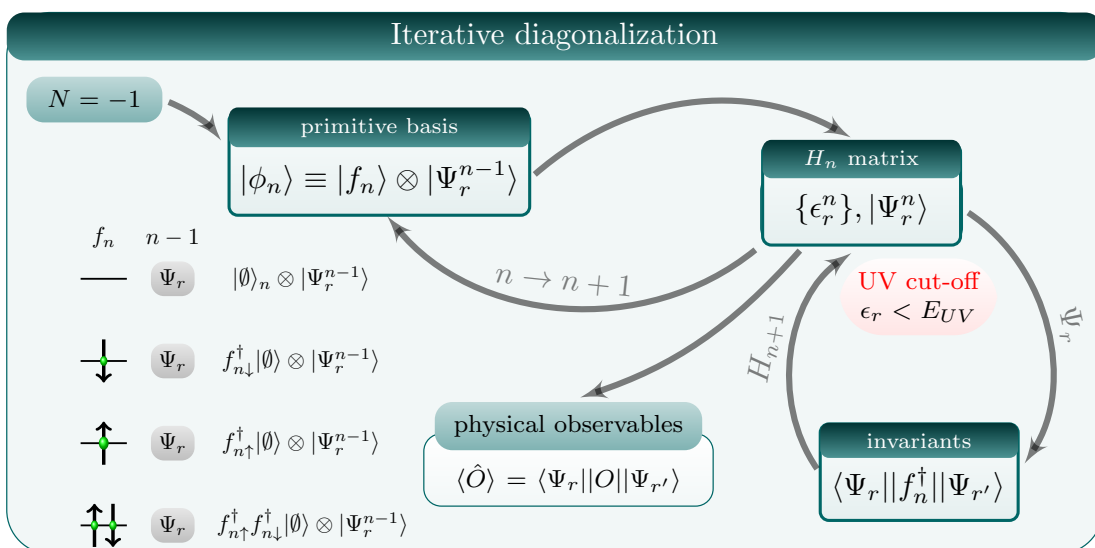
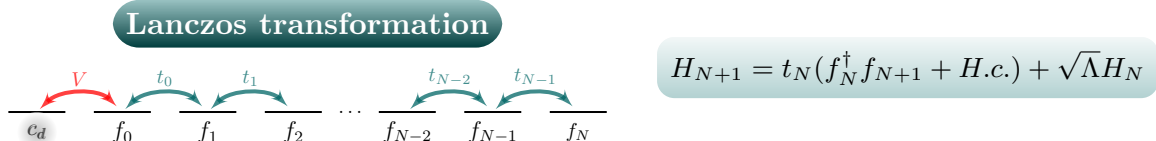
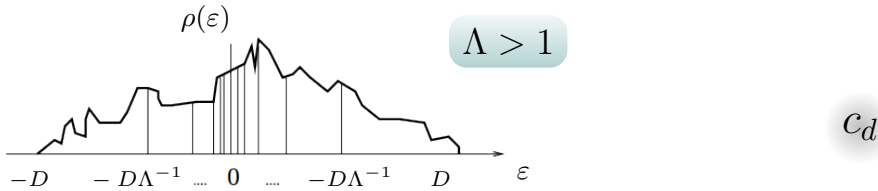


Figure 28 – Iterative cycle of the NRG algorithm to impurity problems. The first iteration labeled by  $N = -1$  contains a single-site  $c_d$ , which is the impurity level. The eigenstates  $|\Psi_p^{N=1}\rangle$  ( $p = 0, 1, 2$  for a single-site impurity) and eigenvalues  $\lambda_{N=-1}$  of  $H_{N=-1}$  are calculated without truncation to preserve the impurity site. From  $N = -1$ , the Lanczos chain of operators  $f_n$  start to be increased iteratively. In  $N = 0$ , the operator  $f_0$  is added to construct the primitive basis of iteration  $N = 0$  as  $|f_0\rangle \otimes |\Psi_r^{N=1}\rangle$ . The Hamiltonian  $H_{N=0}$  is projected onto the states of the primitive basis and the diagonalization is carried out. The eigenstates whose eigenvalues respect  $\epsilon_r < E_{UV}$  are kept and the invariants  $\langle f_0 \rangle$  are calculated and thermodynamical physical observables are calculated. This procedure is repeated for a total number of steps  $N$ , where  $N$  is an integer satisfying condition (4.11) for the the temperature  $T$  of interest.

Source: By the author.

low-temperature regimes underlying the Kondo effect in an impurity system. Now, having the basis of the Renormalization-Group and Wilson's NRG approach, we are ready to understand how the RG flow is able to accurately describe the crossover. Particularly important to the following discussion is the existence of *fixed points*, special points of the RG flow that remain invariant under an RG transformation and whose structure

is reflected in observables of physical systems. Especially, the fixed point description of model Hamiltonians provide a simpler picture, from which one is able to extract properties analytically and therefore understand the physics underlying many-body phenomena.

Here, our aim is to explore the fixed point structure of the Anderson model and show how it explains the Kondo effect in a single-electron transistor. We start recalling a key concept discussed in the present chapter: the scale invariance within the NRG construction. We explained that the NRG solution of the Anderson model yields access to effective energy scales  $D\Lambda^{-n}$  through the iterative diagonalization of the transformed Hamiltonian  $H_N$  with renormalized couplings:  $t_n$ ,  $\Gamma$  and  $U$  in units of  $\mathcal{D}_N$ . As the number of iteration grow, the access of successively smaller scales are ultimately related to the flow from the high ( $k_B T \approx D$ ) to the low temperature ( $T \rightarrow 0$ ) regimes. In between, a characteristic thermal scale  $T_K$  can arise and manifest as the Kondo effect. While for  $T \gg T_K$  the coupling between the impurity and the conduction band can be disregarded, for  $T \ll T_K$  the coupling becomes strong enough to dominate the physics of the system, the most prominent consequence being the formation of the Kondo screening cloud within which there is an enhancement of scattering and spin-flip processes characterizing the Kondo effect. It turns out that the high and low temperature regimes are identified with two fixed points of the Anderson Hamiltonian: *Local Moment* (LM) and *Frozen Level* (FL). As we will show later, both can be described in terms of a single-particle system decoupled from the impurity level with all the effects of the impurity lumped in an effective scattering potential  $W^*$ .

In order to appreciate the structure of the fixed points of the Anderson Hamiltonian, we can, for instance, examine the evolution of properties along iterations in some limits of the model parameters. Consider the spectrum of  $\mathcal{H}_N$  in the case where the Coulomb repulsion is absent  $U = 0$ . Double occupation can be disregarded and double occupied states are described by single particle states with spins up and down decoupled from each other. The Hamiltonian in eq. (4.68) therefore acquires the quadratic form

$$H_N = \frac{1}{\mathcal{D}_N} \left[ \sum_{n=0}^{N-1} t_n (f_n^\dagger f_{n+1} + H.c.) + \sqrt{2}V(f_0^\dagger c_d + H.c.) + \epsilon_d c_d^\dagger c_d \right], \quad (4.72)$$

which is easily diagonalized.

The model parameters  $\Gamma$ ,  $\epsilon_d$  and  $D$  define the single-particle levels  $\tilde{\varepsilon}_j$  ( $j = 0, \dots, N - 1$ ) and the characteristic energies of the system. For  $\Gamma = 0$  and  $\epsilon_d = 0$ , the system is purely metallic with the  $N$  single-particle levels  $\epsilon_j$  ( $j = 0, \dots, N - 1$ ) ultimately defined by the renormalized hopping coefficients  $t_n$  ( $n = 0, \dots, N - 1$ ). If  $\epsilon_d = 0$  and  $\Gamma \neq 0$ , the only characteristic energy is the width  $\Gamma = \pi V^2/D$  associated with the hybridization between the conduction band and the impurity. The energy invariance of the conduction band is broken by the broadening  $\Gamma$  of the impurity level. As a consequence, the Hamiltonian in eq. (4.72) describes conduction electrons whose levels are phase-shifted due to the presence of

to the impurity, i.e.,

$$\tilde{\varepsilon}_j = \epsilon_j - \frac{\delta}{\pi} \Delta, \quad (4.73)$$

where  $\Delta$  is the energy splitting<sup>‡</sup>, and  $\delta$  is the phase-shift.

Conduction electrons with  $\tilde{\varepsilon}_j \gtrsim \Gamma$  are strongly shifted and, in particular, those with energies  $\tilde{\varepsilon}_j \ll \Gamma$  acquire a phase shift of  $\delta = \pi/2$ .

The case  $U = 0$  and  $\epsilon_d$  is illustrative because it provides a insightful view of the how the fixed point structure of the Anderson Hamiltonian manifest in its physical properties; in particular, in the evolution of eigenvalues  $\tilde{\varepsilon}_j$  along NRG iterations. If we follow the evolution of the eigenvalues, we can observe that in both limits the structure of the curves remains invariant for certain ranges of small and large iterations, as shown in figure 29. For small  $N$  ( $N \leq 17$  in the figure), the typical energies  $\tilde{\varepsilon}_j = \tilde{\varepsilon}_j(N)$  are larger compared to  $\Gamma$ , so that the coupling does not play a role and can be neglected as the band was free. By increasing  $N$ , the scales  $\tilde{\varepsilon}_j$  and  $\Gamma$  become comparable and compete with each other until a point in which  $\tilde{\varepsilon}_j$  is very small compared to  $\Gamma$ , so that the coupling dominates the physics of the system. After a few iterations, the eigenvalues become invariant again ( $N \geq 35$  in the figure).

Inspection of the eigenvalues  $\tilde{\varepsilon}_j$  of the Hamiltonian in eq. (4.72) in the limits  $\Gamma \rightarrow 0$  and  $\Gamma \rightarrow \infty$ , illustrated by arrows on the left and right sides of figure 29, reveal they to match the plateaus for small and very large iterations. The equivalence between the coupling regimes regimes  $\Gamma \rightarrow 0$  and  $\Gamma \rightarrow \infty$  with the ranges of the iterations for which the eigenvalues remain invariant allows us to identify two fixed points of the Anderson Hamiltonian. Initial iterations for which the system remains invariant are associated with the so-called the *Free Orbital* (FO) fixed point, which corresponds to the limit  $\Gamma \rightarrow 0$  for  $U = 0$  and  $\epsilon_d = 0$ . For large  $N$ , after the crossover, the new plateaus are associated with the so-called *Frozen Level* (FL) fixed point, which is described by the strong coupling  $\Gamma \rightarrow \infty$  between the impurity and the metallic electrons.

Note that, within the RG flow, the FO fixed point corresponds to high-temperatures of the Anderson Hamiltonian for  $\epsilon_d = 0$ , whereas the FL fixed point is ascribed to the very low temperature regime. As shown by figure 29, the crossover connecting  $k_B T \approx D$  to  $k_B T \rightarrow 0$  is found for iterations  $17 \leq N \leq 35$ . The FO fixed point is unstable: a small perturbation  $\Gamma$ , such as  $\Gamma = 10^{-5}D$  in Fig. 29, will drive the system to FL fixed point.

Another important fixed point of the Anderson Hamiltonian can be identified in the opposite limit of the model parameter  $U$ . By tuning the Coulomb repulsion to the limit  $U \rightarrow \infty$ , the system, again, reduces to a single-particle description because the strong penalty for doubly occupied states of the impurity makes it decouple from the conduction

---

<sup>‡</sup> Usually, we define  $\Delta = D/N_{cb}$ , where  $N_{cb}$  is the number of metallic states.

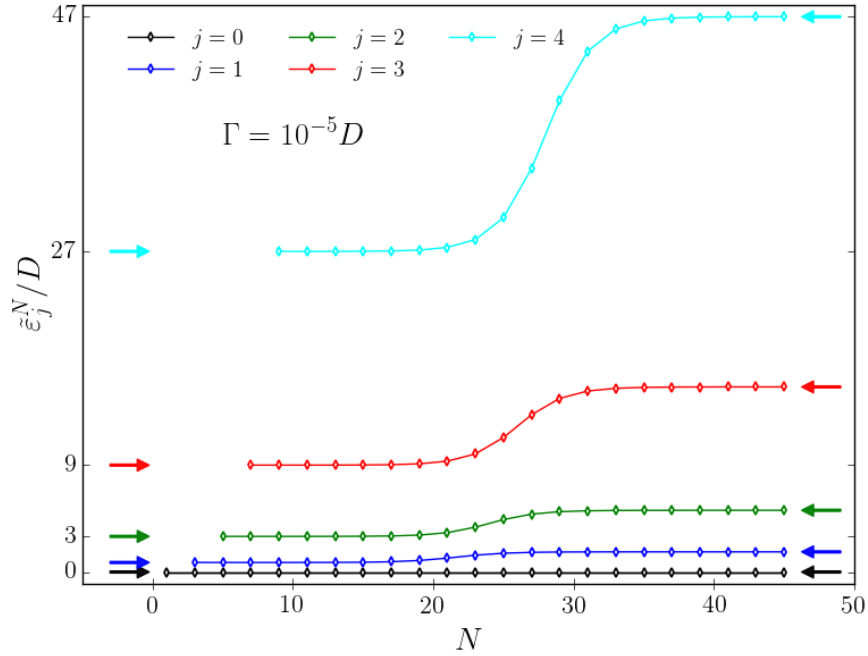


Figure 29 – Single-particle levels  $\tilde{\epsilon}_j$  ( $j = 0, \dots, 4$ ) of the renormalized Anderson Hamiltonian  $\mathcal{H}_N$  along odd iterations  $N$  for  $\Gamma = 10^{-5}D$ . Note the plateaus of all five eigenvalues for iterations  $N \leq 17$  and for  $N \geq 35$ . The invariance of eigenvalues outside the window  $17 < N < 35$  reflects the fixed point structure of the Anderson Hamiltonian. For  $N \leq 17$ , the levels  $\tilde{\epsilon}_j \approx \epsilon_j$  are equivalent to those of a free conduction band ( $\Gamma = 0$ ), shown as colored arrows on the left. For large iterations,  $N \geq 35$ , the levels stagger into constant values matching the eigenvalues of  $H_N$  for  $\Gamma \rightarrow \infty$ , marked by arrows on the right. The limits  $\Gamma \rightarrow 0$  and  $\Gamma \rightarrow \infty$  identify two fixed points of the Anderson Hamiltonian for  $\epsilon_d = 0$ : the *free orbital* and the *frozen level*, respectively.

Source: By the author.

band at the same time that the states  $c_{d\uparrow}$  and  $c_{d\downarrow}$  become degenerate. The limit  $U \rightarrow \infty$  of the Anderson Hamiltonian is identified with the *local moment* (LM) fixed point. Physically, the picture of the LM fixed point corresponds to the case in which the impurity acquires a moment and therefore can be singly occupied with a spin up or a spin down. Similarly to the FO, the LM is also an unstable fixed point of the Anderson Hamiltonian. By making  $U \gg D$ , i.e. large but finite, a small perturbation arising from coupling  $\Gamma > 0$  is able to promote spin-flip processes arising from the virtual transitions that are made to exchange the states  $c_{d\uparrow} \leftrightarrow c_{d\downarrow}$ . If we follow the behavior of the eigenvalues  $\tilde{\epsilon}_j$  of  $\mathcal{H}_N$  for  $U \neq 0$ , we will observe them to re-gain the invariance associated with the FL fixed point because the coupling  $\Gamma$  will renormalize with iterations until the point where it can be regarded as  $\Gamma \rightarrow \infty$ .

With all model parameters  $U \neq 0$ ,  $\Gamma \neq 0$ ,  $\epsilon_d \neq 0$ , the RG flow will drive the system between the LM and the FL fixed points: the first corresponding to high temperatures and the latter corresponding to very low temperatures. We extend the previous analysis to the interacting limit of the Anderson Hamiltonian at the symmetry point  $\epsilon_d = -U/2$ .

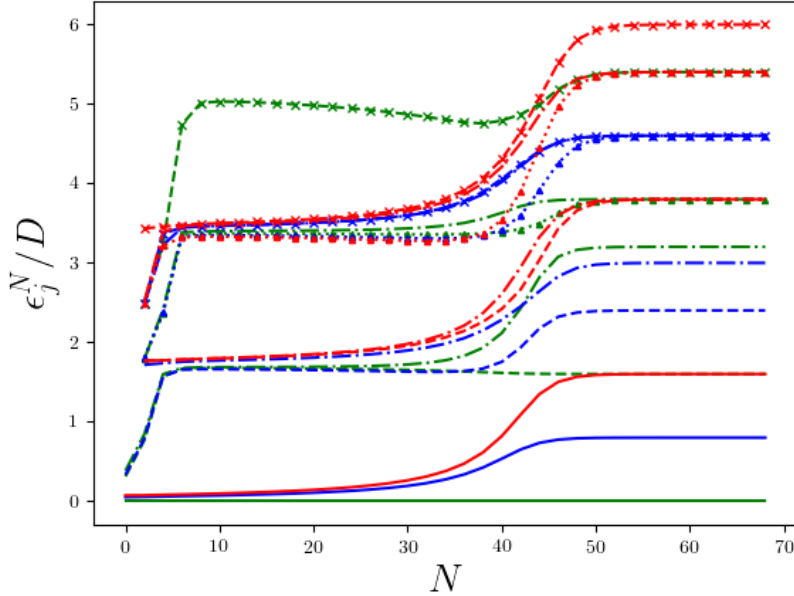


Figure 30 – Evolution of eigenvalues of the Hamiltonian  $\mathcal{H}_N$  along iterations  $N$  for the symmetric case:  $\Gamma = 0.01$ ,  $U = 0.5$  and  $\epsilon_d = -0.25$ . The Kondo temperature is of order  $T_K \approx 10^{-10}$ , while the minimum thermal scale reached by the last NRG iteration  $N = 68$  is of order  $k_b T \approx 10^{-17}$ . The LM fixed point is marked by the plateaus observed in iterations lower than  $N < 30$ . The crossover to the Kondo regime is seen in the window  $35 < N < 55$ . After  $N > 50$ , the eigenvalues become constant, characterizing the FL fixed point.

Source: By the author.

Fig. 30 shows the five lowest eigenvalues  $\tilde{\epsilon}_j$  during the RG flow between the LM and FL fixed points for  $\Gamma = 0.01$ ,  $U = 0.5$  and  $\epsilon_d = -0.25$ . The plateaus for  $N < 30$  and  $N > 50$  mark the LM and FL fixed points, respectively.

In all cases (FO  $\rightarrow$  FL or LM  $\rightarrow$  FL), we can verify a crossover in the eigenvalues during the iterative process. The crossover is ultimately defined by a characteristic scale  $\Gamma_K$  separating the LM ( $\Gamma \rightarrow 0$ ) and FL ( $\Gamma \rightarrow \infty$ ) regimes. We can now argue that  $\Gamma_K$  associates the Anderson and the Kondo Hamiltonians and identifies the so-called *Kondo temperature*  $T_K$ . We mentioned that starting from the LM fixed point, the effect of increasing the coupling  $\Gamma$  is to promote virtual excitations between magnetic and non-magnetic states of the impurity. The description of the coupling between the impurity and the Wannier state  $f_0$  can be regarded as an antiferromagnetic spin interaction, i.e.,

$$H_{\text{int}} = -J \sum_{\mu,\nu} \left( f_{0\mu}^\dagger \vec{\sigma}_{\mu,\nu} f_{0\nu} \right) \cdot \mathbf{S}_d, \quad (4.74)$$

where  $\vec{\sigma}$  are the Pauli matrices,  $\mathbf{S}_d$  describes the moment of the impurity and  $J$  is the coupling strength.

We can identify eq. (4.74) with the second term on the right-hand side of the Kondo Hamiltonian in eq. (2.8) and calculate the coupling constant  $J$  from the parameters of the Anderson Hamiltonian by means of the Schrieffer-Wolf transformation in eq. (2.12). In the Kondo regime, the Hamiltonian crosses between the LM and the FL fixed points.

The Kondo regime therefore defines the crossover between the limits of high and low temperatures. Within the Kondo regime, from the balance between energetic and thermal scales emerges a characteristic coupling  $\Gamma_K$ , related to the coupling  $J$ . It is estimated as follows

$$\Gamma_K \approx D\sqrt{\rho J}e^{-1/\rho J}(1 + \mathcal{O}(\rho J)), \quad (4.75)$$

where  $\rho$  is the density of states of the conduction band with width  $D$ .

Specifically, when  $k_B T = \Gamma_K$ , those states with energies  $\epsilon_j < \Gamma_K$  have a very large spin-flip rate, as it would be for  $J \rightarrow \infty$ . Beyond the crossover, the system evolves to the FL fixed point, which marks the very low-temperature regime.

In chapter 2, we have discussed the Kondo effect in a single-electron transistor and argued that transport measurements, in particular, the zero-bias conductance, can be accurately reproduced by the diagonalization of the Anderson Hamiltonian. In section 2.3.1, we have shown that the Friedel sum rule relates the SET conductance  $\mathcal{G}_d$  with the phase shifts  $\delta$  of the conduction electrons in the limits  $T \gg T_K$  and  $T \ll T_K$ . We have also introduced the universal mapping - eq. (2.43) - relating  $\delta$ ,  $\mathcal{G}_d$  and  $T_K$  and discussed its form at the symmetric point (gate voltage  $V_G = -U/2$ ). Specifically, in Fig. 11 we have presented results of the universal mapping against experimental data, which agreed for all temperatures, i.e., from  $T \gg T_K$  to  $T \ll T_K$ , for a experimental set of data comprising 34 gate voltages.

Now, that we have learned that the behavior of properties during the RG flow contains rich information about fixed points and exemplified how this information can be captured analyzing the structure of eigenvalues of the Anderson Hamiltonian along iterations, we are ready to focus on the conductance through a SET and investigate how  $\mathcal{G}_d$  behaves in crossover between the LM and FL fixed points. The first question to be asked concerns how the model parameters affects transport in the limit of zero bias. Returning to chapter 2, we have learned that the operability of the SET is ultimately determined by a balance between the hybridization  $\Gamma$  and charging energy  $E_c$ , which is defined from  $U$  and  $V_G$ . In the absence of hybridization ( $\Gamma = 0$ ), dot occupation would be conserved and conduction would be impossible, as in the *Coulomb blockade regime*. Electrons are blocked whenever the coupling  $\Gamma \neq 0$  is not high enough to overcome  $E_c$  and the gate voltage  $|V_G| \gg \Gamma$  is not suitable chosen to align the Fermi levels of the leads with the quantum dot. This picture is changed at low temperatures, a regime in which the Kondo effect can take place.

The temperature enters in a SET system the same way as the coupling  $J, \Gamma$  drives the RG flow from the LM to the FL fixed points, passing through the Kondo regime. At high temperatures  $E_c \gg k_B T \gg T_K$ , the coupling between the dot and the leads can be neglected and the SET operates in the *Coulomb blockade regime*: the conductance as a function of the gate voltage behaves as in Fig. 5. Lowering the temperature is equivalent to renormalize the hybridization between the leads and the dot in such a way that it becomes an important scale to the physics of the device. At low temperatures, the hybridization between the dot and the Wannier state  $f_0$  is mapped onto an antiferromagnetic interaction, as in the Kondo model. The valleys that appeared previously at the symmetry points  $V_G = -nU/2$  ( $n$  integer) in the Coulomb blockade mode (see Coulomb oscillations in Fig. 5) start to increase, as the tunneling width introduced by the coupling  $\Gamma$  broadens and allows the flow of electrons between the leads. The Kondo plateau starts to take form. At the temperatures  $T_K$ , the strong coupling  $\Gamma \rightarrow \infty$  between the dot and the leads makes the Wannier level  $f_0$  to form a singlet with the dot. Electrons can flow ballistically through the SET, so that at the symmetric point  $V_G = -U/2$ , the occupation in the dot is unitary, and the conductance within the window  $-U < V_G < 0$ , which vanished in the Coulomb blockade regime, is now characterized by a plateau  $\mathcal{G}_d \rightarrow \mathcal{G}_2$ . The invariance of the Kondo plateau for  $T \ll T_K$ , i.e. the plateau keeps the same no matter how the temperature is cooled below  $T_K$ , marks the emergence of the FL fixed point in a SET.

Figure 31 displays the results of NRG calculations for the conductance  $\mathcal{G}_d$  as a function of the gate voltage  $V_G$  for  $\Gamma = D$  and  $U = 10D$  as the system is cooled from high temperatures  $T \gg T_K$  (bright yellow) to low temperatures  $T \ll T_K$  (dark purple). For such parameter setup, the Kondo plateau takes form at  $T < 10^{-3}D$ , so the Kondo temperature is of the order of  $T_K \approx 10^{-4}D$ . Note the similarity between the numerical calculation in Fig. 31 with results from experimental measurements in Fig. 9.

To illustrate the fixed point structure of conductance, we can consider the curve  $\mathcal{G}_d$  as a function of the temperature for the symmetric model ( $V_G = -U/2$ ) and compare its behavior with that observed for the eigenvalues of  $\mathcal{H}_N$  along the RG flow (Fig. 30). As pointed in section 2.3.1, the symmetric case is special because the conductance for  $V_G = -U/2$  is an universal function of the scaled temperature  $T/T_K$ , defined in eq. (2.41). Fig. 32 presents the curve for the universal zero bias conductance as a function of  $T/T_K$  in the absence of external potential ( $W = 0$ ). It can be reproduced from Fig. 31 by following a vertical line at the symmetry point from yellow (high  $T$ ) to purple (low  $T$ ) colored contour lines. As shown in Figs. 31 and 32, the conductance grows from 0 to  $\mathcal{G}_2$  in the limits  $T \gg T_K$  and  $T \ll T_K$ . In Fig. 32, we can observe that the curve  $\bar{\mathcal{G}}_d$  vs  $T/T_K$  is marked by three regimes: two of these are characterized by the invariance of  $\mathcal{G}_d$  within two separate ranges of temperatures, high ( $T \gg T_K$ ) and low ( $T \ll T_K$ ), and an intermediate region connecting the latter centered at  $T_K$ . This trend is similar of the plot of eigenvalues from small to large iterations in Fig. 30, or, from the LM to the FL fixed points. The flat

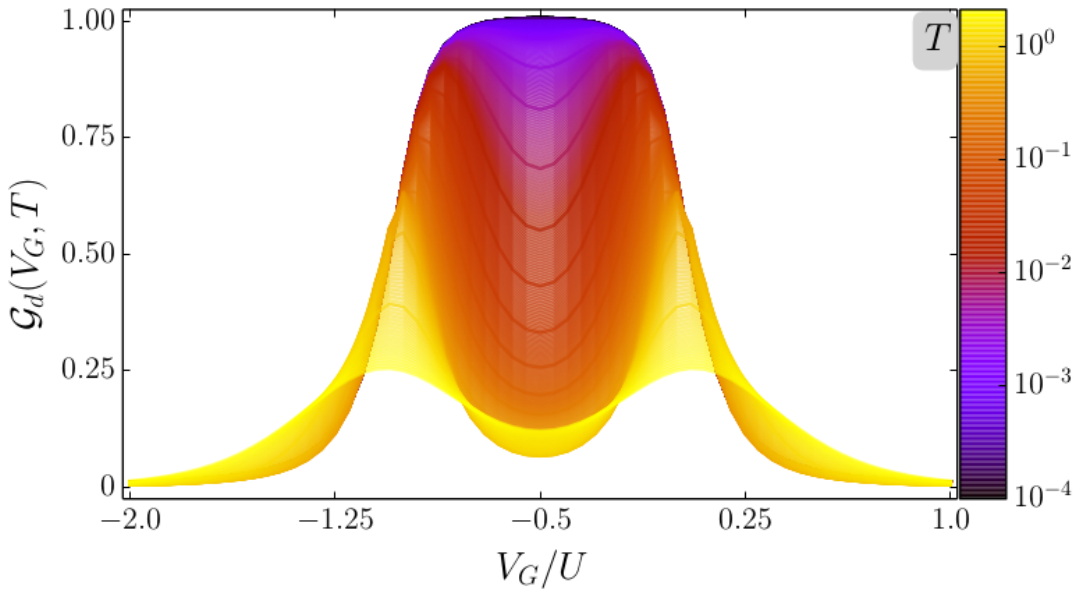


Figure 31 – Conductance  $\mathcal{G}$  as a function of the gate voltage  $V_G$  for temperatures ranging from  $T \gg T_K$  and  $T \ll T_K$ . The color scheme represents high temperatures in light yellow and low temperatures in dark purple. The model parameters of the Anderson Hamiltonian are chosen as  $\Gamma = D$ ,  $U = 10D$ . The NRG discretization parameter is  $\Lambda = 3.0$  and the ultraviolet cutoff is set as  $E_{UV} = 27D$ . As the temperature is cooled, the conductance acquires a plateau characterizing the Kondo effect. When the gate voltage is set to  $V_G = -U/2$ , the Anderson Hamiltonian becomes invariant under particle-hole transformations.

Source: By the author.

behavior of  $\mathcal{G}_d$  observed at high temperatures is associated with the LM fixed point, for which the conductance vanishes, as expected for a SET operating in the Coulomb blockage regime. The plateau  $\mathcal{G}_d = \mathcal{G}_2$  depicted at very low temperatures marks the FL fixed point. The crossover between the LM and FL fixed points occurs at temperatures of the same order of the Kondo temperature  $T_K$ , a point in which the conductance reaches half of the conductance quantum  $0.5\mathcal{G}_2$ .

The same analysis can be carried out at different points of the parametric space of the Anderson model for a SET. To this aim, we can, for instance, monitor the flow between high (yellow) and low (purple) temperatures for a particular gate voltage  $V_G$  in Fig. 31. As discussed in section 2.3.1, a linear relation, defined in eq. (2.42), provides an universal mapping for the zero bias conductance within the entire parametric space. More importantly, we have argued that the coefficients of the linear mapping are extracted from the phase shifts in the limits  $T \gg T_K$  and  $T \ll T_K$ . As mentioned in the present section, fixed points provide a simpler analytical description of model Hamiltonians, from which properties can be straightforwardly extracted.

With this background and with our recent interpretation of the fixed point structure of the properties in a SET, we can now show that the single-particle description of the

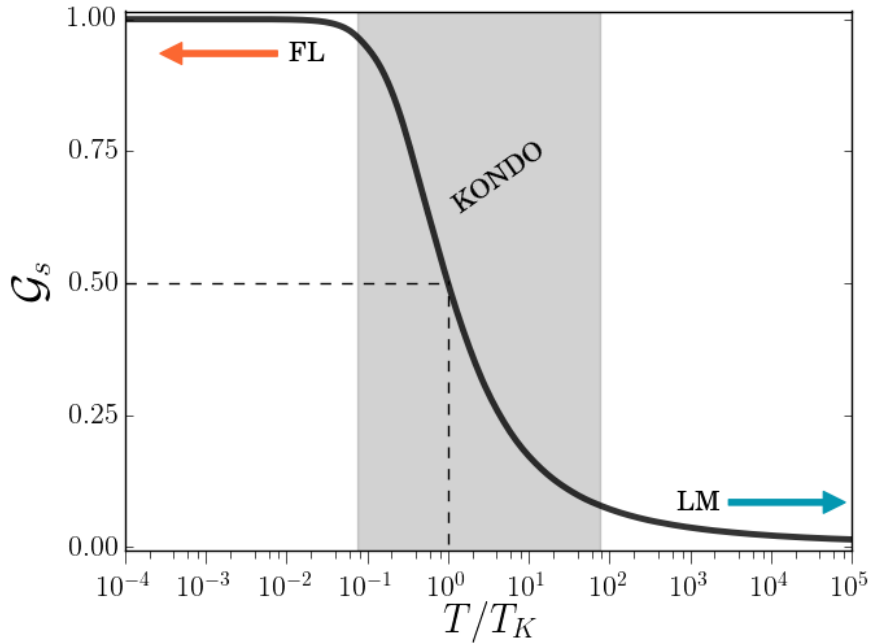


Figure 32 – Universal zero bias conductance  $\mathcal{G}_s$  scaled by the Kondo temperature and the fixed points of the symmetric Anderson Hamiltonian for a single-electron transistor. For  $T \gg T_K$ , the system operates as in the Coulomb blockade. The conductance vanishes at the symmetry point  $V_G = -U/2$  because the Fermi level of the electrons is not aligned with the level of the quantum dot. As the temperature is lowered, tunneling process allows the flow of electrons through the quantum dot. At the characteristic temperature  $T_K$ , the conductance reaches half of the conductance quantum  $\mathcal{G}_2$ . For  $T \ll T_K$ , the conductance reaches its maximum value and the point  $V_G = -U/2$  marks the middle of the Kondo plateau. The invariant behavior of  $\mathcal{G}_d$  for  $T \gg T_K$  and  $T \ll T_K$  and the crossover at  $T_K$  illustrates the fixed point structure of the conductance in a SET. The LM fixed point occurs for  $T \gg T_K$ , a regime in which  $\mathcal{G}_d \rightarrow 0$ . The FL fixed point depicts for  $T \ll T_K$ , when  $\mathcal{G}_d \rightarrow 1$ . The shaded region highlights the temperatures for which the device is found in the Kondo regime.

Source: By the author.

Anderson Hamiltonian in the LM and FL fixed points accurately reproduces the phase shifts in the  $T \gg T_K$  and  $T \ll T_K$  temperature regimes. In the next section, we will briefly present the forms of the LM and FL fixed point Hamiltonians and recapitulate their respective phase shifts.

#### 4.3.1 Local Moment

At high temperatures,  $T \gg T_K$ , the SET is characterized by a conserved number of electrons in the dot and by the *Coulomb blockade* regime. The correspondence with the limit  $D, U \rightarrow \infty$ ,  $V_G \rightarrow \infty$  and  $\Gamma \rightarrow 0$ , in which the dot has a magnetic moment and decouples from the conduction electrons, allows to represent the LM fixed point of a SET by the following single-particle Hamiltonian

$$H_{LM}^* = \sum_k \epsilon_k a_k^\dagger a_k + W_{LM} f_0^\dagger f_0. \quad (4.76)$$

The LM Hamiltonian  $H_{LM}^*$  describes a free electron gas shifted by a phase  $\delta_{LM} = -\pi\rho W_{LM}$  due to the presence of a scattering potential  $W_{LM}$ .

The universal relation for  $T \gg T_K$  is

$$\mathcal{G}_d^{LM} = \kappa \mathcal{G}_2 \cos^2(\delta_{LM}). \quad (4.77)$$

Note that in the case when the Anderson Hamiltonian possesses particle-hole symmetry  $W_{LM} = 0$ , so that  $\delta_{LM}$  vanishes and so does the conductance.

#### 4.3.2 Kondo regime

At moderately high temperatures, the interaction between the quantum dot and the conduction electrons starts to play an important role to the physics of the SET. The emergence of an antiferromagnetic interaction in the system leads its physics to be described by the Kondo model, whose form reads

$$H_K = \sum_k \epsilon_k a_k^\dagger a_k + \tilde{W} f_0^\dagger f_0 + J \vec{S} \cdot \sum_{\mu,\nu=\uparrow,\downarrow} \vec{\sigma}_{\mu\nu} f_{0\mu}^\dagger f_{0\nu}, \quad (4.78)$$

where the components of  $\vec{\sigma}$  are the Pauli matrices, and the coefficients of the second and third terms on the right hand side are given by the following Schrieffer-Wolff <sup>51</sup> relations

$$\rho \tilde{W} = \frac{\Gamma}{V_G} + \frac{\Gamma}{V_G + U} \quad (4.79)$$

and

$$\rho J = \frac{\Gamma}{|V_G|} + \frac{\Gamma}{V_G + U}. \quad (4.80)$$

In the Kondo regime, the phase shift at gate voltages not matching the symmetry point  $V_G = -U/2$  are calculated as

$$\tan \delta = -\pi \left( \frac{\Gamma}{V_G} + \frac{\Gamma}{V_G + U} \right) \quad (4.81)$$

The phase shifts and, therefore, the conductance are sensible to the crossover.

#### 4.3.3 Frozen level

At sufficiently low temperatures,  $T \ll T_K$ , the high entanglement between the quantum dot and the electrons of the Wannier state  $f_0$ , allows to describe the SET as in the limit of strong coupling  $J \rightarrow \infty$  of the Anderson Hamiltonian.

$$H_{FL}^* = \sum_k \bar{\epsilon}_k \bar{a}_k^\dagger \bar{a}_k + W_{FL} \sum_{k,q} \bar{a}_k^\dagger \bar{a}_q, \quad (4.82)$$

where the states  $\bar{a}_k$  describe a modified conduction band, which is orthogonal to the basis  $\{a_k, f_0\}$ , formed by the level  $f_0$  and the original states  $\{a_k\}$ . The energies  $\bar{\epsilon}_k$  are phase-shifted with respect to the original band  $\epsilon_k$ .

The orthogonality condition imposes a phase-shift of  $\pi/2$  with respect to the  $a_k$ . As a consequence, the modified energies  $\bar{\epsilon}_k$  are related with the original band  $\epsilon_k$  by

$$\rho\bar{\epsilon}_k = \rho\epsilon_k - \frac{1}{2}. \quad (4.83)$$

The FL phase shift  $\delta_{FL}$  is therefore phase shifted by  $\pi/2$  with respect to the LM phase shift, i.e.,  $\delta_{FL} = \pi/2 - \delta_{LM}$ .

The universal relation for  $T \ll T_K$  is

$$\mathcal{G}_d^{FL} = \kappa\mathcal{G}_2 \sin^2(\delta_{FL}). \quad (4.84)$$

Under particle-hole symmetry, i.e.  $V_G = -U/2$ , the FL phase shift is  $\delta_{FL} = \pi/2$  and the amplitude of the conductance will be within the interval  $[0, \mathcal{G}_2]$ . Especially at the Kondo plateau,  $\mathcal{G}_d \rightarrow \kappa\mathcal{G}_2$ .

Note that if an external potential  $W$  is applied to the Wannier orbital  $f_0$ , an additional phase shift must be accounted in Friedel sum rule. In practice, this means that, the fixed point phase shifts  $\delta^*$  are determined by two contributions: a contribution  $\delta$  accounting for the phase shift due to the presence of the impurity and a contribution  $\delta_W$  determined by an additional scattering potential due to the application of  $W$ . Therefore, to compute solely the contribution  $\delta$ , we recall to eq. (2.38). Generalizing relations (4.77) and (4.84) follows from eq. (2.38).

#### 4.3.4 Fixed points and Density Functional Theory

With the theoretical baggage acquired from chapters 2, 3 and 4, we can now proceed to the main goal of the present thesis. In our chapter devoted to Density Functional Theory, we have shown that the basis of a density functional approach relies on the Kohn-Sham system, which maps an interacting system into a non-interacting by means of an effective potential accounting for the many-body effects. Here, we have just presented the mapping of the Anderson Hamiltonian at the fixed points into a single-particle system, which, in the case of the SET, allows to represent the effects of interaction between the quantum dot and the electron gases in the limits  $T \gg T_K$  and  $T \ll T_K$  by a free band under the presence of effective scattering potentials  $W_{LM}$  and  $W_{FL}$ .

Note that the Friedel sum rule - eq. (2.38) - connecting the phase shifts with the occupation number  $n_d$  in the quantum dot allows to re-express the conductance in the LM and FL fixed points in terms of  $n_d$ . In particular, the FL fixed point provides a functional relation for the ground-state conductance in terms of  $n_d$ , from which we can extrapolate  $\mathcal{G}_d$

to the limit  $T \rightarrow 0$ . Plugging eq. (2.38) into (4.84), we then can express the ground-state conductance as

$$\mathcal{G}_d(T \rightarrow 0) = \mathcal{G}_2 \sin^2 \left( \frac{\pi n_d}{2} + \varphi_\Gamma \right), \quad (4.85)$$

where the last term in the parenthesis accounts for an additional phase shift accounting for energetic dependencies of the hybridization function  $\Gamma(\epsilon) \neq \text{const}$ . For  $\Gamma(\epsilon) = \Gamma = \text{const}$ ,  $\varphi_\Gamma$  vanishes. On the contrary,  $\varphi_\Gamma$  is determined from the retarded impurity Green's function

$$\begin{aligned} G_d(\epsilon, T) &= \langle\langle c_d; c_d^\dagger \rangle\rangle_\epsilon \\ &= \frac{1}{\epsilon + i0^+ - V_G - \Sigma_d(\epsilon, T)}, \end{aligned} \quad (4.86)$$

where  $\Sigma_d(\epsilon, T)$  is the retarded self-energy of the quantum dot.

Following Ref. <sup>109</sup>, the additional phase shift  $\varphi_\Gamma$  is calculated as follows

$$\varphi_\Gamma = \text{Im} \int_{-\infty}^{\infty} \frac{\partial \Sigma_d^0(\epsilon, T=0)}{\partial \epsilon} G_d(\epsilon, T=0) d\epsilon. \quad (4.87)$$

Realizing that the single-particle description in the fixed points of the Anderson Hamiltonian is equivalent to the core idea in the Kohn-Sham formulation, we can ask if an integrated procedure combining the KS and the RG cycles would be able to describe the transport properties in nano devices. This idea is the inspiration for the hybrid procedure proposed in this work, which we will present in the next chapter.



## 5 THE KOHN-SHAM ANDERSON SYSTEM AND THE HYBRID SELF-CONSISTENT CALCULATION

The increasing complexity of nano-structured devices has required the development of new studies attempting to accurately describe their electronic and magnetic properties in the strong correlated regime. As correlations are highly affected by the electronic structure of materials, an adequate procedure is expected to combine precise band structure calculations with many-body tools for simulating interacting electrons.<sup>17,18</sup> While density functional theory undoubtedly fulfils the first requirement, the second part of the desired approach is still in progress. Recently, works combining ab-initio calculations with Dynamical Mean Field Theory (DMFT), such as LDA-DMFT, have achieved good performance in low dimensional devices and currently there are some implementations available.<sup>17,18,110</sup> Nonetheless, there is much work to be done on the problem of accounting for non-local effects and, also, out-of-equilibrium regimes. From this perspective, numerical algorithms based on the renormalization-group, which yield essentially exact solutions of various strongly correlated systems, offer an alternative route. Here, we propose an approach integrating density functional theory and the numerical renormalization-group technique for predicting transport in nano-structured devices. In this chapter, we will introduce our formulation and discuss its application to the problem of a single-electron transistor.

### 5.1 The non-interacting Kohn-Sham Anderson system

The problem of transport in a nano-structured devices illustrate the challenge in developing density functional approaches for strongly correlated systems.<sup>22</sup> As discussed in section 3.3, even in the elementary problem of a SET, for which the Anderson model allows to qualitatively describe the conductance in all thermal regimes (especially in the limit  $T \rightarrow 0$ , which is the one at the focus of DFT), the available approaches can encounter difficulties to reproduce situations commonly explored in experiments. Consider, for instance, the discussion on the asymmetry index in the paper "How sharply does the Anderson model depict a single-electron transistor".<sup>15</sup> In that work, we have discussed the deviation between results for the asymmetry index as a function of the gate voltage obtained from experimental data points and the NRG calculations upon the Anderson Hamiltonian. Importantly, our results have raised a question on the non-universality of properties in real devices, a characteristic that is exemplified in the disagreement between the measurements and the calculations for the asymmetry index - see Fig. 12. Recalling the example in which a potential  $W$  is applied to the leads of the SET, we have shown that the results for the ground-state conductance through the dot cannot be accurately reproduced from DFT calculations in which the approximations for the exchange-correlation functional

were calculated by two parametrizations based on Bethe Ansatz solutions of the Hubbard and the Anderson Hamiltonians. In practice, it would be difficult to extend such approaches to describe more general nano-structures in different transport regimes, which would be more complex than the zero bias conductance in a SET. In principle, the most acute limitation arises from requiring that the exact solution exists and analytical form can be obtained to construct the parametrization. The Bethe Ansatz, for instance, is limited to integrable model Hamiltonians and a solution yielding an analytical form is not always available.

In the face of these limitations, we can resort to an alternative approach offering a more flexible framework to simulate properties of quantum transistors, such as the numerical procedures based on the Renormalization-Group diagonalization of model Hamiltonians. Inspired by the correspondence between the fictitious Kohn-Sham system and the effective single-particle description arising in the fixed points of the RG flow, we propose a hybrid procedure, in which the exchange-correlation effects can be self-consistently corrected through the RG calculation. Exploring this idea in the context of the transport in quantum dots, the starting point of our approach is the Anderson model, which suits not only the problem of the single-electron transistor, but can also be used to describe other quantum dot devices. For instance, generalizations of the Anderson Hamiltonian are able to cover nano-structures comprising sets of coupled quantum dots (double, triple, etc), multi-band (multi-orbital) structures and also be used to study more complex regimes, such as transport away from zero bias. Based on the numerical diagonalization of the Anderson model for a quantum dot via the NRG method, the ingredients entering in the hybrid self consistent calculation hereby proposed are the band structure and the phase shifts in the fixed points of the RG flow. In the fixed points, properties can be accurately extracted from an effective single-particle Hamiltonian, which is the bridge we explore to interface the calculation for the correlated problem with the Kohn-Sham system. Importantly, at the fixed points, the phase shifts define a modified band, whose structure is determined by an effective scattering potential  $W^*$ , as discussed in chapter 4. Provided with a DFT module to calculate the band structure of the device, the NRG calculation enters as an extra step of the self-consistent cycle, correcting the calculation of properties by means of the phase shifts.

With these concepts in mind, we can describe in more detail our proposal of a hybrid DFT-NRG self-consistent calculation, which is associated with an effective fictitious problem that we will refer to as the *Kohn-Sham Anderson* (KSA) system. As mentioned above, the procedure here proposed is more general than other density functional approaches and can be applied to obtain realistic calculations in nano-structured devices. The hybrid calculation assumes the existence of two modules: a DFT module from which we can extract the electronic structure and model parameters of the device and an RG module implementing the numerical diagonalization of the model for the device.<sup>17,18,110,111</sup> The

RG module, which we propose to implement the NRG procedure, could comprise other RG techniques for strongly correlated systems, such as the Density Matrix Renormalization-Group and its formulation in the context of Tensor Networks (TN). Adapting the RG module to the TN formalism, such as Matrix Product States (MPS), Multi-Scale Entangled Renormalization Ansatz (MERA), Projected Entangled-Pair State (PEPS), one would be able to turn the procedure flexible to work with complex correlated nanostructures in higher dimensions.<sup>6, 101, 112</sup> To this aim, a careful investigation of the high temperature fixed point structure.

In the present thesis, we will concentrate on the problem of a single-electron transistor. Therefore, most of the steps described as follows will be contextualized for the case of the single impurity Anderson Hamiltonian. We therefore, propose to map the model  $H_{\text{SET}}$  for an interacting quantum dot by means of a non-interacting version of the Anderson Hamiltonian in the Kohn-Sham formulation, which we will denominate  $H_{\text{KSA}}$ . The interacting system has the general form

$$H_{\text{SET}} = H_{\text{leads}} + H_{\text{dot}} + H_{\text{coupling}}, \quad (5.1)$$

where each one of the terms retain details of the realistic device, such as band structure, hybridization function, levels and couplings.

In the case of a single-electron transistor, our Kohn-Sham Anderson formulation proposal aims to map the Hamiltonian in eq. (5.1) by the following model

$$H_{\text{KSA}} = \sum_k \epsilon_k c_k^\dagger c_k + H_d + \sum_k V_k^*(c_k^\dagger c_d + H.c.) + \sum_{k,q} W_{k,q} c_k^\dagger c_q, \quad (5.2)$$

where  $\epsilon_k$  and  $V_k$  are obtained from a density functional calculation accounting for the atomistic details of the leads and the hybridization of them with the quantum dot;  $H_d$  is the traditional Hamiltonian for the quantum dot, having the terms with the gate voltage  $V_G$  and the Coulomb repulsion  $U$ ; and  $W_{k,q}$  is the scattering potential accounting for the phase shifts in the LM fixed point.

We propose to solve the model in eq. (5.2) in a hybrid self-consistent calculation combining a DFT stage, followed by an NRG stage.

The self-consistent cycle starts with a DFT calculation to characterize the device. Through DFT calculations, we will obtain the band structure describing the electron gases of the metallic leads and the model parameters of the device. In a SET, this corresponds to obtaining the dispersion relation  $\epsilon_k$  and the parameters  $D$ ,  $\Gamma$ ,  $U$ , and the charging energy  $E_c$ , from which we can determine the set of gate voltages  $V_G$  that allow to turn the device “on” and “off” in the Coulomb blockade regime. While  $\epsilon_k$  and  $V_k$  are calculated in a single run of a DFT calculation, the potential  $W_{k,q}$  is calculated self-consistently in such a way that at each iteration a DFT calculation is followed by a NRG calculation, both stages are integrated to achieve the correct phase shift  $\delta_{LM}$ . The potentials  $W_{k,q}$  are

ultimately dependent on the Kohn-Sham potentials. To carry out an NRG calculation, the impurity Hamiltonian must be written in a renormalized form allowing for an iterative diagonalization. To this aim, the band structure  $\epsilon_k$  must be logarithmically discretized, and the Wannier orbital  $f_0$  calculated. In the context of the SET, this step corresponds to determining the diagonal  $\eta_n$  and co-diagonal  $t_n$  coefficients of the Hamiltonian  $\mathcal{H}_N$  in eq. (4.68). The diagonalization is carried out until the lowest thermal scale allowed for the band of the device is reached. Note that, in the traditional formulation of the Anderson Hamiltonian, whose band describes a continuous of states nearby the Fermi level, this scale corresponds to a given temperature of interest, as in eq. (4.11). Instead, in the case discussed in section 4.2.1.1 dealing with band structures characterized by a gap or a limited number of degrees of freedom, the maximum number of iterations of the NRG calculation will be determined by the scale  $\Delta$  defined by the energy (or gap) closer to the level  $\epsilon_F = 0$ . The results of the NRG calculation are used to obtain the phase shift  $\delta$  in the frozen level fixed point, which corresponds to the limit of the ground-state  $T \rightarrow 0$ . In the case of a SET with a band characterized by  $\Delta$ ,  $\delta$  will be calculated by extrapolating the NRG data to the limit  $T \rightarrow 0$  with help of the universal relation - eq. (2.43) - for the zero bias conductance. The phase shift  $\delta$  defines the scattering potential  $W$  modifying the conductance at the local moment fixed point. With the new value of  $W_{LM}$ , the exchange-correlation contributions to the leads at high temperatures are corrected, so the DFT calculation is performed in a subsequent run to account for this correction. In practice, repeating the DFT and NRG stages of the hybrid procedure can be interpreted as a self-consistent correction to the exchange-correlation potential at low-temperatures taking advantage of the fact that at high temperatures a DFT approach based on local functionals holds. With this idea and the previous , the self-consistent calculation aims to reach the convergence of the  $\delta$

The stages of the hybrid procedure for solving the KSA system can be itemized as follows:

1. DFT calculation of the band structure  $\epsilon_k$  of the material composing the metallic leads, the hybridization function  $\Gamma(\epsilon)$  and the scattering potential  $W_{LM}$  in the coupled leads entering the model for the quantum dot device;
2. Discretization of the conduction band  $\epsilon_k$  and Lanczos transformation to define the Wannier orbital  $f_0$  and the coefficients  $t_n$  and  $\eta_n$  entering the iterative form of the Hamiltonian;
3. Diagonalization of the model Hamiltonian via NRG and calculation of the conductance at the local moment and frozen level fixed point;

4. Extrapolation of LM and FL phase shifts  $\delta_{LM}$  ( $T \gg k_B T$ ) and  $\delta_{FL}$  ( $T \rightarrow 0$ ) by means of the universal mapping in eq. (2.43). From  $\delta_{FL}$ , the high-temperature fixed point  $\delta$  is obtained;
5. Correction of the scattering potential  $W_{LM}$  at the Local Moment fixed point shifted by  $\delta_{LM}$ ;
6. Repetition of all previous steps until  $\delta$  converges.

Figure 33 illustrates the stages of the hybrid self-consistent cycle.

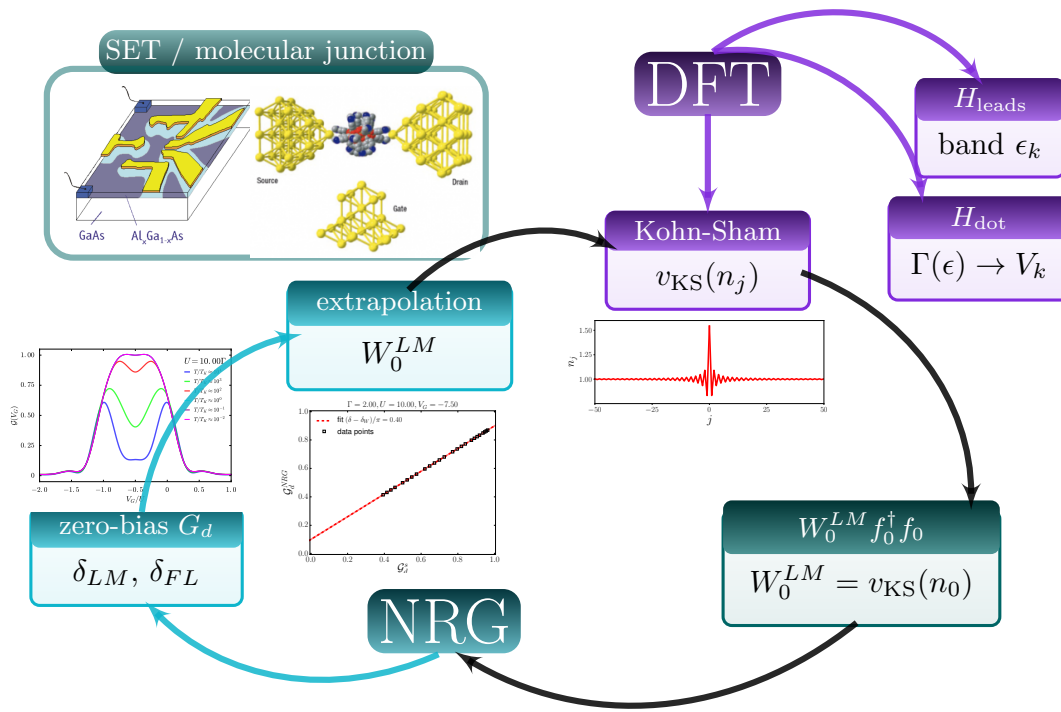


Figure 33 – Hybrid self-consistent calculation combining DFT and NRG calculations to solve the Kohn-Sham Anderson system. In the first steps, we perform ab initio calculations for the band structure of materials and then use the latter as an input for numerical renormalization-group calculations to predict properties, such as the phase shift  $\delta$  in the frozen level fixed point, which corresponds to the limit  $T \rightarrow 0$ . The phase shift  $\delta$  corrects the band structure in order to account for exchange-correlation effects arising in the strongly coupled regime. The corrected band yields the conduction band dispersion relation, which refines the Anderson Hamiltonian. NRG and the new phase shift is calculated. The procedure is repeated until  $\delta$  converges.

Source: By the author.

The computational cost of the hybrid self-consistent calculation depends essentially on the efficiency of the modules DFT (for the band structure) and RG (for the diagonalization of the model for the device). The NRG procedure diagonalized the Anderson Hamiltonian in a fraction of a minute on a standard desktop computer. With respect to the electronic calculation via a DFT package, the computational cost will depend on

various factors, including not only the complexity of the materials composing the device, but also, the efficiency of the package chosen, the basis set used in the calculation, the approximation for the exchange-correlation functional, the convergence criteria, etc.

For the purposes of the present thesis, we will discuss the efficiency of the cycle in the example of calculating the zero bias conductance in a single-electron transistor.

### 5.1.1 Applying the Kohn-Sham Anderson formulation for a single-electron transistor

In order to apply the hybrid KSA self-consistent procedure to the problem of a single-electron transistor, we propose to map the conduction band into a one-dimensional lattice described by a Hubbard-like Hamiltonian. Apart from its simplicity, this choice, which is popular in DMRG calculations for quantum dot devices, will allow us to explore the dependence of the conductance on the band structure of the device. This considered, the conduction electrons in the *source* and *drain* leads will be described by two sets of  $L$  sites connected through a special site  $c_0$ , which stands for the quantum dot. The generic form of the model Hamiltonian is

$$H = - \sum_{j=-L}^L \sum_{\sigma} t_j (c_{j,\sigma}^\dagger c_{j+1,s,\sigma} + H.c.) + \sum_{j=-N}^N U_j n_{j\uparrow} n_{j\downarrow} + \sum_{j=-L}^L V_j n_j, \quad (5.3)$$

where  $c_{j\sigma}^\dagger$  ( $c_{j\sigma}$ ) are the creation (annihilation) operators that creates (destructs) an electron with spin  $\sigma = \uparrow, \downarrow$  in the  $j$ -th site,  $n_{j\sigma} = c_{j\sigma}^\dagger c_{j\sigma}$  accounts for the occupation number in the  $i$ -th site,  $t_j$  ( $j = -L, L-1$ ) are the set of hopping amplitudes between first neighbor sites,  $U_j$  ( $j = -L, \dots, L$ ) is the on-site Coulomb repulsion and  $V_j$  ( $j = -L, \dots, L$ ) are the on-site external potentials.

Negative indexes  $i$  are associated with the electrons in the source  $S$ , while the positive indexes represent conduction electrons in the drain  $D$ . In a first approximation, we will be interested in the case of uniform conduction bands  $S, D$ , so we set  $t_j = t$  for all  $j \neq -1, 0$ , so that the hopping is uniform between neighbor sites, except the ones coupled to  $c_0$ . Similarly to the homogeneous one-dimensional Hubbard Hamiltonian, we can consider  $U_j = U_b$  for all  $j \neq 0$ . In the case we are interested, the external potential in the conduction bands  $V_j$  will have the same role as the scattering potential  $W$  in the Hamiltonian defined in eq. (2.19), so that we set  $V_j = W^*$  for the sites  $j = \pm 1$ . For the special dot site, we associate the hopping amplitude  $t_0$ , the Coulomb repulsion  $U_0$  and the external potential  $V_0$  to the model parameters of the Anderson Hamiltonian for a single electron transistor:  $t_0$  with  $\Gamma$ ,  $U_0$  with  $U$  and  $V_0$  with  $V_G$ . An illustration of the model is shown in Fig. 34.

With the previous considerations, the terms in the model of eq. (5.3) corresponding to the conduction bands  $S, R$  are re-written as the following Hamiltonian

$$H_{S,D} = -t \sum_{j=\pm L}^{\pm 2} (c_{j,\sigma}^\dagger c_{j+1,s,\sigma} + H.c.) + U_b \sum_{j=\pm L}^{\pm 1} n_{j\uparrow} n_{j\downarrow} + W^*(n_{-1} + n_{+1}). \quad (5.4)$$

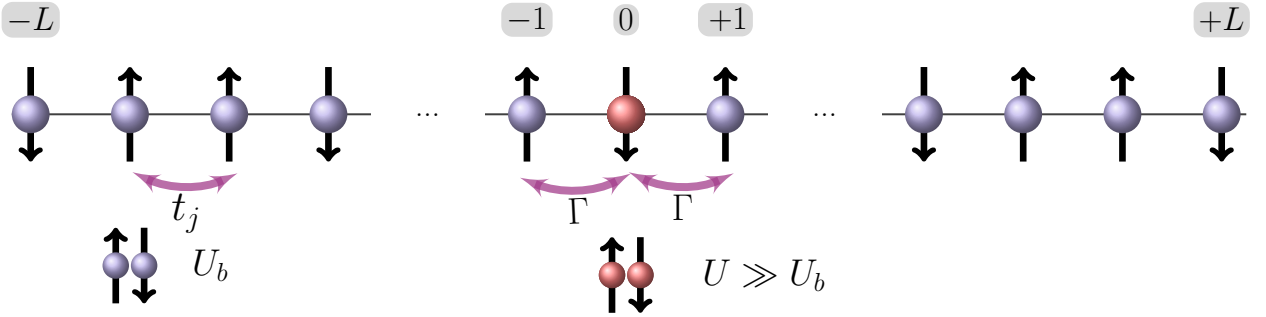


Figure 34 – Schematic representation of the mapping the Anderson Hamiltonian into a Hubbard-like model with inhomogeneous parameters: hopping  $t_j$ , on-site Coulomb repulsion  $U_j$  and on-site external potentials  $V_j$ . The conduction band for the source  $S$  and drain  $D$  leads is represented by two sets of  $L$  lattice sites. They are considered uniform with parameters  $t$  and  $U_b$ , as in the homogeneous one-dimensional Hubbard Hamiltonian. The site in the middle, labeled by the index  $j = 0$  stems for the impurity, with parameters  $U_0$  and  $V_0$ . The coupling to the leads is associated with the hopping coefficients  $t_{-1} = \Gamma$  and  $t_0 = \Gamma$ .

Source: By the author.

The bandwidth therefore will extend from approximately  $-2t$  to  $+2t$ . Explicitly,

$$2D = 4t \cos\left(\frac{\pi}{L+1}\right). \quad (5.5)$$

In the case we are interested in, the self-consistent diagonalization of the conduction band Hamiltonian in eq. (5.4) is the first step of the hybrid procedure. Note that the presence of Coulomb repulsion in the conduction bands is an important aspect to be considered in the ab-initio treatment given by the DFT module. As  $U_b \rightarrow 0$ , the electron gases become single-particle Hamiltonians equivalent to the Kohn-Sham Hamiltonian, there is then no need to perform a self-consistent Kohn-Sham calculation. For  $U_b \neq 0$ , the DFT stage of the calculation will require an approximation for the exchange-correlation potential. Here, we propose to resort to the BALDA parametrization for the exchange-correlation potential. We will be interested in the case  $U_b = 0$ , which is the limit in which we can compare our results for the zero bias conductance with those obtained in previous works, such as BALDA and Bergfield's parametrization.

At the end of the DFT stage to solve the conduction band, we obtain the dispersion relation  $\epsilon_k$  and the Kohn-Sham potentials  $v_{\text{KS}}(n_j)$ . The set of energies  $\epsilon_k$  will enter in traditional formulation for the Anderson impurity model in eq. (2.14). For the uniform half-filled band of (5.4) in the absence of scattering potential  $W^*$ , the coupling  $U_b$  will only shift the dispersion relation, as shown by figure 35. This can be easily understood: the electrons are uniformly distributed along the chain, so  $U_b$  only adds a positive contribution to the energy. The presence of coupling  $U_b \neq 0$  in the band introduces a contribution to  $v_{\text{KS}}$  due to exchange-correlation, which does not vanish for  $U_b \neq 0$ . In the case of a single-electron transistor modeled by the Hamiltonian in eq. (5.3), we define  $W_0^{LM} \equiv v_{\text{KS}}(n_{\pm 1})$ ,

as being the scattering potential in the Wannier orbital to be added to the first step of the Kohn-Sham Anderson cycle.

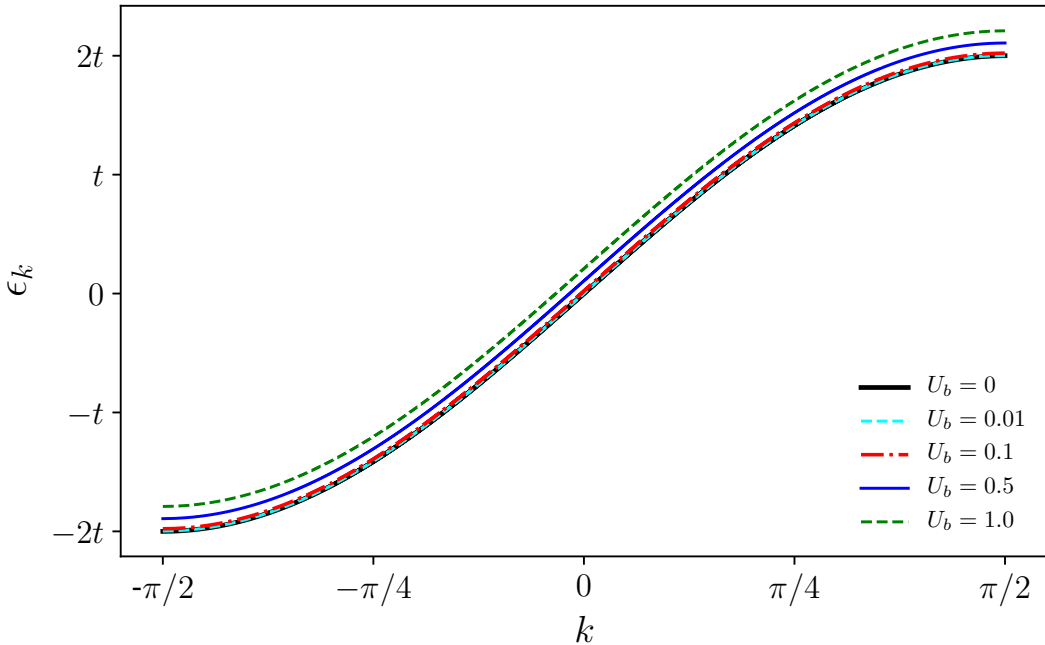


Figure 35 – Dispersion relation obtained in the DFT module implementing the self-consistent Kohn-Sham calculation to solve the band Hamiltonian in eq. (5.4) for  $L = 1000$  and  $U_b/t = 0, 0.01, 0.1, 0.5$  and  $1.0$  and no scattering potential  $W^* = 0$ . Note that the Coulomb repulsion  $U_b$  only shifts the Fermi level of the dispersion relation.

Source: By the author.

The DFT stage is followed by the logarithmic discretization of the band described by  $\epsilon_k$ . Note that in the case of a realistic device having a non-trivial hybridization function  $\Gamma(\epsilon)$ , the energy dependence might be accounted for the logarithmic discretization, as explained in section 4.2.1. In practice, this would not be necessary, however, because the energy dependence would only introduce irrelevant operators. In the case of interest, as  $\Gamma$  is constant and the number of conduction-band degrees of freedom is finite, we follow the approach for discrete bands explained in section 4.2.1.1, in which a support set of logarithmic points introduces the parameters  $\kappa$  and  $M$ . From the discretization, we will obtain the coefficients  $t_n$  and  $\eta_n$  and will use them in the NRG stage. In Fig. 36 we illustrate the profile of the Lanczos coefficients  $t_n$  and  $\eta_n$  as a function of  $n$  for the  $S, D$  bands with  $L = 1000$  sites, Coulomb repulsion  $U_b/t = 0.1$  and scattering potential  $W^*/t = -0.1$ ,  $\Lambda = 3.0$ ,  $M = 8$  and  $\kappa = 32$ . Note that the diagonal coefficients  $\eta_n$  vanish because the conduction band Hamiltonian possesses particle-hole symmetry and therefore the number of states above and below the Fermi level are the same.

The model parameters  $\Gamma, U$  and  $V_G$  and the scattering potential  $W_0^{LM}$  are inputs of the NRG calculation. For the band represented by the model in eq. (5.4), the NRG

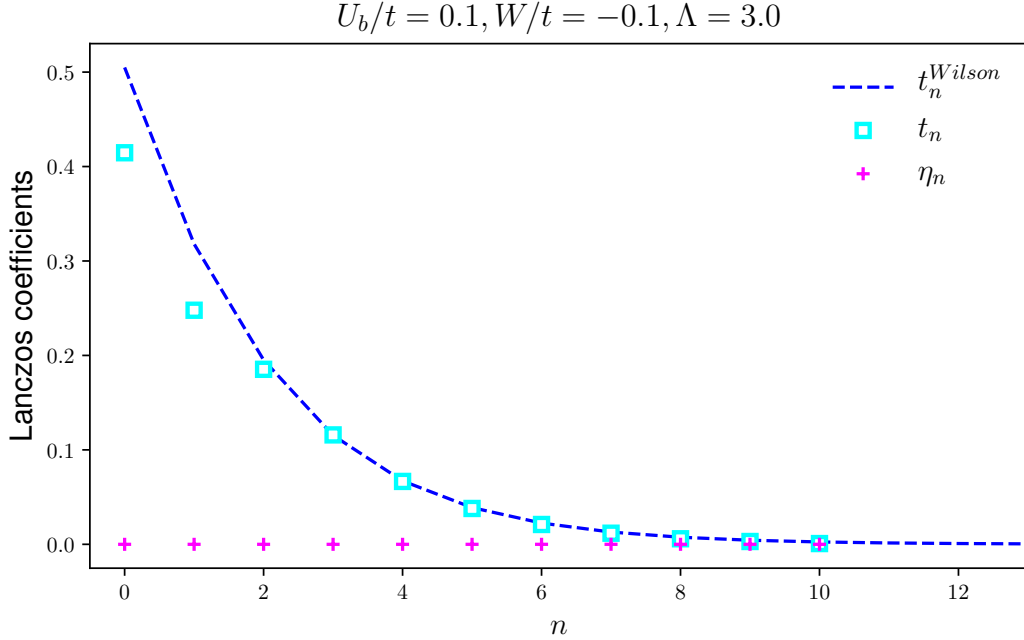


Figure 36 – Lanczos coefficients  $t_n$  (cyan empty squares) and  $\eta_n$  (magenta crosses) calculated for the band Hamiltonian in eq. (5.4) with  $L = 1000$ ,  $U_b/t = 0.1$  and  $W^*/t = -0.1$ . The discretization parameters are  $\Lambda = 3.0$ ,  $M = 8$  and  $\kappa = 32$ . The co-diagonal coefficients  $t_n^{\text{Wilson}}$  calculated by Wilson’s approach for a continuum of states (limit  $L \rightarrow \infty$ ) are plotted as a dashed blue line.

Source: By the author.

iterative diagonalization will run for up to a number of  $N$  iterations, where  $N$  will be determined by the scale  $\Delta$  in eq. (4.38).

The data for the SET conductance extracted from NRG calculations is then used as an input for the fitting to the universal conductance - eq. (2.43). The fitting will yield the Kondo temperature  $T_K$  and the phase shift  $\delta$ . In practice, to carry out the fitting, we can use a root finder algorithm to adjust the best parameters  $T_K$  and  $\delta_{FL}$ . For best, we mean that the correct values of  $T_K$  and  $\delta_{FL}$  fitting eq. (2.43) to the data points are those which produce the highest correlation coefficient  $\mathcal{C}$ . The latter measures how distant is the fit to the original data points and is defined as

$$\mathcal{C}^2 \equiv 1 - \frac{\sum_i (y_i - f_i)^2}{\sum_i (y_i - \bar{y})^2}, \quad (5.6)$$

where  $y_i$  denotes the data points, whose mean value is  $\bar{y}$ , and  $f_i$  are the data points calculated using the fitting function. Note that  $y_i$  correspond to the data points for  $\mathcal{G}_d$ .

In our implementation of the fitting routine, we have used the Newton method, which minimizes the residue  $\mathcal{R}$  over all  $n_T^{NRG}$  data points. The residue is calculated as

$$\mathcal{R} = \sum_{i=1}^{n_T^{NRG}} \left[ \left( \mathcal{G}_{d,i}^{\text{NRG}} - \frac{1}{2} \right) + \cos 2(\delta - \delta_W) \left( G_s^f \log \left( \frac{T_i^{\text{NRG}}}{T_K} \right) - \frac{1}{2} \right) \right]^2, \quad (5.7)$$

where  $\mathcal{G}_{d,i}^{\text{NRG}}$  and  $T_i^{\text{NRG}}$  are data points coming from NRG calculations,  $G_s^f$  is the universal function estimated for this set of NRG,  $\delta$  and  $T_K$  are the parameters we want to estimate.

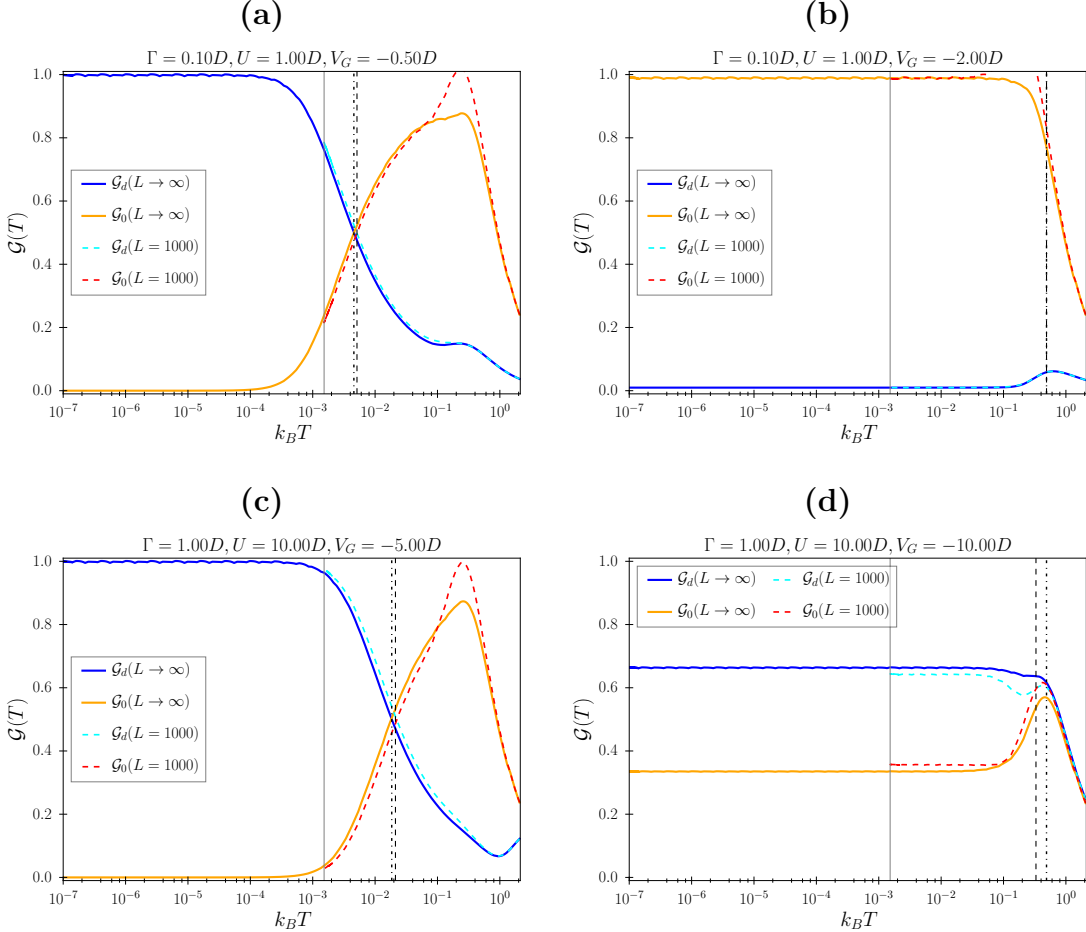


Figure 37 – Comparison of the conductances  $\mathcal{G}_d$  and  $\mathcal{G}_0$  as a function of the temperature  $T$  for  $L = 1000$  and  $L \rightarrow \infty$  and few model parameters: (a)  $\Gamma = 0.1D$ ,  $U = D$  and  $V_G = -0.5D$ , (b)  $\Gamma = 0.1D$ ,  $U = D$  and  $V_G = -2D$ , (c)  $\Gamma = D$ ,  $U = 10D$  and  $V_G = -5D$  (d)  $\Gamma = D$ ,  $U = 10D$  and  $V_G = -10D$ . The orange solid lines represent  $\mathcal{G}_d(L \rightarrow \infty)$  and the blue solid lines represent  $\mathcal{G}_0(L \rightarrow \infty)$ . Dashed red lines represent  $\mathcal{G}_d(L = 1000)$  and dashed cyan lines represent  $\mathcal{G}_0(L = 1000)$ . The vertical black lines mark the Kondo temperatures  $T_K(L \rightarrow \infty)$  (dashed) and  $T_K(L = 1000)$  (dot-dashed). The scale  $\Delta$  is marked as a vertical full black line and indicates the minimum thermal scale reached in NRG calculations for  $L = 1000$ .

Source: By the author.

The ratio between  $\Delta = \min T_i^{\text{NRG}}$  and the Kondo temperature  $T_K$  somewhat controls the accuracy of the universal fitting. If  $T_K \ll \min T_i^{\text{NRG}}$ , the available data points to be fitted will be mostly found in the LM fixed point, which is the regime suffering the most with discretization artifacts. The Kondo temperature  $T_K$  will be ultimately related to the coupling  $J$  discussed in chapter 2, where we have shown the connection between the Kondo and the Anderson model.

From the fitting, we then calculate the phase shift  $\delta_{LM}$  in LM fixed point, which is obtained extrapolating the fitting to the limit  $T \rightarrow \infty$ . We show an example of the fitting of the NRG data points  $[\mathcal{G}_{d,i}^{\text{NRG}}, T_i^{\text{NRG}}]$  to the universal curve  $G_s$  for  $L = 1000$ ,  $U_b = 0$ ,  $W = 0$ ,  $\Gamma = D$ ,  $U = 10D$  and  $V_G = -5D$  is shown in Fig. 38. From the fit, we obtain the Kondo temperature  $T_K$  and the extrapolated FL phase shift  $\delta_{FL}$  to the temperature  $T \rightarrow 0$ . Notice that the fitted data points are the same of dashed cyan lines in panel (c) of Fig. 37, for which the conductance at  $k_B T = \Delta$  does not reach the conductance quantum.

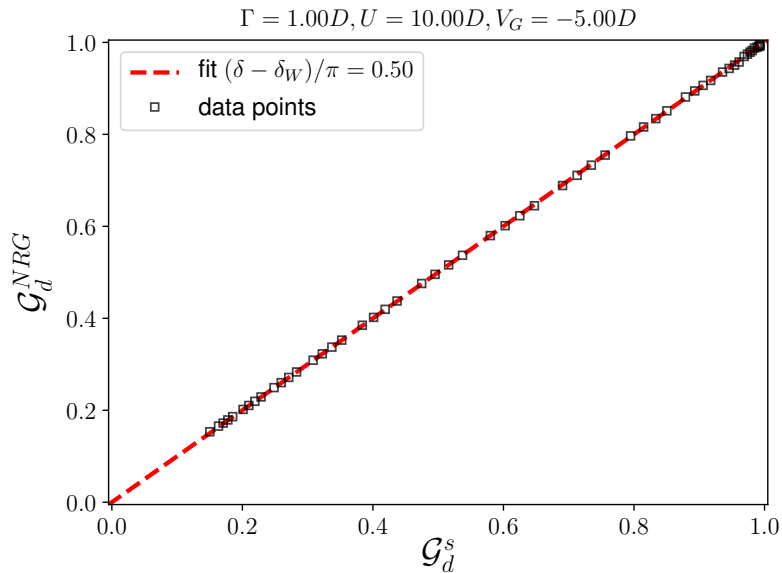


Figure 38 – Fitting of NRG data points to the universal map in eq. (2.43) adjusting the Kondo temperature  $T_K$  and the phase shift  $\delta$ . The black open squares depict the fitting of data points  $\mathcal{G}_d^{\text{NRG}}$  vs  $G_s$ . The fitted curve following eq. (2.43) is represented by the dashed red line. The FL phase shift  $\delta_{FL} = \pi/2$  is estimate as  $\pi/2$ , even though the minimum temperature reached by the NRG calculation lies orders of magnitude above  $\Delta$ . The unitary conductance at  $T \rightarrow 0$  depicts because the model has particle-hole symmetry. The Kondo temperature is calculated as  $T_K \approx 10^{-2}D$ .  
Source: By the author.

The FL phase shift is then used to obtain the scattering potential  $W^*$  to correct the band in the next iteration of the hybrid self-consistent calculation. To this aim, we simply correct the band by finding

$$W^{LM,*} = \tan^{-1} \left( \frac{\pi}{2} - \delta_{FL} \right), \quad (5.8)$$

or, extrapolating the curve to the limit of high temperatures, which corresponds to the point  $(\mathcal{G}_d, \mathcal{G}_s) = (0, 0)$  (bottom left corner) in Fig. 38.

The computation of  $W^*$  concludes an iteration of the hybrid calculation. The next iteration starts with the correction of the band structure of the conduction band Hamiltonian with the scattering potential  $W^*$ . We therefore, use the DFT module to solve

the Hamiltonian in eq. (5.4) with the new potential  $W^*$ . Note that, after the very first iteration, the new scattering potential  $W_{LM}$  to be added to the band in the sites  $j = \pm 1$  is not the same value of the potential  $W^*$  obtained from the NRG computation because this choice would introduce double counting. We denote  $W_{DFT,i}^{LM}$  the scattering potential obtained from the Kohn-Sham potential in the sites  $j = \pm 1$  after the DFT stage in the  $i$ -th iteration of the hybrid cycle and  $W_{NRG,i}^{LM}$  the scattering potential obtained from the extrapolation of the universal fitting after the NRG calculation of the conductance in the  $i$ -th iteration of the hybrid cycle. We therefore save the Kohn-Sham potential  $v_{KS}$  (or,  $W_{DFT,i}^{LM}$ ) obtained in the previous iteration  $i - 1$  and split the contributions due to exchange and Hartree potentials and use as the input of the new DFT stage in the new iteration  $i$  the value  $W_{DFT,i}^{LM} = W_{NRG,i-1}^{LM} - W_{DFT,i-1}^{LM}$ .

All the previously explained steps are carried out again and a new scattering potential  $W^{* \prime}$  is obtained. The full cycle (DFT band calculation, logarithmic discretization, NRG diagonalization, universal fitting) is repeated until we reach the convergence condition

$$|W^* - W^{* \prime}| \leq w \quad (5.9)$$

where  $w$  is a small number.

We will present the results of the hybrid KSA cycle applied to the single-electron transistor in the next chapter.

## 6 RESULTS

In this chapter, we are going to present the results of the self-consistent *Kohn-Sham Anderson* procedure introduced in the previous chapter in the case of a single-electron transistor.

We will briefly discuss the relation between different coupling regimes in a single electron transistor and the formation of the Kondo screening cloud. We review some results of the thermal dependence of the conductance  $\mathcal{G}_d$  in a SET obtained from a Numerical Renormalization-Group calculation and compare the behavior of  $\mathcal{G}_d$  in the continuum limit of band states (traditional formulation for the conduction band of the Anderson Hamiltonian) with the case in which the band is represented by a finite degrees of freedom.

Finally, we will compare NRG results for the ground-state conductance  $\mathcal{G}_d (T \rightarrow 0)$  in a SET with the hybrid procedure proposed in the present thesis. Specifically, we will analyze the accuracy of those different approaches to describe transport in different coupling regimes. Additionally to the physical discussion, we will also comment on the efficiency of the new method in terms of convergence rate and accuracy.

### 6.1 Coupling regimes and the Kondo screening cloud in a single-electron transistor

In chapter 2, we have presented a detailed analysis of the Kondo effect in a single-electron transistor and have also introduced the concept of the Kondo screening cloud. We have discussed that an estimate for the radius  $\xi_K$  of the Kondo cloud is inversely proportional to the Kondo temperature, the latter being calculated from the coupling  $J$  arising in the Kondo regime. In a SET, we can estimate  $T_K$  as follows

$$T_K = \begin{cases} e^{-1/\rho J} & \min(U, |V_G|) < D \\ V_G \sqrt{\rho J} e^{-1/\rho J} & \min(U, |V_G|) \geq D, \end{cases} \quad (6.1)$$

where  $\rho$  is the density of the conduction band ( $\rho = 1/2D$  if the system is at half-filling) and the coupling  $J$  as

$$J = \frac{2\Gamma}{\pi} \frac{U}{|V_G|(V_G + U)}. \quad (6.2)$$

The ratio  $U/\Gamma$  defines  $J$ , which therefore determines the coupling regimes in a single-electron transistor and ultimately define the Kondo temperature  $T_K$  and the radius  $\xi_K$  of the Kondo screening cloud. In Fig. 39 we present a pictorial view of the Kondo screening cloud in a SET for different ratios  $U/\Gamma$ :  $U \approx \Gamma$  (weakly coupling regime),  $U = 10\Gamma$  (intermediate coupling regime) and  $U = 100\Gamma$  (strongly correlated regime). In all regimes, we can investigate the relation between the size of the Kondo cloud  $\xi_K$  and the transport

behavior in the SET as a function of the temperature. In order to examine the connection between coupling regimes,  $\xi_K$  and their influence in transport properties of a SET, we carry out NRG calculations considering the three coupling regimes defined above. In Fig. 40 we show our NRG results for the zero bias conductance  $\mathcal{G}_d$  as a function of the gate voltage  $V_G$  and its dependence on the temperature, in units of  $D/k_B$ . The hybridization was set as  $\Gamma = 0.01D$ . We associate different thermal scales with a color bar in which high temperatures ( $k_B T \approx D$ ) are plotted in yellow, orange and red tones and low temperatures ( $k_B T \ll T_K$ ) are represented by purple and black tones. The limit  $T \rightarrow 0$  from which we can extract the ground-state conductance  $\mathcal{G}_d(T \rightarrow 0)$  is identified inspecting black contour lines. The temperature in the scale of the color-bar is given in units of the band width  $D$  and the conductance  $\mathcal{G}_d$  is given in units of  $\mathcal{G}_2$ .

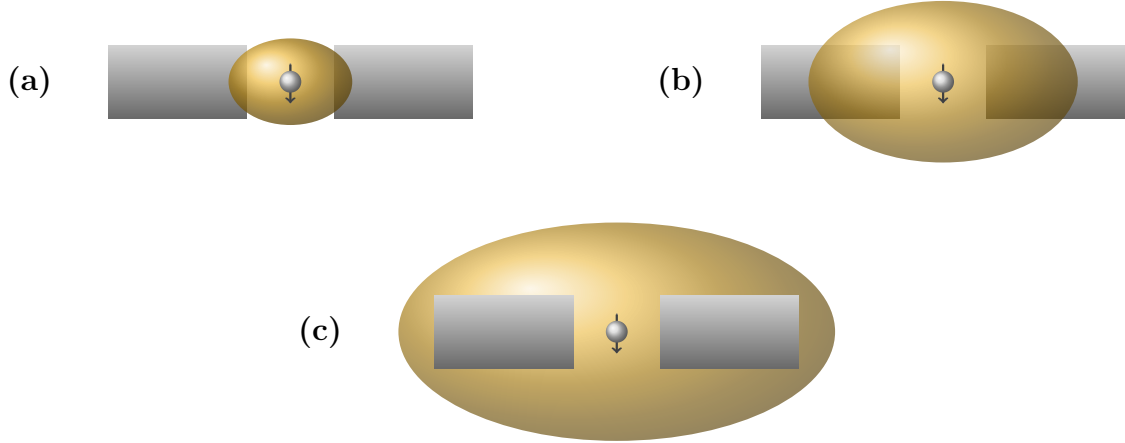


Figure 39 – Kondo screening cloud in a single-electron transistor from the weakly to the strongly coupled regimes. The ratio  $U/\Gamma$  determines the Kondo temperature  $T_K$  and the radius  $\xi_K \propto T_K^{-1}$  of the Kondo screening cloud. (a) For  $U \leq \Gamma$ , the cloud is so small that it extends over a small fraction of the source and drain leads, including solely the  $f_0$  orbital. There is no Kondo effect. (b) As the Coulomb interaction  $U$  grows relative to the dot-level width  $\Gamma$ , the Kondo cloud starts to increase and extends over the leads to form an entangled state with the dot. For sufficiently small temperatures, the Kondo effect arises and generates the Kondo plateau in the plot of the conductance  $\mathcal{G}_d$  as a function of the applied gate voltage  $V_G$ . (c) In the strong interaction regime  $U \gg 10\Gamma$ , the Kondo temperature is very low  $T_K \ll D$ , so that the radius  $\xi_K$  covers the entire device and would, in principle, overpass the boundaries of the experimental setup. Achieving such a small temperature is experimentally unpractical.

Source: By the author.

For  $U \leq \Gamma$ , panel (a) of Fig. 39, the Kondo temperature is high compared to the scale  $k_B/D$ : for such a high Kondo temperature, the Kondo screening cloud is very small compared to the scales of the device, and as illustrated in panel (a) of Fig. 39, we observe that the extension of the cloud is so small that it reaches a small region of the leads of the SET. The RG flow in a SET for such a high temperature does not follow the universal behavior, so that the connection between the LM and the FL fixed points

is not characterized by the crossover typical of the Kondo regime. This behavior can be observed inspecting the thermal dependence of  $\mathcal{G}_d$  for  $U = \Gamma$ , shown in panel **(a)** of Fig. 40. Following the color scale from high (yellow) to low (black), we can observe that, at the symmetric point, the conductance rises from zero to the conductance quantum as  $T$  drops from  $D/k_B$  to  $D/100k_B$ . For  $k_B T/D < 10^{-1}$ , the conductance keeps the same value for all gate voltages. Note that there is no Kondo plateau in the limit  $T \rightarrow 0$  (black lines): the conductance does not vanish at the charge degeneracy points  $V_G = -2U$  and  $V_G = U$ . The mode of the operability of the device is neither in the Coulomb blockade nor in the Kondo regime. The impurity forms an amalgam with the conduction band and the device behaves as a quantum wire.

Increasing the Coulomb interaction by one order of magnitude to  $U = 10\Gamma$  reduces the Kondo temperature  $T_K$ . As a consequence,  $\xi_K$  increases over the metallic electrons of the source and the drain leads, as represented in panel **(b)** of Fig. 39. In this regime, the singlet state between the lead electrons and the quantum dot forms at temperatures  $T \ll T_K$ . In the corresponding curve  $\mathcal{G}_d$  vs  $V_G$  in panel **(b)** of Fig. 40, the conductance reaches the conductance quantum in the temperature range  $10^{-4} < k_B T/D < 10^{-3}$ . As the temperature drops, the RG flow drives the SET from the LM to the FL fixed point. The crossover, which progressively screens the dot moment, starts at temperatures of order  $k_B T/D < 10^{-1}$ . In particular, in the window of gate voltages  $-U < V_G < 0$ ,  $\mathcal{G}_d$  increases from  $\mathcal{G}_d \approx 0.1$  at  $k_B T \approx D$  to  $\mathcal{G}_d \approx 1.0$  at  $k_B T/D \approx 10^{-3}$ . The FL fixed point corresponds to the purple temperatures, below which the Kondo plateau becomes invariant under cooling. At high temperatures (yellow tones) the curve  $\mathcal{G}_d$  vs  $V_G$  shows peaks characteristic of Coulomb blockade behavior, similar to that of Fig. 5. In the limit of very small temperatures ( $T \rightarrow 0$ ), shown in black tones, the Kondo plateau is the signature of the Kondo effect at temperatures  $k_B T/D < 10^{-4}$ . Experiments can come close to satisfying this condition.

Additional increase in  $U$  by one order, i.e.,  $U = 100\Gamma$ , puts the device in the extreme of strong repulsion. The Kondo temperature is very small compared to the thermal scale  $D/k_B$ . The Kondo screening cloud, illustrated in panel **(c)** of Fig. 39 is so large that it covers the entire device. Experimentally, as the device were cooled, one would expect to detect interference effects in transport measurements before the Kondo temperature could be reached. The experimental results of Grobis et al. do show oscillations of very small amplitude, for  $T \approx T_K$  an indication that the experiment came close to this limit, i.e., that  $\hbar v_F/k_B T$  became comparable to the lead size.<sup>1,15</sup> The distinctive feature of a very large Coulomb repulsion is the thermal scale below which the plateau starts to form. As shown in panel **(c)** of Fig. 40, the Kondo plateau emerges only at  $k_B T/D < 10^{-18}$ . At relevant temperatures, several orders of magnitude below the lowest temperature of physical relevance  $\Delta/k_B$ , the device is in the Coulomb Blockade regime. This is, of course,

expected, since the conductance only rises as the temperature becomes comparable to  $T_K$ , which is extremely small for  $U \gg \Gamma$ .

The previous analysis is instructive for understanding the effects of the coupling regimes in the transport properties of a single-electron transistor. Importantly, the results obtained in the intermediate coupling regime of the Anderson Hamiltonian represent the situation of experimental interest in a physical SET. Compare, for instance, panels **(b)** in Figs. 9 and 40. As we argued in this thesis, the Anderson Hamiltonian provides an accurate platform to study a SET and serves as a starting point to understand more realistic descriptions of the device. We have also discussed how DFT can help us to characterize their properties, nonetheless, having difficulty in describing their properties in the strongly correlated regime due to the challenge in accounting for non-local many-body effects. In the context of transport in a SET, in the limit of zero bias, we have presented two examples of situations in which the conductance in the quantum dot can be affected by the leads: the presence of a potential  $W$  and a structured conduction band.

### 6.1.1 Conductance in the continuum limit of conduction states vs bands with finite number of degrees of freedom

A change in the conduction band can be implemented by constraining the number of degrees of freedom the metallic electrons can have. In section 4.2.1.1, we discussed that the finite number of allowed momenta  $k$  introduces a minimum energetic scale  $\Delta$ . We can now carry out the same analysis we have made before for the traditional band of the Anderson Hamiltonian (a continuum of states with equal a linear dispersion relation, so that  $\rho = 1$  with energies in the interval  $[-D, D]$ , as illustrated in the inset of Fig. 22) and compare the results for the zero bias conductance in the case of a system with finite size, such as described in sec. 5.1.1, where we have defined the conduction band Hamiltonian in eq. (5.4).

Figure 41 shows the curves of  $\mathcal{G}_d$  as a function of  $V_G$  from high temperatures to  $T_\Delta$  considering the same coupling regimes analysed before, i.e., weak, intermediate and strongly Coulomb interaction. The model parameters for the conduction band in eq. (5.4) are  $L = 1000$ ,  $U_b = 0$  and  $W_{\pm 1} = 0$ . The discretization parameters are  $\Lambda = 3.0$ ,  $\kappa = 32$  and  $M = 8$ , resulting in a total of 11 NRG iterations to reach  $k_B T_\Delta / D \approx 10^{-3}$ . The color scheme for temperatures is normalized differently from the plots of Fig. 40: purple to black tones correspond to temperatures  $T \rightarrow T_\Delta$ . Comparing panels **(a)** to **(c)** of Figs. 40 and 41, we observe a change in the conductance as the coupling is increased. While the case  $U/\Gamma = 1$  both panels **(a)** agree in the limits  $T \rightarrow 0$  and  $T \rightarrow T_\Delta$ , the same is not true for  $U \geq 10\Gamma$ . For  $U = 10\Gamma$ , the Kondo cloud covers the entire leads, and the dot moment cannot be fully screened. In another words, below  $T_\Delta$ , the gap in energy would result in a insulating state of the band, so the conductance would decrease until it vanishes at  $T \rightarrow 0$ .

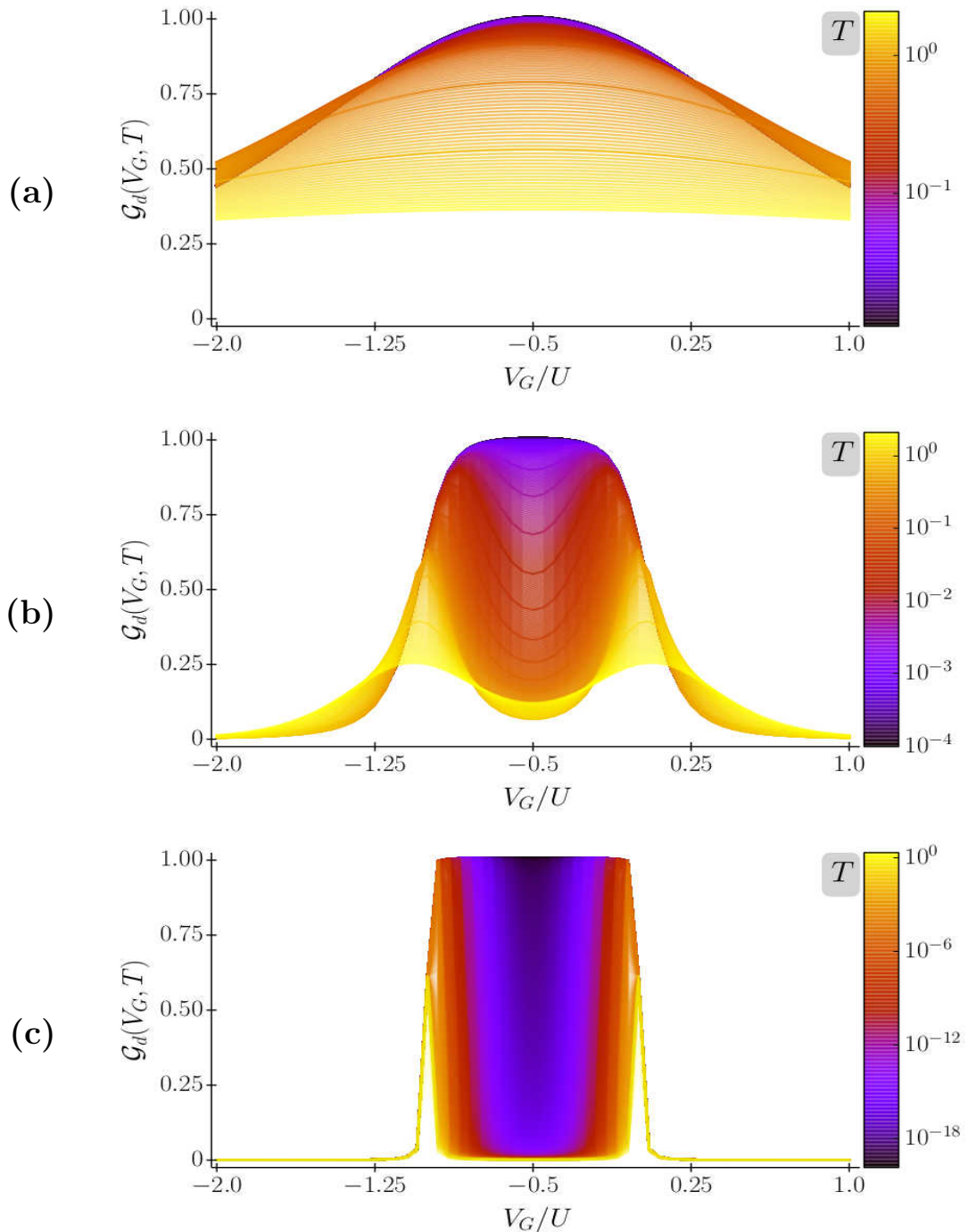


Figure 40 – Conductance  $\mathcal{G}_d$  in a SET as a function of the gate voltage  $V_G$  and its thermal dependence in different coupling regimes. These results were extracted from the NRG diagonalization of the Anderson Hamiltonian using  $\Lambda = 3$ ,  $E_{UV} = 30$ , and  $E_{min} < 10^{-2}T_K$  for  $-2U < V_G < U$  and  $U = \Gamma$  (a),  $U = 10\Gamma$  (b) and  $U = 100\Gamma$  (c). The temperature mapping goes from hottest temperatures in yellow to the coldest in purple. Performing the calculation up to  $N \approx 40$  iterations, which corresponds to temperatures of order of  $k_B T \approx 10^{-10}D$ , the Kondo temperature is not reached in the strongly coupling regime, so the observation of the Kondo plateau requires more calculations.

Source: By the author.

For  $U = 100\Gamma$ , the device behaves as in the Coulomb blockade mode at  $T = T_\Delta$  and there is no Kondo effect.

The results discussed above and obtained from NRG calculations are essentially exact and therefore can serve as the “gold standard” to test other approaches based on a different formalism, such as density functional theory. Specifically, in the problem of transport through quantum dots, we have discussed the limitations that DFT approaches can have and that was the motivation for the work developed in the present thesis. Here, we have proposed a new approach combining density functional and renormalization-group calculations - the Kohn Sham Anderson (KSA) self-consistent procedure - and explored its application to the problem of transport in nano-structures in chapter 5. With the previous analysis of the correlation regimes in a SET within the NRG approach, we can now examine the accuracy of the proposed procedure.

## 6.2 Ground-state conductance from the Kohn-Sham Anderson hybrid procedure

In chapter 3, we have discussed the limitations of DFT for strongly correlated systems and we have presented two density functional approximations for the exchange correlation functional based on the exact Bethe Ansatz solution of two systems that present strong interactions. Specifically, we presented the BALDA approximation for the Hubbard model and the parametrization for the Anderson Hamiltonian due to Bergfield et al. We will refer to results obtained via the parametrization obtained by Bergfield et al. by the acronym BLBS. In the strong-repulsion regime, the exchange-correlation functional is poorly represented by local density approximations. By contrast, for weak interactions, neglecting  $E_{xc}$  altogether may produce relatively small deviations. For this reason, besides the BALDA and the BLBS, we are going to consider the Hartree-Fock approximation, for which the correlation term in  $v_{xc}$  vanishes. A comparison with HF will be illustrative to analyze the role of the exchange correlation potential in each one of the correlation regimes under our investigation.

The results we have obtained self-consistently with the BALDA, BLBS and HF approaches were carried out in a lattice-DFT approach: the calculations consider a lattice with  $2L + 1 = 2001$  sites with the corresponding parameters of the model Hamiltonian in eq. (5.3). In practice, we have implemented the discrete version of Kohn-Sham calculation described in section 3.1.2 and illustrated by Fig. 14. We have considered that the calculation had converged only when the difference between densities in consecutive iterations is  $|n_j^k - n_j^{k-1}| < 10^{-6}$  for all lattice sites  $j = 0, \dots, 2L$ . To obtain the ground-state conductance  $\mathcal{G}_d(T \rightarrow 0)$  as a function of the applied gate voltage  $V_G$ , we solved the system in the KS cycle for fixed  $U, \Gamma$  and  $V_G$  and then plugged the converged density  $n_0 = n_d$  into the eq. 4.85.

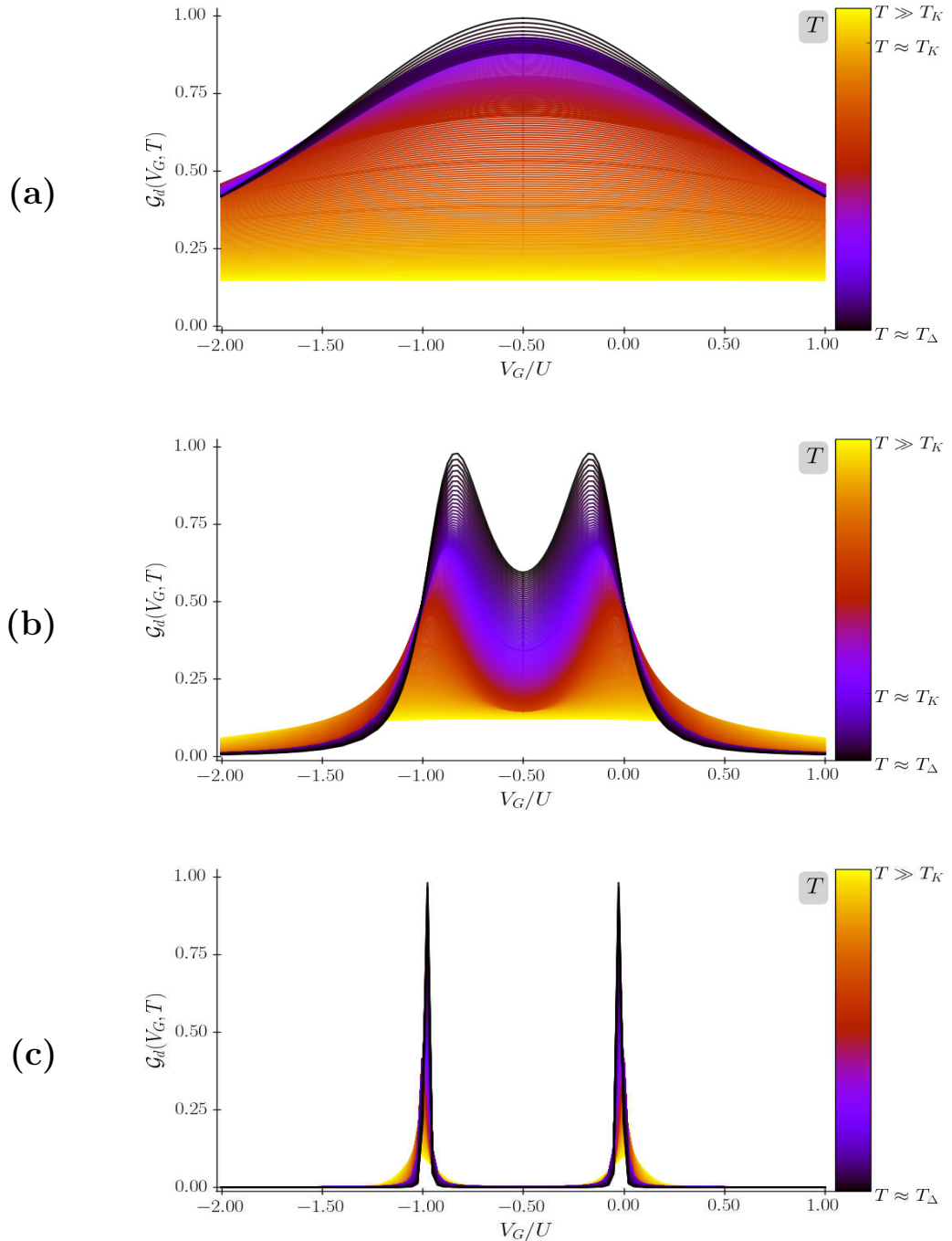


Figure 41 – Conductance  $\mathcal{G}_d$  in a SET with a conduction band with finite momenta as a function of the gate voltage  $V_G$  and its thermal dependence in different coupling regimes. These results were extracted from the NRG diagonalization of the Anderson Hamiltonian with  $L = 1000$ , using the logarithmic discretization for finite bands with parameters  $\Lambda = 3$ ,  $\kappa = 32$  and  $M = 8$ . The ultraviolet truncation is chosen as  $E_{UV} = 30$ . The ratio  $U/\Gamma$  goes from weakly to strong coupling regimes:  $U = \Gamma$  (a),  $U = 10\Gamma$  (b) and  $U = 100\Gamma$  (c). For all coupling regimes, the minimum thermal scale is of order of  $k_B T = 2tL^{-1} \approx 10^{-3}D$ . We have marked  $T \gg T_K$ ,  $T \approx T_K$  and  $T_\Delta$  next to the color-code column.

Source: By the author.

In the case of the calculations implementing the new hybrid method KSA, we considered the convergence criterion as being the difference between the scattering potential  $W_{LM}$  associated with the local moment fixed point obtained in two consecutive hybrid iterations. We refer to hybrid iteration  $k$  to the  $k$ -th step of the calculation in which we run both the DFT and NRG modules, using the results for the band structure obtained in the DFT module as input to the NRG calculations which couples the bands to a quantum dot and calculate the conductance in the fixed points to obtain the phase shift  $\delta$  and the corresponding scattering potential  $W$ . The convergence threshold was  $\delta\%W = |W^k - W^{k-1}|/|W^k| < 0.1\%$ .

With the previous observations, we can now move to the results obtained with the KSA procedure. We start examining the results for the zero bias conductance in a SET for which the bands of the source and drain leads are uniform, free of external potentials and comprise  $L = 1000$  momenta states each. This is the case in which the parameters of the conduction band in eq. (5.4) are  $U_b = 0$  and  $W = 0$ . Again, we examine the curve  $\mathcal{G}_d$  vs  $V_G$  considering three correlation regimes: weak, intermediate and strong. Our results are shown in Fig. 42. The results obtained with the NRG calculations are plotted as black dashed lines and the KSA calculations are represented in cyan by dot-dashed lines and empty diamonds. The results for the BLBS are plotted as full red lines, the HF as blue dashed lines and crosses, and the BALDA is represented by dot-dashed green lines and empty circles.

As in the NRG results shown previously - see Fig. 40 - we set the hybridization as  $\Gamma = 0.01D$ .  $\Gamma$  and the corresponding ratio  $U/\Gamma$  in comparison with the bandwidth  $D$  enter as important parameters for the self-consistent calculations. For  $U > D$ , it would be difficult to achieve convergence in the self-consistent BALDA calculations due to the discontinuity of the exchange-correlation potential  $v_{xc}[n]$  near half-filling. Also, the BLBS approach has limitations, because the Bethe Ansatz solution of the Anderson Hamiltonian assumes that all other model parameters are much smaller than the bandwidth  $D$  and is only valid in the Kondo regime. Additionally, comparing the BALDA functional - Fig. 15 - we see the discontinuity increasing rapidly for  $U > t$  or  $U > \Gamma$ .

In the weakly correlated regime  $U = \Gamma$ , panel (a) of Fig. 42, we observe good agreement between the exact KSA results, the approximations (BALDA, BLBS and HF) and the conductance obtained with the NRG procedure. Note that the highest deviations occur in the charge degeneracy points  $V_G = -2U$  and  $V_G = U$ . The curves for the self-consistent calculations (BALDA, BLBS and HF) match almost exactly and present almost imperceptible deviations from NRG results. The deviations of the KSA results in the two charge degeneracy points are higher (around 0.06%) than those observed for the DFT approximations (less than 0.02%). The good agreement between the HF and the exact calculations allows us to conclude that the corrections due to correlation effects can be

disregarded in the weakly correlated regime. These results understood, we can now move to more interesting regimes.

Correlation regimes allowing for the Kondo effect in a SET are more attractive to examine the performance of the new hybrid procedure against DFT approaches based on a parametrization. As mentioned, as the ratio  $U/\Gamma$  increases, the conductance in a SET generates the Kondo plateau in the window of gate voltages  $-U < V_G < 0$ . In panel **(b)** of Fig. 42 we present the results of all approaches considered for  $U = 10\Gamma$ . Note that the BALDA approximation, which previously presented good results in the weakly correlated regime, misses completely the Kondo plateau. Specifically, at the symmetry point  $V_G = -U/2$ , instead of converging to the quantum of conductance, the conductance obtained with the BALDA almost vanishes. Although the difference between the BLBS and the NRG curves is almost indistinguishable for  $U = \Gamma$  - panel **(a)** of Fig. 42-, deviations start to show for  $U = 10\Gamma$  when the conductance start to increase from nearly zero at the points  $V_G = -1.25U$  (or  $V_G = 0.25U$ ). Note that the BALDA and the BLBS curves follow the same trend for  $V_G < -U$  and  $V_G > 0$  and both deviate around 20% from KSA calculations. For all range of gate voltages considered  $-2U < V_G < U$ , the BLBS approach present a qualitative good agreement. The HF curve performs badly in reproducing the Kondo plateau. The many-body interactions responsible for the manifestation of the Kondo effect become important and dominate the ground-state of the SET, so that neglecting the corrections due to the correlation potential, as in HF, is a poor approximation. Following the black solid lines representing NRG exact calculations, for the whole range of gate voltages, we observe an excellent agreement with cyan curve depicting the results for the KSA procedure. The correction of the phase shift  $\delta_{LM}$  in the high-temperature fixed point from the extrapolation of the limit  $\delta_{LM} = \pi/2 - \delta(T \rightarrow 0)$  is able to capture the low-temperature physics of the SET.

In the extreme correlation regime,  $U = 100\Gamma$ , the Kondo cloud extends over the entire device, but is insufficient to screen the dot moment at very low temperatures. In panel **(c)** of Fig. 42, the flat Kondo plateau emerges in the NRG, the BLBS and the KSA curves. The HF and the BALDA curves present enhanced deviations from the KSA results for  $-U < V_G < 0$ . HF though gives the correct result at the symmetric point  $V_G = -U/2$ . BALDA, on the contrary, misses completely the Kondo plateau and the result for the ground-state conductance is equivalent to that of a SET at the LM fixed point (i.e., at high temperatures). The conductance profile mimics a Coulomb blockade. Results for the BLBS and KSA are indistinguishable from the exact calculations. In particular, the good performance of the KSA procedure shows that the extrapolation of the universal curve yields accurate phase shifts even when the conduction level spacing is much larger than the Kondo energy scale.

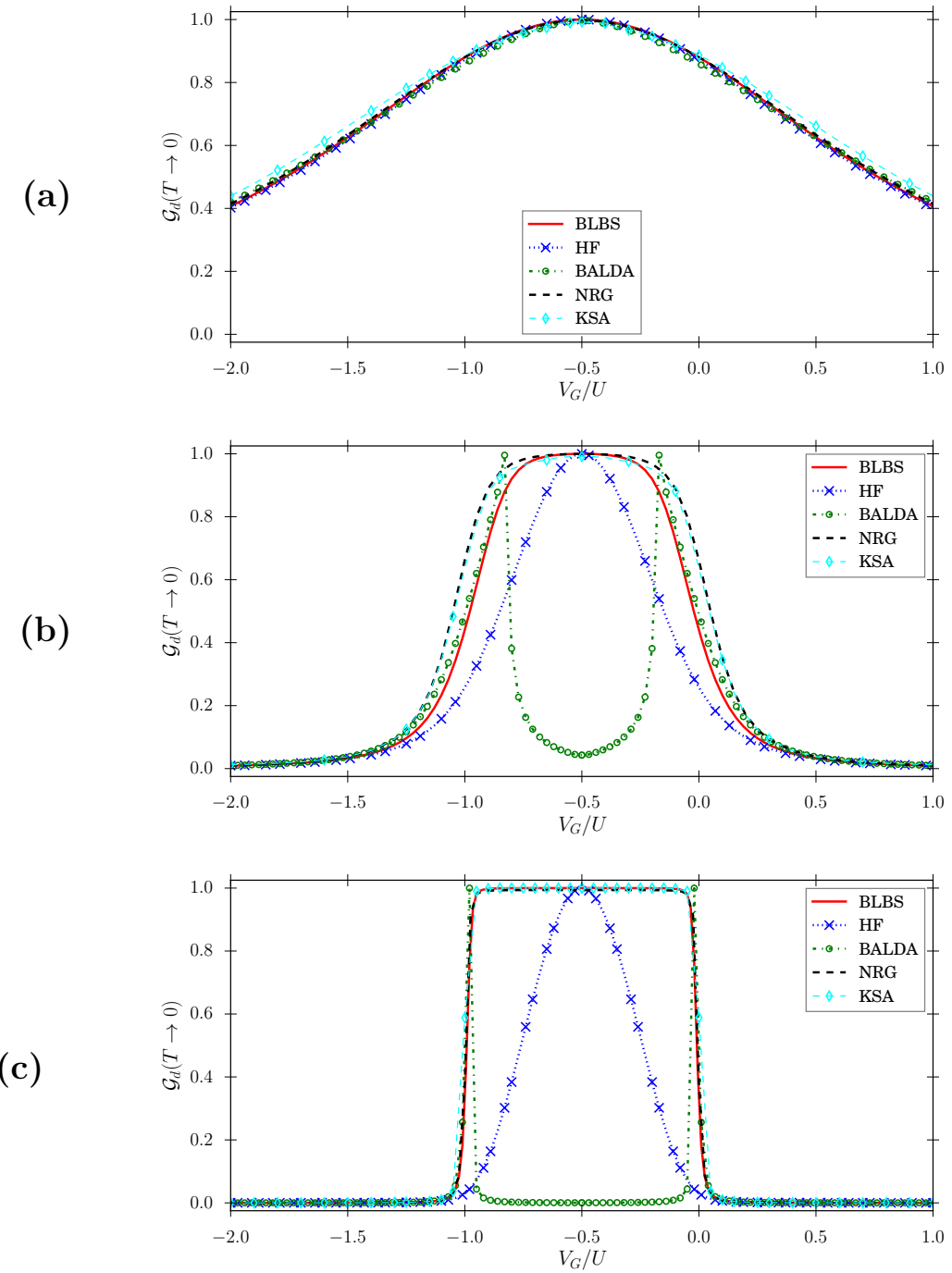


Figure 42 – Results for the ground-state conductance  $\mathcal{G}_d(T \rightarrow 0)$  as a function of the gate voltage  $V_G$  obtained with different approaches from the weakly to the strong correlated regime: (a)  $U = \Gamma$ , (b)  $U = 10\Gamma$  e (c)  $U = 100\Gamma$ . Black dashed curves represent the exact calculations obtained through the NRG, taking the limit  $\mathcal{G}_d(T \rightarrow 0)$  in the low-temperature fixed point. The conductance obtained from self-consistent calculations based on the Hartree-Fock method and the KS-DFT approach are shown as (HF) dot dashed blue lines and crosses, (BLBS) full red lines, and (BALDA) green dashed lines and empty circles. The curve obtained with the KSA procedure present the best correspondence with the results in the presence of the Kondo effect.

Source: By the author.

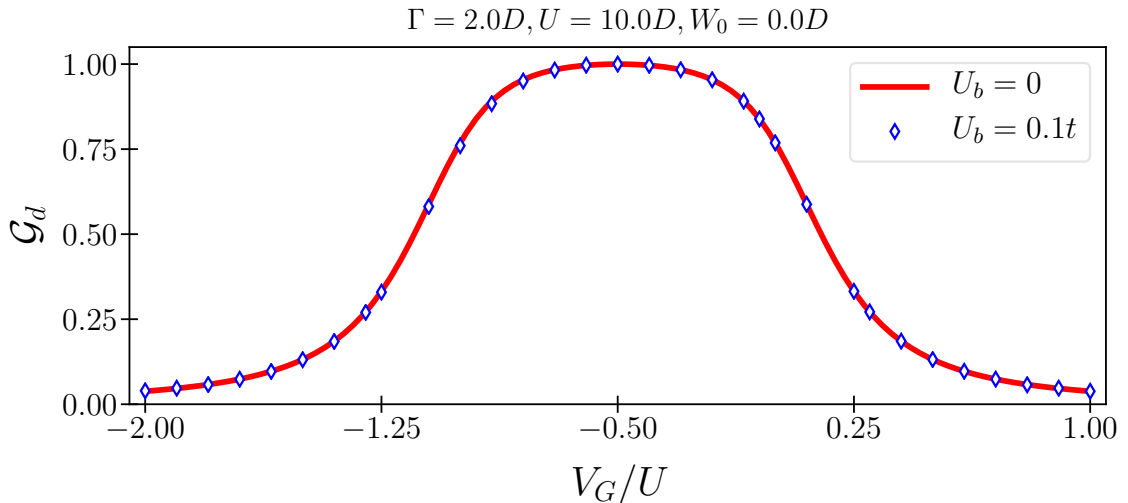


Figure 43 – Ground-state conductance  $\mathcal{G}_d(T \rightarrow 0)$  as a function of the gate voltage  $V_G$  obtained with the KSA procedure for a homogeneous conduction band with coupling  $U_b = 0.1t$  and model parameters  $\Gamma = 2.0D$ ,  $U = 10.0D$  (open blue diamonds), compared with results for  $U_b = 0.0$  (red solid line). Physically, the repulsion  $U_b$  penalizes double occupancy of the orbitals and hence reduces the electronic density. In the Kohn-Sham system, a uniform positive potential pushes the conductance levels up to reduce the density. This uniform potential is equivalent to a (negative) shift of the Fermi level. Shifting down the Fermi level is equivalent to displacing the conductance curve to the right. The displacement is small because the ratio  $U_b/U$  is small.

Source: By the author.

Finally, we can investigate the results of conductance obtained with the new method for a structured band and also the effects of applying an external potential  $W_0$  to coupled leads ( $U_b \neq 0$ ). To this aim, we will analyze the results for the model Hamiltonian in eq. (5.4) with  $L = 2000$ ,  $U_b = 0.1t$ ,  $W_0 = 0$  and  $W_0 \neq 0$  in the Kondo regime. The model parameters are chosen so that the correlation regime is that in which the Kondo plateau becomes visible:  $\Gamma = 2D$  and  $U = 10\Gamma$ . The effect of the Coulomb interaction  $U_b$  is shown in Fig. 35. For  $U_b = t$  (dashed green lines), the Fermi level rises approximately  $\delta\epsilon_F = 0.25t$ . The shift is due to the Hartree energy and the exchange-correlation potentials. The displacement of the Fermi level breaks particle-hole symmetry. The conductance is no longer an even function of  $V_G + U/2$ . As discussed in chapter 2, a shift in the Fermi level of the leads corresponds to shifting the gate voltage  $V_G$  in the opposite direction.  $U_b \neq 0$  is therefore equivalent to a horizontal displacement of the  $\mathcal{G}_d$  vs  $V_G$  curve. The application of a potential  $W$  to the leads introduces an additional term to the phase shifts, so the occupation number  $n_d$  in the dot and the corresponding conductance at  $T \rightarrow 0$  should be sensible to both  $U_b$  and  $W$ . Both effects are observed in our results. The case  $W = 0$  is shown in Fig. 43, where we compare the the curves  $\mathcal{G}_d$  vs  $V_G$  obtained with the KSA procedure for homogeneous band with  $U_b = 0$  (solid red lines) and for a band with

coupling  $U_b = t$  (blue diamonds). Comparing the solid red line with the blue diamonds we note a small horizontal displacement of  $\mathcal{G}_d$  with respect to  $V_G/U$ , which shifts to the right.

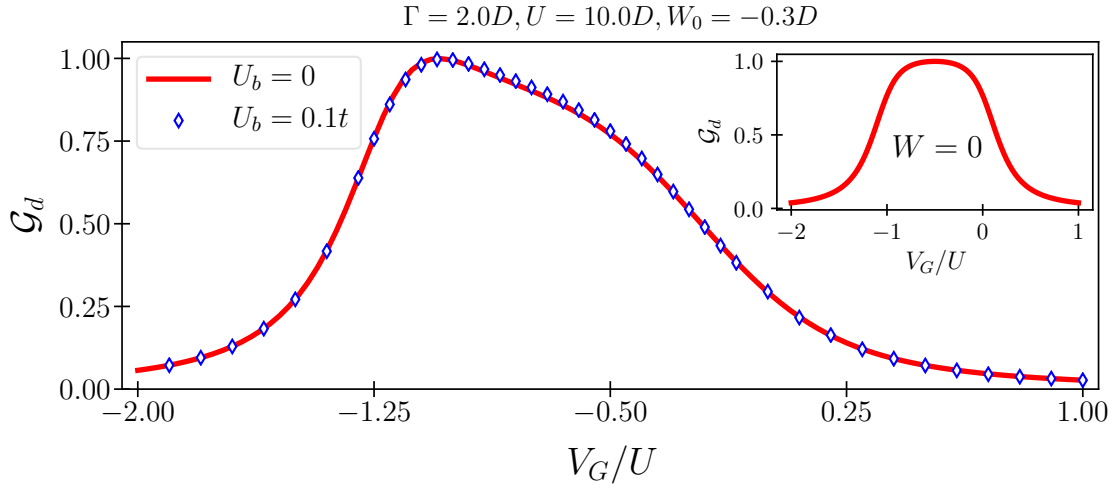


Figure 44 – Results for the ground-state conductance  $\mathcal{G}_d(T \rightarrow 0)$  as a function of the gate voltage  $V_G$  obtained with the KSA procedure for a homogeneous conduction band with applied potential  $W = -0.3D$ , coupling  $U_b = 0.1t$  (blue diamonds) and model parameters  $\Gamma = 2.0D$ ,  $U = 10.0D$  and comparison with results for  $U_b = 0.0$  (solid red lines). For  $W \neq 0$ , besides the displacement of  $\mathcal{G}_d$  to the right, we also observe a change in the profile of the conductance and also in the shape of the plateau. The small displacement is understood because the scale in the  $x$ -axis ( $V_G/U$ ) from  $-2$  to  $1$  is actually much larger than the unit of  $t$ . The inset shows the case  $U_b = W_0 = 0$ . Source: By the author.

Figure 44 displays the results for zero bias conductance through a SET with a potential  $W = -0.3D$  applied to the leads. Here, the coupling  $U_b = 0.1t$  shifts smoothly the conductance to the right, as in the case of  $W_0 = 0$ . The particle-hole asymmetry due to  $W$  is visible in the two curves in Fig. 44. Besides the displacement of  $V_G$  due to the shift of the Fermi level for  $U_b \neq 0$  ( $W = 0$ ), the conductance is also affected by  $W \neq 0$ . The plateau in the window  $-U < V_G < 0$  observed for  $W = 0$  is replaced by a smooth decay occurring from  $V_G \approx U$ , where  $\mathcal{G}_d \approx \mathcal{G}_2$ , to  $V_G \approx -0.3$ , where  $\mathcal{G}_d \approx 0.6\mathcal{G}_2$  for  $W = -0.3D$ . Comparing Figs. 44 and 21, we observe that the new procedure is able to account for the leads, whereas the BA self-consistent calculations fails in retrieving the Kondo plateau for the same  $W$ .

Inspection of the case  $U_b \geq t$  reveals an enhancement in the break of particle-hole symmetry due to the exchange-correlation effects in the leads. The case  $U_b = t$  is shown in Fig. 45, where we observe a clear change in the conductance profile as  $U_b$  goes from  $0$  to  $t$ . Comparing the case  $U_b = 0$  and  $W_0 = -0.3D$  (solid red line in Fig. 44) with the case  $U_b = t$  and  $W_0 = 0$ , we observe the effects of the coupling to be equivalent to an increase in the  $W_{LM}$  potential entering in the very first iteration of the Kohn-Sham Anderson cycle with order of approximately  $W_{DFT,i=0}^{LM} \approx 0.3D$ . The exchange-correlation

potential  $v_{KS}(n_{\pm 1})$  is therefore translated as a scattering potential applied to  $f_0$  in the local moment fixed point (high temperatures). Comparing Figs. 44 and 45, we observe the effect of coupling in the leads to be translated as an effective potential  $W_{LM}$  which controls the occupation number in the leads, provided that with  $U_b = t$ , one expects the competition between the Coulomb repulsion and the phase shift due to the impurity to break particle-hole symmetry, which indirectly renormalizes the gate voltage for which the occupation number of the impurity reaches its maximum value. Interpreting this result in terms of the Kohn-Sham Anderson system, to restore particle-hole symmetry in a quantum dot for which the leads are coupled ( $U_b \neq 0$ ) one can play with an additional potential  $W_0$  applied to the leads in such a way that it can cancel the correlation effects.

To test the idea that an effective external potential can be used to cancel the coupling in the leads and restore particle-hole symmetry, we performed the KSA calculation applying also an additional external potential  $W_0 = -0.3D$  to the leads with coupling  $U_b = t$ . The result is shown in Fig. 46. We can observe that particle-hole symmetry is partially restored and the Kondo plateau depicts. A shift in the curve of conductance to positive gate voltages. We note that the Kondo plateau is not perfectly symmetric due to a small difference between the Kohn-Sham potential and  $W_0 = -0.3D$ . In fact, the horizontal shift of  $\mathcal{G}_d$  reflects the difference between the value of  $W_0$  which should be applied to each gate voltage to compensate exactly the exchange-correlation potential  $v_{KS}$  in the leads.

Concerning the computational cost of the new method with the convergence criteria presented in our discussion of Fig. 42, a single run for fixed model parameters of a SET takes between 5 and 10 minutes to complete the calculations of all stages: solution of the conduction band, logarithmic discretization, NRG diagonalization and fit to the universal conductance. This time is estimated based on the accuracy criteria described above used to obtain the results presented in Fig. 42.

In summary, the previous results show that the KSA procedure is able to accurately reproduce the zero bias conductance through a SET independently of the correlation strength. In particular, the new hybrid procedure reliably describes accurate results for coupling regimes in which the Kondo effect manifest in a SET, as shown in panel (b) of Fig. 42. These results open an inroad path to the description of transport in nano-structured devices. The extension to more realistic description of the device is, however, beyond the scope of this thesis, which has described the procedure and computed the conductance for a generalized Hubbard model as an illustration.

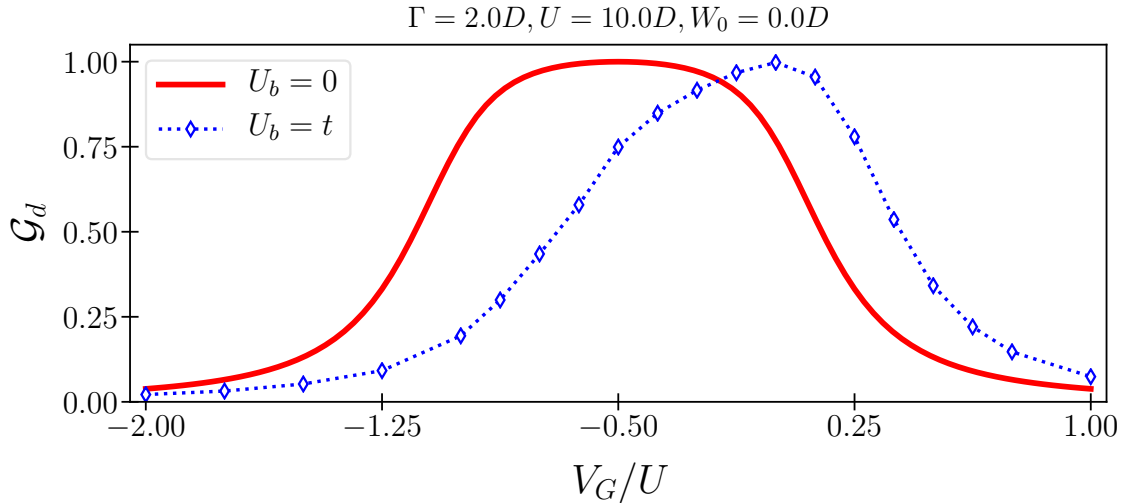


Figure 45 – Results for the ground-state conductance  $G_d(T \rightarrow 0)$  as a function of the gate voltage  $V_G$  obtained with the KSA procedure for a homogeneous conduction band with coupling  $U_b = 1t$  (blue diamonds) and model parameters  $\Gamma = 2.0D$ ,  $U = 10.0D$  and comparison with results for  $U_b = 0.0$  (solid red lines). For  $U_b = t$ , the exchange correlation potential contributing to the potential  $W_{LM}$  is of order of  $0.3D$ . The coupling to the bands breaks particle-hole symmetry and results in a horizontal displacement to the right, inverted in comparison with Fig. 44, which depicts the case  $U_b \ll t$  and  $W = -0.3D$ .

Source: By the author.

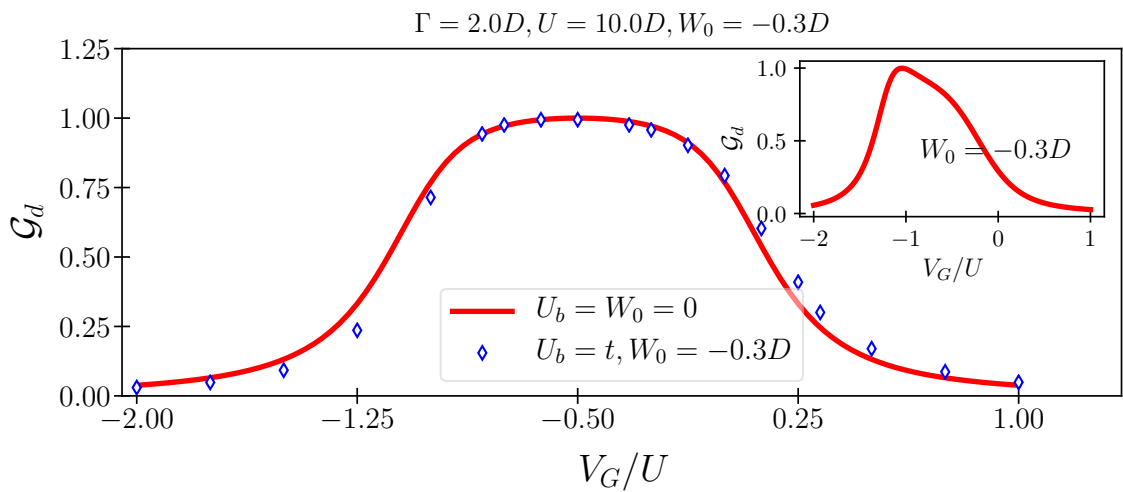


Figure 46 – Results for the ground-state conductance  $G_d(T \rightarrow 0)$  as a function of the gate voltage  $V_G$  obtained with the KSA procedure for a homogeneous conduction band with applied potential  $W_0 = -0.3D$ , coupling  $U_b = 1t$  (blue diamonds) and model parameters  $\Gamma = 2.0D$ ,  $U = 10.0D$  and comparison with results for  $U_b = 0.0$  (solid red lines). For  $U_b = t$ , the exchange correlation potential contributing to the potential  $W_{LM}$  is of order of  $0.3D$ . The coupling to the bands breaks particle-hole symmetry and results in a horizontal displacement to the right, inverted in comparison with Fig. 44, which depicts the case  $U_b \ll t$  and  $W_0 = -0.3D$ . The inset shows the case  $U_b = 0$  and  $W_0 = -0.3D$ .

Source: By the author.

## 7 CONCLUSIONS AND FUTURE PERSPECTIVES

In the present thesis, we have studied the problem of transport in a single-electron transistor and discussed different approaches to investigate the Kondo regime dominating the physics of the device at low temperatures. We have introduced a new hybrid self-consistent procedure combining ideas from Density Functional Theory and the Numerical Renormalization-Group to calculate the zero bias conductance in quantum dot devices in the strong correlated regime. Our study was motivated by the increasing interest in accurately describing transport in semiconductor nano structures, whose understanding is vital to the development of novel quantum technologies.

In chapter 1, we have discussed the challenges involved in studying the strongly correlated regime of many-body interacting problems and discussed the current state of the art of popular approaches such as Density Functional Theory and the numerical implementations of Renormalization-Groups. We have contextualized the study of transport in quantum dots among the problems that can serve as a benchmark case to test new density functional approaches and argued on the study of the single-electron transistor as a starting point.

In chapter 2, we have presented a brief introduction to the single-electron transistor with focus on the manifestation of the Kondo effect at low temperatures. We have discussed quantum tunneling in a SET in the Coulomb blockade regime and shown how this picture differs at low temperatures, which is the limit for which the Kondo effect arises. We have given a historical overview of the Kondo effect and shown how its manifestation in quantum dots become an attractive problem in condensed matter physics. We have introduced the Anderson and the Kondo Hamiltonians for impurity systems and shown how they can be used to model a SET given the correspondence between the physics of a SET and the problem of a magnetic impurity coupled to a conduction band. The source and the drain leads were described as two metallic bands  $\epsilon_{k,S}$  and  $\epsilon_{k,D}$  coupled to the quantum dot via the hybridization  $\Gamma$ . The quantum dot was described by its occupation number  $n_d$  controlled by the gate voltage  $V_G$ . The Coulomb repulsion  $U$  in the dot penalizes double occupation and also related with the correlation regime of the device by means of the ratio  $U/\Gamma$ .

We have then shown the Anderson Hamiltonian for the SET and examined ranges of parameters commonly studied in experiments, with focus on the so-called Kondo temperature  $T_K$ , the scale below which anomalous transport is detected in a SET. In particular, we have discussed how the zero bias conductance in a SET calculated from the diagonalization of the Anderson model matches experimental results. We have also shown that the zero bias conductance in a SET maps onto a universal relation which depends

on the Kondo temperature  $T_K$  and the phase shifts  $\delta$ . Importantly, we have analysed the physics of a SET in the limits of high and low temperatures and argued on how physical properties are sensible to phase shifts.

The third chapter was devoted to the foundations of Density Functional Theory. Especially, we have defined the Kohn-Sham formulation for DFT, according to which the exchange-correlation potential is regarded as the many-body correction that can be added to the fictitious non-interacting KS system. We have argued that new approximations for  $v_{xc}$  as well as density functional approaches suiting strongly-correlated problems are desired in the condensed matter community and we have given a background on current progress in this subject.

In particular, we examined two approximations for the exchange-correlation functional based on the solution of strong correlated models: the Bethe Ansatz Local Density Approximation (BALDA) for the Hubbard Hamiltonian and Bergfield's parametrization extracted from the Bethe Ansatz solution of the Anderson model. We discussed the limitations of approaches with a similar basis and their application to describe transport in general quantum dot devices, showing examples of simple situations in which they do not provide good results even for the elementary single-electron transistor. Based on this discussion, we reasoned on the need to interface DFT with other many-body approaches and argued on the exploration of numerical Renormalization-Group approach.

In chapter 4, we then introduced the concept of Renormalization-Group and explained the NRG procedure conceived by Wilson to solve the Kondo problem. We have reasoned on the success of the NRG ground with respect to the previous attempts, arguing that NRG was the only method able to describe the crossover from high to low temperatures in impurity models. We presented in detail the steps involved in the implementation of the NRG, with special focus on the logarithmic discretization. We have described how the logarithmic discretization is developed for general conduction bands in the limit of a continuum of states. Additionally, we have introduced an alternative discretization scheme adapted for conduction bands with finite degrees of freedom, characterized by a minimum scale of energy  $\Delta$  around the Fermi level.

The end of the fourth chapter was dedicated to the NRG treatment of the Anderson Hamiltonian and the fixed point structure of the RG flow. We have shown that the limits of high and low temperatures are associated with the local moment and the frozen level fixed points, respectively. Importantly, we have demonstrated that in the fixed points, the conduction band Hamiltonian can be approximated by a single-particle system subject to a scattering potential  $W$ , which makes the role of the scattering center for the impurity/quantum dot. We have calculated the phase shifts in the LM and the FL fixed points and shown that in the FL fixed point ground-state conductance can be obtained through the occupation number in the quantum dot.

In chapter 5 we have recapitulated our discussion of the DFT and NRG approaches for a SET and we have emphasized the motivation to develop a hybrid procedure interfacing a density functional calculation and the numerical renormalization-group diagonalization to deal with more complex quantum devices. We have made explicit that the fixed point structure of the RG flow allows to map the interacting problem into an effective non-interacting problem in the same spirit of the Kohn-Sham idea for Density Functional Theory. We then defined the Kohn-Sham Anderson system as being the auxiliary system to map the model for a quantum dot into a non-interacting problem with the correct phase shifts. We then explained our idea of a self-consistent hybrid calculation to incorporate the many-body corrections in general devices. We explored the application of this idea in the calculation of the zero bias conductance in a SET, explaining the details of each step involved in the cycle: from the calculation of the band structure by means of a DFT module to the extrapolation of the phase shifts at low temperatures according to a fit to the universal relation.

The sixth chapter was dedicated to the discussion of our results. We started investigating the relation between the correlation regimes in a single-electron transistor and the formation of the Kondo screening cloud. We have discussed the relation between the ratio  $U/\Gamma$  with the Kondo temperature  $T_K$  and with the radius  $\xi_K$  of the cloud. We have then examined the profile of the zero bias conductance as a function of the gate voltage calculated via NRG for  $U/\Gamma = 1, 10$  and  $100$ , giving an interpretation of the results in terms of the Kondo screening cloud. We have shown exact results for the curves  $\mathcal{G}_d$  vs  $V_G$  at different thermal scales to give a flavour of how the picture of transport changes from high to low temperatures and indicates anomalous transport. Especially, we discussed the manifestation of the Kondo effect in intermediate coupling regimes ( $U \approx 10\Gamma$ ), which is the situation corresponding to experiments in quantum dots. For this coupling regime, the Kondo effect manifests as a plateau in the conductance for gate voltages  $-U < V_G < 0$ .

We have also extended the previous analysis to the case of a conduction band described by a finite number of degrees of freedom. We have shown that the number of degrees of freedom defines the minimum thermal scale reached by the NRG calculations. We compared the NRG calculations for a continuum of states and the finite band and discussed how the conductance is affected by the finite size of the system (finite number of degrees of freedom), especially in the intermediate and strongly coupling regimes.

Finally, in chapter 6, we have shown our results for the ground-state conductance in a SET obtained with the proposed KSA procedure and compared them with the exact NRG calculation for a SET and self-consistent calculations implementing the Kohn-Sham cycle and the HF solution. In the DFT, we compared two density functional approximations for the exchange-correlation functional: BALDA and Bergfield's parametrization for the Anderson junction. Our results indicated that HF and BALDA only perform well in weakly

coupling regimes. In general, we have shown that the results obtained with the KSA yield a reliable framework to accurately describe nano-structured devices. Importantly, the results presented for a single-electron transistor described by a generalized Hubbard Hamiltonian, we have demonstrated that the procedure describes precisely the intermediate coupling regime, which is the region experimentally accessible to probe the Kondo effect in real quantum dots.

As a final comment, we have argued that the hybrid procedure proposed in this thesis can be extended to more complex nano-structures and discussed how the former implementation can be adapted to this aim. The extension will be the subject of future works. Besides examining regimes of SETs of experimental interest, we intend to apply the procedure for molecular junctions and other quantum dot devices. Specifically, we intend to carry out density functional calculations to obtain the band structure of realistic materials and test the KSA calculation for obtaining the transport properties of molecular junctions and other quantum dot devices. This task will include the integration of a massive DFT package for electronic structure calculations, such as VASP, with a library implementing the NRG calculations for more complex band structures. Other route to explore in the RG calculations is to take advantage of the formulation using Tensor Networks as a RG solver. The study of Tensor Networks in condensed matter systems have been feeding the community with many interesting results, including applications to quantum chemistry. Additionally to the extension of the KSA method to other quantum devices, we also aim to explore the structure of the RG flow for better understanding the limitations of density functional approximations in describing thermodynamical properties. For instance, we have reasoned on the accuracy of local and quasi-local approximations for the exchange-correlation potential at the weakly and strongly coupled fixed points. A question that arises concerns quantifying non-local effects and determining properties which are highly sensible to them in the crossover to the Kondo regime. Related to this question, contemporary approaches studying entanglement in the density functional approach have been complementing our understanding of how properties of an interacting system can be accurately described by the Kohn-Sham system. In essence, we expect the present thesis to warm these previous issues and fertilize the community with new discussions.

## REFERENCES

- 1 GROBIS, M. et al. Universal scaling in nonequilibrium transport through a single channel Kondo dot. **Physical Review Letters**, v. 100, p. 246601, 2008. doi: 10.1103/PhysRevLetters100.246601.
- 2 SOH, H. et al. **Scanning probe lithography**. Berlin: Springer, 2013. (Microsystems series).
- 3 AVELLA, A. et al. **Strongly correlated systems: numerical methods**. Berlin Heidelberg: Springer, 2013. (Springer series in solid-state sciences).
- 4 BETHE, H. Zur theorie der metalle. **Zeitschrift für Physik**, v. 71, n. 3, p. 205–226, 1931. doi: 10.1007/BF01341708.
- 5 WILSON, K. G. Renormalization group methods. **Advances in Mathematics**, v. 16, n. 2, p. 170 – 186, 1975. doi: 10.1016/0001-8708(75)90149-8.
- 6 SCHOLLWÖCK, U. The density-matrix renormalization group in the age of matrix product states. **Annals of Physics**, v. 326, n. 1, p. 96 – 192, 2011. doi: 10.1016/j.aop.2010.09.012.
- 7 GROSS, E. et al. **Density functional theory**. Berlin Heidelberg: Springer, 1995. (NATO ASI series).
- 8 BURKE, K. Perspective on density functional theory. **Journal of Chemical Physics**, v. 136, n. 15, p. 150901, 2012.
- 9 NIELSEN, M. et al. **Quantum computation and quantum information**. Cambridge: Cambridge University Press, 2000. (Cambridge series on information and the natural sciences).
- 10 GOSER, K. et al. **Nanoelectronics and nanosystems: from transistors to molecular and quantum devices**. Berlin: Springer, 2004. (Engineering online library).
- 11 KASTNER, M. A. The single-electron transistor. **Reviews of Modern Physics**, v. 64, p. 849–858, 1992. doi: 10.1103/RevModPhys.64.849.
- 12 GOLDHABER-GORDON, D. et al. Kondo effect in a single-electron transistor. **Nature**, v. 391, n. 6663, p. 156–159, 1998. doi: 10.1038/34373.
- 13 ANDERSON, P. W. Localized magnetic states in metals. **Physical Review**, v. 124, p. 41–53, 1961. doi: 10.1103/PhysRev.124.41.
- 14 YOSHIDA, M. et al. Universal zero-bias conductance for the single-electron transistor. **Physical Review B**, v. 80, p. 235317, 2009. doi: 10.1103/PhysRevB.80.235317.
- 15 ZAWADZKI, K. et al. How sharply does the Anderson model depict a molecular junction? **European Physics Journal B**, v. 91, n. 6, 2018. doi: 10.1140/epjb/e2018-90164-y.

- 16 WILSON, K. G. The renormalization group: critical phenomena and the Kondo problem. **Reviews of Modern Physics**, v. 47, n. 4, p. 773–840, 1975. doi: 10.1103/RevModPhys.47.773.
- 17 REIMANN, S. M. et al. Electronic structure of quantum dots. **Reviews of Modern Physics**, v. 74, p. 1283–1342, 2002. doi: 10.1103/RevModPhys.74.1283.
- 18 SCHÜLER, M. et al. Realistic theory of electronic correlations in nanoscopic systems. **European Physical Journal Special Topics**, v. 226, n. 11, p. 2615–2640, 2017. doi: 10.1140/epjst/e2017-70049-3.
- 19 HOHENBERG, P. et al. Inhomogeneous electron gas. **Physical Review**, v. 136, p. B864–B871, 1964. doi: 10.1103/PhysRev.136.B864.
- 20 KOHN, W. et al. Self-consistent equations including exchange and correlation effects. **Physical Review**, v. 140, p. A1133–A1138, 1965. doi: 10.1103/PhysRev.140.A1133.
- 21 SHOLL, D. S. et al. **Density functional theory**: a practical introduction. Hoboken: John Wiley & Sons, 2009.
- 22 COHEN, A. J. et al. Challenges for density functional theory. **Chemical Reviews**, v. 112, n. 1, p. 289–320, 2012. doi: 10.1021/cr200107z.
- 23 JONES, R. O. Density functional theory: its origins, rise to prominence, and future. **Reviews of Modern Physics**, v. 87, p. 897–923, 2015. doi: 10.1103/RevModPhys.87.897.
- 24 MALET, F. et al. Strong correlation in kohn-sham density functional theory. **Physical Review Letters**, v. 109, p. 246402, 2012. doi: 10.1103/PhysRevLetters109.246402.
- 25 SCHENK, S. et al. Successes and failures of bethe ansatz density functional theory. **Physical Review B**, v. 78, p. 165102, 2008. doi: 10.1103/PhysRevB.78.165102.
- 26 LIMA, N. A. et al. Density functionals not based on the electron gas: Local-density approximation for a luttinger liquid. **Physical Review Letters**, v. 90, p. 146402, 2003. doi: 10.1103/PhysRevLetters90.146402.
- 27 \_\_\_\_\_. Density-functional study of the Mott gap in the Hubbard model. **Europhysics Letters**, v. 60, n. 4, p. 601, 2002. doi: 10.1209/epl/i2002-00261-y.
- 28 XIANLONG, G. et al. Bethe Ansatz density-functional theory of ultracold repulsive fermions in one-dimensional optical lattices. **Physical Review B**, v. 73, p. 165120, 2006. doi: 10.1103/PhysRevB.73.165120.
- 29 MORI-SÁNCHEZ, P. et al. Discontinuous nature of the exchange-correlation functional in strongly correlated systems. **Physical Review Letters**, v. 102, p. 066403, 2009. doi: 10.1103/PhysRevLetters102.066403.
- 30 FRANÇA, V. V. et al. Entanglement from density measurements: analytical density functional for the entanglement of strongly correlated fermions. **Physical Review A**, v. 83, p. 042311, 2011. doi: 10.1103/PhysRevA.83.042311.
- 31 BERGFIELD, J. P. et al. Bethe Ansatz approach to the Kondo effect within density-functional theory. **Physical Review Letters**, v. 108, p. 066801, 2012. doi: 10.1103/PhysRevLetters108.066801.

- 32 LUBASCH, M. et al. Systematic construction of density functionals based on matrix product state computations. **New Journal of Physics**, v. 18, n. 8, p. 083039, 2016. doi: 10.1088/1367-2630/18/8/083039.
- 33 STOUDENMIRE, E. M. et al. One-dimensional continuum electronic structure with the density-matrix renormalization group and its implications for density-functional theory. **Physical Review Letters**, v. 109, p. 056402, 2012. doi: 10.1103/PhysRevLetters109.056402.
- 34 SMITH, J. C. et al. Exact thermal density functional theory for a model system: correlation components and accuracy of the zero-temperature exchange-correlation approximation. **Physical Review B**, v. 93, p. 245131, 2016. doi: 10.1103/PhysRevB.93.245131.
- 35 WAGNER, L. O. et al. Kohn-sham calculations with the exact functional. **Physical Review B**, v. 90, p. 045109, 2014. doi: 10.1103/PhysRevB.90.045109.
- 36 STOUDENMIRE, E. M. et al. Sliced basis density matrix renormalization group for electronic structure. **Physical Review Letters**, v. 119, p. 046401, 2017. doi: 10.1103/PhysRevLetters119.046401.
- 37 SILVA, J. W. O. et al. Construction of exchange-correlation potentials for strongly interacting one-dimensional systems. **Brazilian Journal of Physics**, v. 47, n. 4, p. 393–399, 2017. doi: 10.1007/s13538-017-0508-x.
- 38 KOUWENHOVEN, L. P. et al. Revival of the Kondo effect. **Physics World**, v. 14, n. 1, p. 33–38, 2001. doi: 10.1088/2058-7058/14/1/28.
- 39 PUSTILNIK, M. et al. Kondo effect in quantum dots. **Journal of Physics: condensed matter**, v. 16, n. 16, p. R513, 2004. doi: 10.1088/0953-8984/16/16/R01.
- 40 PARK, J. et al. Coulomb blockade and the Kondo effect in single-atom transistors. **Nature**, v. 417, n. 6890, p. 722, 2002. doi: 10.1038/nature00791.
- 41 YOSHIDA, M. et al. Universal zero-bias conductance for the single-electron transistor. **Physical Review B**, v. 80, p. 235317, 2009. doi: 10.1103/PhysRevB.80.235317.
- 42 FULTON, T. A. et al. Observation of single-electron charging effects in small tunnel junctions. **Physical Review Letters**, v. 59, p. 109–112, 1987. doi: 10.1103/PhysRevLetters59.109.
- 43 MEIRAV, U. et al. Single-electron charging and periodic conductance resonances in GaAs nanostructures. **Physical Review Letters**, v. 65, p. 771–774, 1990. doi: 10.1103/PhysRevLetters65.771.
- 44 MEIR, Y. et al. Transport through a strongly interacting electron system: theory of periodic conductance oscillations. **Physical Review Letters**, v. 66, p. 3048–3051, 1991. doi: 10.1103/PhysRevLetters66.3048.
- 45 JOHNSON, A. T. et al. Zero-dimensional states and single electron charging in quantum dots. **Physical Review Letters**, v. 69, p. 1592–1595, 1992. doi: 10.1103/PhysRevLetters69.1592.

- 46 TAO, N. Electron transport in molecular junctions. **Nature Nanotechnology**, v. 1, n. 3, p. 173, 2006. doi: 10.1038/nnano.2006.130.
- 47 BOGANI, L. et al. Molecular spintronics using single-molecule magnets. **Nature Materials**, v. 7, n. 3, p. 179, 2008. doi: 10.1038/nmat2133.
- 48 HAAS, W. de et al. The electrical resistance of gold, copper and lead at low temperatures. **Physica**, v. 1, n. 7–12, p. 1115 – 1124, 1934. doi: 10.1016/S0031-8914(34)80310-2.
- 49 \_\_\_\_\_. Further experiments on the minimum in the resistance-temperature curve of gold. **Physica**, v. 4, n. 8, p. 683–694, 1937. doi: 10.1016/S0031-8914(37)80167-6.
- 50 KONDO, J. Resistance minimum in dilute magnetic alloys. **Progress of Theoretical Physics**, v. 32, n. 1, p. 37–49, 1964. doi: 10.1143/PTP.32.37.
- 51 SCHRIEFFER, J. R. et al. Relation between the Anderson and Kondo Hamiltonians. **Physical Review**, v. 149, p. 491–492, 1966. doi: 10.1103/PhysRev.149.491.
- 52 SØRENSEN, E. S. et al. Scaling theory of the Kondo screening cloud. **Physical Review B**, v. 53, p. 9153–9167, 1996. doi: 10.1103/PhysRevB.53.9153.
- 53 BARZYKIN, V. et al. The Kondo screening cloud: What can we learn from perturbation theory? **Physical Review Letters**, v. 76, n. 26, p. 4959–4962, 1996. doi: 10.1103/PhysRevLetters76.4959.
- 54 EGGER, R. et al. RKKY interaction and Kondo screening cloud for strongly correlated electrons. **Physical Review B**, v. 54, p. 16337–16340, 1996. doi: 10.1103/PhysRevB.54.16337.
- 55 SØRENSEN, E. S. et al. Impurity entanglement entropy and the Kondo screening cloud. **Journal of Statistical Mechanics: theory and experiment**, v. 2007, n. 1, p. L01001, 2007. doi: 10.1088/1742-5468/2007/01/L01001.
- 56 BORDA, L. Kondo screening cloud in a one-dimensional wire: Numerical renormalization group study. **Physical Review B**, v. 75, n. 4, p. 041307, 2007. doi: 10.1103/PhysRevB.75.041307.
- 57 AFFLECK, I. et al. Friedel oscillations and the Kondo screening cloud. **Physical Review B**, v. 77, p. 180404, 2008. doi: 10.1103/PhysRevB.77.180404.
- 58 \_\_\_\_\_. Detecting the Kondo screening cloud around a quantum dot. **Physical Review Letters**, v. 86, p. 2854–2857, 2001. doi: 10.1103/PhysRevLetters86.2854.
- 59 SIMON, P. et al. Finite-size effects in conductance measurements on quantum dots. **Physical Review Letters**, v. 89, p. 206602, 2002. doi: 10.1103/PhysRevLetters89.206602.
- 60 \_\_\_\_\_. Kondo screening cloud effects in mesoscopic devices. **Physical Review B**, v. 68, p. 115304, 2003. doi: 10.1103/PhysRevB.68.115304.
- 61 YANG, C. et al. Unveiling the internal entanglement structure of the Kondo singlet. **Physical Review B**, v. 95, p. 115106, 2017. doi: 10.1103/PhysRevB.95.115106.
- 62 CRONENWETT, S. M. et al. A tunable Kondo effect in quantum dots. **Science**, v. 281, n. 5376, p. 540–544, 1998. doi: 10.1126/science.281.5376.540.

- 63 HUR, K. L. Condensed-matter physics: quantum dots and the Kondo effect. **Nature**, v. 526, n. 7572, p. 203–204, 2015. doi: 10.1038/526203a.
- 64 HIRAKA, R. et al. Single-molecule quantum dot as a Kondo simulator. **Nature Communications**, v. 8, p. 16012, 2017. doi: 10.1038/ncomms16012.
- 65 WICKENBURG, S. et al. Tuning charge and correlation effects for a single molecule on a graphene device. **Nature Communications**, v. 7, p. 13553, 2016. doi: 10.1038/ncomms13553.
- 66 MEIR, Y. et al. Low-temperature transport through a quantum dot: the Anderson model out of equilibrium. **Physical Review Letters**, v. 70, p. 2601–2604, 1993. doi: 10.1103/PhysRevLetters70.2601.
- 67 PUSTILNIK, M. et al. Kondo effect in real quantum dots. **Physical Review Letters**, v. 87, p. 216601, 2001. doi: 10.1103/PhysRevLetters87.216601.
- 68 ANDREI, N. Diagonalization of the Kondo hamiltonian. **Physical Review Letters**, v. 45, p. 379–382, 1980. doi: 10.1103/PhysRevLetters45.379.
- 69 ANDREI, N. et al. Solution of the Kondo problem. **Reviews of Modern Physics**, v. 55, p. 331–402, 1983. doi: 10.1103/RevModPhys.55.331.
- 70 BULLA, R. et al. Numerical renormalization group method for quantum impurity systems. **Reviews of Modern Physics**, v. 80, p. 395–450, 2008. doi: 10.1103/RevModPhys.80.395.
- 71 LANGRETH, D. C. Friedel sum rule for Anderson's model of localized impurity states. **Physical Review**, v. 150, p. 516–518, 1966. doi: 10.1103/PhysRev.150.516.
- 72 TANIGUCHI, T. et al. Friedel phases and phases of transmission amplitudes in quantum scattering systems. **Physical Review B**, v. 60, p. 13814–13823, 1999. doi: 10.1103/PhysRevB.60.13814.
- 73 GERLAND, U. et al. Transmission phase shift of a quantum dot with kondo correlations. **Physical Review Letters**, v. 84, p. 3710–3713, 2000. doi: 10.1103/PhysRevLetters84.3710.
- 74 JI, Y. et al. Phase evolution in a kondo-correlated system. **Science**, v. 290, n. 5492, p. 779–783, 2000. doi: 10.1126/science.290.5492.779.
- 75 CAPELLE, K. A bird's-eye view of density-functional theory. **Brazilian Journal of Physics**, v. 36, p. 1318 – 1343, 2006. doi: 10.1590/S0103-97332006000700035.
- 76 MARQUES, M. et al. **Time-dependent density functional theory**. Berlin Heidelberg: Springer, 2006. (Lecture Notes in Physics).
- 77 LEVY, M. Universal variational functionals of electron densities, first-order density matrices, and natural spin-orbitals and solution of the v-representability problem. **Proceedings of the National Academy of Sciences**, v. 76, n. 12, p. 6062–6065, 1979. doi: 10.1073/pnas.76.12.6062.
- 78 KRESSE, G. et al. Efficient iterative schemes for ab initio total-energy calculations using a plane-wave basis set. **Physical Review B**, v. 54, p. 11169–11186, 1996. doi: 10.1103/PhysRevB.54.11169.

- 79 GIANNONZI, P. et al. Quantum espresso: a modular and open-source software project for quantum simulations of materials. **Journal of Physics: condensed matter**, v. 21, n. 39, p. 395502, 2009. doi: 10.1088/0953-8984/21/39/395502.
- 80 ABINIT: first-principles approach to material and nanosystem properties. **Computer Physics Communications**, v. 180, n. 12, p. 2582 – 2615, 2009.
- 81 GULANS, A. et al. Exciting: a full-potential all-electron package implementing density-functional theory and many-body perturbation theory. **Journal of Physics: condensed matter**, v. 26, n. 36, p. 363202, 2014. doi: 10.1088/0953-8984/26/36/363202.
- 82 MARQUES, M. A. et al. Octopus: a first-principles tool for excited electron–ion dynamics. **Computer Physics Communications**, v. 151, n. 1, p. 60 – 78, 2003. doi: 10.1016/S0010-4655(02)00686-0.
- 83 SEGALL, M. D. et al. First-principles simulation: ideas, illustrations and the CASTEP code. **Journal of Physics: condensed matter**, v. 14, n. 11, p. 2717, 2002.
- 84 JONES, R. Introduction to density functional theory and exchange-correlation energy functionals. **Computational Nanoscience: do it yourself**, v. 31, p. 45–70, 2006.
- 85 SCHÖNHAMMER, K. et al. Density-functional theory on a lattice: comparison with exact numerical results for a model with strongly correlated electrons. **Physical Review B**, v. 52, p. 2504–2510, 1995. doi: 10.1103/PhysRevB.52.2504.
- 86 CAPELLE, K. et al. Density functionals and model Hamiltonians: pillars of many-particle physics. **Physics Reports**, v. 528, n. 3, p. 91 – 159, 2013. doi: 10.1016/j.physrep.2013.03.002.
- 87 LIEB, E. H. et al. The one-dimensional Hubbard model: a reminiscence. **Physica A: statistical mechanics and its applications**, v. 321, n. 1, p. 1 – 27, 2003. doi: 10.1016/S0378-4371(02)01785-5.
- 88 FRANÇA, V. V. et al. Simple parameterization for the ground-state energy of the infinite hubbard chain incorporating mott physics, spin-dependent phenomena and spatial inhomogeneity. **New Journal of Physics**, v. 14, n. 7, p. 073021, 2012. doi: 10.1088/1367-2630/14/7/073021.
- 89 LIECHTENSTEIN, A. I. et al. Density-functional theory and strong interactions: orbital ordering in Mott-Hubbard insulators. **Physical Review B**, v. 52, p. R5467–R5470, 1995. doi: 10.1103/PhysRevB.52.R5467.
- 90 MANMANA, S. R. et al.  $Su(n)$  magnetism in chains of ultracold alkaline-earth-metal atoms: Mott transitions and quantum correlations. **Physical Review A**, v. 84, p. 043601, 2011. doi: 10.1103/PhysRevA.84.043601.
- 91 DIMITROV, T. et al. Exact maps in density functional theory for lattice models. **New Journal of Physics**, v. 18, n. 8, p. 083004, 2016. doi: 10.1088/1367-2630/18/8/083004.
- 92 ZAWADZKI, K. et al. Symmetries and boundary conditions with a twist. **Brazilian Journal of Physics**, v. 47, n. 5, p. 488–511, 2017. doi: 10.1007/s13538-017-0517-9.

- 93 CARRASCAL, D. J. et al. The hubbard dimer: a density functional case study of a many-body problem. **Journal of Physics: condensed matter**, v. 27, n. 39, p. 393001, 2015. doi: 10.1088/0953-8984/27/39/393001.
- 94 TROSTER, P. et al. Transport calculations based on density functional theory, friedel's sum rule, and the kondo effect. **Physical Review B**, v. 85, p. 115409, 2012. doi: 10.1103/PhysRevB.85.115409.
- 95 LIU, Z.-F. et al. Accuracy of density functionals for molecular electronics: the Anderson junction. **Physical Review B**, v. 85, p. 155117, 2012. doi: 10.1103/PhysRevB.85.155117.
- 96 STEFANUCCI, G. et al. Steady-state density functional theory for finite bias conductances. **Nano Letters**, v. 15, n. 12, p. 8020–8025, 2015. doi: 10.1021/acs.nanolett.5b03294.
- 97 KURTH, S. et al. Nonequilibrium anderson model made simple with density functional theory. **Physical Review B**, v. 94, p. 241103, 2016. doi: 10.1103/PhysRevB.94.241103.
- 98 EVERS, F. et al. Broadening of the derivative discontinuity in density functional theory. **Physical Chemistry Chemical Physics**, v. 13, p. 14417–14420, 2011. doi: 10.1039/C1CP21247H.
- 99 STEFANUCCI, G. et al. Towards a description of the Kondo effect using time-dependent density-functional theory. **Physical Review Letters**, v. 107, p. 216401, 2011.
- 100 WHITE, S. R. Density matrix formulation for quantum renormalization groups. **Physical Review Letters**, v. 69, p. 2863–2866, 1992. doi: 10.1103/PhysRevLetters69.2863.
- 101 SCHOLLWÖCK, U. The density-matrix renormalization group. **Reviews of Modern Physics**, v. 77, p. 259–315, 2005. doi: 10.1103/RevModPhys.77.259.
- 102 SHANKAR, R. Renormalization group for interacting fermions in *dgt1*. **Physica A: statistical mechanics and its applications**, v. 177, n. 1–3, p. 530 – 536, 1991. doi: 10.1016/0378-4371(91)90197-K.
- 103 Anderson, P. W. A poor man's derivation of scaling laws for the Kondo problem. **Journal of Physics C: solid state physics**, v. 3, p. 2436–2441, 1970. doi: 10.1088/0022-3719/3/12/008.
- 104 KRISHNA-MURTHY, H. R. et al. Renormalization-group approach to the Anderson model of dilute magnetic alloys. i. static properties for the symmetric case. **Physical Review B**, v. 21, p. 1003–1043, 1980. doi: 10.1103/PhysRevB.21.1003.
- 105 \_\_\_\_\_. Renormalization-group approach to the Anderson model of dilute magnetic alloys. ii. static properties for the asymmetric case. **Physical Review B**, v. 21, p. 1044–1083, 1980. doi: 10.1103/PhysRevB.21.1044.
- 106 PRUSCHKE, R. B. T. et al. Anderson impurity in pseudo-gap Fermi systems. **Journal of Physics: condensed matter**, v. 9, n. 47, p. 10463–10474, 1997. doi: 10.1088/0953-8984/9/47/014.

- 107 OLIVEIRA, W. C. et al. Generalized numerical renormalization-group method to calculate the thermodynamical properties of impurities in metals. **Physical Review B**, v. 49, p. 11986–11994, 1994. doi: 10.1103/PhysRevB.49.11986.
- 108 CAMPO, V. L. et al. Alternative discretization in the numerical renormalization-group method. **Physical Review B**, v. 72, p. 104432, 2005. doi: 10.1103/PhysRevB.72.104432.
- 109 SILVA, L. G. G. V. Dias da et al. Spin-polarized conductance in double quantum dots: Interplay of Kondo, Zeeman, and interference effects. **Physical Review B**, v. 87, p. 205313, 2013. doi: 10.1103/PhysRevB.87.205313.
- 110 Li, J. et al. Band-structure-corrected local density approximation study of semiconductor quantum dots and wires. **Physical Review B**, v. 72, n. 12, p. 125325, 2005. doi: 10.1103/PhysRevB.72.125325.
- 111 GUNNARSSON, O. et al. Density-functional calculation of the parameters in the Anderson model: application to Mn in CdTe. **Physical Review B**, v. 39, p. 1708–1722, 1989. doi: 10.1103/PhysRevB.39.1708.
- 112 ORÚS, R. A practical introduction to tensor networks: matrix product states and projected entangled pair states. **Annals of Physics**, v. 349, p. 117 – 158, 2014. doi: 10.1016/j.aop.2014.06.013.
- 113 PERDEW, J. P. et al. Generalized gradient approximation for the exchange-correlation hole of a many-electron system. **Physical Review B**, v. 54, p. 16533–16539, 1996. doi: 10.1103/PhysRevB.54.16533.
- 114 TAO, J. et al. Climbing the density functional ladder: nonempirical meta-generalized gradient approximation designed for molecules and solids. **Physical Review Letters**, v. 91, p. 146401, 2003. doi: 10.1103/PhysRevLetters91.146401.
- 115 BECKE, A. D. A new mixing of Hartree–Fock and local density-functional theories. **The Journal of Chemical Physics**, v. 98, n. 2, p. 1372–1377, 1993. doi: 10.1063/1.464304.
- 116 PERDEW, J. P. et al. Generalized gradient approximation made simple. **Physical Review Letters**, v. 77, p. 3865–3868, 1996. doi: 10.1103/PhysRevLetters77.3865.
- 117 REN, X. et al. Random-phase approximation and its applications in computational chemistry and materials science. **Journal of Materials Science**, v. 47, n. 21, p. 7447–7471, 2012. doi: 10.1007/s10853-012-6570-4.

## **Appendix**



## APPENDIX A – DENSITY FUNCTIONAL APPROXIMATIONS BEYOND THE LOCAL DENSITY APPROXIMATION

In order to provide a flavour of the level of complexity to construct density functional approximations beyond the LDA, we briefly comment on the general ideas of GGA, meta-GGA, hybrid functionals and the RPA.

### A.1 Generalized Gradient Approximation (GGA)

In the level of sophistication just immediately above LDA, an approximation named *Gradient Expansion Approximation* (GEA) was proposed in a first attempt to improve LDA by means of a power series of gradient corrections  $|\nabla n(\mathbf{r})|^n$ .<sup>113</sup> This approach was shown to perform badly and, in some cases, even worse than LDA. Later, Perdew and colleagues were able to explain the spurious results of GEA in terms of the exchange-correlation hole: the expansion violated two important constraints of  $\rho_{xc}$ . In order to remediate the problems in incorporating gradient corrections, the *Generalized Gradient Approximation* (GGA) was proposed. In GGA, the exchange-correlation functional has the general form  $E_{xc}[n]$  in GGA is defined as

$$E_{xc}^{\text{GGA}}[n] = \int d\mathbf{r} n(\mathbf{r}) f_{xc}^{\text{GGA}}[n(\mathbf{r}), \nabla n(\mathbf{r})], \quad (\text{A.1})$$

where the function  $f^{\text{GGA}}$  is a correction over LDA satisfying two constraints for exchange-correlation hole charges, explicitly,

$$n_x(\mathbf{r}, \mathbf{r}') \leq 0 \quad (\text{A.2})$$

$$\int d\mathbf{r}' n_x(\mathbf{r}, \mathbf{r}') = -1 \quad (\text{A.3})$$

$$\int d\mathbf{r}' n_c(\mathbf{r}, \mathbf{r}') = 0. \quad (\text{A.4})$$

By ensuring eqs. (A.2),  $E_{xc}^{\text{GGA}}[n]$  can be conveniently re-written as

$$E_{xc}^{\text{GGA}}[n] = \int d\mathbf{r} n(\mathbf{r}) \epsilon_{xc}^{\text{LDA}}[n(\mathbf{r})] F_{xc}^{\text{GGA}} \left[ n(\mathbf{r}), \frac{\nabla n(\mathbf{r})}{n^{4/3}(\mathbf{r})} \right], \quad (\text{A.5})$$

where  $F_{xc}^{\text{GGA}}$  is the enhancement factor, a functional of the density and the re-scaled gradient which weights the enhancement of LDA the exchange-correlation energy  $E_{xc}^{\text{LDA}}$ .

A list of possible choices for the enhancement factor  $F_{xc}^{\text{GGA}}$  defines the zoo of “surname initials” GGA functionals, famous examples being PBE, B88, LYP, BLYP. They are divided in two categories: non-empirical and empirical. While in the first approach, the functional form for  $F_{xc}$  is built from physical constraints, the second are extracted from fittings to experimental results. It is important to mention that most of the available

functionals based on GGA are suitable for the class of systems for which they have been proposed, in such a way that functionals performing well for solid state physics are not expected to work in quantum chemistry and vice-versa. For instance, in comparison with LDA, the standard form of the PBE approximation improved remarkably the error in the bond dissociation energy of atoms in molecules and solids, whereas the corrections to lattice constants are comparable. An improvement suiting solids, known as PBEsol, was designed to give accurate lattice constants and surface energies.

## A.2 Meta GGA

In the third rung of the Jacob's ladder there is the Meta GGA approximation.<sup>114</sup> Its proposal arose with the aim to obtain an accurate description of typical atoms, molecules and solids in their equilibrium geometries.

$$E_{\text{xc}}^{\text{meta-GGA}}[n] = \int d\mathbf{r} n(\mathbf{r}) f_{\text{xc}}^{\text{meta-GGA}}[n, \nabla n, \nabla^2 n, \tau], \quad (\text{A.6})$$

where

$$\tau = \frac{1}{2} \sum_{q=\text{occ}} |\nabla \varphi_q|^2 \quad (\text{A.7})$$

is the non-interacting kinetic energy.

Similarly to GGA, meta-GGA functionals abound, all of them are constructed using experimental molecular data.

## A.3 Hybrid functionals and the Adiabatic Connection

The roots of hybrid functionals were grounded in Becke's paper titled "A new mixing of Hartree–Fock and local density–functional theories".<sup>115</sup> Becke's idea resorted to the concept of *Adiabatic Connection* (AC), a rigorous ab initio formulation for the exact exchange-correlation functional

$$E_{\text{xc}}[n] = \int_0^1 d\lambda \langle \Psi_\lambda | \hat{U} | \Psi_\lambda \rangle - U_H[n], \quad (\text{A.8})$$

where  $0 \leq \lambda \leq 1$  is an adimensional parameter whose limits corresponds to fully non-interacting system  $\lambda = 0$  and fully interacting system  $\lambda = 1$ , and  $|\Psi_\lambda\rangle$  is the ground-state wave function for the system with interaction weighted by  $\lambda$ .

Becke realised that a weighted mixture of the exact exchange with a semi-local approximation for the full  $E_{\text{xc}}$  could yield improvements upon GGA and meta-GGA functionals, as in  $\lambda = 0$  the  $E_{\text{xc}}$  reduces to the Hartree-Fock exchange only, whereas semi-local approximations (such as GGA or meta-GGA) provide a good description in

$\lambda = 1$ . An interpolation formula was therefore proposed and, currently, it is referred in the following general form

$$E_{\text{xc}}^{\text{hyb}}[n] = \alpha E_{\text{x}}^{\text{exact}}[n] + (1 - \alpha)E_{\text{x}}[n] + E_{\text{c}}[n], \quad (\text{A.9})$$

where  $E_{\text{x}}$  and  $E_{\text{c}}$  are some semi-local approximation for the functionals of the exchange and correlation energies, respectively;  $E_{\text{x}}^{\text{exact}}$  is the exact exchange energy calculated as in eq. (3.29), and  $0 \leq \alpha \leq 1$  is a mixing parameter, generally obtained by fitting onto empirical data.

In the same fashion of the GGA and meta-GGA families, hybrid functionals are commonly referred by the author's surname initial and a number.<sup>113, 116</sup> Examples include B3LYP, PBE0, HSE, and the meta-GGA subfamily M06.<sup>114</sup> By including an almost exact expression for the exchange contribution to the total  $E_{\text{xc}}$ , results of DFT calculations with hybrid functionals have proven accurate to predict the change of Gibb's free energy in a system, to optimize geometry and, specially, to compute properties depending on the energy spectrum of the material, such as the gap in semiconductors.

#### A.4 Random Phase Approximation (RPA)

Finally, the highest rung of the Jacob's ladder stems from a fully nonlocal approach known as *Random Phase Approximation* (RPA).<sup>117</sup> Besides the common ingredients used in the previous levels, RPA involves occupied and virtual Kohn–Sham orbitals. Shortly, RPA uses the exact expression for  $E_{\text{xc}}[n]$  in terms of the exchange-correlation hole - definition (3.30) - and recall to the adiabatic connection formalism to re-express it in terms of the linear density-response function  $\chi^{\lambda}(\mathbf{r}, \mathbf{r}', \omega)$ , where  $\omega$  is the frequency. To derive the general expression for  $E_{\text{xc}}^{\text{RPA}}$ , we start from the AC formulation for  $E_{\text{xc}}$ , which reads

$$E_{\text{xc}}^{\text{AC}} = \frac{e^2}{2} \int_0^1 d\lambda \int d\mathbf{r} n(\mathbf{r}) \int d\mathbf{r}' \frac{n_{\text{xc}}^{\lambda}(\mathbf{r}, \mathbf{r}')}{|\mathbf{r} - \mathbf{r}'|}, \quad (\text{A.10})$$

where

$$n_{\text{xc}}^{\lambda}(\mathbf{r}, \mathbf{r}') = \frac{\langle \Psi_{\lambda} | \delta\hat{n}(\mathbf{r}) \delta\hat{n}(\mathbf{r}') | \Psi_{\lambda} \rangle}{n(\mathbf{r})} - \delta(\mathbf{r} - \mathbf{r}'), \quad (\text{A.11})$$

where  $\delta\hat{n}(\mathbf{r}) \equiv \hat{n}(\mathbf{r}) - n(\mathbf{r})$  measures the fluctuation of the density operator with its expected value at  $\mathbf{r}$ .

Using the Fluctuation Dissipation Theorem (citar Nozieres) at  $T = 0$ , the first term on the right-hand side of eq. (A.11) can be expressed as follows

$$\langle \Psi_{\lambda} | \delta\hat{n}(\mathbf{r}) \delta\hat{n}(\mathbf{r}') | \Psi_{\lambda} \rangle = -\frac{1}{\pi} \int_0^{\infty} d\omega \text{Im}[\chi^{\lambda}(\mathbf{r}, \mathbf{r}', \omega)]. \quad (\text{A.12})$$

The RPA is employed as an approximation for  $\chi^{\lambda}(\mathbf{r}, \mathbf{r}', \omega)$  and a subsequent expansion of  $|\Psi_{\lambda}\rangle$  followed by the integration of  $\lambda$  yields an expression for orders of corrections

of energy in terms of the occupied and unoccupied orbitals. For a deep introduction to the RPA we refer to Ren et al. <sup>117</sup>

Such a sophisticated level of approximation implies in increasing of the computational cost to perform calculations, a known fatal consequence of climbing the Jacob's ladder for DFT. In fact, many theoretical efforts have been recently combined in order to improve approximations for functionals in a non-empirical approach and, at the same time, to create feasible methodologies to be implemented in efficient computational platforms.

## APPENDIX B – THE NUMERICAL RENORMALIZATION-GROUP IMPLEMENTATION

### B.1 Sectors ( $Q, S$ ), primitive and truncated basis

The Hamiltonian  $\mathcal{H}_N$  in eq. (4.66) conserves two important quantum numbers: the charge  $S$  and the total spin  $S$ . The preservation of these two symmetries can be easily verified calculating the commutators of the corresponding operators  $\hat{Q}$  and  $\hat{\mathbf{S}}$ , which are defined as

$$\hat{Q} = (c_d^\dagger c_d - 1/2) + \sum_{n=0}^N (f_n^\dagger f_n - 1/2), \quad (\text{B.1})$$

and

$$\vec{\mathbf{S}} = \frac{1}{2} \left( c_{d\mu}^\dagger \vec{\sigma}_{\mu\nu} c_{d\nu} + \sum_{n=0}^N f_{n\mu}^\dagger \vec{\sigma}^{\mu\nu} f_{n\nu} \right), \quad (\text{B.2})$$

where  $\vec{\sigma} = \sigma^x \hat{x} + \sigma^y \hat{y} + \sigma^z \hat{z}$  are the Pauli matrices.

It follows that

$$[\mathcal{H}_N, \hat{Q}] = 0 \quad (\text{B.3})$$

$$[\mathcal{H}_N, \hat{\mathbf{S}}] = 0. \quad (\text{B.4})$$

Note that in the  $N$ -th iteration the Hamiltonian described a one-dimensional chain with  $N + 2$  sites. From the definition in eq. (B.1), the maximum and minimum values of charge are therefore  $+(N/2 + 1)$  and  $-(N/2 + 1)$ , respectively.

The conservation of quantum numbers allows to use a convenient basis to carry out the diagonalization of the Hamiltonian. As mentioned in section 4.1, in the iterative solution of the Anderson Hamiltonian on the basis  $\{c_d, f_n\}$ , the conservation of  $Q, S$  and  $S_z$  allows us to combine the operators  $c_d$  and  $f_n$  ( $n = 0, \dots, N$ ) to form a new quantum basis  $\{|Q, S, S_z\rangle\}$  of states with definite  $Q, S, S_z$ . The combination forms subspaces  $(Q, S)$ , which we denote by sectors. The advantage of this choice is that the Hamiltonian operator projected into the basis  $\{|Q, S, S_z\rangle\}$  is block diagonal, each block having a reduced dimension in comparison with the dimension of the full matrix Hamiltonian  $H_N$ .

To give an example, consider that we are going to project the operator  $\mathcal{H}_0$  into the basis  $\{c_d, f_0\}$ , which comprises 16 possible states, as each site can be empty, singly occupied with spin up or down, or double occupied. The matrix Hamiltonian will then have dimension  $16 \times 16$  and a general eigenstate will have the form

$$|\Psi\rangle^{N=0} = \sum_{\sigma_d, \sigma_0 = \_, \downarrow, \uparrow, \ddagger} \psi_{\sigma_d, \sigma_0} |\sigma_d, \sigma_0\rangle. \quad (\text{B.5})$$

The combinations of the states  $|\sigma_d, \sigma_0\rangle$  with definite charge and spin are:

$$|Q = 2, S = 0, S_z = 0, 1\rangle = c_{d\uparrow}^\dagger c_{d\downarrow}^\dagger f_{0\uparrow}^\dagger f_{0\downarrow}^\dagger |0\rangle \quad (\text{B.6})$$

$$|Q = 1, S = 1/2, S_z = +1/2, 1\rangle = c_{d\uparrow}^\dagger c_{d\downarrow}^\dagger f_{0\uparrow}^\dagger |0\rangle$$

$$|Q = 1, S = 1/2, S_z = +1/2, 2\rangle = c_{d\uparrow}^\dagger f_{0\uparrow}^\dagger f_{0\downarrow}^\dagger |0\rangle \quad (\text{B.7})$$

$$|Q = 1, S = 1/2, S_z = -1/2, 1\rangle = c_{d\uparrow}^\dagger c_{d\downarrow}^\dagger f_{0\downarrow}^\dagger |0\rangle$$

$$|Q = 1, S = 1/2, S_z = -1/2, 2\rangle = c_{d\downarrow}^\dagger f_{0\uparrow}^\dagger f_{0\downarrow}^\dagger |0\rangle \quad (\text{B.8})$$

$$|Q = 0, S = 1, S_z = 1, 1\rangle = (c_{d\uparrow}^\dagger c_{d\downarrow}^\dagger + f_{0\downarrow}^\dagger f_{0\uparrow}^\dagger) |0\rangle \quad (\text{B.9})$$

$$|Q = 0, S = 0, S_z = 0, 1\rangle = c_{d\uparrow}^\dagger c_{d\downarrow}^\dagger |0\rangle$$

$$|Q = 0, S = 0, S_z = 0, 2\rangle = (c_{d\uparrow}^\dagger c_{d\downarrow}^\dagger - f_{0\downarrow}^\dagger f_{0\uparrow}^\dagger) |0\rangle$$

$$|Q = 0, S = 0, S_z = 0, 3\rangle = f_{0\downarrow}^\dagger f_{0\uparrow}^\dagger |0\rangle \quad (\text{B.10})$$

$$|Q = -1, S = 1/2, S_z = +1/2, 1\rangle = c_{d\uparrow}^\dagger |0\rangle$$

$$|Q = -1, S = 1/2, S_z = +1/2, 2\rangle = f_{0\uparrow}^\dagger |0\rangle \quad (\text{B.11})$$

$$|Q = -1, S = 1/2, S_z = -1/2, 1\rangle = c_{d\downarrow}^\dagger |0\rangle$$

$$|Q = -1, S = 1/2, S_z = -1/2, 2\rangle = f_{0\downarrow}^\dagger |0\rangle \quad (\text{B.12})$$

$$|Q = -2, S = 0, S_z = 0, 1\rangle = |0\rangle. \quad (\text{B.13})$$

The projection of  $\mathcal{H}_0$  into the basis  $\{Q = 2, S = 0, S_z = 0, p\}$  will result in a matrix  $1 \times 1$ , into the basis  $\{Q = 2, S = 1/2, S_z = +1/2, p\}$ , a matrix  $2 \times 2$ , and so on. The largest block diagonal is found in the sector  $(Q = 0, S = 0)$  with dimension 3.

If there is no magnetic field applied into the Hamiltonian, the  $z$  components of the spin are degenerate, so there is no difference in energy between the states  $|Q, S, S_z\rangle$  and  $|Q, S, -S_z\rangle$ . With this, it is convenient to store only the components  $|Q, S, S_z = +S\rangle$  to carry out the projection and the following diagonalization.

With the previous overview, we can now show how to implement the iterative diagonalization of  $H_N$  in an NRG code. We start in the iteration  $N = -1$ , comprising only the impurity site. Among the four configurations  $|\sigma_d\rangle = |\uparrow\rangle, |\uparrow\rangle, |\downarrow\rangle, |\downarrow\rangle$ , we find three combinations of states  $|Q, S, S_z = S\rangle$  with definite  $Q$  and  $S$ . They are illustrated in Fig. 47.

For a single site in  $N = -1$ , the Hamiltonian reduces to  $H_d$  and we are able to solve exactly the problem by constructing the block of matrix Hamiltonian inside each of the active sectors  $(Q = -1, S = 0)$ ,  $(Q = 0, S = 1/2)$  and  $(Q = 1, S = 0)$  and diagonalizing it to obtain the eigenvalues and eigenvectors. It is simple to show that the basis match the

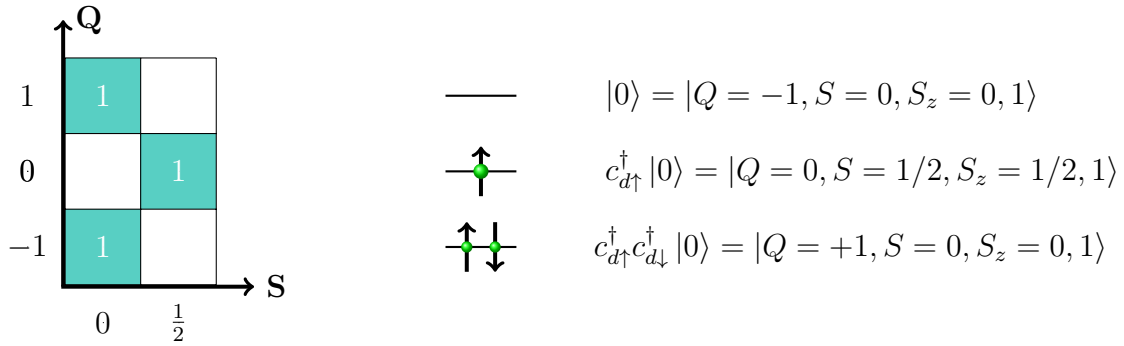


Figure 47 – Sectors of charge and spin active in the iteration  $N = -1$  (cyan squares) and their corresponding number of states (white numbers). This iteration comprises a chain with a single site representing the impurity level  $c_d$ , whose possible states are depicted on the right.

Source: By the author.

eigenstates with eigenenergies

$$\begin{aligned}
 \mathcal{H}_N |Q = +1, S = 0, S_z = 0, 1\rangle &= (2\epsilon_d + U) |Q = +1, S = 0, S_z = 0, 1\rangle \\
 \mathcal{H}_N |Q = 0, S = 1/2, S_z = 1/2, 1\rangle &= \epsilon_d |Q = 0, S = 1/2, S_z = 1/2, 1\rangle \\
 \mathcal{H}_N |Q = -1, S = 0, S_z = 0, 1\rangle &= 0 |Q = -1, S = 0, S_z = 0, 1\rangle. \tag{B.14}
 \end{aligned}$$

As the basis set in the sectors  $(Q, S)$  of the  $N$ -th iteration do not connect to each other, we can store them separately in a numerical data structure. In practice, this means keeping a bidimensional data structure of dimension  $2Q_{max} + 1 \times S_{max} + 1$  to save the information for all sectors  $(Q, S)$ . Here  $Q_{max}$  and  $S_{max}$  are chosen in the begin of the calculation. For instance, we can consider  $Q_{max} = 10$  and  $S_{max} = 10$ . In a pictorial view, the active sectors in a given interaction will be populated with data, whereas the non-active ones will be empty, as illustrated on the left of Fig. 47. The same idea will be used to the next iterations, as we will explain.

Backing to our example with the diagonalization in  $N = -1$ , we proceed to the iteration  $N = 0$  by adding the site representing the Wannier state  $f_0$  to the chain and finding the combinations with definite charge and spin. We have already presented them in eq. (B.6). Note that the new combinations in  $N = 0$  for each sector  $(Q, S)$  were generated from the combinations of the states of  $N = -1$  coming from neighbor sectors, i.e.,  $(Q, S)$  received states of  $c_d$  from the sectors  $(Q \pm 1, S)$  and  $(Q, S \pm 1/2)$  from the iteration  $N = -1$ . For example, the states with  $Q = 1, S = 1/2$  in  $N = 0$  were generated from the states  $|Q = +1, S = 0, S_z = 0\rangle$  and  $|Q = 0, S = 1/2, S_z = 1/2\rangle$  in  $N = -1$ ; the basis with  $Q = 0$  and  $S = 0$  in  $N = 0$  were generated from the states  $|Q = -1, S = 0, S_z = 0\rangle$ ,  $|Q = +1, S = 0, S_z = 0\rangle$  and  $|Q = +1, S = 0, S_z = 0\rangle$  in  $N = -1$ , and so on.

In order to show how to obtain the basis set for all next iterations, we define a systematic strategy to automatically recognise the sectors in  $N$  contributing to the basis in  $N + 1$  as well as calculate the coefficients of the combinations.

Based on the concept of heritage of states from one iteration to the next, we denote by "child" the basis of the current iteration that will be generated from the basis of the previous iteration. The latter is called "parent". Since parents and children sectors are neighbors in the board of sectors in the directions north, south, east, west, we can use a geographical notation to define the rules of heritage to build the child basis from the parent basis.

We introduce a set of operators  $\mathcal{O}_g$ , with  $g = \mathcal{N}, \mathcal{E}, \mathcal{S}, \mathcal{W}$  denoting the directions to which states are being inherited, so that each state of sector  $(Q, S)$  can be generated from adding a spin to the states of sectors  $(Q \pm 1, S \pm 1/2)$ . They are defined as follows

$$\begin{aligned} |Q_c = Q + 1, S_c = S, S_{zc}, p_N\rangle &= \mathcal{O}_{\mathcal{N}} |Q, S, S_z, p_N\rangle_{N-1} \\ |Q_c = Q, S_c = S + 1/2, S_{zc}, p_E\rangle &= \mathcal{O}_{\mathcal{E}} |Q, S, S_z, p_E\rangle_{N-1} \\ |Q_c = Q + 1, S_c = S, S_{zc}, p_S\rangle &= \mathcal{O}_{\mathcal{S}} |Q, S, S_z, p_S\rangle_{N-1} \\ |Q_c = Q, S_c = S - 1/2, S_{zc}, p_W\rangle &= \mathcal{O}_{\mathcal{W}} |Q, S, S_z, p_W\rangle_{N-1}, \end{aligned} \quad (\text{B.15})$$

where the indexes  $p_g$  varies according to the number of states inherited in the direction  $g$  and the operators are defined as

$$\mathcal{O}_{\mathcal{N}} |Q_c, S_c, S_{zc}, p_N\rangle_{N-1} = f_{N\uparrow}^\dagger f_{N\downarrow}^\dagger |Q_c, S, S_z, p_N\rangle_{N-1}, \quad (\text{B.16})$$

$$\begin{aligned} \mathcal{O}_{\mathcal{E}} |Q_c, S_c, S_{zc}, p_E\rangle_{N-1} &= \left( \begin{array}{cc} S_c & \frac{1}{2} \quad S - \frac{1}{2} \\ S_{zc} & \frac{1}{2} \quad S_{zc} - \frac{1}{2} \end{array} \right) f_{N\uparrow}^\dagger |Q_c, S_c - \frac{1}{2}, S_{zc} - \frac{1}{2}, p_E\rangle_{N-1} \\ &+ \left( \begin{array}{cc} S_c & \frac{1}{2} \quad S_c - \frac{1}{2} \\ S_{zc} & -\frac{1}{2} \quad S_{zc} + \frac{1}{2} \end{array} \right) f_{N\downarrow}^\dagger |Q_c, S_c - \frac{1}{2}, S_{zc} + \frac{1}{2}, p_E\rangle_{N-1}, \end{aligned} \quad (\text{B.17})$$

$$\mathcal{O}_{\mathcal{S}} |Q_c, S_c, S_{zc}, p_S\rangle_{N-1} = |Q_c, S, S_z, p_S\rangle_{N-1}, \quad (\text{B.18})$$

$$\begin{aligned} \mathcal{O}_{\mathcal{W}} |Q_c, S_c, S_{zc}, p_N\rangle_{N-1} &= \left( \begin{array}{cc} S_c & \frac{1}{2} \quad S_c + \frac{1}{2} \\ S_{zc} & \frac{1}{2} \quad S_{zc} - \frac{1}{2} \end{array} \right) f_{N\uparrow}^\dagger |Q_c, S_c - \frac{1}{2}, S_{zc} - \frac{1}{2}, p_N\rangle_{N-1} \\ &+ \left( \begin{array}{cc} S_c & \frac{1}{2} \quad S_c + \frac{1}{2} \\ S_{zc} & -\frac{1}{2} \quad S_{zc} + \frac{1}{2} \end{array} \right) f_{N\downarrow}^\dagger |Q_c, S_c - \frac{1}{2}, S_{zc} + \frac{1}{2}, p_N\rangle_{N-1}. \end{aligned} \quad (\text{B.19})$$

The terms in parenthesis in eqs. (B.17) and (B.19) are Clebsch-Gordan coefficients, whose general form considers the addition of two spins  $|S_1, S_{z1}\rangle$  and  $|S_2, S_{z2}\rangle$  yielding a final state with spin  $S$  and  $S_z$ . Explicitly,

$$\left( \begin{array}{c|cc} S & S_1 & S_2 \\ S_z & S_{z1} & S_{z2} \end{array} \right). \quad (\text{B.20})$$

Note that as each child sector inherits states of up to 4 parent sectors (in the directions  $g = \mathcal{N}, \mathcal{E}, \mathcal{S}, \mathcal{W}$ ), the total number of states of  $(Q, S)$  in  $N$  will be

$$P(Q, S)^N = R(Q + 1, S)^{N-1} + R(Q, S - 1/2)^{N-1} + R(Q, S + 1/2)^{N-1} + R(Q - 1, S)^{N-1}, \quad (\text{B.21})$$

where  $R(Q, S)$  denotes the number of states of the sector  $(Q, S)$  after truncation.

At this point, we should mention the terminology used in the NRG diagonalization. We denote *primitive* the basis of states  $|\psi_p\rangle = |Q, S, S_z, p\rangle$  upon which the Hamiltonian operator is projected and diagonalized. The basis of eigenstates  $|\Psi_r\rangle$  after diagonalization and truncation is referred to *truncated* basis.

In Fig. 48 we show how the heritage of states implements the transference of states from the *truncated* basis to the *primitive* basis.

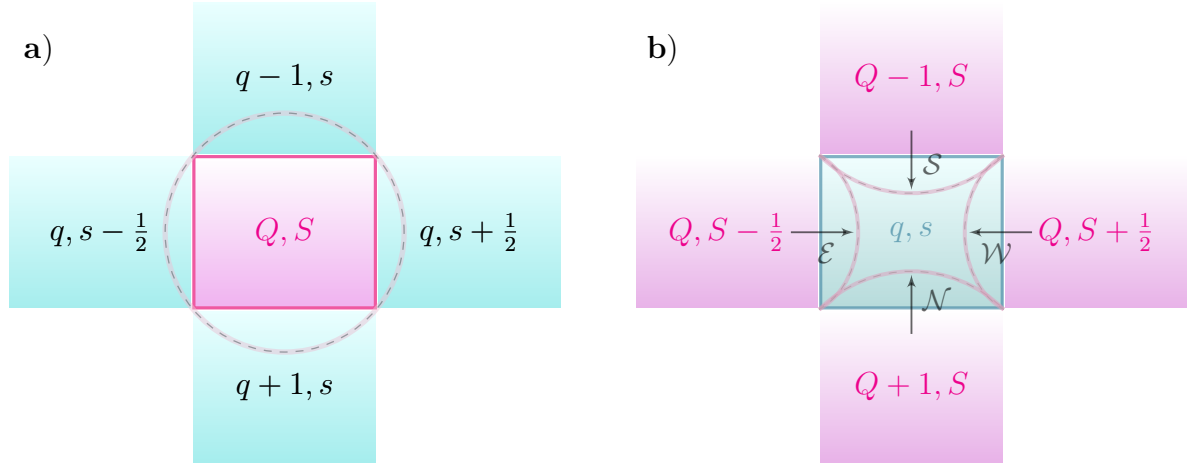


Figure 48 – Construction of the primitive basis of sector  $(Q, S)$  of the  $N$ -th iteration from the states of the iteration  $N - 1$ . Parent and child sectors are coloured in magenta and cyan, respectively. Let  $\{|Q, S, S_z, l\rangle\}$  be the basis of eigenstates of the sector  $(Q, S)$  obtained in iteration  $N - 1$ . The projection of operators  $O_g$  ( $g = \mathcal{S}, \mathcal{W}, \mathcal{E}, \mathcal{N}$ ) onto these states generates the child states in the sectors  $(q - 1, s)$ ,  $(q, s + 1/2)$ ,  $(q + 1, s)$  e  $(q, s - 1/2)$  in the  $N$ -th iteration. The gender  $g$  labelling the operators  $O_g$  correspond to the geographical localization of the neighbor sectors (child sectors): north ( $\mathcal{N}$ ), east ( $\mathcal{E}$ ), south ( $\mathcal{S}$ ) and west ( $\mathcal{W}$ ). **b)** The primitive basis of a child sector  $(q, s)$  in the  $N$ -th iteration is implemented through the heritage of states from parent sectors obtained in  $N - 1$ . The sector  $q, s$  receives states from sectors  $(Q - 1, S)$  via the operators  $O_S$ ,  $(Q, S + 1/2)$  via  $O_W$ ,  $(Q + 1, S)$  via  $O_N$  and  $(Q, S - 1/2)$  via  $O_E$ . Source: By the author.

## B.2 Calculating the matrix elements of the Hamiltonian $H_N$

We have briefly commented about the primitive and truncated basis on section 4.2.3 of chapter 4. We also mentioned that the eigenenergies  $\epsilon_r$  and the matrix elements  $\langle \Psi_r | \mathcal{H}_N | \Psi'_r \rangle$  ingredients needed to calculate the matrix Hamiltonian. To clarify this

statement, let's consider the calculation of the matrix elements in the diagonal, i.e,

$$\langle \psi_p | \mathcal{H}_N | \psi_p \rangle = \langle Q, S, S_z, p | \mathcal{H}_N | Q, S, S_z, p \rangle. \quad (\text{B.22})$$

Using the definition for the RG transformation in eq. (4.69) and recognising that the addition of the states of  $f_n$  cancel in bra's and ket's, we find that

$$\langle Q, S, S_z, p | \mathcal{H}_N | Q, S, S_z, p \rangle = \frac{\sqrt{\Lambda}}{D_N} \epsilon_{r(g)}, \quad (\text{B.23})$$

where  $\epsilon_{r(g)}$  is the energy of the  $r$ -th state inherited from a parent sector  $(Q_g, S_g)$  from the direction  $g$ .

Note that the index  $r(g)$  is defined from a hash table for the heritage of the  $p$ -th state in  $(Q, S)$  and its parents in all directions. An easy way to implement the hash consist in defining an heritage order. For instance, we can define the order as  $\mathcal{S}, \mathcal{E}, \mathcal{W}$  and  $\mathcal{N}$ , in such a way that the first indexes  $p$  will match the  $r(\mathcal{S})$  and range from 0 to  $R(Q+1, S)$ , the next will match  $r(\mathcal{E})$  and will run from  $R(Q+1, S)$  to  $R(Q+1, S) + R(Q, S - 1/2)$ , the next match  $r(\mathcal{W})$  and will run from  $R(Q+1, S) + R(Q, S - 1/2)$  to  $R(Q+1, S) + R(Q, S - 1/2) + R(Q, S + 1/2)$  and finally the next match  $r(\mathcal{N})$  and will run from  $R(Q+1, S) + R(Q, S - 1/2) + R(Q, S + 1/2)$  to  $R(Q+1, S) + R(Q, S - 1/2) + R(Q, S + 1/2) + R(Q, S - 1, S)$ .

To compute the non-diagonal elements, we calculate

$$\begin{aligned} {}^{g'} \langle \psi_{p'} | \mathcal{H}_N | \psi_p \rangle^g &= \frac{t_{N-1}}{D_N} \left( \sum_{\mu} \alpha_{g',g}(S, S_z, \mu) \langle Q, S, S_z, r | f_{N-1\mu}^\dagger | Q', S', S'_z, r' \rangle_{N-1} \right. \\ &\quad \left. + \sum_{\mu} \alpha_{g,g'}(S, S_z, \mu) \langle Q', S', S'_z, r' | f_{N-1\mu} | Q, S, S_z, r \rangle_{N-1} \right), \end{aligned} \quad (\text{B.24})$$

where  $\mu = \uparrow, \downarrow$ ,  $|Q, S, S_z, r\rangle_{N-1}$  is the parent state of  $|q, s, s_z, p\rangle_N^g$ , and the coefficients  $\alpha_{g,g'}$  are calculated according to the definitions (B.16) to (B.19) and are related to the Clebsch-Gordan coefficients. Note that we defined  $|\Psi_r\rangle(Q, S) \equiv |Q, S, S_z, r\rangle$ .

We see from eq. (B.24) that the calculation of the off-diagonal matrix elements involves the computation of matrix elements of the form  $\langle Q', S', S'_z, r' | f_{N-1\mu} | Q, S, S_z, r \rangle_{N-1}$ . To save memory, we can also rely on the independence of the  $S_z$  components to store only reduced matrix elements of form  $\langle Q', S', r' | f_N^\dagger | Q, S, r \rangle$ , which are denoted *invariants*. They are related with the matrix elements  $\langle Q', S', S'_z, r' | f_{N-1\mu} | Q, S, S_z, r \rangle_{N-1}$  through the Wigner-Eckart Theorem, which allows us to write

$$\langle Q+1, S', s_z + \mu | f_{N\mu}^\dagger | Q, S, S_z \rangle = \langle Q+1, S' | f_{N\mu}^\dagger | Q, S \rangle \left( \begin{array}{c|cc} S' & \frac{1}{2} & S \\ \hline S_z + \mu & \mu & S_z \end{array} \right). \quad (\text{B.25})$$

Similarly to the calculation of the primitive basis, recovering the remaining  $S_z$  components from the invariants is more efficient than storing the full matrix elements  $\langle Q', S', S'_z, r' | f_{N-1\mu}^\dagger | Q, S, S_z, r \rangle_{N-1}$ .

Plugging eq. (B.25) into (B.24), we arrive to table 1 for the non vanishing off-diagonal matrix elements of  $H_N$ .

Table 1 – Off-diagonal matrix elements of  $H_N$ . The factors appearing in front of the invariants correspond to the Clebsch-Gordan coefficients  $\alpha_{g,g'}$ . Unlisted combinations of genders  $g$  and  $g'$  vanish.

$g$	$g'$	${}^{g'} \langle \psi_{p'}   H_N   \psi_p \rangle_N^g$
$\mathcal{E}$	$\mathcal{N}$	$\sqrt{\frac{2S}{2S+1}} \langle Q, S - \frac{1}{2}, r'   f_{N-1}^\dagger   Q - 1, S, r \rangle_{N-1}$
$\mathcal{W}$	$\mathcal{N}$	$-\sqrt{\frac{2S+2}{2S+1}} \langle Q, S - \frac{1}{2}, r'   f_{N-1}^\dagger   Q - 1, S, r \rangle_{N-1}$
$\mathcal{N}$	$\mathcal{E}$	$\sqrt{\frac{2S}{2S+1}} \langle Q - 1, S, r'   f_{N-1}^\dagger   Q, S - \frac{1}{2}, r \rangle_{N-1}$
$\mathcal{S}$	$\mathcal{E}$	$\langle Q + 1, S, r'   f_{N-1}^\dagger   Q, S - \frac{1}{2}, r \rangle_{N-1}$
$\mathcal{E}$	$\mathcal{S}$	$\langle Q, S - \frac{1}{2}, r'   f_{N-1}^\dagger   Q + 1, S, r \rangle_{N-1}$
$\mathcal{W}$	$\mathcal{S}$	$\langle Q, S + \frac{1}{2}, r'   f_{N-1}^\dagger   Q + 1, S, r \rangle_{N-1}$
$\mathcal{N}$	$\mathcal{W}$	$-\sqrt{\frac{2s+2}{2s+1}} \langle Q - 1, S, r'   f_{N-1}^\dagger   Q, S + \frac{1}{2}, r \rangle_{N-1}$
$\mathcal{S}$	$\mathcal{W}$	$\langle Q + 1, S, r'   f_{N-1}^\dagger   Q, S + \frac{1}{2}, r \rangle_{N-1}$

Source: By the author.

### B.3 Calculation of invariants

In order to calculate the invariants, we note that the action of the creation operator into a eigenstate  $|Q, S, S_z, r\rangle$  of  $H_N$  changes its charge by 1 and its spin by  $1/2$ . It follows that the non-vanishing matrix elements  $\langle Q', S', S'_z, r' | f_{N\mu}^\dagger | Q, S, S_z, r \rangle$  are

$$\langle Q \pm 1, S, S_z, r' | f_{N\mu}^\dagger | Q, S, S_z, r \rangle \quad (\text{B.26})$$

and

$$\langle Q, S \pm \frac{1}{2}, S_z + \mu, r' | f_{N\mu}^\dagger | Q, S, S_z, r \rangle, \quad (\text{B.27})$$

where  $\mu = \uparrow, \downarrow$ .

Inspecting the genders  $g$  and  $g'$  that correspond to the matrix elements of eqs. (B.26) and (B.27), we conclude that the only possible combinations producing non-zero invariants are  $\mathcal{NW}, \mathcal{NE}, \mathcal{SW}$  and  $\mathcal{SE}$ .

The eigenstates  $|Q, S, S_z, r\rangle_N$  can be written as combinations of the primitive basis, i.e,

$$|Q, S, S_z, r\rangle_N = \sum_p U_{r,p} |Q, S, S_z, p\rangle_N, \quad (\text{B.28})$$

where  $U_{r,p}$  are the unitary matrix that diagonalize  $H_N$  projected onto the basis  $|Q, S, S_z, p\rangle_N$ .

With the relation (B.28), we can write eq. (B.25) as

$$\langle Q \pm 1, S \pm \frac{1}{2}, r' \| f_N^\dagger \| Q, S, r \rangle_N = \sum_{p,p'} U_{r',p'}^\dagger (Q \pm 1, S \pm \frac{1}{2}) \mathcal{M}_{g,g'} U_{r,p}(Q, S), \quad (\text{B.29})$$

where the coefficients  $\mathcal{M}_{g,g'}$  are calculated as

$$\mathcal{M}_{\mathcal{N},\mathcal{W}} = \sqrt{\frac{2S+1}{2S+2}} \quad (\text{B.30})$$

$$\mathcal{M}_{\mathcal{S},\mathcal{E}} = 1 \quad (\text{B.31})$$

$$\mathcal{M}_{\mathcal{N},\mathcal{W}} = -\sqrt{\frac{2S+1}{2S}} \quad (\text{B.32})$$

$$\mathcal{M}_{\mathcal{S},\mathcal{W}} = 1. \quad (\text{B.33})$$

With these definitions we are able to develop the iterative NRG code as follows: in the start of the iteration  $N$ , applying equations (B.16) (B.19) to the primitive basis of  $N - 1$  yields a new set of states in their respective sectors  $(Q, S)$ . The block matrix Hamiltonian  $H_N$  is constructed inside each active sector  $(Q, S)$  and we diagonalize it to find the set of eigenvalues and eigenvectors. From the latter, we truncate the basis set according to  $E_{UV}$  and use the remaining eigenstates to compute physical properties and to construct the basis set of the following iteration. The process is repeated until the iteration  $N_{max}$  obeying equation (4.11).

#### B.4 Calculation of properties

As the diagonalization evolves iteratively, alongside with the calculation of the eigenvalues  $\epsilon_r^N$ , eigenstates  $|\Psi_r\rangle^N$  and invariant matrix elements  $\langle Q \pm 1, S \pm \frac{1}{2}, r' \| f_N^\dagger \| Q, S, r \rangle_N$ , the NRG computation involves the calculation of thermodynamical properties. An example is the zero-bias conductance explored in section 2.3.1 chapter 4.

In order to exemplify how to obtain numerical results for  $\mathcal{G}_\Gamma$  as a function of the temperature  $T$ , we recall to eqs. (2.33) and (2.37). Manipulating these equations allow us to obtain the following expression for  $\mathcal{G}_d$  as a function of  $T$

$$\mathcal{G}_{SET}(T|_{\beta \in \{\beta_N\}}) = \mathcal{G}_2 \frac{\beta \pi \Gamma}{Z} \sum_{r,r'} \frac{|\langle \Psi_r | c_d^\dagger | \Psi_{r'} \rangle|^2}{e^{\beta E_{r'}} + e^{\beta E_r}}, \quad (\text{B.34})$$

where  $|\Psi_r\rangle$  and  $\Psi_{r'}$  are eigenstates of  $H_N$ ,  $\{\beta_N\}$  defines a set of thermal energies accessed in the  $N$ -th iteration and  $\beta = 1/k_B T$ .

To carry out the computation we need to obtain the matrix elements of the operator  $c_d$ . We have shown previously how to obtain the invariants associated with the operator  $f_N$ , which are stored in memory and used when requested. Now, we will show that the matrix elements of all the operators  $f_n$  ( $n = 0, \dots, N-1$ ) and of the operator  $c_d$  can be calculated recursively using the RG transformation in (4.69).

We start calculating the commutator of  $\mathcal{H}_N$  with  $f_n$ , which relates  $f_n$ ,  $f_{n+1}$  and  $f_{n-1}$ . Explicitly

$$\begin{aligned} [\mathcal{H}_N, f_n^\dagger] &= \frac{1}{D_N} \sum_l t_l \left( [f_l^\dagger f_{l+1}, f_n^\dagger] + [f_l^\dagger f_l, f_n^\dagger] \right) \\ &= \frac{t_{n-1}}{D_N} f_{n-1}^\dagger + \frac{t_n}{D_N} f_{n+1}^\dagger. \end{aligned} \quad (\text{B.35})$$

In particular, for  $n = N$ , we have

$$[\mathcal{H}_N, f_N^\dagger] = \frac{t_{N-1}}{D_N} f_{N-1}^\dagger. \quad (\text{B.36})$$

If we calculate the invariant matrix elements of the commutator, we have

$$\begin{aligned} \langle Q, S, S_z, r \| [\mathcal{H}_N, f_N^\dagger] \| Q', S', S'_z, r' \rangle &= \frac{t_{N-1}}{D_N} \langle Q, S, S_z, r \| f_{N-1}^\dagger \| Q', S', S'_z, r' \rangle \\ &= \langle Q, S, S_z, r \| \mathcal{H}_N f_N^\dagger \| Q', S', S'_z, r' \rangle \\ &\quad - \langle Q, S, S_z, r \| f_N^\dagger \mathcal{H}_N \| Q', S', S'_z, r' \rangle \\ &= (\epsilon_r - \epsilon_{r'}) \langle Q, S, S_z, r \| f_N^\dagger \| Q', S', S'_z, r' \rangle, \end{aligned} \quad (\text{B.37})$$

i.e.,

$$\langle Q, S, S_z, r \| f_{N-1}^\dagger \| Q', S', S'_z, r' \rangle = \frac{\Delta \epsilon_{r,r'} D_N}{t_{N-1}}, \quad (\text{B.38})$$

where  $\Delta \epsilon_{r,r'} \equiv (\epsilon_r - \epsilon_{r'})$ .

Extending the previous calculations to the remaining  $f_n$ 's and  $c_d$ , we find

$$\begin{aligned} \langle Q, S, S_z, r \| f_n^\dagger \| Q', S', S'_z, r' \rangle &= - \frac{t_{n+1}}{t_n} \langle Q, S, S_z, r \| f_{n+2}^\dagger \| Q', S', S'_z, r' \rangle \\ &\quad + \frac{D_N}{t_n} \Delta \epsilon_{r,r'} \langle Q, S, S_z, r \| f_{n+1}^\dagger \| Q', S', S'_z, r' \rangle \end{aligned} \quad (\text{B.39})$$

and

$$\begin{aligned} \langle Q, S, S_z, r \| c_d^\dagger \| Q', S', S'_z, r' \rangle &= -\frac{t_0}{\sqrt{2V}} \langle Q, S, S_z, r \| f_{n+2}^\dagger \| Q', S', S'_z, r' \rangle \\ &\quad + \frac{\mathcal{D}_N}{\sqrt{2V}} \Delta\epsilon_{r,r'} \langle Q, S, S_z, r \| f_{n+1}^\dagger \| Q', S', S'_z, r' \rangle. \end{aligned} \quad (\text{B.40})$$

Note that in the previous passages, we considered  $\eta_n = 0$  for all  $n = 0, \dots, N$  and  $W = 0$ . The inclusion of these and additional terms in  $H_N$  only change the first relation obtained in (B.35).

In practice, the calculation of the conductance in  $\mathcal{G}_d$  in eq. (B.34) for a thermal scale  $\beta_N$  is carried out after the calculation of the invariants, from which we retrieve the matrix elements of  $c_d$  according to eq. (B.40).

## APPENDIX C – ANALYTICAL STEPS WITHIN THE NUMERICAL RENORMALIZATION GROUP

This appendix presents a few more steps involved in the analytical formulation of the Renormalization-Group procedure.

### C.1 Lanczos coefficients in Wilson's formulation

In his Numerical Renormalization-Group formulation, which is widely used in most computations of impurity models, Wilson provided a simple formula for the co-diagonal coefficients obtained after the the Lanczos transformation.<sup>16</sup> They are calculated as follows

$$t_n = D\Lambda^{-n/2} \frac{1 - \Lambda^{-(n+1)}}{\sqrt{1 - \Lambda^{-(2n+3)}} \sqrt{1 - \Lambda^{-(2n+1)}}} \frac{1 + \Lambda^{-1}}{\log \Lambda}. \quad (\text{C.1})$$

The diagonal coefficients  $\eta_n$  did not enter in his calculation because they vanished. As we explained in chapter 4, the diagonal coefficients will be different from zero only when the conduction band is asymmetric with respect to the Fermi level, which is set as  $\epsilon_F = 0$ .

The possibility to derive an analytical expression for the Lanczos coefficients, such as that in eq. (C.1), depends on some assumptions on the characteristics of the conduction band. In his approach, Wilson considered a half-filled band defined in the interval  $[-D, D]$  with a flat density of states  $\rho(\epsilon) = 1$ . The hybridization function was also considered constant, i.e.,  $\Gamma(\epsilon) = \Gamma$ , so that  $V = \sqrt{2\Gamma/\rho\pi}$  is also constant. From the recursion formula connecting the coefficients  $t_n$ ,  $\eta_n$ ,  $u_{n,m}$  and  $v_{n,m}$ , he was able to find an analytical generation functional and solve it. Details of his calculation can be found in Appendix VII in Wilson et al.<sup>16</sup>

To exemplify how the recursion relation can be derived, below, we will review few steps of the Lanczos transformation.

### C.2 Numerical Renormalization-Group approach for impurity models

Most models describing the interaction of magnetic impurities coupled to a free metallic band can be modelled through the Anderson Hamiltonian, which have the general form

$$H_A = \sum_{\mathbf{k}} \epsilon_{\mathbf{k}} c_{\mathbf{k}}^\dagger c_{\mathbf{k}} + \sum_j \epsilon_{d,j} n_j + \sum_j U_j n_{d,j,\uparrow} n_{d,j,\downarrow} + \sum_{\mathbf{k},j} V_{\mathbf{k},j} (c_{\mathbf{k}}^\dagger c_{d,j} + H.c.), \quad (\text{C.2})$$

where  $c_{\mathbf{k}}^\dagger$  ( $c_{\mathbf{k}}$ ) are the operators that creates (destroy) one electron in the energy level  $\epsilon_{\mathbf{k}}$  of the conduction band with momentum  $\mathbf{k}$ ,  $c_{d,j}^\dagger$  ( $c_{d,j}$ ) creates (annihilates) one electron in

the  $j$ -th localized orbital  $\epsilon_{d,j}$  of the impurity,  $n_{d,j} \equiv c_{d,j}^\dagger c_{d,j}$  are the number operators,  $U_j$  is the Coulomb repulsion of the  $j$ -th level and  $V_{\mathbf{k},j}$  is the hybridization between the  $j$ -th level and the conduction band.

The conduction band extends to the domain  $[-D_-, D_+]$ , having a band width  $D_+ + D_-$ , and has the dispersion relation  $\epsilon_{\mathbf{k}}$  and density of states

$$\rho(\epsilon) = \sum_{\mathbf{k}} \delta(\epsilon - \epsilon_{\mathbf{k}}), \quad (\text{C.3})$$

which in most approaches is considered to be constant  $\rho = \frac{1}{2D}$  for symmetric one-dimensional free electron systems  $D_- = D_+$ .

The recipe to employ a Numerical Renormalization-Group scheme to solve the Hamiltonian described by eq. (C.2) starts with the logarithmic discretization of the conduction band. This task must be carried out in such a way that the interaction of the impurity with the conduction band is preserved. In practice, we want to bring the Hamiltonian of eq. (C.2) into the discrete iterative form

$$H = \sum_n (t_n f_{n+1}^\dagger f_n + H.c.) + \eta_n f_n^\dagger f_n + \tilde{V}(f_0^\dagger c_d + H.c.) + \epsilon_d n_d + U n_{d,\uparrow} n_{d,\downarrow}, \quad (\text{C.4})$$

where, for simplicity, we assume that  $j = 1$  and  $\mathbf{k} = k\hat{x}$ .

Mapping each term, we would like to construct a basis transformation for that

$$H_{cb} = \sum_{\mathbf{k}} \epsilon_{\mathbf{k}} c_{\mathbf{k}}^\dagger c_{\mathbf{k}} \rightarrow \sum_n (t_n f_{n+1}^\dagger f_n + H.c.) + \eta_n f_n^\dagger f_n, \quad (\text{C.5})$$

and

$$H_{hyb} = \sum_{\mathbf{k},j} V_{\mathbf{k},j} (c_{\mathbf{k}}^\dagger c_{d,j} + H.c.) \rightarrow \tilde{V}(f_0^\dagger c_d + H.c.), \quad (\text{C.6})$$

the operator  $f_0$  being defined as

$$f_0 \equiv \mathcal{N} \sum_{\mathbf{k}} V_{\mathbf{k}} c_{\mathbf{k}}, \quad (\text{C.7})$$

$\mathcal{N}$  is a normalization constant.

In the following, we are going to summarize the steps of the procedure.

### C.2.1 Continuous base

It is convenient to define a continuous base connecting the momenta  $\mathbf{k}$  with the energies  $\epsilon$ . We define

$$c_\epsilon = \mathcal{N}_\epsilon \sum_{\mathbf{k}} \delta(\epsilon - \epsilon_{\mathbf{k}}) c_{\mathbf{k}} \quad (\text{C.8})$$

, where the normalization factor  $\mathcal{N}_\epsilon$  can be calculated from the traditional commutation relation

$$\begin{aligned}
 \{c_\epsilon^\dagger c_{\epsilon'}\} &= \delta(\epsilon - \epsilon') \\
 &= \mathcal{N}_\epsilon \mathcal{N}_{\epsilon'} \sum_{\mathbf{k}} \sum_{\mathbf{k}'} \delta(\epsilon - \epsilon_{\mathbf{k}}) \delta(\epsilon' - \epsilon_{\mathbf{k}'}) \{c_{\mathbf{k}}^\dagger, c_{\mathbf{k}'}\} \\
 &= \mathcal{N}_\epsilon \mathcal{N}_{\epsilon'} \sum_{\mathbf{k}} \sum_{\mathbf{k}'} \delta(\epsilon - \epsilon_{\mathbf{k}}) \delta(\epsilon' - \epsilon_{\mathbf{k}'}) \delta_{\mathbf{k}, \mathbf{k}'} \\
 &= \mathcal{N}_\epsilon \mathcal{N}_{\epsilon'} \sum_{\mathbf{k}} \delta(\epsilon - \epsilon') \delta(\epsilon - \epsilon_{\mathbf{k}}) \\
 &= \mathcal{N}_\epsilon \mathcal{N}_{\epsilon'} \delta(\epsilon - \epsilon') \sum_{\mathbf{k}} \delta(\epsilon - \epsilon_{\mathbf{k}}) \\
 &= \mathcal{N}_\epsilon \mathcal{N}_{\epsilon'} \delta(\epsilon - \epsilon') \rho(\epsilon).
 \end{aligned} \tag{C.9}$$

Therefore,

$$\mathcal{N}_\epsilon = \frac{1}{\sqrt{\rho(\epsilon)}}. \tag{C.10}$$

By inverting eq. (C.8), we find

$$\begin{aligned}
 \int_{-D_-}^{+D_+} d\epsilon \sqrt{\rho(\epsilon)} c_\epsilon &= \int_{-D_-}^{+D_+} d\epsilon \sum_{\mathbf{k}} \delta(\epsilon - \epsilon_{\mathbf{k}}) c_{\mathbf{k}} \\
 &= \int_{-D_-}^{+D_+} d\epsilon \rho(\epsilon) c_{\mathbf{k}} \\
 c_{\mathbf{k}} &= \int_{-D_-}^{+D_+} d\epsilon \sqrt{\rho(\epsilon)} c_\epsilon.
 \end{aligned} \tag{C.11}$$

For a flat band, as in Wilson's approach  $\mathcal{N}_\epsilon = (\rho)^{-1/2}$ , and we do not need to carry the dependence on  $\epsilon$  on the density of states. For a constant couplings  $V_j$ , the calculations involving the coupling term of the Hamiltonian are also simplified.

For instance, we can re-write the Hamiltonian of eq. (C.2) by identifying

$$H_{cb} = \int_{-D_-}^{+D_+} d\epsilon \epsilon c_\epsilon^\dagger c_\epsilon, \tag{C.12}$$

$$H_{hyb} = \sum_j V_j \int_{-D_-}^{+D_+} d\epsilon (c_\epsilon^\dagger c_{d,j} + H.c.). \tag{C.13}$$

### C.2.2 Logarithmic discretization

We divide the interval  $[-D_-, D_+]$  into subintervals  $I_m$  according to a parameter  $\Lambda > 1$  and a parameter  $0 < z \leq 1$ , so that

$$\begin{aligned} I_m^+ &= [\varepsilon_m^+, \varepsilon_{m-1}^+] \\ I_m^- &= [\varepsilon_{m-1}^-, \varepsilon_m^-] \quad (m = 0, 1, 2, 3, \dots), \end{aligned} \quad (\text{C.14})$$

where

$$\varepsilon_m^\pm = \begin{cases} \pm D_\pm, & m = 0 \\ \pm D_\pm \Lambda^{-m-z}, & \text{otherwise} \end{cases}. \quad (\text{C.15})$$

Each interval has width

$$d_m^\pm = D_\pm \Lambda^{-m-z} (1 - \Lambda^{-1}). \quad (\text{C.16})$$

In the limit  $\Lambda \rightarrow 1$ , the discretization scheme is linear, so that each interval  $I_m$  has the same width. If the intervals are made as little as possible, we recover the continuous limit.

In Wilson's formulation, all steps above can be obtained by making  $z = 1$ .

Within each interval  $I_m^\pm$ , we define a complete set of operators

$$\begin{aligned} a_m &= \mathcal{N}_{m+} \int_{I_m^+} d\epsilon c_\epsilon \\ b_m &= \mathcal{N}_{m-} \int_{I_m^-} d\epsilon c_\epsilon. \end{aligned} \quad (\text{C.17})$$

The normalization constants can be calculated, for instance, as follows

$$\begin{aligned} \{a_m^\dagger, a_{m'}'\} &= \delta_{m,m'} \\ &= \mathcal{N}_{m+} \mathcal{N}_{m'-} \int_{I_m^+} \int_{I_{m'}^+} d\epsilon d\epsilon' \{c_\epsilon^\dagger, c_{\epsilon'}'\} \\ &= \mathcal{N}_{m+} \mathcal{N}_{m'-} \int_{I_m^+} \int_{I_{m'}^+} d\epsilon d\epsilon' \delta(\epsilon - \epsilon') \\ &= \mathcal{N}_{m+} \mathcal{N}_{m'-} \int_{\varepsilon_m^+}^{\varepsilon_{m-1}^+} d\epsilon \\ &= \mathcal{N}_{m+} \mathcal{N}_{m'-} D_+ \Lambda^{1-z-m} (1 - \Lambda^{-1}), \end{aligned} \quad (\text{C.18})$$

so that

$$\mathcal{N}_{m\pm} = \frac{1}{D_\pm^{1/2}} \frac{\Lambda^{(m+z-1)/2}}{(1 - \Lambda^{-1})^{1/2}}. \quad (\text{C.19})$$

Notice, that for  $m = 0$ ,

$$\begin{aligned} a_0 &= \frac{1}{\sqrt{D_+(1 - \Lambda^{-1})}} \int_{D_+\Lambda^{-z}}^{D_+} d\epsilon c_\epsilon \\ b_0 &= \frac{1}{\sqrt{D_-(1 - \Lambda^{-1})}} \int_{D_-}^{D_-\Lambda^{-z}} d\epsilon c_\epsilon. \end{aligned} \quad (\text{C.20})$$

We want to project the conduction-band Hamiltonian into the basis of operators  $a_m$  and corresponding  $b_m$ , i.e.

$$\begin{aligned} H_{cb} &= (\mathcal{E}_0^+(z, \Lambda) a_0^\dagger a_0 + \mathcal{E}_0^-(z, \Lambda) b_0^\dagger b_0) + \sum_{m=1}^{\infty} (\mathcal{E}_m^+(z, \Lambda) a_m^\dagger a_m + \mathcal{E}_m^-(z, \Lambda) b_m^\dagger b_m) \\ &= \sum_m (\mathcal{E}_m^+(z, \Lambda) a_m^\dagger a_m + \mathcal{E}_m^-(z, \Lambda) b_m^\dagger b_m) \end{aligned} \quad (\text{C.21})$$

We can define the energies  $\mathcal{E}_m^\pm$  as

$$\mathcal{E}_m^\pm = \frac{1}{d_m} \int_{I_{m\pm}} g(\epsilon) d\epsilon, \quad (\text{C.22})$$

or, in terms of the hybridization function

$$\mathcal{E}_m^\pm = \frac{\int_{I_{m\pm}} d\epsilon \epsilon \Delta(\epsilon)}{\int_{I_{m\pm}} d\epsilon \Delta(\epsilon)}. \quad (\text{C.23})$$

To adapt the previous form to the generalized NRG using the parameter  $z$ , we can also define

$$\mathcal{E}_m^\pm(z, \Lambda) = A_\Lambda \frac{\int_{I_{m\pm}} d\epsilon \Delta(\epsilon)}{\int_{I_{m\pm}} \frac{d\epsilon}{\epsilon} \Delta(\epsilon)}, \quad (\text{C.24})$$

where  $A_\Lambda$  is a recurrent factor in Numerical Renormalization-Group calculations given by

$$A_\Lambda = \frac{\Lambda + 1}{\Lambda - 1} \frac{\log \Lambda}{2}. \quad (\text{C.25})$$

Projecting the operator  $f_0$  defined in eq. (C.7) on to the basis comprising the fermionic states  $a_m$  and  $b_m$ , we have

$$f_0 = \frac{1}{\sqrt{\bar{\gamma}}} \sum_m \gamma_m^+ a_m + \gamma_m^- b_m, \quad (\text{C.26})$$

where

$$(\gamma_m^\pm)^2 = \int_{I_{m\pm}} d\epsilon \Delta(\epsilon) \quad (\text{C.27})$$

$$\bar{\gamma} = \sum_{I_{m+}} (\gamma_m^+)^2 + \sum_{I_{m-}} (\gamma_m^-)^2 = \int_{-D_-}^{D_+} d\epsilon \Delta(\epsilon) \quad (\text{C.28})$$

### C.2.3 Lanczos transformation

Finally, we will construct the discrete basis upon which the Hamiltonian of eq. (C.2) can be numerically diagonalized. Our task is now to express the conduction band Hamiltonian as

$$\begin{aligned} H_{cb} &= \sum_{\mathbf{k}} \epsilon_{\mathbf{k}} c_{\mathbf{k}}^\dagger c_{\mathbf{k}} \\ &= \sum_m (\mathcal{E}_m^+(z, \Lambda) a_m^\dagger a_m + \mathcal{E}_m^-(z, \Lambda) b_m^\dagger b_m) \\ &= \sum_n (t_n f_n^\dagger f_{n+1} + H.c.) + \eta_n f_n^\dagger f_n. \end{aligned} \quad (\text{C.29})$$

To this end, we define the basis of orthonormal operators  $\{f_n\}$ :

$$f_n = \sum_m u_{nm} a_m + v_{nm} b_m, \quad (\text{C.30})$$

obeying the commutation relations

$$\{f_n^\dagger, f_{n'}\} = \delta_{n,n'}. \quad (\text{C.31})$$

The inverse transformation is also provided

$$\begin{aligned} a_m &= \sum_n u_{nm} f_n \\ b_m &= \sum_n v_{nm} f_n. \end{aligned} \quad (\text{C.32})$$

Notice that from eqs. (C.27) and (C.28), we already have the coefficients  $u_{0m} = \frac{\gamma_m^+}{\sqrt{\gamma}}$  and  $v_{0m} = \frac{\gamma_m^-}{\sqrt{\gamma}}$ . This allow us to devise a recursive procedure to determine the coefficients  $t_n$  and  $\eta_n$  in eq. (C.29).

To see how it works, let start with the coefficients  $t_0$  and  $\eta_0$ . They can be recognised by substituting eqs. (C.32) into (C.21) and expanding the sum

$$\begin{aligned} \sum_m \mathcal{E}_m^+ a_m^\dagger a_m + \mathcal{E}_m^- b_m^\dagger b_m &= \sum_m \mathcal{E}_m^+ \sum_{n,n'} u_{n,m} u_{n',m} f_n^\dagger f_{n'} + \sum_m \mathcal{E}_m^- \sum_{n,n'} v_{n,m} v_{n',m} f_n^\dagger f_{n'} \\ &= \sum_m (\mathcal{E}_m^+ u_{0,m} u_{0,m} + \mathcal{E}_m^- v_{0,m} v_{0,m'}) f_0^\dagger f_0 \\ &\quad + \sum_m (\mathcal{E}_m^+ u_{0,m} u_{1,m} + \mathcal{E}_m^- v_{0,m} v_{1,m'}) f_0^\dagger f_1 \\ &\quad + \text{non-}f_0 \text{ terms.} \end{aligned} \quad (\text{C.33})$$

We want the coefficient of  $f_0^\dagger f_0$  to be  $\eta_0$ . Therefore,

$$\begin{aligned}
\eta_0 &= \sum_m \mathcal{E}_m^+ u_{0,m}^2 + \mathcal{E}_m^- v_{0,m}^2 \\
&= \frac{1}{\bar{\gamma}} \sum_m \mathcal{E}_m^+(\gamma_m^+)^2 + \mathcal{E}_m^-(\gamma_m^-)^2 \\
&= \frac{1}{\bar{\gamma}} \sum_m \frac{\int_{I_{m+}} d\epsilon \epsilon \Delta(\epsilon)}{\int_{I_{m+}} d\epsilon \Delta(\epsilon)} (\gamma_m^+)^2 + \frac{\int_{I_{m-}} d\epsilon \epsilon \Delta(\epsilon)}{\int_{I_{m-}} d\epsilon \Delta(\epsilon)} (\gamma_m^-)^2 \\
&= \frac{1}{\bar{\gamma}} \sum_m \int_{I_{m+}} d\epsilon \epsilon \Delta(\epsilon) + \int_{I_{m-}} d\epsilon \epsilon \Delta(\epsilon) \\
&= \frac{1}{\bar{\gamma}} \int_{-D_-}^{+D_+} d\epsilon \Delta(\epsilon).
\end{aligned} \tag{C.34}$$

Now, we would like to have the coefficient of the last term on the right-hand side of eq. (C.33) equal to

$$t_0 f_1 = \sum_m (\mathcal{E}_m^+ u_{0,m} u_{1,m} + \mathcal{E}_m^- v_{0,m} v_{1,m'}) f_1. \tag{C.35}$$

We can go back to eq. (C.33) and write

$$\left( \sum_m \mathcal{E}_m^+ a_m^\dagger u_{0m} + \mathcal{E}_m^- b_m^\dagger v_{0m} \right) f_0 = t_0 f_1^\dagger f_0 + \eta_0 f_0^\dagger f_0, \tag{C.36}$$

i.e.

$$t_0 f_1^\dagger = \sum_m \mathcal{E}_m^+ u_{0m} a_m^\dagger + \mathcal{E}_m^- v_{0m} b_m^\dagger - \eta_0 f_0^\dagger \tag{C.37}$$

Computing the commutator of the previous eq. (C.38) with its complex conjugate, we find

$$\begin{aligned}
t_0^2 \{f_1^\dagger, f_1\} &= \sum_{m,m'} \left[ \mathcal{E}_m^+ \mathcal{E}_{m'}^+ u_{0,m} u_{0,m'} \{a_m^\dagger, a_{m'}^\dagger\} + \mathcal{E}_m^- \mathcal{E}_{m'}^- v_{0,m} v_{0,m'} \{b_m^\dagger, b_{m'}^\dagger\} + \mathcal{E}_m^- v_{0,m} v_{1,m'} \right] f_1 \\
&\quad - 2\eta_0 \sum_m \mathcal{E}_m^+ u_{0m} \{a_m^\dagger, f_0\} - 2\eta_0 \mathcal{E}_m^- v_{0m} \{b_m^\dagger, f_0\} + \eta_0^2 \{f_0^\dagger, f_0\} \\
&= \sum_m (\mathcal{E}_m^+ u_{0,m})^2 + (\mathcal{E}_m^- v_{0,m})^2 - 2\eta_0 \mathcal{E}_m^+ u_{0,m}^2 - 2\eta_0 \mathcal{E}_m^- v_{0,m}^2 + \eta_0^2 (u_{0,m}^2 + v_{0,m}^2) \\
&= \sum_m u_{0,m}^2 (\mathcal{E}_m^+ - \eta_0)^2 + v_{0,m}^2 (\mathcal{E}_m^- - \eta_0)^2 \\
&= \frac{1}{\bar{\gamma}} \sum_m (\gamma_m^+)^2 (\mathcal{E}_m^+ - \eta_0)^2 + (\gamma_m^-)^2 (\mathcal{E}_m^- - \eta_0)^2.
\end{aligned} \tag{C.38}$$

By doing this, we find that

$$t_0^2 = \sum_m (\mathcal{E}_m^+ - \eta_0)^2 u_{0,m}^2 + (\mathcal{E}_m^- - \eta_0)^2 v_{0,m}^2, \tag{C.39}$$

and identify also the coefficients of  $f_1$  as

$$\begin{aligned} u_{1,m} &= \frac{1}{t_0}(\mathcal{E}_m^+ - \eta_0)u_{0,m} \\ v_{1,m} &= \frac{1}{t_0}(\mathcal{E}_m^- - \eta_0)v_{0,m}. \end{aligned} \quad (\text{C.40})$$

By repeating the same procedure described above, we can show that the following coefficients can be calculated recursively from the relations

$$\begin{aligned} \eta_n &= \sum_m (\mathcal{E}_m^+ u_{n,m}^2 + \mathcal{E}_m^- v_{n,m}^2) \\ t_n^2 &= \sum_m (\mathcal{E}_m^+ u_{n,m}^2 + \mathcal{E}_m^- v_{n,m}^2) - t_{n-1}^2 - \eta_n^2, \end{aligned} \quad (\text{C.41})$$

and

$$\begin{aligned} u_{n+1,m} &= \frac{1}{t_n}[(\mathcal{E}_m^+ - \eta_n)u_{n,m} - t_{n-1}u_{n-1,m}] \\ v_{n+1,m} &= \frac{1}{t_n}[(\mathcal{E}_m^- - \eta_n)v_{n,m} - t_{n-1}v_{n-1,m}]. \end{aligned} \quad (\text{C.42})$$

In practice, to avoid numerical error propagation, we compute the set of  $u_{n,m}$  and  $v_{n,m}$  for a given  $n$  and use a Gram-Schmidt procedure to assure that the basis for the  $f_n$  operators is orthonormalized.